Electronic Structure of the Silicon Vacancy Color Center in Diamond

Dissertation

zur Erlangung des Grades
des Doktors der Naturwissenschaften
der Naturwissenschaftlich-Technischen Fakultät II
- Physik und Mechatronik -
der Universität des Saarlandes

vorgelegt von

Christian Joachim Hepp

Saarbrücken

2014

Tag des Kolloquiums:	12.12.2014
Dekan:	Univ.-Prof. Dr.-Ing. Georg Frey
Mitglieder des Prüfungsausschusses:	Univ.-Prof. Dr. rer. nat. Rolf Pelster Univ.-Prof. Dr. rer. nat. Christoph Becher Univ.-Prof. Dr. rer. nat. Gregor Jung Dr. rer. nat. Philipp Bender

Meiner Familie, für die Vergangenheit.
Meiner Frau, für die Gegenwart.
Unserem Kind, für die Zukunft.

Zusammenfassung

Diese Dissertation befasst sich mit der elektronischen Struktur des Silizium-Fehlstellen (SiV) Farbzentrums in Diamant. Neben detaillierten spektroskopischen Untersuchungen werden erste Experimente zur Nutzung des Defekts als Quantenbit (Qubit) gezeigt. Ausgehend von der molekularen Struktur des Defekts leiten wir unter Verwendung von Gruppentheorie ein detailliertes Modell her, für das wir die irreduziblen Darstellungen der elektronischen Zustände bestimmen. Wir berechnen Wechselwirkungsterme, welche die bestehende energetische Entartung der Zustände aufheben, und zur Ausbildung einer Feinstruktur im Emissionsspektrum des Defekts führen. Diese Feinstruktur wird experimentell an einzelnen SiV-Zentren in Diamantproben hoher kristalliner Güte untersucht. Hierzu verwenden wir konfokale Mikroskopie bei kryogenen Temperaturen. Zudem legen wir magnetische Felder an, wodurch die Entartung magnetischer Unterniveaus aufgehoben wird, und somit der Spin-Zustand des Defektzentrums eindeutig bestimmt wird. Unsere Untersuchungen ermöglichen eine widerspruchsfreie Beschreibung der SiV Niveaustruktur und zeigen, dass die Zustände eine hohe Spin-Polarisation aufweisen können. Darauf aufbauend demonstrieren wir Spin-selektive Anregung und evaluieren die Ergebnisse im Kontext des hergeleiteten Modells. Zusätzlich wird das theoretische Modell erweitert, um den Einfluss von Kristallverspannung auf die Niveaustruktur zu beschreiben. Zur experimentellen Überprüfung untersuchen wir einzelne SiV-Zentren in Nanodiamanten, welche hohe Verspannungsfelder aufweisen. Auch hier zeigt sich eine hervorragende Übereinstimmung mit den Vorhersagen des theoretischen Modells.

Abstract

This thesis investigates the electronic structure of the silicon vacancy (SiV) color center in diamond. We show detailed spectroscopic investigations and demonstrate first steps towards using the defect as quantum bit (qubit). Starting from the molecular structure of the defect, we first derive a detailed theoretical model using the concept of group theory. With this approach, we calculate the irreducible representation of the electronic states, and determine the interaction terms which lift the energetic degeneracy of these states. Owing to this level splitting, the optical emission spectrum of the defect shows a fine structure, which is observed for individual SiV centers in high quality diamond samples, using confocal microscopy at cryogenic temperatures. We apply magnetic fields in order to lift the degeneracy of magnetic sublevels and to reveal the spin state of the defect. From the excellent agreement with the proposed theoretical model, we obtain a consistent picture of the level structure and reveal, that these states can exhibit near unity spin polarization. As a first step towards spin initialization, we demonstrate spin selective excitation and discuss the results in the context of the derived electronic structure. After having determined the properties of the SiV center in an ideal environment, we extend the theoretical model to include the effect of crystal strain on the level structure. As an experimental test-bench for emitters in strained environments, we investigate nanodiamonds with single SiV centers. Again, we find an excellent agreement with the theoretical predictions.

Contents

Introduction

In this thesis, we study the electronic structure of a defect center in diamond, and we investigate its suitability for an application in quantum information sciences. To motivate this study, we here briefly review how solid state defects can be utilized to implement elements of quantum information processing (QIP). The key idea of QIP is to use the laws of quantum mechanics to enhance the capabilities of transferring and manipulating data [1]. In classical information technology, a conventional computer performs operations on the binary units (bits), which can either have the value 1 or 0. In QIP, the basic units are called quantum bits or qubits. In contrast to their classical counterparts, qubits can be prepared in so-called superposition states, thus they represent 0 and 1 at the same time. Qubits are implemented using isolated quantum systems, e.g. the electronic states of an atom or the polarization states of a single photon, and many other physical systems [2].

Multiple qubits in a superposition state can be combined to form quantum registers, which then represent larger numbers. The information content stored in a quantum register of N qubits scales with 2^N, resulting in a massive computational parallelism. However, this information is fragile as the superposition state collapses upon a projective measurement. To harness the power of such a quantum computer, one must assure that the manipulation of the quantum register is performed in a coherent manner and that projective measurements are made only at well-defined stages of an algorithm. Such coherent manipulations are called quantum logic gates, where it can be shown that all necessary computation tasks can be performed using a set of universal gates (single qubit rotations and the so-called conditional-not gate, see Ref. [3]). Algorithms using quantum logic gates can reduce the complexity in a number of computational problems. A particular example is the factorization of large numbers, as proposed in 1994 by Peter Shor [4]. In addition to this quantum computation, QIP shows large prospects for secure data communication ("quantum cryptography" [5]), quantum simulation [6] and metrology [7].

Qubit implementations as well as single and multi-qubit operations have been performed on a number of systems, including trapped ions [8, 9], nuclear spins [10, 11], superconducting circuits [12–15], semiconductor quantum dots [16–18], defects in diamond [19–21], and all optical-schemes using single photons [22–25]. To characterize whether a physical system meets the requirements for an implementation of a quantum computer, a number of criteria have been proposed by DiVincenzo [26]. These criteria concern among others the scalability, the initialization and the coherence times of the qubits. All the systems cited above have their pros and cons as far as it concerns DiVincenzo's criteria, and to date it is not evident which of the systems is the most promising [27]. Hence, an appealing idea is to combine different qubits and thus, to harness their specific advantages.

To connect two or more qubits, we require their quantum states to become entangled. Entanglement means to prepare two qubits in an inseparable state, in which they show a well-defined correlation. Moreover, if we move the qubits far away from each other and perform a projective measurement on one of the qubits, we *instantaneously* project the entangled partner in a corresponding state. This scheme is also called quantum teleportation, and is a non-local phenomenon which has no classical counterpart. Entanglement plays an important role when distributing information over a network of separate computation entities [28].

We consider a hybrid system consisting of stationary qubits ("nodes") which are linked to each other using flying qubits. For the flying qubits, single photons appear to be a perfect match as they transfer the information rapidly over long distances with little decoherence. The quantum information can be encoded using their polarization state, but also their location and timing (time-bin entanglement [29, 30]). The distant stationary qubits serve as long-term memories and have been implemented for different systems: The entanglement of a trapped ion with the polarization state of an emitted photon has been realized in 2004 by Blinov *et al.* [31], and was extended to a photon-mediated entanglement of two distant atoms [32] and ions [33], recently . Two similar schemes were realized for the nitrogen-vacancy color center in diamond [34, 35]. We will discuss these two experimental realizations of quantum entanglement in more detail later on, because they reveal the limitations for this particular defect center in diamond. Before we address this subject, we first introduce the reader to color centers in diamond, and their prospects for a qubit realization.

A color center is a defect on an atomic level of a solid-state material, which shows electronic transitions in the band gap of an surrounding solid. As a consequence, color centers absorb light for which the host material is transparent and give a characteristic color to the host. They consist of lattice vacancies, impurity atoms or combinations of the two. Owing to their atom-like, discrete energy terms, color centers can be considered as "artificial atoms". To provide an individual access to these artificial atoms by means of optical excitation, the defects can be spatially isolated in the host material. Diamond is a particularly interesting material for optically active defect centers, because it shows a wide band-gap, and therefore, is transparent from the ultraviolet to the far infrared spectrum. As consequence, more than 500 diamond color centers are cited in the literature [36].

Compared to other isolated quantum systems, diamond color centers stand out because they offer a straight-forward access: For instance, trapped ions require a tremendous technical overhead ranging from ultra high vacuum chambers to extensively stabilized trap lasers. Other solid-state systems like semiconductor quantum dots only operate at liquid helium temperature. On the other hand, individual defect centers in diamond have been successfully investigated at room temperature with fairly simple experimental setups (cf. Sec. 3). However, the disadvantage of a color center is the interaction with the surrounding host lattice. The covalent bonds in diamond create a strong crystal field which modifies the energy levels of the impurity atoms. Therefore, it is both a theoretical and experimental challenge to reveal the electronic structure of a given defect center. In addition, the coupling of the electronic wave function to vibrational modes (so-called vibronic coupling) affects the optical emission spectrum: When a defect relaxes from its excited to the ground state without the influence of vibronic coupling, we call this purely electronic transition a zero-phonon line. In contrast, when vibrational quanta are created or annihilated during the transition, we speak of a phonon sideband. The interaction with the rapidly decaying vibrational quanta can lead to a significant broadening of optical transitions, hence it is desirable for a defect when its vibronic coupling is small.

Among the most prominent color center in diamond is the negatively charged nitrogen-vacancy (NV) center, consisting of a substitutional nitrogen atom and a neighboring lattice vacancy. At the same time, the NV center ranges among the defect centers in diamond which are the most understood. The NV center was first observed by du Preez in 1965 [37]. Subsequent studies on ensembles of NV centers showed that the NV center is related to an emission band at 1.94 eV (corresponding to ~ 640 nm), and revealed some of the electronic propertiers of the defect [38]. The dawn of the NV center for quantum applications was in 1997, when for the first time, single photon emission was measured from an individual NV center using scanning confocal microscopy [39]. Since 1997, the annual number of publications about the NV center has increased exponentially [40], underlining the importance of this quantum system.

The key to its success lies in the electronic structure of the NV center. The defect was identified to show a spin triplet ($S = 1$) ground state. Due to spin-spin interaction [41,42], this ground state is split at zero magnetic field into two spin sublevels ($m_S = 0$ and $m_S = \pm 1$). The splitting amounts to a frequency of about 2.9 GHz, thus the spin state can be manipulated using convenient microwave techniques derived from nuclear magnetic resonance experiments. When being optically excited, the spin state is preserved – even for a non-resonant optical excitation. Following an optical excitation, there is a spin-dependent probability to trap the NV center in a metastable ($S = 0$) shelving state: While the $m_s = 0$ states decays rapidly to the ground state under emission of a fluorescence photon, the $m_s = \pm 1$ state can be trapped in the shelving state from where it decays non-radiatively to the ground state. Hence, the resulting NV fluorescence depends on the spin state and enables an optical read-out of the spin state. This combination of microwave spin manipulation and straight-forward optical read-out successfully promoted the NV center to a promising spin qubit.

The figures of merit for a spin qubit are its coherence times. It has been shown that the main sources of decoherence for the electron spin are nuclear magnetic momenta originating from single substitutional nitrogen impurities (N^S) and ^{13}C nuclei in the vicinity of an NV center. By growing isotopically enriched ^{12}C diamond at high purity levels (N^S concentration below 1 part per billion), spin coherence times of up to 2 ms were achieved [43]. Even for diamonds with only a technical-grade purity, dynamic decoupling mechanisms enabled spin coherence times of up to 60 µs [44]. All these properties are preserved at room temperature rendering the NV center an extremely attractive qubit implementation.

The disadvantage of the NV center is its optical emission spectrum. Due to a strong coupling of the electronic wave function a local vibration mode, the emission spectrum of NV center shows a width of about 100 nm. Only 3-5 % of the NV emission is found in the zero phonon line (ZPL), whereas the overwhelming part of the fluorescence is contained in the phonon sidebands. While this drawback has only little consequence for a simple optical spin read-out, it is crucial when the optical detection is limited to the ZPL. We will illustrate the consequences of this limitation for the usage of the NV center in QIP. To employ the NV center as a node in quantum network, two entanglement experiments have been published recently, which we here discuss briefly.

In 2010, Togan *et al.* showed the entanglement between the spin state of a single NV center and the polarization state of an emitted photon [34]. In this experiment, the NV is prepared in a specific excited state which decays with equal probability into two different spin states of the ground state. The entangled state is created because the photon polarization is uniquely correlated to the final spin state. This scheme is fully equivalent to the approach using atomic qubits [31,45]. Optical dipole transitions are spin preserving, but the orbital angular momentum of an electronic state can be changed depending on the photon polarization. In order to identify which optical transition is suitable for the entanglement, a profound understanding of the NV level structure was necessary for this approach. To provide this understanding, detailed studies of NV excited state preceded the experiment - both experimentally [46–50] and theoretically [41,42].

In 2013, Bernien *et al.* reported on the entanglement of two NV centers, located in separate cryostats [35]. For their approach, the authors used a measurement-based entanglement protocol [51, 52]: First, each NV center is brought into a superposition of spin up ($m_S = 0$) and down states ($m_S = -1$) using a sequence of microwave pulses. Next, each NV center is excited using a pulsed laser, which is resonant only for the spin up state. If one of the defects has been excited, it will decay back to its ground state under the emission of a fluorescence photon. Hence, the photon number in the optical mode is entangled with the spin state of each NV center. The two photon modes are superimposed on an optical beamsplitter, such that the photons observed at the output port of the beamsplitter could have originated from either NV center. If the photons emitted by the two NV centers are indistinguishable, their interference at the beamsplitter erases the which-path information and projects the two qubits onto a maximally entangled state. Hence, the detection of the photon heralds the entanglement generation.

While these experiments mark milestones for the usage of the NV center in a quantum network, they also reveal the limitations of the NV center for this purpose. In these experiments, the detection is strictly limited to the ZPL, which contains only 3 - 5 % of the NV emission. Hence, the probability to generate an entangled photon is on order of 10^{-6} [34]. As a consequence, the rate of entanglement events was very low in both experiments, which imposes a clear limitation for the entanglement generation when using NV centers. Furthermore, the NV center suffers from spectral diffusion in the experiments discussed above, which is a time dependent change in the optical transition frequencies due to charge fluctuations in the vicinity of the defect. In order to tune the two NV centers into resonance and to compensate for spectral diffusion, Bernien *et al.* implement a sophisticated feed-back mechanism, which shifts the electronic levels by applying electrostatic potentials to the samples [49, 53].

There is a vivid activity in the quantum optics community to enhance the NV emission into the ZPL using coupling to resonant microcavities. In the so-called weak-coupling regime, the radiative emission into the cavity mode can be increased by the Purcell effect, which in turn depends on the spatial and temporal confinement of the resonator mode. Consequently, if the cavity is in resonance with the ZPL of the NV center at cryogenic temperatures, the ZPL can be enhanced while the phonon sideband can be suppressed.

Coupling of NV centers to microcavities has been realized recently in a number of experiments (see Refs. [54, 55] for an overview).

In this thesis, we set out to investigate an alternative color center in diamond which has more promising optical properties than the NV center. The silicon-vacancy (SiV) color center consists of a substitutional silicon impurity and an adjacent lattice vacancy. Compared to the NV center, the SiV center is a relatively "young" defect and there are far less publications about it as compared to the NV center [36]. The defect is presumed to exist in a negative and a neutral charge state. The spectrum of the negatively charged SiV center is dominated by a ZPL at 1.68 eV (738 nm), whereas the neutral charge state shows a considerably weaker emission at 1.31 eV (946 nm). We here focus the discussion on the negative charge state. Its ZPL has a typical line width of only a few nanometers, even for fairly large defect ensembles at room temperature. In contrast to the NV center, approximately 80 % of the emission is concentrated in the ZPL [56]. The first demonstration of SiV single photon emission was published in 2006 [57], using individual SiV centers in bulk diamond. However, these first investigations showed only moderate photon count rates.

A breakthrough for the SiV center was achieved in 2011, when Neu *et al.* investigated individual SiV centers in diamond nanocrystals grown on iridium substrates [56]. These samples showed single photon emission with fluorescence count rates exceeding 1 million photons per second. In addition, these single SiV centers exhibited room temperature line widths below 1 nm. These results promoted the SiV center to the brightest diamond-based single photon emitter, and enabled a detailed study of further optical properties of the defect: The emission dynamics could be described using an effective three-level system, which includes a metastable shelving state similar to the NV center. At room temperature, the polarization of the emitted light was measured to be fully linear [58]. These excellent optical properties proved the SiV center to be a practical room temperature single photon source, and it would be tempting to employ the defect as a qubit similar to the NV center. An additional advantage of the SiV defect is, that there are will-defined and reproducible fabrication strategies for it, while other novel color centers in diamond (e.g. Cr-related defects [59]) still face many open questions regarding their creation [60].

Very recently, the emission of indistinguishable photons from two distant SiV centers was shown [61]. The authors of Ref. [61] emphasize, that the SiV centers in their samples show vanishing spectral diffusion, resulting in small inhomogeneous line widths. Hence, as far as it concerns the optical prerequisites, the SiV center is an ideal candidate for the photon-heralded entanglement of two distant color centers, which we discussed above. To be employed as a spin-photon interface, the the SiV defect is also required to show similar spin properties as compared to the NV center. However, the molecular structure and the electronic level scheme of the defect have been subject to debate up to the present date, thus the spin properties of the defect are completely unknown. The "fingerprint" of the electronic structure is the ZPL fine structure of the defect which is observed when cooling the center to liquid helium temperature. The fine structure consists of four optical transitions, which give rise to split ground and excited states [62]. There have been competing theoretical models (cf. Sec. 1.2 for details) to explain the ZPL fine structure, yet, these models lack a clear and detailed experimental verification. Moreover, the spin state of the SiV center has not been identified unequivocally. Recently published electron paramagnetic resonance (EPR) measurements showed that the presumed neutral charge state SiV^0 is a spin triplet system ($S = 1$) [63]. This suggests that its negative counterpart is a paramagnetic $S = 1/2$ system, although this has not been confirmed by independent EPR measurements so far.

In summary, the SiV center faces opposite challenges compared to the NV center: While the SiV center currently offers promising optical properties in comparison to other color centers in diamond, the electronic structure of SiV center has so far remained elusive. The open questions about its molecular structure and its electronic states so far obstructed the way to employ the SiV center as a qubit. Hence, it is the main objective of this thesis to provide a comprehensive theoretical model for the defect and to test this model in different experimental geometries. Furthermore, the model needs to provide consistent explanations for the existing experimental reports in the literature. Most importantly, we set out to answer the question about the spin state of the defect and to demonstrate the first steps towards employing its spin degree of freedom as a qubit in diamond.

To attain this goal at an experimental level, it appears straight-forward to use the promising nanodiamond samples of Neu *et al.* [56]. However, crystal strain is present inside these nanodiamonds. The strain is revealed in an inhomogeneous distribution of the ZPL wavelengths, and a considerable variation in the emission dynamics parameters for emitters in different nanodiamonds. Hence, we expect crystal strain to significantly affect the electronic states of the defect, rendering a clear identification of the electronic structure very challenging in these samples. Therefore, the crucial prerequisite for our studies is the availability of SiV centers in low strain samples. To verify whether the SiV center is suitable as a qubit in first place, a complementary condition is the ability to investigate it on a single emitter level.

In this work, we first discuss the known properties of the SiV color center, and investigate the existing theoretical models for it (Chap. 1). A key element of this discussion is the molecular structure of the defect, which in turn defines the symmetry of the defect. In Chap. 2, we use the concept of group theory, in order to classify the symmetry properties of the SiV center, and to deduce the electronic electronic ground and excited states of the defect. These two states initially show a fourfold energetic degeneracy, i.e. a twofold orbital and a twofold spin degeneracy. This degeneracy can be lifted by several interaction terms, which we model in a perturbative approach. For all interaction terms, we calculate explicit matrix representations and show theoretically their action on the eigenstates of the SiV center.

In Chap. 3, we introduce the experimental setups and the diamond samples for the spectroscopic investigation of the SiV electronic structure. To provide experimental access to the optical properties of individual SiV centers, we employ confocal microscopy at cryogenic temperatures. First, we introduce the concept of confocal microscopy and discuss its advantages over conventional microscopy, then we present the two experimental realizations. Next, we describe the fabrication of the three samples which have been employed in this thesis.

Chap. 4 summarizes the experimental results. In this chapter, we present spectroscopical measurements on the samples mentioned before. The chapter is loosely divided in a part about SiV centers in low-strain diamond, and another part, where we discuss the influence of crystal strain. The spectroscopic results are compared to the theoretical model established in Chap. 2. From this comparison, we deduce the leading molecular interaction terms, and discuss the resulting electronic states as well as the expected spin purity. In the course of this thesis, a spin selective optical excitation was achieved, which can be considered as a first step towards using the SiV center as quantum bit. These experiments were conducted together with Tina Müller from the Cavendish Laboratory in Cambridge, UK [64, 65]. We show that these experiments can be consistently interpreted using the model developed in this thesis.

Finally, Chap. 5 gives an outlook on further verification of the theoretical model, and discusses how the spin purity can be increased in an optimized measurement configuration.

Chapter 1

The silicon vacancy color center in diamond

This chapter provides an overview over the existing literature on silicon vacancy (SiV) color centers in diamond. It also shows which open questions we address in this work and where we add to current knowledge. However, before we treat the SiV defect in detail, Sec. 1.1 introduces the host material: We briefly review the fabrication of diamond, and we also present the relevant electronic and optical properties. Subsequently, we introduce the "molecular" properties of the SiV centers (Sec. 1.2), i.e. its composition, its charge state and its molecular configuration. Finally, as this experimental work mainly relies on spectroscopy, we cover the known spectral properties of SiV centers (Sec. 1.3). First, we distinguish between room temperature and low temperature spectra and second, we dedicate Sec. 1.3.3 to the existing research on individual SiV centers.

1.1 Diamond as host material for defects

Diamond is – besides graphite – one of the two main crystalline forms of carbon. In principle, diamond is a metastable phase as graphite is thermodynamically more stable than diamond. However, the phase transition from diamond to graphite usually requires temperatures above 1500°C at normal pressure. Diamond consists of sp^3 hybridized, covalently bound carbon atoms which crystallize in a cubic structure. The so-called diamond structure consists of a face-centered cubic (fcc) lattice with a basis at $(0,0,0)$ and $(\frac{a}{4},\frac{a}{4},\frac{a}{4})$ and a lattice constant of $a = 3.567$ Å. Hence, this structure is often visualized as two fcc lattices which are displaced by $(\frac{a}{4},\frac{a}{4},\frac{a}{4})$ from each other (Fig. 1.1a on page 8).

Formation and synthesis of diamond While the geological formation history of diamond is still subject to debate, one assumes that natural diamond is a conversion product of other carbon modifications, such as graphite [66]. At depths of 150 km inside Earth's mantle, high pressures (> 4.5 GPa) and high temperatures ($900 - 1300$°C) lead to a transformation of graphite into diamond, as the latter is the most stable carbon modification at these conditions. One hundred million years ago, volcanic eruptions transported these diamonds rapidly to Earth's surface. These "blowouts" happened so fast that no back-conversion into graphite occurred.

Natural diamond can exhibit high purity, however their composition is strongly varying and depends on the origin of the diamonds. This makes a deterministic study of defects in natural diamond cumbersome and expensive. Hence, we exclusively employ synthetic diamond throughout this work. Before we describe the creation of synthetic diamond, we briefly review the classification of diamond in terms of purity as it will be important for the fabrication strategies, too. In 1934, Robertson *et al.* suggested to classify diamond into type I and II according to the presence of certain infrared absorption bands [67]. Later, it has been shown that these bands in type I diamond are related to the abundance of nitrogen impurities [68]. We further distinguish between type Ia which contains aggregated nitrogen (so-called "platelets"), and type Ib with singly substitutional nitrogen. Type II diamond lacks these absorption bands and is transparent up to the fundamental absorption edge at 5.5 eV. Type II is sub-divided in type IIa and type IIb, where the latter shows p-type conductivity and usually comprises boron impurities.

We now address the fabrication of synthetic diamond. The natural mining of diamond (135 Mct worldwide in 2011) is largely outbalanced by the synthetic production of diamond which exceeded 4 Gct = 800 t in 2011 [69]. There are two main synthetic methods: High-pressure-high-temperature (HPHT) synthesis and chemical vapor deposition (CVD). The HPHT method mimics the natural creation process and is the main industrial source for diamond: In an hydraulic anvil cell, Gigapascal pressures are applied to graphitic carbon precursors while temperature is kept above 1400°C [70]. Small diamond crystals serve as "seeds" to start the growth, and the addition of metals (predominantly iron, cobalt and nickel) as catalysts helps to accelerate the growth process. These catalysts however limit the purity of HPHT diamonds of which most are graded as type Ib with large amounts of nitrogen. The advantage of HPHT is a high crystalline quality, i.e. large domains of the diamonds are free from imperfections and thus can be relatively free of crystal strain. In order to achieve high purity HPHT diamonds of type IIa, attempts have been made to add group IVa elements (Ti, Zr or Hf) to the solvent metal, which act as nitrogen getters [71]. However, when nitrogen getters are added to the growth process, carbide inclusions (e.g. TiC or ZrC) can be trapped in the diamond crystal. In 1996, Sumiya and Satoh showed that the addition of copper leads to a decrease in carbide inclusions while maintaining a relatively high growth rate [72].

The second method, CVD, produces diamond in the metastable phase and relies on reaction kinetics [73]: For this method, methane acts as carbon gas source which is dissociated by a highly reactive hydrogen plasma. The carbon fragments adsorb onto a substrate where they form sp^2- and sp^3-bound carbon. The atomic hydrogen has the function of etching the graphite phases selectively while keeping the diamond phases stable [74], hence, this non-equilibrium etching favors a net production of diamond. While the underlying chemistry remains the same, different methods have been proposed to dissociate the precursor gas mixture: hot-filament CVD [75], microwave CVD [76] or combustion flame CVD [77].

Growth in the CVD process starts at sp^3-bound carbon phases, hence this process also requires the presence of a seed material. For polycrystalline diamond films, diamond powder with grain diameters down to ≈ 10 nm are employed. The growth of single crystalline diamond has so far only been possible on diamond substrates (so-called *homoepitaxial* growth). In addition, there are promising approaches to use iridium as substrate for the *heteroepitaxial* growth of single crystalline diamond [78]. In general, diamonds grown by CVD can exhibit a high purity – most commercially available CVD diamonds are type IIa. Throughout this work, we exclusively investigate defect centers in CVD diamond samples, however we make use of a selected HPHT diamond as substrate for a CVD film (details on samples are found in Sec. 3.2).

Band structure of diamond and color centers Diamond is a semiconductor. Its band structure has been calculated using various methods [79] and exhibits a large indirect band gap of $E_{gap} = 5.5$ eV [80]. At the Brillouin zone center Γ, the direct gap energy equals 7.3 eV [80]. This makes pure, single crystalline diamond transparent from about 230 nm in the ultraviolet spectral region to the far-infrared [36], hence a pure diamond is colorless.

Local imperfections in the diamond lattice can lead to discrete, localized energy states in the band gap. These imperfections can consist of impurity atoms, vacancies or complexes of the two. Optically active impurities or impurity complexes can lead to absorption of light in the visible spectrum. When a diamond is heavily doped with a certain imperfection, this absorption gives rise to its color. Hence, these impurities are commonly termed color centers. Owing to the large band gap, there are many possible color centers in diamond: Over 500 species have been reported [36].

The formation of color centers can happen on the one hand via unintentional contamination during growth. For instance, nitrogen is a common impurity in both natural and HPHT diamonds as it is usually present in these growth processes. On the other hand, color centers can be created on purpose by introducing solid or gaseous additives deterministically into the growth process. For instance, nickel related color centers were created by exposing substrates for diamond growth to a nickel containing slurry [81] prior to growth. In similar fashion, the lanthanide europium (Eu) was recently introduced into nanodiamonds by applying a Eu-containing polymer to the substrates before subjecting them to a microwave CVD process [82]. The tradeoff for these methods is, that additives can modify the growth conditions leading to an increased presence of non-diamond-phases. A further drawback is, that the doping concentration on a low levels is challenging.

An alternative method to incorporate defects into diamond is ion implantation, for which the ionized impurity atoms are accelerated onto the diamond sample [83]. With this technique, the incorporated dose can be controlled deterministically and any influence of the growth process can be ruled out if the diamonds are investigated before and after implantation. However, the ions penetrating the diamond introduce radiation damage to the lattice, thus ion implantation usually requires a subsequent annealing step. We return to the process of ion implantation in Sec. 3.3 when describing the samples employed for this work.

Optical properties of diamond Connected to the electronic properties of diamond are its optical properties. As optical properties of natural and synthetic diamonds vary within wide ranges depending on morphology, growth and impurity content [36, 84], we here only review the aspects which are the most relevant for this work. Diamond has a high index of refraction which amounts to $n = 2.4$ in the visible [85]. On the one hand, this promotes diamond to an attractive material for photonic structures, such as photonic crystal cavities [86–89], ring and microdisk resonators [90–92] and nanowires [93], because these concepts are based on high refractive index-differences between a dielectric and air. On the other hand, when investigating the faint light of individual defects in diamond, the high index of refraction is disadvantageous: The critical angle for total internal reflection at a diamond-air interface amounts only to 24.6°. Thus, depending on the radiation pattern, a large amount of the color center's fluorescence is not extracted from the diamond [73]. Even for light impinging perpendicularly to the surface, a fraction of 17% is reflected back into the diamond material due to Fresnel reflection. To overcome this low extraction efficiency, different groups suggested to fabricate solid immersion lenses into the diamond surface [94, 95] in order to inhibit total internal reflection and increase the collected light by factors of up to 10 [94]. We will pursue this approach in this work as well and demonstrate the fabrication of solid immersion lenses in Sec. 3.4. An alternative method to increase the extraction efficiency is to fabricate diamond nanowires, which typically have diameters of ~ 200 nm and heights of $1 - 2$ µm. The nanowire provides a waveguide mode that an enclosed defect center can couple to and thus allows for efficient photon exchange between the optical apparatus and the emitter [93].

An alternative approach would be the usage of isolated, microscopic diamonds crystals. If these crystals are significantly smaller than the wavelength of light (then usually termed *nanodiamonds*), the total internal reflection is inhibited and the extraction efficiency is considerably increased [56, 96, 97]. However, nanodiamonds are known to exert crystal strain on the included defect centers. This imposes an additional perturbation for the electronic states of defects centers (cf. Sec. 2.2.5) and makes an unambiguous determination of the electronic structure more challenging.

We have learned a few important electronic and optical properties of diamond in this section. While pure diamond is a fascinating material on its own, its defects render it even more interesting. In this work we focus on the silicon vacancy color center, and we will take a closer look onto it in the next section.

1.2 Molecular structure of silicon vacancy centers

This section delivers insight into the molecular structure of the SiV center which is also referred to as the 1.68 eV line, owing to the energy of its pronounced zero phonon line (ZPL). Along with a short historic overview, we address the three main points about its molecular structure: First, we review the identification of silicon as the impurity atom and discuss the experimental evidences for a neighboring lattice vacancy. Second, we consider measurements in the literature about the charge state of the defect, and third, we briefly discuss theoretical approaches which estimated the most probable molecular arrangement of the defect.

1.2.1 Constituents of the defect: A silicon impurity and a lattice vacancy

Compared to the nitrogen vacancy (NV) center, which is the most prominent defect center in diamond and has been studied for over 5 decades, the SiV center is a relatively “young” defect and there are far less publications on it than on the NV center. The reason for this fact is that the SiV center is mainly found in diamonds grown using CVD – which itself is a rather young method [75, 98] – and is far less prominent in natural or HPHT diamond as compared to the NV center. The first observation of the 1.68 eV luminescence was reported in 1980 by Vavilov *et al.* who investigated the cathodoluminescence (CL) of epitaxial CVD diamond films [99]. One year later, Zaitsev, Vavilov and Gippius attributed this luminescence to a defect center with silicon involved [100]. In their studies, they implanted 25 different ion species into natural diamonds (type Ia and IIa) and recorded CL spectra. Only the regions irradiated with silicon ions exhibited the 1.68 eV luminescence. Zaitsev *et al.* observed a quadratic dependence of the CL intensity on the implantation dose which points either towards a defect with either two Si atoms involved or to a defect comprising a lattice vacancy; the authors of Ref. [100] interpreted their results as a sign for two Si atoms being involved in the defect. This is already a strong experimental indication for silicon being the impurity atom involved in the 1.68 eV defect.

In 1989, Robins *et al.* investigated polycrystalline films grown using hot filament CVD on silicon and observed luminescence at 1.675 eV in CL [101]. However, they attributed the luminescence to the neutral vacancy defect (GR1, see below) which emits close to the SiV wavelength at 1.673 eV [68]. Further observations of 1.68 eV luminescence in diamond grown on silicon using CVD have been reported in Refs. [56, 58, 102–117] which show impressively the correlation between the defect and silicon based CVD diamond. In 1993, Bergman *et al.* formulated first the underlying incorporation mechanism which is today widely accepted [112]: the Si substrate is etched due to the close contact to the reactive hydrogen plasma, thus atomic Si is present in the plasma. These Si atoms can then be incorporated into the diamond. SiV centers are also formed when placing a piece of Si close to the substrate [113]. Clark and Dickerson proposed that also the CVD reaction chambers themselves exhibit Si sources: For hot filament CVD, the filament alloy can contain Si [103] and for microwave CVD, the vessel walls are made of fused silica. All these are strong and consistent evidences for Si being part of the defect.

While the presence of Si in the defect is straightforward to show, the contribution of lattice vacancies is more challenging to prove. The first experimental evidence is that for ion implantation, an annealing process with temperatures above 800°C is required to create SiV centers [100, 108]. Clark and Dickerson investigated this effect in greater detail [108]: They irradiated CVD diamond films which already exhibited SiV centers with a 2 MeV electron beam. After the exposure to the electron beam, the sample showed additional luminescence at 1.67 eV which was attributed to the GR1 defect [68]. The GR1 is a neutral vacancy created in diamond after irradiation with ions or electrons (GR stands for “general radiation”). Clark and Dickerson subsequently annealed their centers above 800°C where lattice vacancies become mobile. After annealing, the GR1 luminescence was not observable anymore but the SiV luminescence was strongly increased. The widely accepted mechanism is that vacancies migrate to the Si impurities to form SiV centers upon annealing. While this argument holds for SiV centers created via ion implantation, the *in situ* formation via CVD growth requires a deeper investigation.

In principle it is possible that lattice vacancies, which are close to the diamond surface [118], migrate during growth to the impurity inside the diamond to form defects complexes [119]. However, recent results showed some evidences that the vacancy is directly formed at the defect site: D'Haenens-Johansson *et al.* have investigated electron paramagnetic resonance (EPR) and optical spectra on single crystalline diamond grown along the [110] direction [63]. They identify an emission at 946 nm to be the neutral charge state of the SiV center (see below). EPR spectra indicate a defect orientation along the four equivalent $\langle 111\rangle$ directions. Two of these four orientations point out of the growth plane. From the relative EPR intensities for the different defect orientations, D'Haenens-Johansson *et al.* have deduced that the SiV orientations pointing out of the growth plane are created more often than the ones with orientation in plane. The authors have proposed the following model: First, a Si atom is incorporated on a substitutional site in the uppermost diamond layer. When the next layer is grown, the Si atom below inhibits the adsorption of a carbon atom, hence creating a lattice vacancy. Following layers "overcoat" the SiV complex and stabilize it. This type of growth process has also been successfully verified for the NV center [120, 121].

1.2.2 Charge state

Before we address the geometrical structure and orientation of the SiV defect in the diamond lattice, we briefly review the literature on the charge state of the defect. Color centers in diamond can exhibit different charge states, e.g. for the NV center, it is widely accepted that its negative charge state NV^- is responsible for the ZPL at 637 nm, whereas the neutral counterpart NV^0 emits at 575 nm. The charge state of the SiV center is still subject to debate: The theoretical considerations of Goss *et al.* attribute the 1.68 eV emission to an SiV^- defect [122]. In contrast, the calculations of Moliver [123] suggest, that the 1.68 eV center is rather a neutral defect.

In the experimental work of Iakoubovskii *et al.* [124], a quenching of the 1.68 eV emission under simultaneous VIS and UV excitation is interpreted as transfer from a luminescent to a non-luminescent charge state. The UV light would in this picture excite an electron from the SiV ground state to the diamond conduction band, from where the electron can be trapped at another acceptor nearby. This process is called photoionization or photochromism. The authors of Ref. [124] thus attribute the 1.68 eV emission to a more negative charge state $(\mathrm{SiV})^{x-1}$ which transforms under photochromism to $(\mathrm{SiV})^{x}$. In their first publication [124], they claim that $x = 0$ referring to the results from Goss *et al.* [122]. One year later, they revoke this statement, claiming that $x = 1$.

For a second experimental work about the charge state, we return to the report from D'Haenens-Johansson *et al.* (see above): Using EPR spectroscopy, they relate an emission at 1.31 eV (946 nm) to a spin triplet system $S = 1$. In their model, this is attributed to a neutral charge state SiV^0 of the silicon vacancy center. When applying an annealing step to their sample, the authors observe an increase of the 1.68 eV luminescence which they interpret as a charge transfer of the SiV center from SiV^0 to SiV^-. Applying UV-light decreases the 1.68 eV emission and restores the 1.31 eV luminescence. This indicates a quenching mechanism similar to the works of Iakoubovskii *et al.* [124], and is a strong argument for the 1.68 eV emission arising from SiV^-.

In the present work, we assume that the 1.68 eV emission relates to a negatively charged defect. This implies a single unpaired electron and thus a $S = 1/2$ spin doublet system. The high agreement which we observe between our theory and the experiment is an indication, that this assumption is justified.

1.2.3 Orientation and molecular structure of the defect

Finally, we review existing literature about the orientation of the SiV center in the diamond host lattice. We treat the defect in a molecular orbital approximation and its molecular structure will be directly linked to the orientation in the surrounding lattice.

The questions about orientation and structure have so far mainly been addressed in theoretical proposals, and can *experimentally* only be determined indirectly (see below). We here first review the theoretical works. A particularity for the SiV center is the presence of a spectral fine structure observed at low temperature which was known before the first theoretical proposal on its structure appeared (Sec. 1.3.2). This fine structure is usually assigned to a lifted orbital degeneracy. Hence, to explain the fine structure, the theoretical proposals on the SiV structure have to predict degenerated electronic states which are then separated by a small perturbation.

Theoretical approaches about the SiV structure The first theoretical work on the structure of the SiV defect was published 1996 by Goss *et al.* [122]. The authors employ density functional theory (DFT) in their work to calculate the most probable electron density distribution for the defect. The DFT method reduces the complex calculation of a many-body problem (including interactions between the particles) to the interaction of a generalized electron density with an environment. Physical observables, such as the total energy of a given electron density in a surrounding field, are approximated by a *functional.* The most probable configuration of a molecular system is then obtained by minimizing the functional for a given electron density distribution. The distribution is iteratively varied to find a global energy minimum. The field describing the interactions involved is usually chosen from a set of known functionals, and thus, the success of the method depends largely on this choice of the functional. DFT is considered to be a reliable technique for acquiring molecule structures. However, band structures calculated using DFT often show systematic errors, leading to e.g. incorrect band gap energies for semiconductors [125].

In the work of Goss *et al.*, the authors simulated the SiV center using a substitutional Si impurity and an adjacent vacancy, oriented along the $\langle 111 \rangle$ crystal axes. They obtained from their calculations that the Si atom is not stable on its position but rather moves along the [111] axis to an interstitial position, such that the Si atom is placed in the middle between a divacancy (Fig. 1.1b. This structure is also called a split vacancy configuration, and gives rise to a D_{3d} defect symmetry (Sec. 2.1.1). In this symmetry, a negatively charged defect has a double orbital degeneracy in both ground and excited state. Goss *et al.* have assumed that this degeneracy might be lifted via a Jahn-Teller interaction (Sec. 2.2.3) or spin-orbit coupling (Sec. 2.2.2), which give rise to four possible

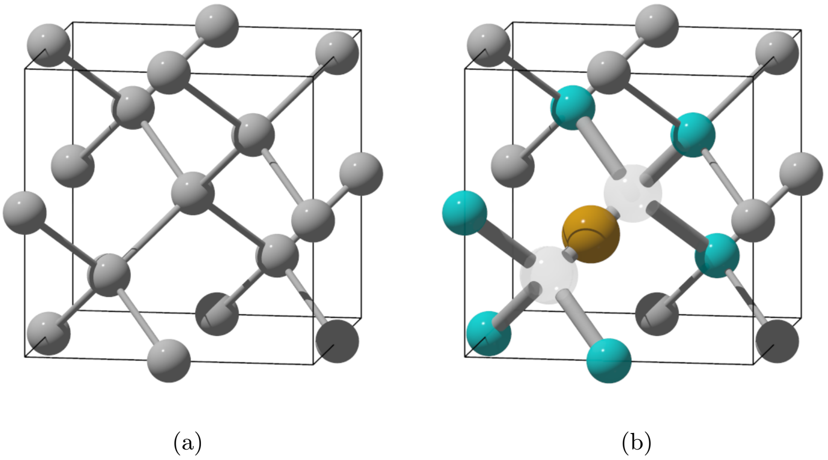
(a) (b)

Figure 1.1: The diamond lattice (panel a) and the molecular structure cof the SiV center in it (panel b) according to Goss *et al.* [122]. The carbon atoms (grey) crystallize as a face centered cubic lattice with a basis at $(0,0,0)$ and $(\frac{a}{4},\frac{a}{4},\frac{a}{4})$ with a lattice constant of $a = 3.567$ Å. The Si impurity (yellow) is situated on an interstitial position along the $\langle 111 \rangle$ bond axis and surrounded by a split vacancy (transparent). The next-neighbor carbon atoms around the SiV defect (light blue) have unsaturated bond orbitals which contribute to the electronic states (c.f. Sec. 2.1.4).

optical transitions between ground and excited state. This is consistent with the spectral fine structure of the defect, observed at low temperature (Sec. 1.3.2).

The orientation of the SiV defect in this model is consistent with Ref. [63], but no other experimental confirmation is known. Goss *et al.* revisited their work in 2007, confirming the main results of their earlier publication [126]. Recently, *ab initio* calculations on the SiV center have been revisited by Gali and Maze [127]. In their study, they confirm the defect orientation of Goss *et al.* and additionally, their calculation gives indications about the energetic position of the SiV defect in the diamond band gap (cf. Sec. 2.1.4 on page 45). The simulations of Goss, Gali and Maze build the foundations of the work presented here, and we will return to other aspects of their publications in Chap. 2.

While the DFT calculations mentioned above attribute the 1.68 eV emission to the negative charge state of the SiV center, Moliver assigns it to the neutral charge state [123]. He uses restricted open-shell Hartree-Fock (ROHF) calculation to obtain the defect structure. In contrast to DFT which calculates the interaction between an electronic distribution and a functional, ROHF calculates exchange and Coulomb interactions between different electrons [128]. Moliver's calculations indicate that the SiV is not positioned exactly in the middle of the split vacancy but rather moves slightly along the bond axis towards one substitutional site. This reduces the symmetry from D_{3d} to C_{3v} since the inversion center is missing. In C_{3v} the orbital ground state of a negatively charged SiV center is orbitally non-degenerate.

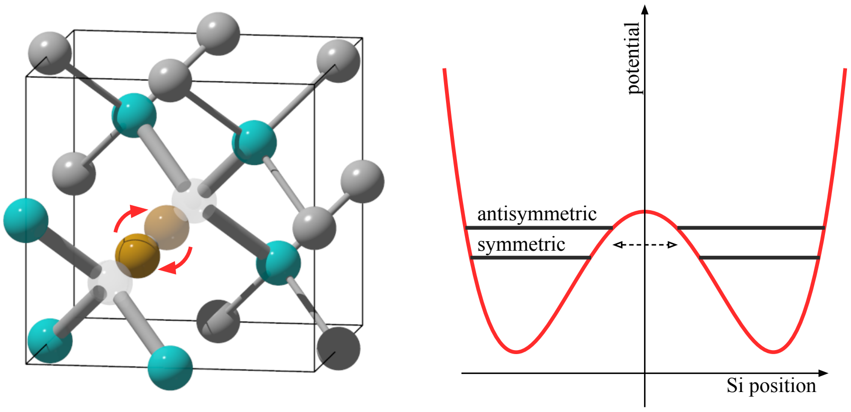

(a) (b)

Figure 1.2: In the theoretical model of Moliver [123] for the molecular structure of the SiV center, the Si impurity is not positioned exactly in the middle of the split vacancy but moves slightly along the bond axis towards one substitutional site giving rise to two equivalent positions (panel a). Energetically, this resembles a double well potential and Si atom is believed to tunnel between the positions (panel b). The two resulting wave functions are then either a symmetric or an anti-symmetric superposition of the two positions, which leads to a level splitting in ground and/or excited state.

To explain the spectral fine structure, consisting of four transition lines at low temperature, Moliver suggests a so-called tunnel splitting. The repositioning of the Si atom towards one of the two substitutional lattice sites gives rise to two equivalent positions (Fig. 1.2a). Energetically, this resembles a double well potential (Fig. 1.2b). The Si atom is believed to tunnel between these positions. This situation is similar to the ammonia molecule NH_3 where the nitrogen atom can tunnel through the potential well created by the three in-plane hydrogen atoms [129]. The two resulting wave functions are then either a symmetric or an anti-symmetric superposition of the two positions. The symmetric or anti-symmetric wave functions have different energies which lead to a splitting in ground and/or excited state. Hence, the tunnel splitting effect explains the fine structure splitting also for orbitally non-degenerate states. However as stated above, the 1.68 eV emission in Moliver's model is assigned to the neutral charge state SiV^0 which exhibits a total spin $S = 1$. As we will see in Chap. 4, our spectroscopic measurements in magnetic fields indicate, that the 1.68 eV emission has $S = 1/2$ which is in agreement with the models of Goss, Gali and Maze. In this work, we therefore start from the latter theoretical model.

Experimental findings on the SiV structure We now review experimental works about the structure of the SiV defect and its orientation in the diamond host lattice. The orientation of a defect is usually not observed directly, although high resolution transmission electron microscopes have been employed in single cases to visualize individual defects, e.g. for defects in graphite [130]. Instead, experimentalists often apply external fields (electric, magnetic or crystal strain) to the defect [131]. The response of the defect to the external perturbation is characteristic for a given symmetry. From the symmetry, a number of respective orientations can be deduced [132].

Already in an early publication by Zaitsev *et al.* [100], uniaxial stress measurements are mentioned although no conclusion was drawn from them as the center apparently showed a weak response to the applied stress field. In 1995, Sternschulte *et al.* applied uniaxial stress onto a diamond containing an ensemble of SiV defects and measured the response of the spectral fine structure at low temperature [133]. To unambiguously identify a defect symmetry, uniaxial stress needs to be applied along at least three crystallographic directions. Due to technical restrictions, Sternschulte *et al.* could not apply the stress other than in ⟨100⟩ direction and therefore they did not interpret the data in terms of an orientation.

In addition, the authors applied magnetic field along ⟨100⟩, ⟨110⟩ and ⟨111⟩ directions. Unfortunately, the spectral lines of the fine structure were overlapping in their measurements which makes a clear assignment to optical transition and hence an analysis difficult. The authors observed a relatively weak response to the magnetic field when applied in ⟨111⟩ direction leading them to the conclusion of a possible orientation along ⟨100⟩ direction.

To the best of our knowledge, these are the only measurements that apply external fields to the defect while observing the 1.68 eV emission. D'Haenens-Johansson *et al.* employ EPR spectroscopy on the presumed neutral charge state SiV^0 emitting at 1.31 eV (see above) and determine a ⟨111⟩ orientation of the defect [63]. However, the correlation between the 1.31 eV and 1.68 eV luminescence has not been confirmed by independent measurements, yet.

An alternative method to indirectly determine the defect orientation is the investigation of its fluorescence polarization. In 1995, Brown and Rand measured the emission polarization of an SiV ensemble in oriented diamond films on silicon [134] – so-called mosaic type diamond. Their experiments were conducted at room temperature, where the spectral fine structure of the ZPL is not resolved. They measured the fluorescence intensity with a fixed detection polarizer while rotating the excitation polarization. When working with an ensemble of color centers, the evaluation of the polarization data takes in account equivalent orientations of the defect in the lattice. Hence, the polarization contrast of the fluorescence, i.e. the relative difference between maxima and minima, is different for different defect orientations [135]. From the observed contrast, Brown and Rand deduced a ⟨110⟩ orientation for the SiV center. According to Kaplyanskii [136], defects aligned along ⟨110⟩ exhibit C_2 or D_2 symmetry. In these symmetries, no degenerate orbital states are present [132], hence there is no evident explanation for the SiV fine structure for such an orientation. Brown and Rand did not focus in their work on the SiV fine structure, neither did they indicate a possible mechanism to explain it with their observed orientation. We will revisit the measurements of Brown and Rand in Sec. 4.1.3.

With the availability of individual SiV centers (Sec. 1.3.3), the polarization can be measured without ensemble effects. Although Wang *et al.* already had access to single SiV centers in bulk diamond in 2006 [57], no polarization measurements on single defects have been reported before 2011: Neu *et al.* measured the absorption and emission polarization for individual SiV defects in nanodiamond [56] and in heteroepitaxial diamond "nanoislands" [58] on an iridium substrate. They measured the polarization of ≈ 20 individual defects using a rotated polarizer in the detection path. Subsequently, the excitation polarization was rotated using a half-wave plate without a polarizer in the detection arm. As the nanoislands grow with defined crystal orientation on the (001) single crystalline iridium, the polarization angles can be related to crystal axes of the diamond. Neu *et al.* observe polarization maxima in the equivalent $\langle 110 \rangle$ directions and additionally along the [100] and [010] axes.

While a polarization along $\langle 110 \rangle$ can also be the projection of $\langle 111 \rangle$ oriented dipoles onto the (001) surface plane, the presence of defects with maxima [100] and [010] contradicts this hypothesis. Neu *et al.* thus assume a $\langle 110 \rangle$ alignment of the defect which is consistent with the abundance of the different polarization angles in their measurements. Consequently, as already noted for the results of Brown and Rand, for centers in $\langle 110 \rangle$ orientation there is no orbital degeneracy. Neu *et al.* refer to the Moliver's tunnel coupling model (see above) or a stress-related effect to explain the four level fine structure, although their measurements were carried out at room temperature, and no information can be given whether the characteristic spectral fine structure would have been observed for the investigated SiV centers.

We note, that the heteroepitaxial diamond used by Neu *et al.* is susceptible to crystal strain, which is revealed by a shift of the ZPL wavelength for different emitters. It stands to reason that strain also influences the polarization properties of individual color centers. In the course of this thesis, we develop a model for the SiV which also takes into account strain. Therefore, we will revisit the measurements of Neu *et al.* later (Sec. 5.1.2).

1.3 Spectral properties of silicon vacancy centers

We have already noted some of the spectral properties of the SiV center in the previous section where it was necessary to mention them in the context of the molecular structure of the defect. In this section, we take a closer look at these spectral properties. First, we discuss the emission and absorption properties of the defect at room temperature (Sec. 1.3.1), then we review its spectral fine structure visible at low temperatures (Sec. 1.3.2) and finally we give a brief overview on single photon creation using individual SiV centers (Sec. 1.3.3).

1.3.1 Spectral properties at room temperature

The emission of a defect in a solid state material shows some differences from a purely atomic transition because the defect can interact with vibrations of the host material. This is generally referred to as electron-phonon coupling or vibronic coupling. The term "phonon" here refers both to vibrations of the diamond (lattice vibrations) and local vibrations of the defect, which are similar to the vibrations of a molecule. A purely electronic transition is called a zero phonon line (ZPL), whereas any transitions involving vibrations are called phonon sidebands (for a detailed description, see below). The sideband is red (blue) shifted from the zero phonon line by the energy necessary to create (annihilate) the phonon and, in general, the zero phonon line shows a smaller line width compared to the phonon sidebands.

The room temperature emission spectrum of the SiV center is dominated by a ZPL in the near infrared spectral region. The wavelength of the ZPL is usually centered at 738 nm or 1.68 eV. This value has been measured for the peak wavelength of SiV ensembles (see for example Ref. [134]), whereas the ZPL wavelength for single emitters can deviate from this [56, 58]. Similarly, the room temperature line width of the ZPL ranges from about $7-8$ nm for ensembles of SiV center in polycrystalline diamond [105] to below 1 nm for individual SiV centers [56, 58]. In addition to the weak phonon sidebands, this narrow emission makes the SiV center a very attractive candidate for room temperature single photon emission, because essentially all fluorescence light is concentrated in a narrow ZPL.

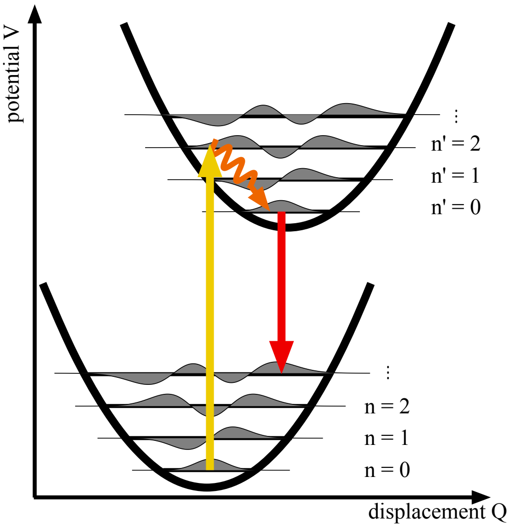

Figure 1.3: Electron phonon coupling approximated using harmonic oscillator potentials for the vibrational modes n in the ground and n' in the excited state. After an excitation to a higher lying vibrational state (yellow arrow), the color center quickly relaxes to the vibrational state $n' = 0$, from where it decays to the ground state via the emission of a photon (red arrow). The most probable transition is the one with the highest overlap between vibrational eigenfunctions ($n' = 0 \longrightarrow n = 3$).

We do not discuss the sideband energies here in detail (see Refs. [58, 137, 138] for a detailed discussion). Still, electron phonon coupling allows to draw qualitative conclusions for the strength of vibrational interactions which we include in the theoretical model (Sec. 2.2.3). Therefore we briefly indicate the main mechanisms. When a defect is excited from its ground state to a higher lying electronic state, the electron wave function and therefore the charge distribution changes. Consequently, the atoms around the defect are either attracted or repulsed from the now modified charge distribution and relax to a new position. This relaxation induces the vibrations, hence there is a coupling between the electron cloud and the possible vibration modes of the defect. Following the arguments of Davies [139], we assume a defect interacting with one dominant vibrational mode which can be approximated using a harmonic oscillator potential, thus the total energy in the electronic ground state is given by the potential:

$$V_g = \tfrac{1}{2} m\omega^2 Q^2, \tag{1.1}$$

where the mode has the frequency ω, the mass m and the displacement Q (in a generalized coordinate frame) from the equilibrium position. The potential for the excited state ist then:

$$V_e = V_0 + aQ + \tfrac{1}{2} m\omega^2 Q^2 + bQ^2, \tag{1.2}$$

where V_0 is the purely electronic energy, aQ (bQ^2) is called linear (quadratic) electron phonon coupling. The term aQ expresses the displacement of the vibrational equilibrium position which is due to the difference in charge density for ground and excited state. Hence, if we draw parabolas for the ground and excited state vibrational potentials (Fig. 1.3), these parabolas will be displaced from each other.

The vibronic coupling potentials give rise to vibrational states which are eigenfunctions of the harmonic oscillator (grey shaded functions in Fig. 1.3) and have quantum numbers $n, n' = 0, 1, 2, \ldots$. For a ZPL transition the vibrational modes do not change ($n = n'$). The Franck-Condon principle assumes that the absorption and emission of a photon and the related change in the electronic distribution are much faster than the vibrations of the surrounding nuclei. Hence optical transitions in Fig. 1.3 always occur vertically.

After an excitation to a higher lying vibrational state ($n' = 2$ in Fig. 1.3), the color center quickly relaxes to the vibrational state $n' = 0$, from where it decays to the ground state via the emission of a photon. The transition strength is proportional to transition dipole matrix element. In the Condon approximation, this matrix element can again be separated into a vibrational and an electronic overlap integral. Therefore, the most probable transition is the one with the highest overlap between vibrational eigenfunctions ($n' = 0 \longrightarrow n = 3$). Such a transition is a phonon sideband which is red shifted to the frequency of the ZPL.

Since we noted that optical transitions are always vertical in this scheme, the probability for a sideband to occur is given by the displacement of the parabola, which in turn depends on the linear electron phonon coupling. As a result, the larger the difference in charge distribution between ground and excited state is, the stronger are the phonon sidebands. To quantify the electron phonon coupling, one introduces the Huang-Rhys factor S which is defined by

$$e^{-S} = \frac{I_{ZPL}}{I_{ZPL} + I_{PSB}}, \tag{1.3}$$

where I_{ZPL} is the intensity of the ZPL and I_{PSB} the one of the phonon sideband. In consequence to the discussion above, $n = S$ denotes the most probable vibrational ground state into which the defect decays from the excited state. Ê The Huang-Rhys factor for the SiV center is found to lie between $S = 0.08$ and $S = 0.24$ for SiV ensembles [56, 102, 140]. This low value means, that the linear electron-phonon coupling is small and, in fact, the

ZPL is the most probable transition. Therefore, we assume that the electron density and hence the electron wave function does not change much between excited and ground state. This will be an important statement when modeling the susceptibility of the electronic states to the Jahn-Teller effect in Sec. 2.2.3.

Before we move on to the fine structure spectrum of the SiV center in the next section, we briefly review its absorption properties: While the first spectroscopic measurements were performed using cathodoluminescence [99, 100], we focus here on optical excitation of the SiV center. It has been shown that SiV centers can be excited non-resonantly in a broad spectral range. Iakoubovskii *et al.* present optical excitation between 1.7 eV and 2.5 eV [141]. For non-resonant excitation, a population of higher vibronic states takes place as we have indicated above. Wang *et al.* employ a 685 nm diode laser to excite single SiV centers, and similarly, Neu *et al.* utilize wavelengths between 671 nm and 700 nm [56, 115]. It appears reasonable for non-resonant excitation to employ a wavelength relatively close to the resonance to prevent excitation of other defects in the diamond which would overlap with the SiV fluorescence.

While non-resonant excitation of defects in solids with detection on their ZPL is relatively straight-forward, resonant optical excitation can be challenging: In contrast to e.g. atom vapor cells or trapped ions, where the optical detection can be placed at 90° to the excitation, solid state spectroscopy is often performed in confocal reflection microscopes (c.f. Sec. 3.1) where the excitation laser is reflected from the sample surface and overlaps the fluorescence. When exciting the defects using a non-resonant laser, the reflected excitation light can be conveniently suppressed using optical band pass filters, but this technique cannot be applied when exciting resonantly. Resonant excitation of the SiV ZPL has been performed in absorption geometry in Refs. [140, 142], but this requires a high defect concentration.

However, owing to the presence of phonon sidebands – though they may be weak for the SiV center – an alternative method is feasible: The phonon sidebands of the SiV center are more than 20 nm red shifted from the ZPL wavelength [138]. When the excitation laser is tuned to the ZPL wavelength and the spectral detection window is set to the phonon sidebands, both wavelengths can be separated again using band pass filters. In this case, one probes absorption on the ZPL while monitoring the sideband intensity (PLE). In contrast, spectroscopic measurements utilizing non-resonant excitation with detection on the ZPL are often termed photoluminescence (PL) measurements. As an optical excitation *on resonance* with the ZPL is particularly interesting when the defect shows narrow transition lines, we will review the results of this technique in the next section.

While the preceeding discussion of the room temperature spectra provides a first insight into the level structure of the SiV center, the next section covers the low temperature spectroscopy on the defect, revealing the spectral fine structure.

1.3.2 Fine structure at low temperature

The first spectroscopy experiments on SiV centers were carried out at liquid nitrogen temperature [99, 100]. However, the spectral resolution of the utilized detection apparatus was not sufficient, no fine structure was observed in these experiments. Besides the spectral resolution of the experimental setup being a limitation, the ZPL wavelength is susceptible to crystal strain and shows broadening effects which “wash out” the fine structure. This is especially the case for inhomogeneous media, such as polycrystalline diamond films [108,142]. In 1994, Collins *et al.* first identified the SiV fine structure center to be a doublet when investigating polycrystalline films at temperatures down to 1.7 K. One year later, Clark *et al.* [62] and Sternschulte *et al.* [137] independently observed, that the fine structure splits into more lines, when studying homoepitaxial, single crystalline diamond films grown by CVD (Fig. 1.4a). They observed that the doublet splits into a quartet below approximately 50 K. In addition to the four main peaks, they observed eight other peaks. The total number of 12 peaks can grouped into three subsets. From the relative intensity of the three subsets, it was deduced that the three groups are due to the three silicon isotopes ^{28}Si, ^{29}Si and ^{30}Si. We focus our attention in this work exclusively on the four lines attributed to ^{28}Si which is the most common isotope. These four lines with their characteristic splittings (see below) and relative intensities can be seen as the spectral fingerprint of the SiV center and make an unambiguous attribution to the defect straightforward.

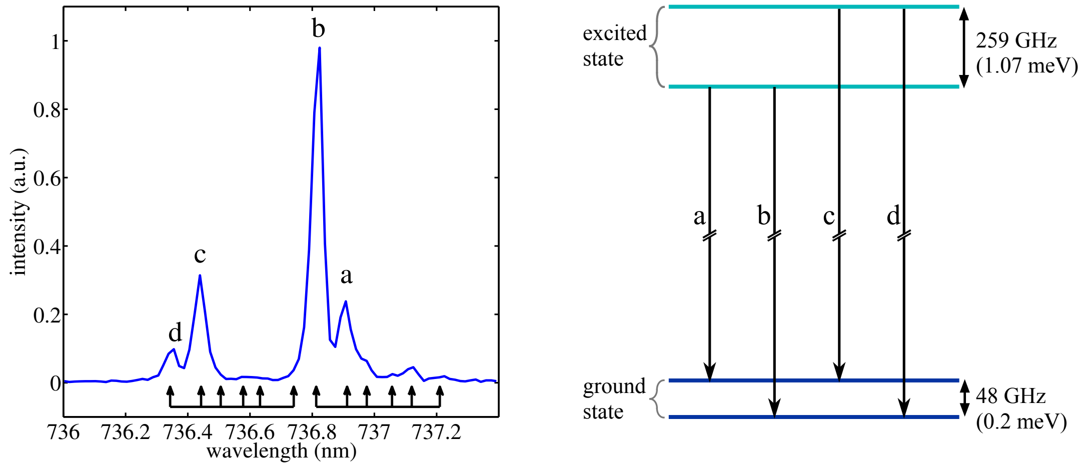

(a) (b)

Figure 1.4: The spectral fine structure of the SiV center (panel a), observed at 6 K on a homoepitaxial diamond film similar to the one employed in Refs. [62, 133] (see also Sec. 4.1.1). Of the twelve visible peaks (black arrows below the spectrum), the strongest four a, b, c, d refer to the ^{28}Si isotope. The four peaks are interpreted to arise form a split ground and excited state (panel b).

Both, Clark and Sternschulte have interpreted the four peak fine structure as optical transitions between a doubly split ground and excited state (Fig. 1.4b). The spectral splitting between peak a and peak c is equal to the excited state splitting $\Delta\nu_e = 259$ GHz (the same is true for peaks b and d). Similarly, the splitting between a and b (c and d) represents the ground state splitting $\Delta\nu_e = 49$ GHz. With increasing temperature, a change in the relative peak heights is observed, which can be explained by a thermalization mechanism: The relative intensity of an optical transition is proportional to the occupation n_i of the initial electronic state. When an electronic system can freely exchange the occupation from one excited (ground) state i (with energy E_i) to another, this results in a Boltzmann distribution $n_i(T)$ for a given temperature T:

$$n_i(T) = n_0 \exp\left(\frac{E_i - E_0}{k_B T}\right). \tag{1.4}$$

Here, n_0 is the occupation of the lowest lying state with energy E_0 and k_B the Boltzmann constant. When calculating the intensity ratio of two transitions, which end on the same final state, e.g. I_a/I_c for peaks a and c, the variables n_0 and E_0 cancel out:

$$\frac{I_a}{I_c} \propto \frac{n_i}{n_j} = \exp\left(\frac{E_i - E_j}{k_B T}\right), \tag{1.5}$$

Hence, a logarithmic plot of the intensity ratio of the peaks versus the reciprocal temperature (a so-called Arrhenius plot) should reveal a straight line for a thermalizing electronic system. The slope of the line is then equal to the spectral spacing, i.e. $\Delta\nu = \frac{E_i - E_j}{h}$, with h being Planck's constant.

Clark *et al.* and Sternschulte *et al.* observed such a thermalization for both ground and excited state: Absorption measurements (PLE, see above) proved that the two ground states thermalize. For the excited states, investigation of the emission in PL revealed that they thermalize as well. Sternschulte *et al.* reported in Ref. [137], that the SiV center has a rather short excited state lifetime between 1 ns and 4 ns. This means, that the excited state relaxation happens on a timescale much faster than the luminescent lifetime of the defect. We will return in Sec. 4.2 to the relaxation mechanism in the excited state, and discuss mechanisms which could be responsible for it.

Sternschulte *et al.* applied external fields to SiV ensembles: In their first publication in 1994, they discuss uniaxial stress measurements, which we already have briefly addressed in Sec. 1.2.3. The application of uniaxial stress along the [100] crystal direction leads to a shift of the outer fine structure peaks a and d while the inner b, c almost show no response to the applied stress. The stress measurements were performed both in PL and PLE. In PL, all peaks except b vanish with increasing stress, thus at high strain fields, only one single peak is visible. In the course of the thesis, we will discuss an interaction Hamiltonian for uniaxial stress, and we return to the SiV spectrum under the influence of crystal strain in Chap. 5, where we show that we can qualitatively model the spectra obtained by Sternschulte *et al.*.

As a second experiment, Sternschulte *et al.* applied magnetic fields [133] to the same sample which they exposed to uniaxial stress. In a magnetic field, the Zeeman effect splits the magnetic sublevels and the spectral fine structure splits into a multitude of peaks. As the SiV ensemble in Ref. [133] shows a significant inhomogeneous broadening, the peaks in their measurement are not spectrally resolved. Hence, the authors did not analyze this measurement in greater detail.

We repeat the exposure of SiV ensembles to magnetic fields in the course of this work, and it is this measurement, which is central to the understanding of the electronic structure of the defect. To show a progress compared to Ref. [133], we fabricated SiV ensemble samples with very low inhomogeneous broadening. Finally, we also observe single SiV defects in magnetic fields which completely eliminates ensemble effects and makes an unambiguous assignment of transitions possible. For the latter experiment, we briefly review the literature on individual SiV centers in the next section.

1.3.3 Investigation of single silicon vacancy defects

The first access to single defect centers in diamond, which was reported in 1997 by Gruber *et al.* [39], marked a milestone in the history of solid state quantum optics. Before, research on individual quantum systems was available from atom beams [143], trapped ions [144], semiconductor quantum dots [145] and fluorescent dye molecules [146]. All these previous systems have their disadvantages [147]: Trapped ions require a considerable technical effort, semiconductor quantum dots need to be cooled to low temperatures and dye molecules exhibit photobleaching. In contrast, individual color centers in diamond are accessible at room temperature with relatively low technical overhead. While the first quantum optics experiments were carried out using nitrogen-vacancy centers, in the mid-2000s new defects centers were investigated at the single defect level. In 2004, single photon emission from single nickel-related (NE8) defects were studied by Gaebel *et al.* [148]. The first experimental investigation of individual SiV defects was performed in 2006 by Wang *et al.* [57].

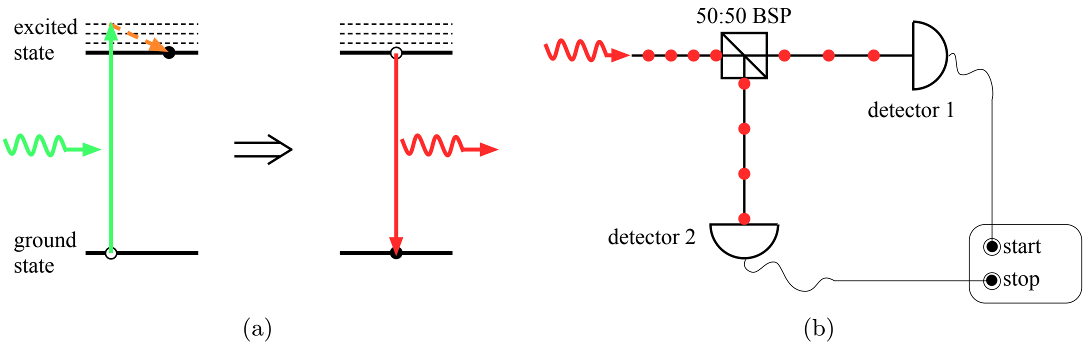

Figure 1.5: Single photon generation and detection: The absorption (green arrow) and emission (red arrow) cycle on a two-level quantum system gives rise to time separated, single photons (panel a). These are analyzed in a Hanbury-Brown Twiss interferometer (panel b), consisting of a 50 : 50 beamsplitter (BSP) and two single photon detectors which are connect a fast correlation electronics.

Before we discuss the studies of Wang, we review how the optical emission of single centers is different from defect ensembles. We approximate a single defect as a quantum system consisting of an electronic ground and excited state coupled to vibrational states. For simplicity, we only consider the vibrational states for the excited state (Fig. 1.5a). Non-resonant optical excitation (green arrow) populates a higher lying vibrational state which quickly relaxes to the vibrational mode $n' = 0$ (see also Sec. 1.3.1). After a certain time, the defect relaxes to its electronic ground state again with the emission of a single photon (red arrow). Then the absorption-emission cycle starts over. The finite lifetime which the electron spends in the excited state, separates consecutively emitted photons. This results in a stream of time separated (so-called antibunched) photons. In the wave-particle dualism of light, antibunched light reveals the particle nature for light. Therefore, it is a pure quantum phenomenon that has no classical counterpart, thus, we also speak of non-classical light. When an ensemble of defects emits fluorescence light in an uncorrelated way, then this non-classical character is lost.

The presence of a single defect is then revealed by measuring the intensity autocorrelation function $g^{(2)}(\tau)$, which is equal to the conditional probability of detecting two individual photons with a time delay τ [1]. As we have just seen, it is not possible for an ideal single photon emitter to emit two photons at a time. Hence, the intensity autocorrelation for zero delay $g^{(2)}(\tau = 0)$ equals 0 for a perfect single photon source. We here only describe the measurement of the $g^{(2)}$-function in this phenomenological manner, for a detailed mathematical analysis we refer the reader to Refs. [1, 149].

The $g^{(2)}$-function is measured using a Hanbury-Brown Twiss interferometer, which is sketched schematically in Fig. 1.5b. The light emitted by the defect center under investigation passes a 50:50 beamsplitter cube where it is either transmitted to detector 1 or reflected to detector 2. Each photon impinging on a detector triggers an electric pulse (a "click"). The arrival times of the detector clicks are then correlated: In a simplified scheme, a click from detector 1 starts a timer which is then stopped by a click from detector 2. From this measurement, the $g^{(2)}$-function is obtained by plotting the occurrence of consecutive photons in a histogram versus the delay in between them. For long time delays, there is usually no correlation between photons, thus the $g^{(2)}$-function is constant for $\tau \to \infty$ and can be readily normalized to $g^{(2)}(\tau) = 1$ for these regions. For antibunched light, the probability for two photons to arrive *simultaneously* at both detectors is small, hence, the resulting $g^{(2)}$-function is inferior to 1 for $\tau \to 0$. This characteristic antibunching dip for zero delay is usually taken as the experimental proof for the non-classical light of a single emitter.

In addition, the intensity autocorrelation reveals the dynamics of the electronic transitions of a quantum system. When $g^{(2)}(\tau) > 1$, we speak of correlated emission or "bunched" light, which e.g. can be found for the thermal emission of classical light sources. Bunched light for a single emitter indicates the presence of a metastable shelving state (see below). For such an effective three-level system, the $g^{(2)}$-function exhibits the functional dependence

$$g^{(2)}(\tau) = 1 - (1 + a) \cdot \mathrm{e}^{-|\tau|/\tau_1} + a \cdot \mathrm{e}^{|\tau|/\tau_2}, \tag{1.6}$$

where the time constants τ_1 and τ_2 characterize the photon antibunching and bunching, respectively. The strength of the bunching is quantified by the parameter a; for a simple two-level system $a = 0$.

We now return to the experimental demonstration of SiV single photon emission from Wang *et al.* [57]. Utilizing confocal microscopy (c.f. Sec. 3.1.1) with an optical excitation at 685 nm, they investigated natural IIa diamond which had been irradiated with 10 MeV

Si^{2+} ions. In regions, where the implantation dose was estimated to be 10^9 ions/cm^2, they identified individual SiV centers with ZPL emission at 738 nm. The intensity autocorrelation function showed a dip for zero time of $g^{(2)}(\tau = 0) = 0.7$ and featured also a characteristic bunching which points towards a shelving state. In addition to the $g^{(2)}$-measurement, Wang *et al.* also presented fluorescence lifetime measurements indicating a lifetime of about $\tau_r = 1$ ns. In comparison with the nitrogen vacancy center ($\tau_r \approx 10$ ns [150]), this is a relatively short lifetime, thus one would expect a fast absorption and emission cycle and therefore a bright single photon emission. In contrast, Wang *et al.* only observed about 700 photons per second on saturation. They explained this weak emission by the presence of a non-radiative transition path which also involves the metastable shelving state.

In 2011, Neu *et al.* reported on single SiV defects in isolated nanodiamonds grown on iridium [56]. In contrast to the bulk diamond samples from Wang *et al.*, the defects in nanodiamonds showed a very high brightness, exhibiting fluorescence count rates of several million photons per second. Owing to this increased brightness, several spectroscopic properties of single SiV centers, which had been inaccessible before, could be investigated. Neu's publication [56] entailed a series of other papers in which – together with the first one – they analyzed the following properties:

- The authors analyzed the spectral position of the ZPL and the phonon sidebands for different emitters [56, 58]. Both varied strongly from emitter to emitter, with a spread in ZPL wavelength over 20 nm and strong deviations in the phonon sidebands. In addition, they discovered further optical transitions between 820 nm and 840 nm which are attributed to the defect utilizing cross-correlation measurements between these emission lines and the ZPL.

- For the first time, the polarization of an individual SiV center was measured. This measurement was first performed on nanodiamonds [56], however, as nanodiamonds grow from randomly oriented seed crystals, it was difficult to determine the crystallographic orientation from the polarization graphs. In a follow-up paper [58], SiV defects in oriented "nano-islands" were therefore investigated. We already discussed the results of this study in Sec. 1.2.3.

- The measurement of the intensity autocorrelation $g^{(2)}$ yields information about the population dynamics because the time constants τ_1, τ_2 in Eq. (1.6) relate to the transition rates between the ground, the excited and the metastable state. To understand these dynamics for the SiV center, Neu *et al.* measured the $g^{(2)}$-function at room temperature for different excitation intensities and compared the resulting data with the simulation of an effective three level system [56, 117]. The high agreement of the simulation with the experiment justifies the assumption of a three-level system including a long living shelving state.

- With the resulting transition rates, the quantum efficiency of the SiV center, i.e. the probability of emitting a photon after an optical excitation, can be determined. For this, the measured photon count rate is compared to the radiative decay rate from the excited to the ground state. This comparison needs to take into account the dipole emission, the collection efficiency, the transmission of all optical components and the detection efficiency of the photon counting modules involved. While the latter two properties are relatively straightforward to measure, the emission and collection of the defect needed to be simulated. Neu *et al.* employ a numerical algorithm which develops the emission of an individual dipole in a series of plane waves and calculate the collection of the microscope objective with a given numerical aperture [117].

The rather low quantum efficiency of about 5 %, which they find in their studies, points towards an additional non-radiative decay, which reduces the observable photon emission. As a side result, they discover that the emission and collection for SiV centers in nanodiamonds is at least one order of magnitude larger than for SiV centers in bulk diamond. This partly explains the strong difference in count rates compared to the measurements of Wang *et al.* [57].

- Neu *et al.* present low temperature spectra of individual SiV centers. Since the defects show the characteristic fine structure, they can be unambiguously attributed to SiV centers [56, 115]. Similarly to the spectral spread of room temperature ZPL wavelength, the position, the splitting and the relative peak intensities of fine structure spectrum show large variations from one emitter to another.

  At low temperatures, the line widths of the fine structure peaks vary between 25 and 160 GHz. These widths are found to be two orders of magnitude larger than the estimated lifetime limited peak widths, hence Neu *et al.* assume an additional broadening mechanism: Additional defects in the nanodiamonds, such as substitutional nitrogen $[N_\mathrm{S}]$, might be photoionized forming $[N_\mathrm{S}]^+$ and free electrons in the diamond conduction band. A similar mechanism has been discussed for fluctuating surface charges [151]. It has been shown for the nitrogen-vacancy color center, that these charge fluctuations can shift the color center energy levels via the Stark effect [152, 153], leading to spectral jumps and broadening of the optical transitions. This effect is commonly referred to as spectral diffusion. Hence, Neu *et al.* attribute spectral diffusion as the main additional broadening mechanism for single SiV center in nanodiamonds. Spectral diffusion imposes an obstacle when we address the electronic structure of the SiV center.

We begin this work, where the publications of Neu *et al.* ended. While their studies revealed many properties of the room temperature emission and the intra-level dynamics of the defect, there is only little access to the spectra fine structure in their measurements: The strong strain fields in their samples imply that, essentially, every nanodiamond shows a different fine structure splitting. This makes a clear assignment to a faithful model for the SiV level structure very challenging.

We therefore use an alternative approach: Neu *et al.* succeeded in finding individual SiV defects with unprecedented photon count rates at the cost of a possibly non-optimal crystal environment. We here start from an optimal SiV defect, i.e. we fabricate single defects in a mostly unperturbed environment using single crystalline diamond. For this “ideal” defect we develop a theoretical model and compare the model to the results of several spectroscopic measurements. The tradeoff for our approach is, that the single defects in single crystalline diamond exhibit low photon count rates due to total internal reflection and necessitate therefore additional efforts to be detected with a sufficient signal-to-noise ratio.

After establishing a theoretical description for these ideal defects, we extend our model to cover the cases of crystal strain in terms of an additional perturbation and compare the outcome of this extended model with the measurement on individual SiV centers in strained nanodiamonds. As we repeat the magnetic field measurement of Sternschulte *et al.* (Sec. 1.3.2), our model needs to readily explain the outcome of these and earlier experiments (cf. Chap. 5).

Before we address the fabrication of the defect centers in an oriented, low strain environment in Chap. 3, we first introduce the theoretical model in the following chapter. We restrict ourselves to a model describing the ZPL fine structure. Hence, the phonon sidebands and the additional infrared fluorescence peaks found by Neu *et al.* are not in the focus of our research. Neither do we investigate the metastable state, because no optical emission has been attributed to it so far.

Chapter 2

Theoretical description

This chapter covers the theoretical model which we develop to describe the spectroscopic results of Chap. 4. The model was developed in corporation with Victor Waselowski and Jeronimo Maze from Pontificia Universidad Catolica de Chile. We have seen in the previous chapter, that there are several molecular geometries which have been discussed for the SiV center. Related to the molecular geometries are defect symmetries which determine the orbital level structure of the defect. We restrict ourselves here to the trigonal antiprismatic structure proposed by Goss *et al.* [122]. To deduce which level scheme follows from this symmetry, we first give a general introduction to the concept of group theory in Sec. 2.1. After this introduction, we apply the discussed concepts to the particular case of the SiV center in D_{3d} symmetry and derive the orbital basis states for it (Sec. 2.1.4).

The basis states which we deduce will be energetically degenerated. However from the spectral measurements discussed in the previous chapter, we know that the defect exhibits a spectral fine structure which must be related to a level splitting. We model this level splitting using perturbation terms for spin-orbit (SO) coupling (Sec. 2.2.2) and Jahn-Teller interaction (Sec. 2.2.3). These two interactions lead to the orbital splitting responsible for the spectral fine structure as it is seen for low temperature spectra. In addition, we model the effect of crystal strain (Sec. 2.2.5) and of magnetic fields (Sec. 2.2.6). With all these interaction terms, we form the total Hamiltonian of the electronic system, which is numerically diagonalized to calculate its eigenvalues and eigenvectors.

With the eigenvectors at hand, we model optical dipole transitions (Sec. 2.3) to describe the emission intensity for each fine structure peak. This also enables us to predict the polarization of a given optical transition. Finally, we model a general orbital operator to account for a relaxation among the excited states (Sec. 2.3.3), which will be necessary for the interpretation of resonance fluorescence spectra in Sec. 4.2.

2.1 Fundamentals of group theory for the description of orbital states

To derive the orbital states of the SiV center we make use of the defect symmetry in the context of group theory. Group theory on the one hand provides a systematic calculus to classify symmetry elements and operations. On the other hand, it introduces a shorthand notation to embrace all the symmetry inherent to a molecular system by the concept of point groups, character tables and representations [154]. We here introduce these notions on the example for the SiV defect, but also refer to a more generalized theory whenever necessary [132, 155].

Mathematically, a *group* is defined by a set of the *elements* $A, B, C, \ldots$ under the operation of a binary *group multiplication* such that the following requirements are fulfilled [132]:

i. The product of any two elements AB corresponds to a unique element of the group, i.e. the set is *closed* under group multiplication.

ii. The associative law holds, e.g. $A(BC) = (AB)C$.

iii. There exists an *element* E such that for all elements A of the group $EA = AE = A$. This element is called the *identity* element.

iv. Corresponding to each element A of the group, there is an element B such that $AB = BA = E$. This element is called the *inverse* of the element A.

We restrict our attention to a *finite* group consisting of h group elements. If the group multiplication is commutative, so that $AB = BA$ for all A and B, then the group is said to be *Abelian.*

For an illustrative example, we imagine an equilateral triangle which we rotate (clockwise) by 120° about an axis running through its midpoint. Unless we label the corners of the triangle with numbers so we can follow their movement, the resulting triangle is indistinguishable from the original.

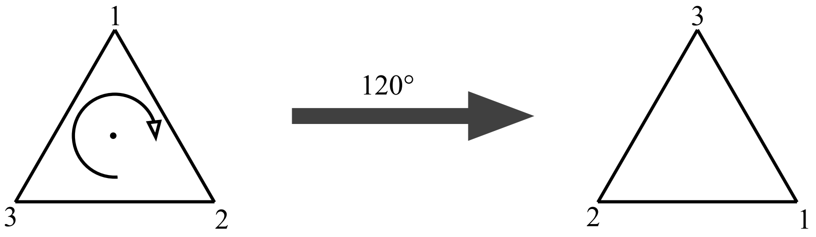

We define an operation which leaves an object unchanged, e.g. a rotation, as a *symmetry* operation which is performed with respect to a given *symmetry element.* The symmetry element here is the axis about which the rotation takes place. There are four principal symmetry elements which we will review for the SiV center in the following section. All symmetry elements of a given object (or molecule, point defect) together constitute the elements of a group.

2.1.1 Point group and symmetry operations

We start our description by reviewing the molecular structure as deduced by Goss [122] as well as by Gali and Maze [127]. Following their calculations (Sec. 1.2), the Si impurity re-sides on an interstitial position, positioned in the middle of two lattice vacancies (Fig. 1.1b on page 8). The missing atoms at the vacancy sites create unsatisfied valences or dangling bonds on each carbon site. We build the defect states as combinations between the dangling bond orbitals and the orbitals of the Si-impurity. Therefore we consider the SiV as an isolated "molecule" consisting of the Si impurity in the split vacancy, surrounded by the next neighbor carbon atoms (Fig. 2.1).

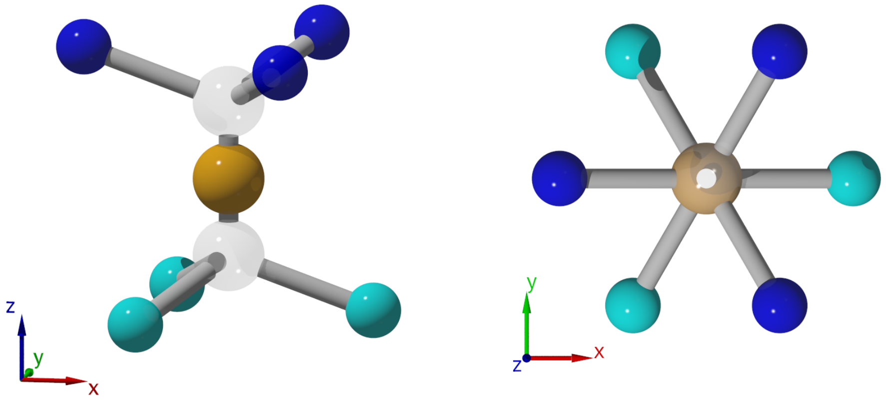

(a) side view (b) top view

Figure 2.1: Molecular model of the SiV center, without the surrounding diamond lattice: The Si impurity (yellow) is situated on an interstitial position along the ⟨111⟩ bond axis and surrounded by a split vacancy (transparent). The next-neighbor carbon atoms around the SiV defect (blue and light blue) have unsaturated bond orbitals which contribute to the electronic states. This graph also defines the internal coordinate frame of the defect; we set the origin of this coordinate system to the position of the Si impurity.

We now review the four principal symmetry elements which all occur for the SiV defect. After having established these symmetry elements, we present a scheme how to unambiguously assign an object with given symmetry elements to a so called point group. In the course of the assignment we will make use of the Schoenflies notation for symmetry elements.

The most trivial of all symmetry element is the *identity*, corresponding to the identity element E of a group. It leaves all coordinates of an object untouched, and therefore every molecule is invariant under the identity operation. Therefore, this operation is also included in the set of group elements for the SiV center.

Rotation axes We have already encountered a rotation operation about 120° in the illustrative example on the equilateral triangle above. We remember that a symmetry operation is carried out with respect to a symmetry element. The element in the case above was a three-fold rotation axis through the midpoint of the triangle and is called a C_3-axis. The symmetry operations corresponding to this axis are rotations about 120°, 240° and 360° and are given the abbreviations C_3^1, C_3^2, C_3^3, respectively.

In general, an n-fold C_n axis generates n rotations through multiples of (360/n)°. When more than one rotation axis is present in a molecule, the one of highest order n is called the main axis. The SiV center exhibits one C_3 axis along the “bond axis” of the split vacancy and the Si atom, and three C_2 axes, named C_2, C_2' and C_2'', perpendicular to the main symmetry axis (Fig. 2.2a,b). As the highest order is $n = 3$, we also refer to the SiV center as a *trigonal* defect.

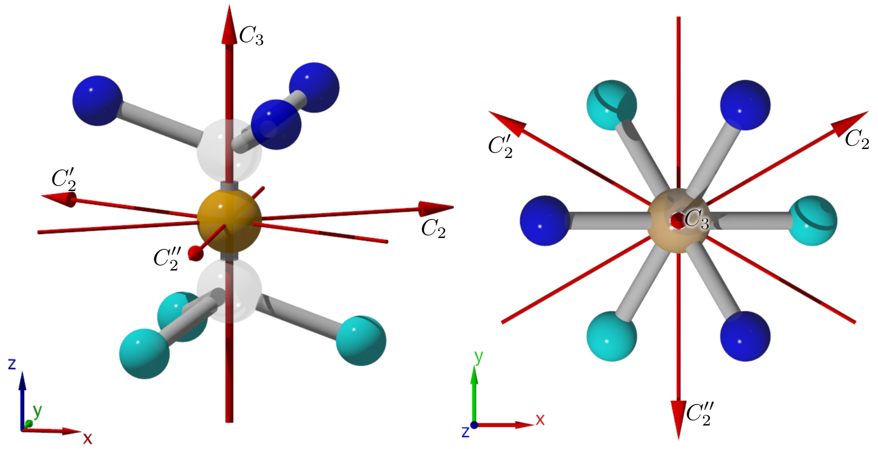

(a) rotation axes side view (b) rotation axes top view

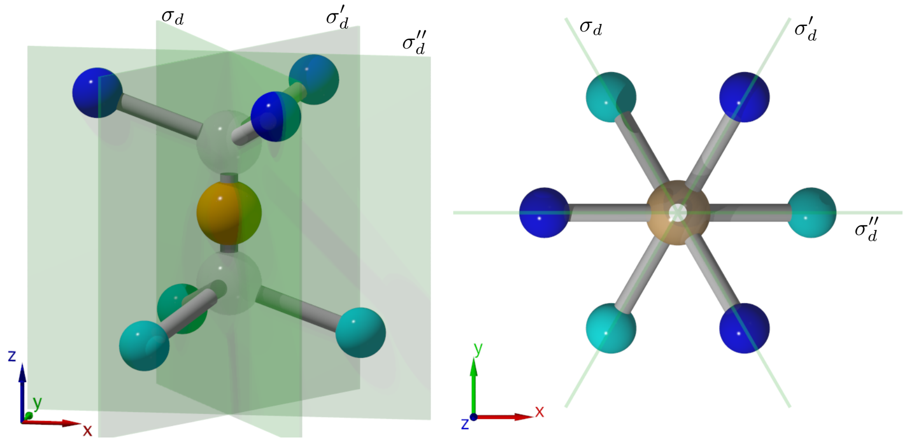

(c) mirror planes side view (d) mirror planes top view

Figure 2.2: The SiV center exhibits one C_3 axis along the “bond axis” of the split vacancy and the Si atom, and three C_2 axes perpendicular to this main symmetry axis (panels a,b). We number the C_2 axes using primes. There are three dihedral mirror planes (panel c,d).

Reflections and mirror planes The second important symmetry operation is the reflection which takes place with respect to a mirror plane. Reflections are usually given the symbol σ. While an n-fold rotation axis implies n possible symmetry operations, mirror planes exhibit only one operation, as two consecutive reflections with respect to the same mirror plane are always equivalent to the identity operation. We distinguish between three types of mirror planes: A horizontal mirror plane is perpendicular to the main rotation axis and it is denoted with the symbol σ_h. A vertical mirror plane contains the main symmetry axis and is called σ_v. A vertical plane which bisects two σ_v planes or two C_2 axes, is called a dihedral plane σ_d. The SiV center exhibits three mirror planes which each contain a next-neighbor carbon atom. As they lie in between the C_2 axes, they correspond to dihedral σ_d planes (Fig. 2.2c,d).

Inversion The inversion operation is carried out with respect to the center of inversion. This operation negates the coordinates of every point of the molecule $(x, y, z) \rightarrow (-x, -y, -z)$, and is denoted with the symbol i. A defect exhibiting a center of inversion is called *centrosymmetric*. The center of inversion for the SiV center is located at the position of the Si impurity.

The inversion is not a fundamental symmetry operation, because its action is equal to a rotation about a C_2 axis followed by a reflection on a σ_v plane perpendicular to this axis. However, owing to the importance of the operation, it is usually listed among the principal symmetry operations. When a molecule shows an inversion symmetry, the resulting electronic wave functions (cf. Sec. 2.1.4) carry the parity labels even and odd, which are abbreviated with the letters "g" (for the german gerade) and "u" (ungerade), respectively. An odd wave function Ψ_u changes sign under the parity operation: $\Psi_u(-r) = -\Psi_u(r)$. When calculating matrix elements for the perturbative interactions (Sec. 2.2), the parity of a state is a helpful property to determine which matrix elements are vanishing.

Improper Rotations The final symmetry element is called an improper rotation axis. The corresponding operation can be broken down into a rotation about a C_n axis followed by a reflection on a mirror plane σ_v perpendicular to this axis. An improper axis is abbreviated with the symbol S_n, where n corresponds to a (360/n)° rotation axis.

The SiV center has an S_6 improper axis, which coincides with the main C_3 symmetry axis (Fig. 2.3) and rotates the molecule first by 60°. The following reflection is carried out on a horizontal mirror plane σ_h. It is important to note that the improper rotation is a unique operation although it is combined from two other operations. Hence for the SiV defect, there is an S_6 axis which involves a rotation of 60°, but this does not imply the presence of a C_6 axis. We note, that some applications of the S_6 rotation-reflection leads to simpler symmetry operations which we have listed before, e.g. $S_6^2 = C_3^1$, $S_6^3 = i$, $S_6^4 = C_3^2$ and $S_6^6 = E$. Hence, the improper S_6 axis leads to only two new symmetry operations, which we denote S_6^1 and S_6^5. Consequently, when we later list the characters for the symmetry classes (Tab. 2.3), the class of improper rotations S_6 only has two elements.

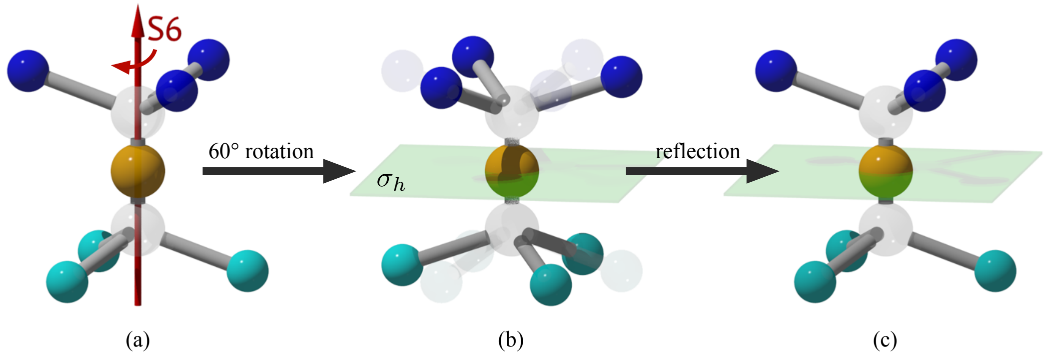

Figure 2.3: The improper rotation first rotates the SiV defect by 60° about the main symmetry axis (a), then reflects all coordinates on a mirror plane perpendicular to the rotation axis (b). Hence, the two operations together leave the defect invariant (c).

Point groups One could in principle characterize the symmetry of a molecule or defect by listing all the symmetry elements it possesses, but this is impractical – especially for highly symmetric molecules which exhibit many symmetry elements. Moreover, some symmetry elements automatically imply others, e.g. the presence of a C_2 axis and a σ_h mirror plane entails an inversion center i.

Hence, we define a *point group* as a collection of symmetry elements and operations which unambiguously classifies a molecule. The term point group comes from the fact that all symmetry elements of a molecule pass through at least one point which is unmoved by these actions. Furthermore, the notion point group is opposed to the term space group which classifies systems which include translational symmetry, e.g. for the description of crystal lattices.

Point groups are often labeled by a symbol according to the main symmetry element. We first name a few examples here: A molecule exhibiting only one C_n rotation axis belongs to the C_n point group. Consequently, a linear molecule has an infinite number of possible rotation angles, and therefore belongs to C_∞. When a molecule possesses one C_n axis in combination with a σ_v (σ_h) mirror plane, it belongs to the C_{nv} (C_{nh}) point group. An important example in the context of diamond defects is the nitrogen vacancy color center which belongs to the C_{3v} group. If several rotation axes are present for a molecule, then this molecule belongs to one of the dihedral point groups, which begin with the letter D. Finally, there are the cubic point groups which feature the tetrahedral (T, T_h, T_d) and octahedral (O, O_h) groups. The diamond unit cell exhibits cubic (O_h) symmetry. This implies that all defects in diamond will be in a sub-group of O_h [136]. The group O_h has a number of 48 symmetry elements and is only surpassed in size by the icosahedral group I_h which however only occurs for special cases like the C_{60} molecule.

To clarify which group the SiV center belongs to, we employ the assignment scheme depicted in Fig. 2.4. The scheme shows in a hierarchic manner which key decisions are required to assign a molecule to a given point group. With one C_3 axis, 3 C_2 axes and 3 σ_d planes, we assign the SiV defect to the D_{3d} point group.

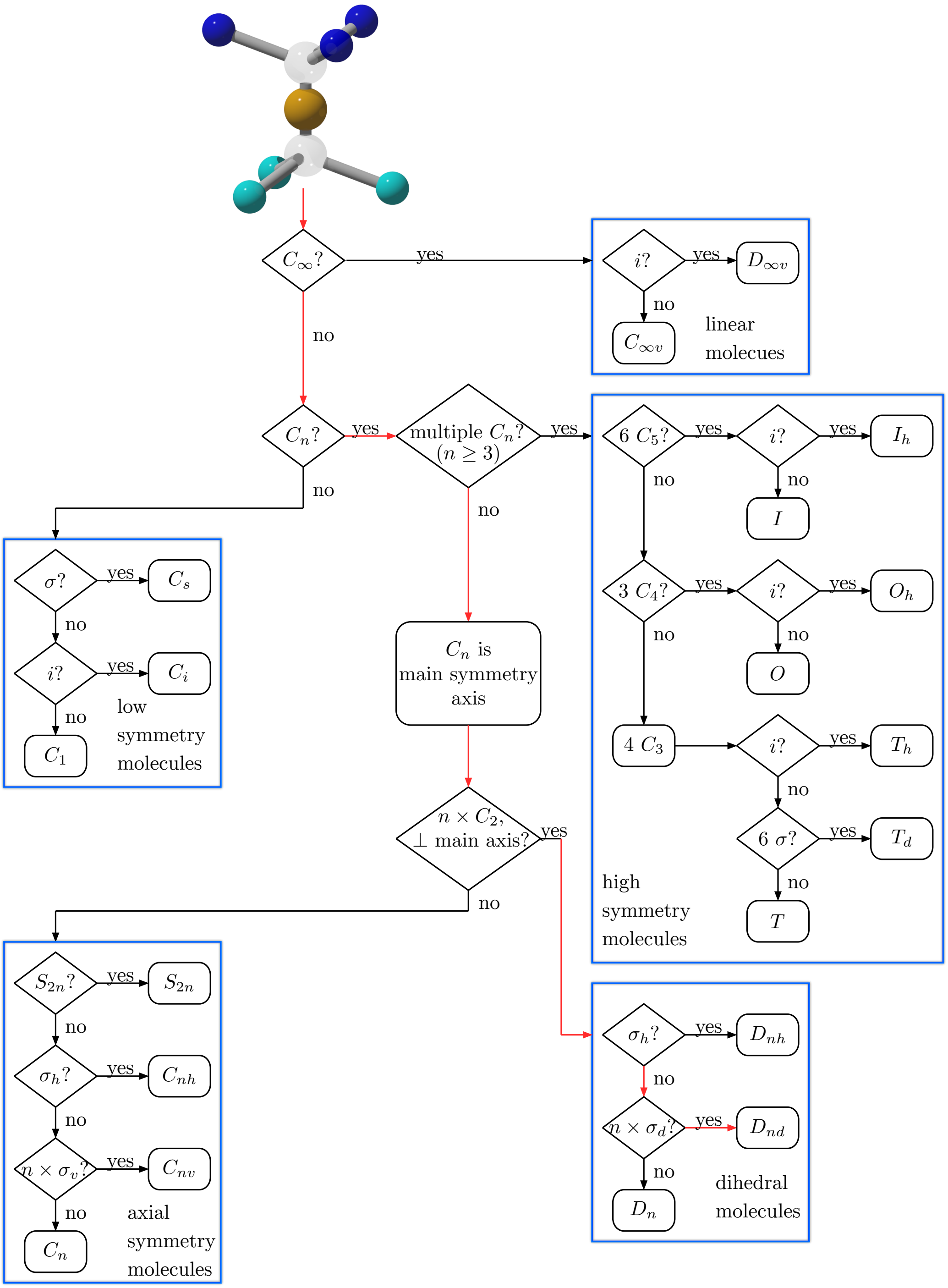

Figure 2.4: Flow diagram for the assignment of point groups. The path for the assignment of the SiV center is highlighted in red.

We have so far implicitly assumed that the symmetry operations of the D_{3d} point group really obey to the group axioms which we defined at the beginning of this chapter. With the help of a group multiplication table (Tab. 2.1), this is straightforward to prove. The D_{3d} group contains 12 symmetry operations which are listed in the top row and left column of Tab. 2.1. First, we see that the group is closed under group multiplication, i.e. each multiplication results in a member of the group. Second, it can be shown that the associative law holds, as we see in the following example

$$\left(C_3^1\ i\right)\ C_2 = \left(S_6^5\right)\ C_2 = \sigma_d' = C_3^1\ \left(i\ C_2\right) = C_3^1\ \left(\sigma_d\right)$$

Third, the existence of the identity operation is given. Finally, there is an inverse operation for each operation, such that their product equals the identity. This is verified by the presence of the identity element in each column of the multiplication table. Hence, all requirements for a group are fulfilled.

Table 2.1: Group multiplication table of the D_{3d} group. The multiplication $O_1 O_2$ is performed such that the columns denote the first symmetry operation O_1, and the rows the second operation O_2. All symmetry operations are corresponding to Figs. 2.2, 2.3.

$\mathbf{D_{3d}}$	E	C_3^1	C_3^2	C_2	C_2'	C_2''	i	S_6^1	S_6^5	σ_d	σ_d'	σ_d''
E	E	C_3^1	C_3^2	C_2	C_2'	C_2''	i	S_6^1	S_6^5	σ_d	σ_d'	σ_d''
C_3^1	C_3^1	C_3^2	E	C_2''	C_2	C_2'	S_6^5	i	S_6^1	σ_d''	σ_d	σ_d'
C_3^2	C_3^2	E	C_3^1	C_2'	C_2''	C_2	S_6^1	S_6^5	i	σ_d'	σ_d''	σ_d
C_2	C_2	C_2'	C_2''	E	C_3^1	C_3^2	σ_d	σ_d''	σ_d'	i	S_6^5	S_6^1
C_2'	C_2'	C_2''	C_2	C_3^2	E	C_3^1	σ_d'	σ_d	σ_d''	S_6^1	i	S_6^5
C_2''	C_2''	C_2	C_2'	C_3^1	C_3^2	E	σ_d''	σ_d'	σ_d	S_6^5	S_6^1	i
i	i	S_6^5	S_6^1	σ_d	σ_d'	σ_d''	E	C_3^2	C_3^1	C_2	C_2'	C_2''
S_6^1	S_6^1	i	S_6^5	σ_d'	σ_d''	σ_d	C_3^2	C_3^1	E	C_2'	C_2''	C_2
S_6^5	S_6^5	S_6^1	i	σ_d''	σ_d	σ_d'	C_3^1	E	C_3^2	C_2''	C_2	C_2'
σ_d	σ_d	σ_d'	σ_d''	i	S_6^5	S_5^1	C_2	C_2''	C_2'	E	C_3^1	C_3^2
σ_d'	σ_d'	σ_d''	σ_d	S_6^1	i	S_6^5	C_2'	C_2	C_2''	C_3^2	E	C_3^1
σ_d''	σ_d''	σ_d	σ_d'	S_6^5	S_6^1	i	C_2''	C_2'	C_2	C_3^1	C_3^2	E

So far, we have seen how the point group classifies a molecule according to the symmetry elements the molecule possesses, and we have verified that these elements actually form a group. To characterize which possible electronic states arise from a given point group, we first need to introduce the concept of representations and characters.

2.1.2 Representations and Character Tables

In the previous section, we have seen how to apply symmetry operations in an illustrative manner, e.g. describing the result of C_3^1 as a geometrical rotation. For a mathematical treatment, we will replace these geometrical descriptors by numerical operators. These numerical operators again form a group which is said to be homomorphic to the original group. Such a homomorphic group is called a *representation*. By a representation of a group, we here always associate a square matrix $\Gamma(A)$ with each group element A, such that $\Gamma(A)\,\Gamma(B) = \Gamma(AB)$. It can be shown [132, page 18] that the group of transformation matrices again satisfies the group axioms stated above.

One way to generate a point group representation is to look at the effect of the symmetry operations on a set of basis vectors $\{\hat{x}, \hat{y}, \hat{z}\}$:

$$
\begin{array}{ccc}
\underset{\Gamma(E)}{\begin{bmatrix} 1 & 0 & 0 \\ 0 & 1 & 0 \\ 0 & 0 & 1 \end{bmatrix}} &
\underset{\Gamma(C_3^1)}{\begin{bmatrix} -\frac{1}{2} & -\frac{1}{2}\sqrt{3} & 0 \\ \frac{1}{2}\sqrt{3} & -\frac{1}{2} & 0 \\ 0 & 0 & 1 \end{bmatrix}} &
\underset{\Gamma(C_3^2)}{\begin{bmatrix} -\frac{1}{2} & \frac{1}{2}\sqrt{3} & 0 \\ -\frac{1}{2}\sqrt{3} & -\frac{1}{2} & 0 \\ 0 & 0 & 1 \end{bmatrix}} \\[2ex]
\underset{\Gamma(C_2)}{\begin{bmatrix} \frac{1}{2} & \frac{1}{2}\sqrt{3} & 0 \\ \frac{1}{2}\sqrt{3} & -\frac{1}{2} & 0 \\ 0 & 0 & -1 \end{bmatrix}} &
\underset{\Gamma(C_2')}{\begin{bmatrix} \frac{1}{2} & -\frac{1}{2}\sqrt{3} & 0 \\ -\frac{1}{2}\sqrt{3} & -\frac{1}{2} & 0 \\ 0 & 0 & -1 \end{bmatrix}} &
\underset{\Gamma(C_2'')}{\begin{bmatrix} -1 & 0 & 0 \\ 0 & 1 & 0 \\ 0 & 0 & -1 \end{bmatrix}} \\[2ex]
\underset{\Gamma(i)}{\begin{bmatrix} -1 & 0 & 0 \\ 0 & -1 & 0 \\ 0 & 0 & -1 \end{bmatrix}} &
\underset{\Gamma(S_6^1)}{\begin{bmatrix} \frac{1}{2} & \frac{1}{2}\sqrt{3} & 0 \\ -\frac{1}{2}\sqrt{3} & \frac{1}{2} & 0 \\ 0 & 0 & -1 \end{bmatrix}} &
\underset{\Gamma(S_6^5)}{\begin{bmatrix} \frac{1}{2} & -\frac{1}{2}\sqrt{3} & 0 \\ \frac{1}{2}\sqrt{3} & \frac{1}{2} & 0 \\ 0 & 0 & -1 \end{bmatrix}} \\[2ex]
\underset{\Gamma(\sigma_d)}{\begin{bmatrix} -\frac{1}{2} & -\frac{1}{2}\sqrt{3} & 0 \\ -\frac{1}{2}\sqrt{3} & \frac{1}{2} & 0 \\ 0 & 0 & 1 \end{bmatrix}} &
\underset{\Gamma(\sigma_d')}{\begin{bmatrix} -\frac{1}{2} & \frac{1}{2}\sqrt{3} & 0 \\ \frac{1}{2}\sqrt{3} & \frac{1}{2} & 0 \\ 0 & 0 & 1 \end{bmatrix}} &
\underset{\Gamma(\sigma_d'')}{\begin{bmatrix} 1 & 0 & 0 \\ 0 & -1 & 0 \\ 0 & 0 & 1 \end{bmatrix}}
\end{array}
\tag{2.1}
$$

The 3×3-matrices are applied the following way: Imagine, the coordinate of a next-neighbor carbon atom is denoted by $\mathbf{r} = (x, y, z)$. Under a symmetry operation $R = E, C_3^1, C_3^2, \ldots$, these coordinates will change according to $\Gamma(R)\mathbf{r} = \mathbf{r}'$. The transformation matrices $\Gamma(R)$ in (2.1) satisfy the multiplication table 2.1, and hence they form a representation of the D_{3d} point group. However, the representations $\Gamma(R)$ are not unique, and this is true in two respects: First, the choice of basis functions to generate $\Gamma(R)$ was arbitrary, and transforming $\Gamma(R)$ using an unitary operation would result in an equally valid representation [155]. To overcome this first problem, we will work with the trace of the matrices, which stays invariant under unitary transformation (see below). As a second ambiguity, we now show that the representation $\Gamma(R)$ can be decomposed into other, equally valid representations of smaller dimensionality.

We see, that all matrices in (2.1) have a block diagonal form, i.e.

$$\Gamma(R) = \left[\begin{array}{cc|c} \Gamma^{(1)}(R) & & 0 \\ & & 0 \\ \hline 0 & 0 & \Gamma^{(2)}(R) \end{array}\right], \quad R = E, C_3^1, C_3^2, C_2', \ldots \tag{2.2}$$

where $\Gamma^{(1)}(R)$ acts on the pair of basis vectors $(\hat{x}, \hat{y})$ and $\Gamma^{(2)}(R)$ acts on $\hat{z}$. This block form means, that the representations $\Gamma(R)$ in (2.1) contain two representations of smaller dimension. Therefore, we call Γ a *reducible* representation. Clearly, $\Gamma^{(2)}(R)$ is one-dimensional and cannot be reduced further, thus we call it an *irreducible* representation.

To check whether a representation is reducible in general, we need to check whether we can bring all its transformation matrices into a block form similar to Eq. (2.2). If there exists a transformation, which converts all the matrices in the representation of a group into the same block form, then the representation is said to be reducible; otherwise it is irreducible. Thus, an irreducible representation cannot be expressed in terms of representations of lower dimensionality [155]. In contrast, a reducible representation Γ can be written as a linear combination of irreducible representations Γ_{IR}:

$$\Gamma = \sum_j a_j \Gamma_{\mathrm{IR}}^{(j)}, \tag{2.3}$$

where the coefficients a_j determine, how often the irreducible representation $\Gamma_{\mathrm{IR}}^{(j)}$ appears in Γ. In our example above, $\Gamma = 1 \cdot \Gamma^{(1)} + 1 \cdot \Gamma^{(2)}$. We will see in Sec. 2.1.4, how we decompose a reducible representation into its irreducible constituents.

If we take a closer look, the representation $\Gamma^{(2)}$ only specifies whether the unit vector $\hat{z}$ is unchanged under a symmetry operation or whether it is inverted. In Tab. 2.2, we summarize the representation $\Gamma^{(2)}$ by simply copying the bottom right 1×1 block matrices from the transformation matrices (2.1). We have merged the representations for similar symmetry operations into symmetry *classes*, such as the two three-fold rotations C_3^1 and C_3^2, which we sum up as $2C_3$.

Table 2.2: The representation $\Gamma^{(2)}$ generated by the basis vector $\hat{z}$.

$\mathbf{D_{3d}}$	E	$2C_3$	$3C_2$	i	$2S_6$	3σ	
$\Gamma^{(2)}$	1	1	-1	-1	-1	1	$\hat{z}$

The representation $\Gamma^{(2)}$ still obeys the group axioms and is homomorphic to the D_{3d} group, which can be verified by inspection of the multiplication table 2.1. However, $\Gamma^{(2)}$ is not the only irreducible representation of D_{3d}. The two-dimensional representation $\Gamma^{(1)}$ is also irreducible, and other irreducible representations can be generated using other basis sets, e.g. abstract basis vectors $\{R_x, R_y, R_z\}$ which describe rotations around the x, y, z axes [154].

As we stated above, the two-dimensional representation $\Gamma^{(1)}$ is not unique: If we imagine a two-dimensional unitary matrix U, e.g. a simple rotation, then the product

$U^{-1}\,\Gamma^{(1)}\,U$ would still be a valid irreducible representation. To eliminate this ambiguity, we define the *character* $\chi^{(j)}(R)$ of a representation j under the symmetry operation R as the *trace*, i.e. the sum of the diagonal elements, of the matrix $\Gamma^{(j)}(R)$ of the representation:

$$\chi^{(j)}(R) = \mathrm{Tr}\left[\Gamma^{(j)}(R)\right] = \sum_{\mu=1}^{l_j}\left[\Gamma^{(j)}(R)\right]_{\mu\mu} \tag{2.4}$$

It can be shown, that the trace of a matrix is invariant under unitary transformations, therefore the character unambiguously identifies a given representation.

Character tables For all existing point groups, the characters $\chi^{(j)}(R)$ have been tabulated and these *character tables* can be found in many textbooks, e.g. Refs. [132,154,155]. We outline the character table of the D_{3d} group in Tab. 2.3. The first row of the character table lists the symmetry classes, corresponding to Tab. 2.2 above. The left-most column lists the names for the representations according to the Mulliken notation. We identify our former $\Gamma^{(2)}$ to be A_{2u} and – after calculating the traces – $\Gamma^{(1)}$ to be E_u.

Table 2.3: The D_{3d} character table [154].

$\mathbf{D_{3d}}$	E	$2C_3$	$3C_2$	i	$2S_6$	3σ	linear, rotations	quadratic
A_{1g}	1	1	1	1	1	1		x^2+y^2, z^2
A_{2g}	1	1	-1	1	1	-1	R_z	
E_g	2	-1	0	2	-1	0	(R_x, R_y)	(x^2-y^2, xy), (xz, yz)
A_{1u}	1	1	1	-1	-1	-1		
A_{2u}	1	1	-1	-1	-1	1	z	
E_u	2	-1	0	-2	1	0	(x, y)	

Mulliken symbols provide a shorthand notation for the description of the irreducible representations. First, the capital letters A, B, E, T refer to the dimensionality of a irreducible representation, i.e. the size of the corresponding transformation matrix: A and B are one-dimensional (e.g. our example of $\Gamma^{(2)} = A_{2u}$ above), E are two-dimensional (e.g. $\Gamma^{(1)} = E_u$), T are three-dimensional. The dimensionality is always equal to the character $\chi^{(j)}(E)$ of the identity operation, e.g. $\chi^{(A_{1g})}(E) = 1$ and $\chi^{(E_g)}(E) = 2$. Second, the symbols indicate whether a representation is symmetric ($\chi = +1$) or anti-symmetric ($\chi = -1$) under particular operations: Representations denoted by A are symmetric under the main C_n operations, whereas the ones with B are anti-symmetric. We see Tab. 2.3 that all one-dimensional representations have the character $\chi(C_3) = +1$ under the C_3 rotations, thus we call them all A. The subscripts g and u denote the parity of an irreducible representation (Sec. 2.1.1) and refer to the sign of the character $\chi^{(j)}(i)$ under the inversion. Finally, the subscripts 1 and 2 refer to the character under C_2 rotations, and the primes $'$ and $''$ to the character under a σ_h reflection (not shown here). The representation A_{1g} plays a special role, as all its characters are equal to 1. It is therefore called the totally symmetric representation.

On the right of Tab. 2.3, there are two columns which list the generating functions of the representations. We have seen above, that A_{2u} is generated by z and E_u by the pair (x, y). In addition, there are representations generated by quadratic functions, such as $x^2 + y^2$ for A_{1g}. These functions are also called basis functions. Basis functions play an important role for the interpretation of irreducible representations in a quantum mechanical context.

The great orthogonality theorem for representations and characters Before we concretize this rather phenomenological statement in the next section, we name here the central property of irreducible representations. This property is expressed in the *great orthogonality theorem*, which is the most important theorem of group theory. It states for all inequivalent, irreducible, unitary representations $\Gamma^{(i)}, \Gamma^{(j)}$ of a group of the order h, that

$$\sum_R \left[\Gamma^{(i)}(R)\right]^*_{\mu\nu} \left[\Gamma^{(j)}(R)\right]_{\alpha\beta} = \frac{h}{l_i}\delta_{ij}\delta_{\mu\alpha}\delta_{\nu\beta}, \tag{2.5}$$

where the summation R runs over all group (symmetry) elements and l_i is the dimensionality of $\Gamma^{(i)}$ [132]. The great orthogonality theorem is interpreted as stating the orthogonality of a set of vectors in a "group-element space". This is a h-dimensional vector space in which the axes or components are labeled by the various group elements $R = E, C_3^1, \ldots$, thus the representations $\Gamma^{(i)}_{\mu\nu}(R)$ are the elements of the vectors $V^{(i)}_{\mu\nu}$. The vectors $V^{(i)}_{\mu\nu}$ are labeled by three indices – the representation index i and the subscripts $\mu\nu$, indicating row and column within the representation matrix. All vectors which differ in one or more of these indices are orthogonal.

As an example, we return to the representation E_u of D_{3d}, which spans a vector:

$$V^{E_u}_{\mu\nu} = \left(\left[\Gamma^{E_g}(E)\right]_{\mu\nu}, \left[\Gamma^{E_g}(C_3^1)\right]_{\mu\nu}, \ldots, \left[\Gamma^{E_g}(\sigma_d'')\right]_{\mu\nu}\right), \tag{2.6}$$

so, for $\mu = 1$ and $\nu = 1$ we take the element of the first row and of the first column from the representation (2.1), which yields:

$$V^{E_u}_{1,1} = \left(1, -\tfrac{1}{2}, -\tfrac{1}{2}, \tfrac{1}{2}, \tfrac{1}{2}, -1, -1, \tfrac{1}{2}, \tfrac{1}{2}, -\tfrac{1}{2}, -\tfrac{1}{2}, 1\right). \tag{2.7}$$

If we construct similarly for $\mu = 2$ and $\nu = 1$ the vector

$$V^{E_u}_{2,1} = \left(0, \frac{\sqrt{3}}{2}, -\frac{\sqrt{3}}{2}, \frac{\sqrt{3}}{2}, -\frac{\sqrt{3}}{2}, 0, 0, -\frac{\sqrt{3}}{2}, \frac{\sqrt{3}}{2}, -\frac{\sqrt{3}}{2}, -\frac{\sqrt{3}}{2},\right), \tag{2.8}$$

then we clearly see, that the scalar product between $V^{E_u}_{1,1}$ and $V^{E_u}_{2,1}$ (which is calculated component-wise like for an ordinary three-dimensional vector) is equal to zero, as it is postulated by the great orthogonality theorem. In the h-dimensional group-element space, only h vectors can be mutually orthogonal. As a consequence, it can be shown that the number of irreducible representations $\Gamma^{(j)}$ is equal to the number of symmetry classes of a group.

The great orthogonality theorem can be "translated" to characters: If we only use the diagonal elements of the matrices $\Gamma^{(i)}, \Gamma^{(j)}$ in Eq. (2.5), we set $\nu = \mu$ and $\beta = \alpha$ and obtain

$$\sum_R \left[\Gamma^{(i)}(R)\right]^*_{\mu\mu} \left[\Gamma^{(j)}(R)\right]_{\alpha\alpha} = \frac{h}{l_i}\delta_{ij}\delta_{\mu\alpha}. \tag{2.9}$$

We remember, that the character is defined as the sum over the diagonal elements $\Gamma^{(i)}(R)_{\mu\mu}$, so we sum both sides over all μ and α to obtain

$$\sum_\mu \sum_\alpha \sum_R \left[\Gamma^{(i)}(R)\right]^*_{\mu\mu} \left[\Gamma^{(j)}(R)\right]_{\alpha\alpha} = \sum_\mu \sum_\alpha \frac{h}{l_i}\delta_{ij}\delta_{\mu\alpha}.$$

The sums over R, μ, α can be rearranged, such that we get:

$$\sum_R \underbrace{\sum_\mu \left[\Gamma^{(i)}(R)\right]^*_{\mu\mu}}_{=\chi^{(i)}(R)^*} \underbrace{\sum_\alpha \left[\Gamma^{(j)}(R)\right]_{\alpha\alpha}}_{=\chi^{(j)}(R)} = \frac{h}{l_i}\delta_{ij} \sum_\mu \underbrace{\sum_\alpha \delta_{\mu\alpha}}_{=\delta_{\mu\mu}=1}$$

The sum over μ on the right side of the equation yields the dimension l_i of the representation $\Gamma^{(i)}$ and we obtain

$$\sum_R \left[\chi^{(i)}(R)\right]^* \chi^{(j)}(R) = \frac{h}{l_i}\delta_{ij} \sum_\mu 1 = \frac{h}{l_i}\delta_{ij} l_i = h\delta_{ij} \tag{2.10}$$

Hence, the characters of an irreducible representation also form a set of orthogonal vectors in group-element space, the space spanned by h vectors which we encountered already for the great orthogonality theorem. As the characters for one class of symmetry operations (e.g. all C_2 rotations) are the same, the orthogonality relation (2.10) can be generalized to the characters of symmetry classes $\mathcal{C}_k$

$$\sum_k N_k \left[\chi^{(i)}(\mathcal{C}_k)\right]^* \chi^{(j)}(\mathcal{C}_k) = h\delta_{ij}, \tag{2.11}$$

where N_k denotes the number of elements in the class $\mathcal{C}_k$. As an example, the characters of representations A_{2u} and E_u of the group D_{3d} are orthogonal because

$$\begin{aligned} \sum_k N_k \left[\chi^{A_{2u}}(\mathcal{C}_k)\right]^* \chi^{E_u}(\mathcal{C}_k) = & \; [1 \cdot 1 \cdot 2] + [2 \cdot 1 \cdot (-1)] + [3 \cdot (-1) \cdot 0] \\ & + [1 \cdot (-1) \cdot (-2)] + [2 \cdot (-1) \cdot 1] + [3 \cdot 1 \cdot 0] \\ = & \; 2 - 2 + 0 + 2 - 2 + 0 \\ = & \; 0. \end{aligned}$$

We can check whether a given representation is irreducible by checking whether the orthogonality relation holds for its characters. In addition, the orthogonality theorem for characters is important as it enables a straight-forward algorithm to decompose reducible representations into irreducible ones. Before we make use of this decomposition technique in Sec. 2.1.4, we discuss the interpretation of irreducible representations and characters in quantum mechanics.

2.1.3 Irreducible representations in quantum mechanics

While we started the last section with a very graphic description of representation, the notion of irreducible representations and characters is to this point rather abstract. We therefore express in this section briefly how irreducible representations come into play when solving quantum mechanics problems. First, we introduce transformation operators: The transformation matrices $\Gamma(R)$ in (2.1) for the D_{3d} group established how coordinates $\mathbf{r}$ are transformed upon the application of symmetry operations; we have shown exemplarily that $\Gamma(R)$ form a group. We now introduce another group isomorphic to (2.1) which acts on functions $f(\mathbf{r})$ instead of coordinates $\mathbf{r}$. We define the operator P_R for all R which needs to satisfy

$$\begin{aligned} & P_R f(\Gamma(R)\mathbf{r}) = f(\mathbf{r}) \\ \Leftrightarrow \qquad & P_R f(\mathbf{r}) = f(\Gamma(R)^{-1}\mathbf{r}), \end{aligned} \tag{2.12}$$

or in other words, P_R changes the functional form of $f(\mathbf{r})$ in such a way as to compensate the change of the variables under the action of $\Gamma(R)$ [132]. The idea behind this construction is to apply symmetry operations to quantum mechanical properties like wave functions or interactions. Imagine, a property of a molecule (e.g. the electron density of a dangling bond orbital) has a functional dependence $f(x, y, z)$. Application of e.g. the C_3^1 rotation changes the arguments of this function such that:

$$P_{C_3^1} f(\mathbf{r}) = f\left(\Gamma(C_3^1)^{-1}\,\mathbf{r}\right) = f\left(\Gamma(C_3^2)\,\mathbf{r}\right) = f\left(-\tfrac{1}{2}x + \tfrac{\sqrt{3}}{2}y, -\tfrac{\sqrt{3}}{2}x - \tfrac{1}{2}y, z\right). \tag{2.13}$$

Remember that according to Eq. (2.12), we need to employ the inverse $\Gamma(R)^{-1}$, which in the case of C_3^1 is simply C_3^2.

We now consider a special group of operators P_R which commute with the Hamilton operator $\mathbb{H}$ for a given physical system. Hence, for an arbitrary eigenfunction $\psi^{(n)}$ of $\mathbb{H}$ with eigenvalue E_n, we have Schrödinger's equation

$$\mathbb{H}\psi^{(n)} = E_n\psi^{(n)}$$

We apply the transformation operator P_R from the left:

$$\begin{aligned} & P_R\mathbb{H}\psi^{(n)} = P_R E_n\psi^{(n)} \\ \Leftrightarrow \quad & \mathbb{H}P_R\psi^{(n)} = E_n P_R\psi^{(n)}, \end{aligned} \tag{2.14}$$

because we have postulated that the operators P_R and $\mathbb{H}$ commute and because P_R commutes of course with the eigenvalue E_n. From the action of P_R on the eigenfunction $\psi^{(n)}$ we obtain a new function $\phi^{(n)} \equiv P_R\psi^{(n)}$ which is according to Eq. (2.14) also an eigenfunction of $\mathbb{H}$. Generally speaking, the consecutive application of a transformation operator on an eigenfunction helps to find the other degenerate eigenfunctions. This tremendously simplifies the search for eigenfunctions as soon as one eigenfunction is known. We denote the set of operators P_R commuting with $\mathbb{H}$ as the group of Schrödinger's equation.

In the previous section, we have seen that the transformation matrices $\Gamma(R)$ of the symmetry operations R are considered as representations. We now combine the transformation operators from the group of Schrödinger's equation with the concept of irreducible representations. We consider an l_n-fold degenerated eigenvalue E_n with a corresponding set of l_n mutually orthogonal eigenfunctions $\psi_\kappa^{(n)}$, $\kappa = 1, \ldots, l_n$. If we apply an operator P_R out of the group of Schrödinger's equation onto one particular eigenfunction, called $\psi_\nu^{(n)}$, then we obtain another function which has the same energy and which can be expressed as a linear combination of the eigenfunctions $\psi_\kappa^{(n)}$. We write this application of the operator P_R in terms of a multiplication with a matrix $\Gamma^{(n)}(R)$:

$$P_R \psi_\nu^{(n)} = \sum_{\kappa=1}^{l_n} \psi_\kappa^{(n)} \left[\Gamma^{(n)}(R)\right]_{\kappa\nu} . \tag{2.15}$$

There is an important analogy to the previous section: There, we wrote the transformation matrices (2.1) such that they express the action of symmetry operations on the coordinates (x, y) and z. Thus, these coordinates served as generating functions for the representation (2.1). In the same spirit, we now constructed a representation $\Gamma^{(n)}(R)$ for the group of Schrödinger's equation using the eigenfunctions $\psi_\kappa^{(n)}$ as generators. It can be shown that the representation $\Gamma^{(n)}(R)$ is irreducible. Hence, the set of l_n degenerate eigenfunctions $\psi_\kappa^{(n)}$ of energy E_n forms a basis for an l_n-dimensional irreducible representation $\Gamma^{(n)}$.

Conversely speaking, there is a direct correspondence between irreducible representations and the eigenfunctions of a given quantum mechanical problem: Irreducible representations of the symmetry group of Schrödinger's equation label the resulting states and specify their degeneracies. This degeneracy is equal to the dimension of the irreducible representation. We stress however, that group theory does not yield the absolute energy of a state.

In addition, the new eigenfunction $\phi^{(n)}$ acquired under the application of P_R is not automatically orthogonal to the generating function $\psi^{(n)}$. As Eq. (2.15) indicates, the application of P_R on a basis function yields a linear combination of all basis functions. An example: We remember the application of a rotation C_3^1 around a threefold axis on the simple basis function $\psi(x, y) = x$, which yielded $\phi(x, y) = P_{C_3^1}\psi(x, y) = -\frac{1}{2}x - \frac{1}{2}\sqrt{3}y$ (see Eq. (2.13)). The resulting function $\phi(x, y)$ is clearly a linear combination of x and y, and – most importantly – it is not orthogonal to x. But, we can decompose $\phi(x, y)$ into orthogonal basis functions by inspection into $\phi(x, y) = -\frac{1}{2}\psi(x, y) - \frac{1}{2}\sqrt{3}\xi(x, y)$, with $\psi(x, y) = x$ as we stated initially and $\xi(x, y) = y$. Now, the functions $\psi(x, y)$ and $\xi(x, y)$ are orthogonal and therefore truly basis functions. A special case can be, that P_R leaves $\psi^{(n)}$ unchanged – a trivial example would be the application of the identity P_E.

We remember that the character tables (Tab. 2.3) list generating functions in the right columns, which are linear or quadratic in x, y, z (in some extended tables even higher orders are given). These functional dependences are by no means accidental: Often, the properties of a molecular system, such as the electronic wave function of a given state, depend on these spatial coordinates in this exact functional form, e.g. the electronic wave function for an s-orbital depends on $x^2 + y^2 + z^2$. We then say, this property *transforms as* or *belongs to* the corresponding irreducible representation. For example, an s-orbital of an atom transforms as A_{1g} and has no degeneracy because the dimension of its irreducible representation is equal to 1. Hence, if we know the functional dependence of the eigenfunctions $\psi^{(n)}(x, y, z)$ of a Hamilton operator, we can identify unambiguously to which representation they belong.

However, very often, no explicit functional form of the eigenfunctions is known. In the next section, we therefore go the opposite way: We show how eigenfunctions or basis states are obtained with the help of group theory.

2.1.4 Calculation of the basis states of the SiV center

We have seen in the preceding section, that much of the relevant information for quantum mechanical problem is given by the irreducible representations, as the irreducible representations determine the degeneracy of the eigenfunctions for this problem. We use this important property here to derive the eigenstates of the SiV defect. Although the resulting states will not show in detail the functional dependence on x, y, z, we denote them as the basis states of the SiV center, because they will serve as basis for the perturbation calculation that follows.

In the previous chapter and in Sec. 2.1.1, we have seen that the SiV defect comprises six next-neighboring carbon atoms. Due to the two missing carbon atoms in the split-vacancy configuration, these carbon atoms have unsaturated bonds, so-called dangling bonds. We first construct a representation based on these dangling-bond orbitals. As this representation is reducible, we will show a procedure how to decompose it into irreducible representations. The resulting irreducible representation will outline the degeneracy of the possible orbital states of the defect. Using the character table for the D_{3d} group, we then derive the symmetry adapted linear combinations of the dangling bond orbitals which correspond to the irreducible representations and which form the basis states for the following perturbation study.

Dangling bond representation We sketch the dangling bond orbitals centered on the next-neighbor carbon atoms in Fig. 2.5. As the carbon atoms are sp^3-hybridized, the bond nature of these orbitals will most likely be of σ-type. Therefore, we denote the dangling bond orbitals σ_i from σ_1 to σ_3 and σ'_1 to σ'_3. In an molecular orbital approach, the electron wave functions of the σ-bond exhibit a *phase* which gives rise to either a bonding (constructive) or an anti-bonding (destructive) character of the molecular orbital. We indicate this phase using the color of the lobes in Fig. 2.5, where red means positive phase and blue means negative phase for the part of the sp^3-orbital which points towards the center of the defect. Therefore, the case in Fig. 2.5 with all σ_i in phase is just one example.

In Sec. 2.1.2, we constructed the representation Γ from the generating functions x, y, z as transformation matrices (2.1) which acted on (x, y, z). In completely analogous manner, we construct here a representation in terms of transformation matrices $\Gamma^{(\sigma)}(R)$ which act on the dangling-bonds σ_i. Like for Eq. (2.1), we apply the matrices $\Gamma^{(\sigma)}(R)$ to a vector $\mathbf{v} = (\sigma_1, \sigma_2, \ldots, \sigma'_3)$ composed of the generating functions, and obtain $\mathbf{v}' = \Gamma^{(\sigma)}(R)\mathbf{v}$. As we are mainly interested in the character of this representation, which is identical for all operations of one symmetry class, we list one transformation matrix for each class, and

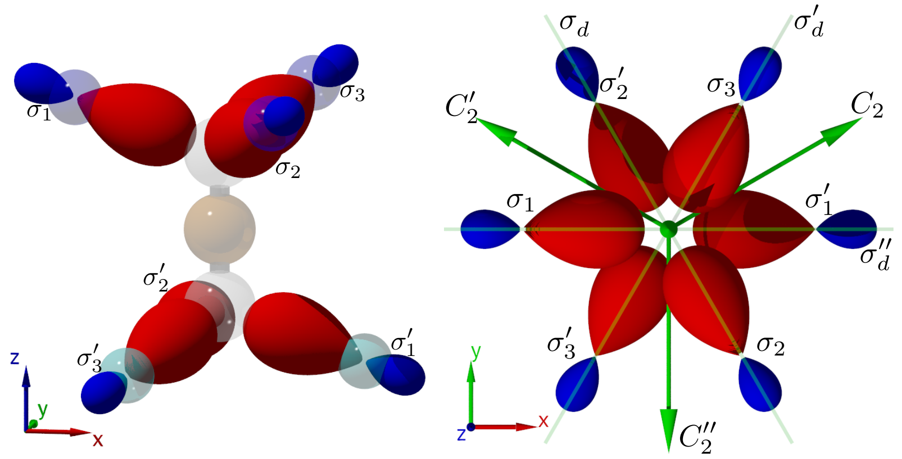

(a) side view (b) top view

Figure 2.5: The unsaturated bonds of the next-neighbor carbon atoms form so-called dangling bond orbitals, which we sketch schematically as sp^3-orbitals. The view from the side (panel a) also shows a transparent picture of the Si-impurity surrounded by the split vacancy and the next-neighbor carbon atoms.

write the corresponding characters below each matrix:

$$
\begin{array}{ccc}
E & C_3^1 & C_2 \\
\begin{bmatrix}1&0&0&0&0&0\\0&1&0&0&0&0\\0&0&1&0&0&0\\0&0&0&1&0&0\\0&0&0&0&1&0\\0&0&0&0&0&1\end{bmatrix} &
\begin{bmatrix}0&0&1&0&0&0\\1&0&0&0&0&0\\0&1&0&0&0&0\\0&0&0&0&0&1\\0&0&0&1&0&0\\0&0&0&0&1&0\end{bmatrix} &
\begin{bmatrix}0&0&0&0&0&1\\0&0&0&0&1&0\\0&0&0&1&0&0\\0&0&1&0&0&0\\0&1&0&0&0&0\\1&0&0&0&0&0\end{bmatrix} \\
\chi^{(\sigma)}(E)=6 & \chi^{(\sigma)}(C_3)=0 & \chi^{(\sigma)}(C_2)=0 \\
\\
i & S_6^1 & \sigma_d \\
\begin{bmatrix}0&0&0&1&0&0\\0&0&0&0&1&0\\0&0&0&0&0&1\\1&0&0&0&0&0\\0&1&0&0&0&0\\0&0&1&0&0&0\end{bmatrix} &
\begin{bmatrix}0&0&0&0&1&0\\0&0&0&0&0&1\\0&0&0&1&0&0\\0&1&0&0&0&0\\0&0&1&0&0&0\\1&0&0&0&0&0\end{bmatrix} &
\begin{bmatrix}0&0&1&0&0&0\\0&1&0&0&0&0\\1&0&0&0&0&0\\0&0&0&0&0&1\\0&0&0&0&1&0\\0&0&0&1&0&0\end{bmatrix} \\
\chi^{(\sigma)}(i)=0 & \chi^{(\sigma)}(S_6)=0 & \chi^{(\sigma)}(\sigma_d)=2
\end{array}
\tag{2.16}
$$

Decomposition of the dangling bond representation Clearly, the representation (2.16) is reducible, and we now show how to express it as a linear combination of irreducible representations. In principle, we could try to "guess" a similarity transformation which brings all $\Gamma^{(\sigma)}(R)$ into block form and then obtain the irreducible representations by inspection of the blocks, but this method is cumbersome. Therefore, we employ an alternative approach: We have seen at the end of Sec. 2.1.2, that the characters of an irreducible representation Γ_{IR} form a set of orthogonal vectors. Owing to this orthogonality, we can write the characters $\chi^{(\sigma)}(R)$ of every (reducible) representation $\Gamma^{(\sigma)}(R)$ as a linear combination of the characters $\chi_{\mathrm{IR}}^{(j)}(R)$ of irreducible representations $\Gamma_{\mathrm{IR}}^{(j)}(R)$:

$$\chi^{(\sigma)}(R) = \sum_j a_j \; \chi_{\mathrm{IR}}^{(j)}(R). \tag{2.17}$$

The coefficients a_j determine how often the irreducible representation $\chi_{\mathrm{IR}}^{(j)}(R)$ appears in the reducible one. Again, instead of considering every symmetry operation R independently, we group the operations in classes $\mathcal{C}_k$, and obtain

$$\chi^{(\sigma)}(\mathcal{C}_k) = \sum_j a_j \; \chi_{\mathrm{IR}}^{(j)}(\mathcal{C}_k). \tag{2.18}$$

It can be shown, that this decomposition is unique [155] and that the coefficients a_j are given by the relation

$$a_j = \frac{1}{h} \sum_k N_k \; \left[\chi_{\mathrm{IR}}^{(j)}(\mathcal{C}_k)\right]^* \chi^{(\sigma)}(\mathcal{C}_k), \tag{2.19}$$

where we now sum over the classes $\mathcal{C}_k$. For the example of the dangling bond representation $\Gamma^{(\sigma)}$, this decomposition is particularly simple as all characters $\chi^{(\sigma)}$ are zero except those for the operations E and σ_d. The decomposition algorithm is shown in Tab. 2.4 and yields that $\Gamma^{(\sigma)} = A_{1g} + E_g + A_{2u} + E_u$.

The decomposition into irreducible representations tells us, that the representation $\Gamma^{(\sigma)}$ contains two non-degenerate representations A_{1g} and A_{2u} and two two-fold degenerate representations E_g and E_u. As a result, there will be four possible electronic states for the SiV center, of which two are non-degenerate and two are two-fold degenerate.

Projecting out basis functions As a next step, we derive how the basis functions of the four irreducible states are composed of the dangling bond orbitals. This can be done using the so-called projection operator or projector $\mathcal{P}^{(j)}$ for the irreducible representation $\Gamma_{\mathrm{IR}}^{(j)}$; we stress, that this operator must not be confounded with the transformation operator P_R which we encountered in the previous section, neither with the relaxation operator $\mathbb{P}_R$ of Sec. 4.2.2. The projection operator is defined by

$$\mathcal{P}^{(j)} = \frac{1}{N} \sum_R \left[\chi_{\mathrm{IR}}^{(j)}(R)\right]^* P_R, \tag{2.20}$$

where $\chi_{\mathrm{IR}}^{(j)}(R)$ are the characters of the irreducible representation $\Gamma^{(j)}$, P_R is the transformation operator of the previous section, and N is a normalization factor. In our case, the projector $\mathcal{P}^{(j)}$ is applied onto one dangling bond orbital σ_i, or onto a linear combination of them, and the symmetry operations on the σ_i can be conveniently read from Figs. 2.2, 2.3 and the matrices (2.16).

Table 2.4: The decomposition formula for the representation $\Gamma^{(\sigma)}$ in D_{3d} symmetry. The table is to be read in blocks of three rows, where the first row of each block lists repeatedly the character $\chi^{(\sigma)}$, the second row denotes the characters for the irreducible representation of D_{3d}, and the third row shows the calculation of the coefficients a_j according to Eq. (2.19).

$\mathbf{D_{3d}}$	E	$2C_3$	$3C_2$	i	$2S_6$	$3\sigma_d$	coefficients a_j
$\Gamma^{(\sigma)}$	6	0	0	0	0	2	
A_{1g}	1	1	1	1	1	1	
$N_k \cdot \chi^{A_{1g}}(\mathcal{C}_k)\chi^{(\sigma)}(\mathcal{C}_k)$	$1 \cdot 1 \cdot 6$	0	0	0	0	$3 \cdot 2 \cdot 1$	$a_{A_{1g}} = \frac{1}{12}(6+6) = 1$
$\Gamma^{(\sigma)}$	6	0	0	0	0	2	
A_{2g}	1	1	-1	1	1	-1	
$N_k \cdot \chi^{A_{2g}}(\mathcal{C}_k)\chi^{(\sigma)}(\mathcal{C}_k)$	$1 \cdot 1 \cdot 6$	0	0	0	0	$3 \cdot 2 \cdot (-1)$	$a_{A_{2g}} = \frac{1}{12}(6-6) = 0$
$\Gamma^{(\sigma)}$	6	0	0	0	0	2	
E_g	2	-1	0	2	-1	0	
$N_k \cdot \chi^{E_g}(\mathcal{C}_k)\chi^{(\sigma)}(\mathcal{C}_k)$	$1 \cdot 2 \cdot 6$	0	0	0	0	$3 \cdot 2 \cdot 0$	$a_{E_g} = \frac{1}{12}(12+0) = 1$
$\Gamma^{(\sigma)}$	6	0	0	0	0	2	
A_{1u}	1	1	1	-1	-1	-1	
$N_k \cdot \chi^{A_{1u}}(\mathcal{C}_k)\chi^{(\sigma)}(\mathcal{C}_k)$	$1 \cdot 1 \cdot 6$	0	0	0	0	$3 \cdot 2 \cdot (-1)$	$a_{A_{1u}} = \frac{1}{12}(6-6) = 0$
$\Gamma^{(\sigma)}$	6	0	0	0	0	2	
A_{2u}	1	1	-1	-1	-1	1	
$N_k \cdot \chi^{A_{2u}}(\mathcal{C}_k)\chi^{(\sigma)}(\mathcal{C}_k)$	$1 \cdot 1 \cdot 6$	0	0	0	0	$3 \cdot 2 \cdot (-1)$	$a_{A_{2u}} = \frac{1}{12}(6+6) = 1$
$\Gamma^{(\sigma)}$	6	0	0	0	0	2	
E_u	2	-1	0	-2	1	0	
$N_k \cdot \chi^{E_u}(\mathcal{C}_k)\chi^{(\sigma)}(\mathcal{C}_k)$	$1 \cdot 2 \cdot 6$	0	0	0	0	$3 \cdot 2 \cdot 0$	$a_{E_u} = \frac{1}{12}(12+0) = 1$

The action of $\mathcal{P}^{(j)}$ is to *project out* the basis states of the corresponding irreducible representation $\Gamma^{(j)}$. This is shown most intuitively using an example: For the calculation of the basis functions for A_{1g} we apply $\mathcal{P}^{A_{1g}}$ to the dangling bond orbital σ_1. We show the steps of the calculation in Tab. 2.5, where the top row lists all symmetry operations of the D_{3d} point group. The second row shows the result of the symmetry operations P_R on σ_1, which we multiply with the characters of A_{1g} (third row). The bottom row then denotes the product $\chi^{A_{1g}}(R)P_R\sigma_1$.

Table 2.5: Projecting out the basis states of the irreducible representation A_{1g}.

$\mathcal{P}^{A_{1g}}$	E	C_3^1	C_3^2	C_2	C_2'	C_2''	i	S_6^1	S_6^5	σ_d	σ_d'	σ_d''
$P_R\,\sigma_1$	σ_1	σ_3	σ_2	σ_3'	σ_2'	σ_1'	σ_1'	σ_2'	σ_3'	σ_3	σ_2	σ_1
$\chi^{A_{1g}}$	1	1	1	1	1	1	1	1	1	1	1	1
$\chi^{A_{1g}}\,P_R\,\sigma_1$	σ_1	σ_3	σ_2	σ_3'	σ_2'	σ_1'	σ_1'	σ_2'	σ_3'	σ_3	σ_2	σ_1

We sum up the cells of the bottom row of Tab. 2.5, and normalize the sum using the ratio $\frac{1}{2\sqrt{6}}$. We obtain:

$$A_{1g} = \frac{1}{\sqrt{6}}\left(\sigma_1 + \sigma_2 + \sigma_3 + \sigma_1' + \sigma_2' + \sigma_3'\right). \tag{2.21}$$

This superposition of orbitals is termed a symmetry adapted linear combination (SALC). We see in Tab. 2.5, that all dangling bond orbitals contribute equally and all have the same phase, as we expect it from the totally symmetric representation A_{1g}. Graphically, this SALC corresponds to the combination shown in Fig. 2.5. The choice of the function σ_1, to which we applied the projector, was completely arbitrary and the application of $\mathcal{P}^{A_{1g}}$ on any other dangling bond orbital would have lead to the same result.

As a following example, we calculate the SALC for representation A_{2g}, again by applying the projection operator $\mathcal{P}^{A_{2g}}$ onto σ_1. Now, the characters for the C_2 rotations and the σ_d rotation are equal to -1 and we obtain:

$$\begin{aligned}\mathcal{P}^{A_{2g}}\sigma_1 &= \sigma_1 + \sigma_3 + \sigma_2 - \sigma_3' - \sigma_2' - \sigma_1' + \sigma_1' + \sigma_2' + \sigma_3' - \sigma_3 - \sigma_2 - \sigma_1 \\ &= 0. \end{aligned} \tag{2.22}$$

Hence, there is no combination of the dangling bonds which satisfies the symmetry constraints of the representation A_{2g} in D_{3d} symmetry. We could have anticipated this result already from the decomposition of the representation $\Gamma^{(\sigma)}$, where A_{2g} did not appear.

For the two-dimensional representation E_g, we will need two orthogonal basis functions, which we denote without loss of generality E_{gx} and E_{gy}. By orthogonal we mean, that the scalar product $\langle E_{gx}|E_{gy}\rangle$ needs to vanish, where we assume for the dangling bond orbitals that $\langle\sigma_i|\sigma_j\rangle = \delta_{ij}$. A first function is constructed as above by applying $\mathcal{P}^{E_g}$ on σ_1. We list the result in Tab. 2.6, where the symmetry operations P_R on σ_1 yield of course the same results as in Tab. 2.5 above, and the calculation is further simplified by the characters for the C_2 rotations and σ_d reflections being zero.

Table 2.6: Projecting out the first basis state of the two-dimensional irreducible representation E_g.

$\mathcal{P}^{A_{1g}}$	E	C_3^1	C_3^2	C_2	C_2'	C_2''	i	S_6^1	S_6^5	σ_d	σ_d'	σ_d''
$P_R\,\sigma_1$	σ_1	σ_3	σ_2	σ_3'	σ_2'	σ_1'	σ_1'	σ_2'	σ_3'	σ_3	σ_2	σ_1
$\chi^{A_{1g}}$	2	-1	-1	0	0	0	2	-1	-1	0	0	0
$\chi^{A_{1g}}\,P_R\,\sigma_1$	$2\sigma_1$	$-\sigma_3$	$-\sigma_2$	0	0	0	$2\sigma_1'$	$-\sigma_2'$	$-\sigma_3'$	0	0	0

We obtain for the first basis vector of E_g, which we denote E_{gx},

$$E_{gx} = \frac{1}{\sqrt{12}} \left(2\sigma_1 - \sigma_2 - \sigma_3 + 2\sigma_1' - \sigma_2' - \sigma_3'.\right) \tag{2.23}$$

In order to find a second basis function, called E_{gy}, we use the following approach: In Sec. 2.1.3, we learned that applying a suitable transformation operator P_R to E_{gx} yields a linear combination of the basis functions E_{gx} and E_{gy} [Eq. (2.15)]. This linear combination then needs to be decomposed into two orthogonal functions. As E_{gx} is already known, the procedure is straightforward: For P_R, we choose the three-fold rotation C_3^1 which transforms E_{gx} into (disregarding the normalization factor):

$$\begin{aligned} P_{C_3^1} E_{gx} &= 2P_{C_3^1}\sigma_1 - P_{C_3^1}\sigma_2 - P_{C_3^1}\sigma_3 + 2P_{C_3^1}\sigma_1' - P_{C_3^1}\sigma_2' - P_{C_3^1}\sigma_3' \\ &= 2\sigma_3 - \sigma_1 - \sigma_2 + 2\sigma_3' - \sigma_1' - \sigma_2' \\ &\overset{!}{=} c_1 E_{gx} + c_2 E_{gy}, \end{aligned} \tag{2.24}$$

where c_1 and c_2 are the coefficients of the linear combination which we need to find by inspection. Without loss of generality, we set $c_1 = -\frac{1}{2}$ to simplify the following calculation and rearrange Eq. (2.24) to obtain

$$\begin{aligned} P_{C_3^1} E_{gx} - c_1 E_{gx} &= c_2 E_{gy} \\ \Leftrightarrow\ P_{C_3^1} E_{gx} + \tfrac{1}{2} E_{gx} &= 2\sigma_3 - \sigma_1 - \sigma_2 + 2\sigma_3' - \sigma_1' - \sigma_2' \\ &\qquad + \sigma_1 - \tfrac{1}{2}\sigma_2 - \tfrac{1}{2}\sigma_3 + \sigma_1' - \tfrac{1}{2}\sigma_2' - \tfrac{1}{2}\sigma_3' \\ &= -\tfrac{3}{2}\sigma_2 + \tfrac{3}{2}\sigma_3 - \tfrac{3}{2}\sigma_2' + \tfrac{3}{2}\sigma_3' \\ &= -\tfrac{3}{2}\left(\sigma_2 - \sigma_3 + \sigma_2' - \sigma_3'\right) \overset{!}{=} c_2 E_{gy}. \end{aligned} \tag{2.25}$$

Hence, we see that $c_2 = -\frac{3}{2}$, and the second basis function

$$E_{gy} = \tfrac{1}{2}\left(\sigma_2 - \sigma_3 + \sigma_2' - \sigma_3'\right) \tag{2.26}$$

is indeed orthogonal to the first function E_{gx}, where we introduced a factor 1/2 for normalization. By repeating the procedures above, we also obtain the SALCs for the irreducible representations exhibiting odd parity A_{1u}, A_{2u} and E_u, where A_{1u} is again found to be zero. We list all functions in Tab. 2.7 together with a molecular orbital sketch of the electronic wave functions.

Table 2.7: The symmetry adapted linear combinations a_{1g}, a_{2u}, e_g and e_u of the dangling bond orbitals for their corresponding irreducible representations. We omit the scaling factor 2 for the e_{gx} and e_{ux} orbitals in the illustrations.

$$a_{1g} = \frac{1}{\sqrt{6}}\left(\sigma_1 + \sigma_2 + \sigma_3 + \sigma_1' + \sigma_2' + \sigma_3'\right)$$

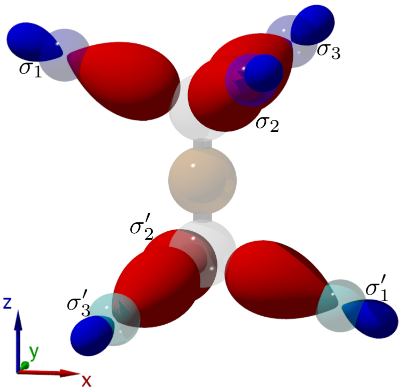

$$a_{2u} = \frac{1}{\sqrt{6}}\left(\sigma_1 + \sigma_2 + \sigma_3 - \sigma_1' - \sigma_2' - \sigma_3'\right)$$

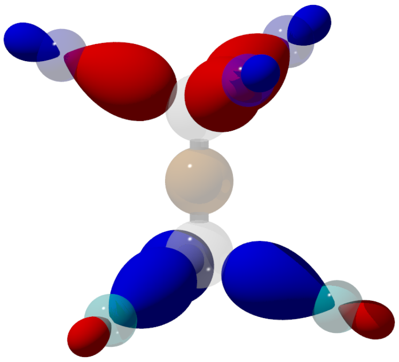

$$e_{gx} = \frac{1}{\sqrt{12}}\left(2\sigma_1 - \sigma_2 - \sigma_3 + 2\sigma_1' - \sigma_2' - \sigma_3'\right)$$

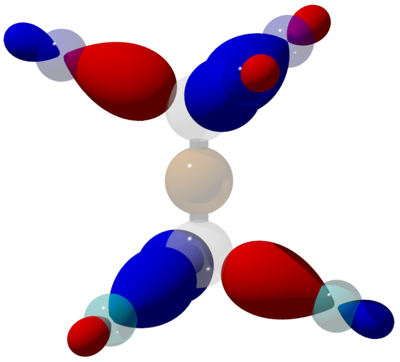

$$e_{gy} = \frac{1}{2}\left(\sigma_2 - \sigma_3 + \sigma_2' - \sigma_3'\right)$$

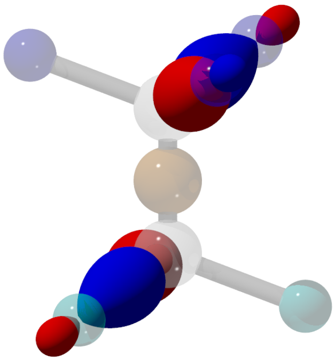

$$e_{ux} = \frac{1}{\sqrt{12}}\left(2\sigma_1 - \sigma_2 - \sigma_3 - 2\sigma_1' + \sigma_2' + \sigma_3'\right)$$

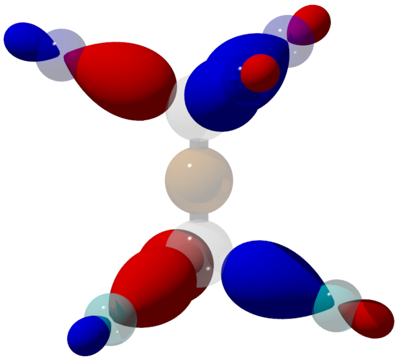

$$e_{uy} = \frac{1}{2}\left(\sigma_2 - \sigma_3 - \sigma_2' + \sigma_3'\right)$$

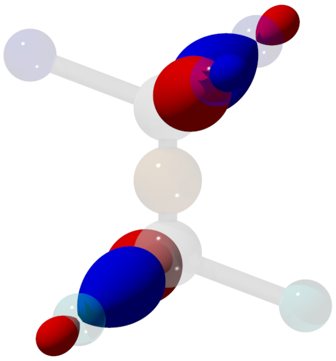

So far, we have denoted the SALCs with capital letters, according to which irreducible representation they belong. Building the SALCs for a given molecular geometry corresponds to defining new orbitals for the electrons of the molecule. Hence, instead of populating e.g. σ_1 only, the electron is delocalized over the orbitals which take part in a particular SALC. It is common in group theory, to denote these new orbitals with small letters, e.g. a_{1g}, to distinguish the actual orbital from the abstract representation. We deliberately follow this convention.

Admixture of Si atomic orbitals So far, we have completely neglected the atomic orbitals of the Si impurity. There are four valence electrons of the Si atom which can populate the $3s$, $3p_x$, $3p_y$ and $3p_z$ orbitals. The $3s$ orbital is spherical symmetric, i.e. it depends on the spatial coordinates $x^2 + y^2 + z^2$. Using the D_{3d} character table 2.3, we can identify this functional dependence to form a basis function for the irreducible representation A_{1g}, hence the $3s$ orbital of the Si atom transforms as A_{1g}. The orbitals $3p_x, 3p_y$ depend on the coordinates x, y which in turn form the basis for the representation E_u, thus they transform as E_u, and finally, $3p_z$ belongs to A_{2u}.

The Si atomic orbitals mix with the SALCs involving the carbon-related dangling bonds via the Coulomb interaction. We show in the next section, that such an interaction can be expressed as a direct product of representations, and anticipate here already the rule that this direct product under Coulomb interaction is only non-zero if the Si orbital belongs to the same irreducible representation as the dangling bond SALC. For example, a_{1g} mixes with a_{1g}^{Si}, such that we obtain a superposition $\alpha a_{1g} + \beta a_{1g}^{Si}$, with α, β quantifying the admixture. At the same time, we note that the states e_g have no admixture at all with the Si atom.

This admixture can also be explained graphically: For the a_{2u} SALC of the dangling bonds (Tab. 2.7), the phase of the upper orbitals $\sigma_{1,2,3}$ is positive while it is negative for $\sigma'_{1,2,3}$. Hence, the wave functions of the upper and lower orbitals form an anti-bonding configuration with vanishing electron probability distribution in the middle of the defect.We then say that this orbital has a node along its z-axis. The only Si orbital which also has a vertical node is the p_z orbital, hence it is the only orbital which "fits into" the dangling bond orbital. Similarly, a_{1g} has no node at all, as does the Si s orbital. Finally, the SALCs e_{ux} and e_{uy} have horizontal nodes along the x- and y-direction, respectively, hence they couple to the p_x, p_y orbitals of the Si impurity.

The strength of the mixing between dangling bonds and Si orbitals cannot be calculated using group theory. The *ab initio* calculations of Gali and Maze [127] show that this admixture is small for the occupied orbital states in the ground and first excited electronic configuration, i.e. $\beta \ll 1$. Hence, we approximate the SiV states to be purely formed of the carbon dangling bond combinations. However, we note that even a small admixture with the orbitals involving the Si atom might results in a higher spin-orbit interaction as it is commented below.

Ordering of the states and filling with electrons As we have stated above, group theory predicts the degeneracy of electronic states, e.g. the e_g and e_u orbitals of the SiV are predicted to be two-fold degenerate. However, group theory does not indicate the absolute energy and thus the ordering of these states, therefore, we require other techniques to order the SiV levels energetically.

A first method is commonly utilized in molecular orbital approaches: We have introduced the notion of “nodes” of the electron wave function for the dangling bond SALCs in the previous paragraph. If there exists a node in an SALC then the charge density at this node vanishes. Hence, the positively charged nuclei experience a stronger Coulomb repulsion and the defect typically has a higher energy [154]. Thus, the more nodes are present in an SALC, the higher its energy is. Although there are exceptions from this rule of thump, it is usually a good approximation. The a_{1g} orbital has no nodes, therefore it will be the lowest energy state, then the a_{2u} state has one (vertical) node. The e_u states both have horizontal nodes, and finally the e_g states exhibit vertical and horizontal modes, thus, they are expected to show the highest energy.

As a second method, density functional theory can predict the ordering of states. The *ab initio* calculations of Gali and Maze [127] confirm the intuitive ordering a_{1g} a_{2u} e_u e_g which we have deduced using orbital nodes above.

We now fill these levels with the electrons present for the negatively charged SiV defect: The center hosts a total number of eleven electrons: Six electrons are contributed by the dangling bonds σ_i, four electrons originate from the Si-atom and an one electron is trapped from nearby donors to account for the negative charge [63]. In addition to orbital degeneracy which we deduced from group theory, the levels are spin degenerate. Taking into account this spin degeneracy, the a states host two electrons of opposite spin projection, and the e states accommodate four electrons.

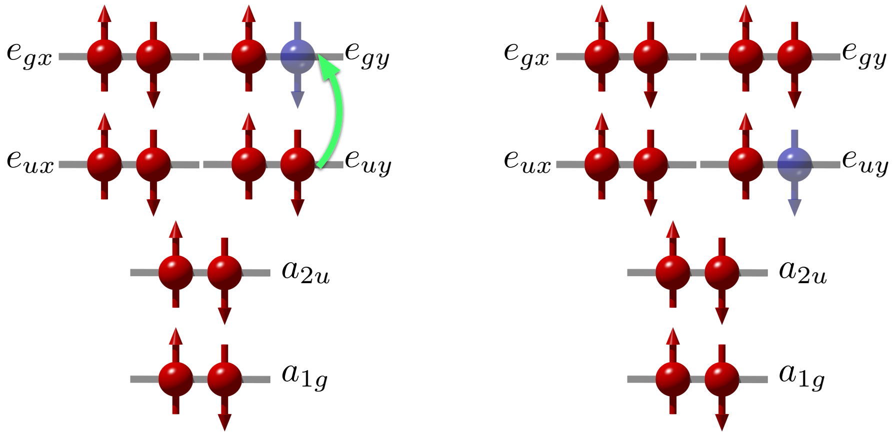

(a) (b)

Figure 2.6: Ground (a) and excited (b) state configuration for the SiV center (red arrows denote electrons and blue arrows denote electron holes). The optical transition occurs when exciting one electron from the e_u to the e_g orbital.

The ground state configuration is $a_{1g}^2 a_{2u}^2 e_u^4 e_g^3$, i.e. there is one electron hole in the e_{gx} or e_{gy} state (Fig. 2.6a). This hole can be treated in an analogous manner to a single electron [41]. Hence, the total spin of the defect in this ground state configuration is equal to $S = 1/2$. We abbreviate this configuration in spectroscopic notation as the ${}^2E_g$ ground state. We assume, that the optical transition responsible for the 1.68 eV (or 738 nm) absorption or emission occurs when one electron is excited to the e_{gx} or e_{gy} orbital. In consequence, the excited state has the configuration $a_{1g}^2, a_{2u}^2, e_{ux,y}^3, e_{gx,y}^4$ (Fig. 2.6b), and we denote this excited state as ${}^2E_u$.

Graphically, the hole in either ground or excited state can be on any of the four positions of e_g or e_u as seen in Fig. 2.6, which expresses the four-fold degeneracy of the system. Each of the "positions" corresponds to a basis vector, such that we obtain the following basis sets for ground and excited state in Dirac notation:

$$ {}^2E_g \text{ ground state } : \{|e_{gx}\uparrow\rangle, |e_{gx}\downarrow\rangle, |e_{gy}\uparrow\rangle, |e_{gy}\downarrow\rangle\} \tag{2.27a} $$

$$ {}^2E_u \text{ excited state } : \{|e_{ux}\uparrow\rangle, |e_{ux}\downarrow\rangle, |e_{uy}\uparrow\rangle, |e_{uy}\downarrow\rangle\}. \tag{2.27b} $$

It can be verified by inspection that the state vectors (2.27) are mutually orthogonal, where we remember that the dangling bond orbitals σ_i are orthogonal states, i.e. $\langle\sigma_i|\sigma_j\rangle = \delta_{ij}$. The degeneracy which we obtained for (2.27) appears to be well suited for the description of the SiV center, because of the following reasons: We have learned in Chap. 1 that the SiV center shows a spectral fine structure at low temperatures. The fine structure consists of four optical transition peaks [62] and splits into further components when a magnetic field is applied [133]. The two-fold orbital degeneracy of the e-states can be lifted via internal perturbations, such as spin-orbit interaction or the Jahn-Teller effect (cf. next section). With these perturbations present, the defect shows a level splitting into two ground and two excited states with four optical transitions between them, thus readily explaining the spectral fine structure. If the SiV defect exhibited a considerably lower symmetry, then our group theoretical discussion would have resulted in basis states without any orbital degeneracy and there would be no straight-forward model to explain the spectral fine structure.

Absolute position of the SiV energy levels In Ref. [127], Gali and Maze discuss the energetic position of the SiV ground and excited states in the band gap of the diamond using a DFT calculation. In the ground state configuration, the e_u orbital is filled with four electrons. The DFT calculations predict, that the energy of the e_u orbital lies in the valence band (Fig. 2.7a). When one electron is promoted from the e_u to the e_g orbital, i.e. the excited state configuration $e_u^3\, e_g^4$, then the e_u level rises slightly above the valence band edge (Fig. 2.7b). The calculated transition energy between the excited and the ground state is found to equal 1.72 eV (Fig. 2.7e), which is in good approximation with the experimentally observed value of 1.68 eV (cf. Sec. 1.3).

The DFT calculations of Gali and Maze show, that the valence band states are strongly perturbed by the presence of the SiV defect, giving rise to additional, localized $a_{1g,\mathrm{VBM}}$ and $e_{g,\mathrm{VBM}}$ valence band states (Fig. 2.7a-d). These valence band orbital are filled with two and four electrons, respectively. They are resonant to the SiV defect, i.e. one electron of the valence band states can be excited to the e_g orbital of the SiV center. When an electron is excited from the $a_{1g,\mathrm{VBM}}$ to the e_g orbital, a hole is left in the $a_{1g,\mathrm{VBM}}$ state, which gives rise to a ${}^2A_{1g,\mathrm{VBM}}$ configuration (Fig. 2.7c). Similarly, a hole drawn from the $e_{g,\mathrm{VBM}}$

state yields a ${}^2E_{g,\mathrm{VBM}}$ configuration (Fig. 2.7d). Energetically, the ${}^2E_{g,\mathrm{VBM}}$ configuration lies close to the ${}^2E_u$ excited state of the SiV center (Fig. 2.7e). Since ${}^2A_{1g,\mathrm{VBM}}$, ${}^2E_{g,\mathrm{VBM}}$ and ${}^2E_{g,\mathrm{SiV}}$ all have the same parity, a direct optical transition between them is parity forbidden (for the parity selection rules, cf. Sec. 2.2.1). Hence, the two valence band states can be considered as shelving states. The presence of a metastable shelving state for the SiV center is supported by the experimental findings of Wang *et al.* [57] and Neu *et al.* [56, 117].

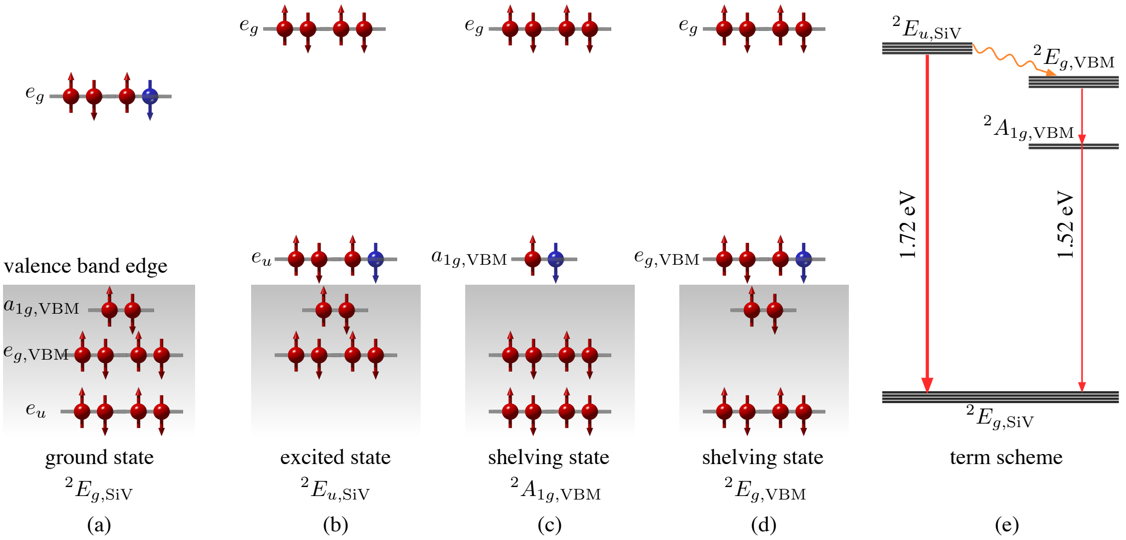

Figure 2.7: Ground (a), excited (b) and shelving state configurations (c,d) for the SiV center as calculated by Gali and Maze [127]. Panel (e) shows the term scheme (black lines indicating the degeneracy) and the transitions (red arrows), which connect these configurations. The transitions indicated by thin red arrows are parity forbidden.

According to Gali and Maze, the parity selection rule, which forbids a direct transition between ${}^2A_{1g,\mathrm{VBM}}$ and ${}^2E_{g,\mathrm{VBM}}$, is weakened when the SiV defect is subject to crystal strain. In this case, a de-excitation via the shelving state becomes more pronounced, giving rise to another optical transition at 1.59 eV. This theoretical value is in good agreement with the energy of an additional optical transition at ~ 1.52 eV, which was discovered using spectroscopy on individual SiV centers in nanodiamonds [114]. As we will show in Sec. 4.3, crystal strain can be present for the nanodiamonds employed in Ref. [114]. It is remarkable, that this additional transition has not been observed in the low strain samples, which we introduce in Sec. 3.2. It would be particularly interesting to probe whether the 1.52 eV transition appears, when uniaxial stress is applied to the sample. Unfortunately, this technique was not available during the present studies, hence, we focus here on the zero phonon line transition between the ${}^2E_u$ and ${}^2E_g$ states of the SiV center.

Summary on the electronic states In summary, we have shown in this first part of the chapter how group theory helps to unambiguously classify the symmetry properties of a defect, and how it builds the mathematical foundations for the further analysis. As an actual example, we have deduced the basis states for the SiV center. In the following section, we introduce interaction terms which lift the degeneracy in ground and excited state. For the calculation of the effect of these interactions, group theory will be helpful in two respects: First, it simplifies the construction of the interaction matrices, as these can be deduced from symmetry principles. Second, group theory predicts which matrix elements in the interaction are zero from a symmetry point of view. We will start with the discussion of this second point in the next section.

2.2 Interaction terms

We have seen in the previous chapter, that the electronic states of the SiV defect can be constructed from group theoretical considerations, and that they transform under symmetry operations as the given irreducible representations. Connected to the irreducible representations are basis functions, which show a corresponding functional dependence on either the cartesian coordinates x, y, z or on the rotations R_x, R_y, R_z around the respective axes. In summary, we stated, that if the wave function of an electronic state has a given functional dependence on these coordinates, then we can clearly identify to which irreducible representation(s) it belongs.

The concept of irreducible representation and their basis functions is however not exclusive to wave functions. Typically, interaction terms also show a functional dependence on coordinates or rotations. Hence, we can assign a given interaction to irreducible representations, too. We have encountered a particularly simple example at the end of the previous section: The dangling bond orbitals, i.e. the SALCs, mix weakly with the atomic orbitals of the Si impurity via the Coulomb interaction. The Coulomb interaction is spherically symmetric – it is proportional to $1/r = 1/(x^2+y^2+z^2)$ – hence it transforms as the totally symmetric representation A_{1g}.

We will be dealing primarily with matrix elements and selection rules for the interactions in this section. The interactions are given by a perturbation Hamiltonian $\mathbb{H}$ that couples two states $|\psi_i\rangle$ and $|\psi_j\rangle$ out of the basis set (2.27). The states $|\psi_i\rangle$ and $|\psi_j\rangle$ are orthogonal eigenstates of a Hamilton operator $\mathbb{H}_0$, which describes the unperturbed SiV center. We employ group theory to decide whether or not the states $|\psi_i\rangle$ and $|\psi_j\rangle$ are coupled by the perturbative interaction $\mathbb{H}$. This is done by investigating whether or not the matrix element $\langle\psi_j|\mathbb{H}|\psi_i\rangle$ vanishes by symmetry. We consider the perturbation $\mathbb{H}$ to be invariant under all the symmetry operations of the group of the Schrödinger equation. For such a perturbation, all symmetry operations commute with $\mathbb{H}$. This commutation is only possible if the matrix element $\langle\psi_j|\mathbb{H}|\psi_i\rangle$ is a number, i.e. if it transforms as a scalar. A constant scalar is invariant under all symmetry operations, as it does not depend on any coordinates, and consequently, $\langle\psi_j|\mathbb{H}|\psi_i\rangle$ must transform as the fully symmetric representation A_1 (or A_{1g} in the D_{3d} point group). Thus, if $\langle\psi_j|\mathbb{H}|\psi_i\rangle$ does not transform as A_{1g}, it vanishes. As we stated above, the perturbation $\mathbb{H}$ is expressed as one irreducible representation or as a linear combination of irreducible representations. Therefore, the matrix elements we calculate involve the *direct product* of two (or more) representations. We will briefly outline the theory behind the direct product (Sec. 2.2.1) and list the algebra on how to calculate direct products. In Secs. 2.2.2 - 2.3.3, we calculate actual interactions present for the SiV defect in order to construct a complete model to analyze the spectroscopic experiments in Chap. 4.

2.2.1 Direct products of groups and representations

We have already introduced the basis functions $|\psi_i\rangle$ and $|\psi_j\rangle$ which we assume to be elements of the basis sets (2.27). It is important to stress that these states are orthonormal to each other, i.e. their scalar product $\langle\psi_i|\psi_j\rangle = \delta_{ij}$. In general, it can be shown that two basis functions, which belong either to different irreducible representations or to different columns (rows) of the same representation, are orthogonal [155].

We first define the direct product of two groups: Let $\mathcal{G}_A = \{A_1, A_2, A_3, \dots A_{h_A}\}$ and $\mathcal{G}_B = \{B_1, B_2, B_3, \dots B_{h_B}\}$ be two groups such that that all operators A_i commute with all operators B_j. Then, the direct product of $\mathcal{G}_A$ and $\mathcal{G}_B$ is defined as the set

$$\begin{aligned} \mathcal{G}_A \otimes \mathcal{G}_B = \{ & A_1B_1, \dots, A_{h_A}B_1, \\ & \vdots \quad \ddots \quad \vdots \\ & A_1B_{h_B}, \dots, A_{h_A}B_{h_B}\}. \end{aligned} \tag{2.28}$$

It can be shown that, if $\mathcal{G}_A$ and $\mathcal{G}_B$ form groups, then also the product $\mathcal{G}_A \otimes \mathcal{G}_B \equiv \mathcal{G}_C$ forms a group. An example for the multiplication of two groups is the dihedral point group D_{3d} which results from a multiplication $D_3 \otimes i$, where i is the inversion group which consists of the identity element and the inversion.

In addition to direct product groups, we define the direct product of two representations in terms of the direct product of two matrices $\Gamma^{(A)}$, $\Gamma^{(B)}$. For the direct product of two matrices $\Gamma^{(A)} \otimes \Gamma^{(B)} = \Gamma^{(C)}$ every element of $\Gamma^{(A)}$ is multiplied by every element of $\Gamma^{(B)}$. Thus, the direct product matrix $\Gamma^{(C)}$ has a double set of indices

$$\Gamma^{(A)}_{ij} \otimes \Gamma^{(B)}_{kl} = \Gamma^{(C)}_{ik,jl}, \tag{2.29}$$

and if $\Gamma^{(A)}$ is a (2×2) matrix and $\Gamma^{(B)}$ a (3×3) matrix, then $\Gamma^{(C)}$ will have (6×6) entries. The direct product of two representations taken from groups $\mathcal{G}_A$ and $\mathcal{G}_B$ forms a representation of the direct group [155]. Furthermore, it can be shown that the direct product of two irreducible representations of groups $\mathcal{G}_A$ and $\mathcal{G}_B$ yields an irreducible representation of the direct product group. Hence, all irreducible representations of the direct product group can be generated from the irreducible representations of the original groups before they are joined. We can also take direct products between two representations of the same group. The direct product of two representations of the same group is also a representation of that group, though in general, it is a reducible representation [155].

Finally, we introduce the direct product of the characters of irreducible representations. It is straightforward to prove that the characters $\chi^{(C)}$ for the irreducible representations $\Gamma^{(C)}$ in the direct product group $\mathcal{G}_C$ are given by multiplication of the characters $\chi^{(A)}, \chi^{(B)}$

of the original groups $\mathcal{G}_A, \mathcal{G}_B$ according to

$$\chi^{(C)}(A_k B_l) = \chi^{(A)}(A_k)\,\chi^{(B)}(B_l). \tag{2.30}$$

When we construct the direct product between two representations $\Gamma^{(1)}, \Gamma^{(2)}$ of the same group, then the characters of the product group are obtained as

$$\chi^{\Gamma^{(1)} \otimes \Gamma^{(2)}}(R) = \chi^{\Gamma^{(1)}}(R)\,\chi^{\Gamma^{(2)}}(R). \tag{2.31}$$

In general, if we calculate the direct product between two irreducible representations of a group, the resulting direct product representation will be reducible. If it is reducible, the characters for the direct product $\chi^{(\lambda)}\chi^{(\mu)}$ can then be written as a linear combination of the characters $\chi^{(\nu)}$ for irreducible representations of the group, and we can decompose the reducible representation into a sum of irreducible ones:

$$\chi^{(\lambda)}(R)\,\chi^{(\nu)}(R) = \sum_{\nu} a_{\lambda\mu\nu}\chi^{(\nu)}(R). \tag{2.32}$$

The coefficients for this sum $a_{\lambda\mu\nu}$ denote, how often the irreducible representation $\chi^{(\nu)}(R)$ occurs in this sum, and they can be written in analogy to Eq. (2.19) as

$$a_{\lambda\mu\nu} = \frac{1}{h}\sum_{\mathcal{C}_k} N_k \chi^{(\nu)}(\mathcal{C}_k)\left[\chi^{(\lambda)}(\mathcal{C}_k)\chi^{(\mu)}(\mathcal{C}_k)\right], \tag{2.33}$$

where $\mathcal{C}_k$ denotes the classes of symmetry operations with N_k elements in class $\mathcal{C}_k$. From this decomposition formula for direct products, we can deduce rules for the multiplication of irreducible representations (Tab. 2.8).

Table 2.8: Computational rules for the decomposition of direct products relevant for the D_{3d} point group.

representations:	
$A \otimes A = B \otimes B = A$	$A \otimes B = B$
$A \otimes E = B \otimes E = E$	$A \otimes T = B \otimes T = T$
subscripts, superscripts:	
$1 \otimes 1 = 2 \otimes 2 = 1$	$1 \otimes 2 = 2$
$g \otimes g = u \otimes u = g$	$u \otimes g = u$
twofold degenerate representations:	
$E_g \otimes E_g = E_u \otimes E_u = A_{1g} + A_{2g} + E_g$	
$E_g \otimes E_u = A_{1u} + A_{2u} + E_u$	

Having defined the computational rules for direct products, we return to the calculation of matrix elements for quantum mechanical problems. The matrix element $\langle\psi_j|\mathbb{H}|\psi_i\rangle$ can be computed by integrating the scalar product over all space:

$$\langle\psi_j|\mathbb{H}|\psi_i\rangle \cong \int\limits_{\mathbb{R}^3} \psi_j^*(\mathbf{r})\mathbb{H}\psi_i(\mathbf{r})\ \mathrm{d}^3 r \tag{2.34}$$

This matrix element must transform as a constant (or a scalar) c if we apply one or multiple symmetry operations P_R of the group $\mathcal{G}$ of Schrödinger's equation, and c must be independent of P_R:

$$P_R\langle\psi_j|\mathbb{H}|\psi_i\rangle = c\cdot\langle\psi_j|\mathbb{H}|\psi_i\rangle, \quad \forall P_R\in\mathcal{G} \tag{2.35}$$

For all groups, the only representation which satisfies Eq. (2.35) is the totally symmetric representation A_1, because it has the same character ($\chi(R) = 1$) for all operations R. Conversely, if the matrix element is not invariant under the symmetry operations which form the group of Schrödinger's equation, then the matrix element must vanish.

As we stated above, the actual calculation matrix element $\langle\psi_j|\mathbb{H}|\psi_i\rangle$ is replaced by the direct product of the three respective representations for ψ_i, ψ_j and $\mathbb{H}$. We assume that the wave functions ψ_i, ψ_j transform as partners α and α' of irreducible representations $\Gamma^{(i)}$ and $\Gamma^{(j)}$, and that the operator $\mathbb{H}$ transforms as a third representation $\Gamma^{(k)}$:

$$\langle\psi_j|\mathbb{H}|\psi_i\rangle = \Gamma^{(j)}\otimes\Gamma^{(k)}\otimes\Gamma^{(i)}. \tag{2.36}$$

If the direct product $\Gamma^{(k)}\otimes\Gamma^{(i)}$ is orthogonal to $\Gamma^{(j)}$, then the matrix matrix element vanishes. It is equivalent to say: If $\Gamma^{(j)}\otimes\Gamma^{(k)}\otimes\Gamma^{(i)}$ does not contain the fully symmetric representation A_1, then the matrix element vanishes.

Before we address the actual, and slightly more complex, interactions present for SiV defect, we show two simple examples. For the first example we return to the Coulomb interaction $\mathbb{H}_{\text{Coulomb}}$ which mixes the atomic orbitals of the Si impurity with the dangling bond SALCs (cf. previous section). As we have stated above, the Coulomb interaction transforms as the irreducible representation A_{1g}. From Tab. 2.8, we recognize the representation A_{1g} to leave all representations invariant under a direct product. Thus, the application of $\mathbb{H}_{\text{Coulomb}}$ on the state ψ_i which transforms as the irreducible representation $\Gamma^{(i)}$ is equivalent to the direct product $A_{1g}\otimes\Gamma^{(i)} = \Gamma^{(i)}$, and we obtain

$$\langle\psi_j|\mathbb{H}_{\text{Coulomb}}|\psi_i\rangle \cong \Gamma^{(j)}\otimes A_{1g}\otimes\Gamma^{(i)} = \Gamma^{(j)}\otimes\Gamma^{(i)}. \tag{2.37}$$

If the basis functions $\psi_{(i)}, \psi_{(j)}$ belong to different irreducible representations, i.e. $\Gamma^{(i)} \neq \Gamma^{(j)}$, then they are orthogonal and the matrix element in Eq. (2.37) vanishes. It is equal to say, if $\Gamma^{(i)} \neq \Gamma^{(j)}$, then the direct product in Eq. (2.37) does not contain the totally symmetric representation A_{1g}. This result implies that the Coulomb interaction only mixes orbitals which belong to the same irreducible representation, e.g. the p_z orbital of the Si impurity couples to the a_{2u} orbital of the dangling bond representation.

The second example, which we consider, involves the optical dipole transition between the e_g and e_u states of the SiV center. The perturbation to the defect in a dipole transition is caused by the electric field amplitude $\mathcal{E}_0$ of the incident or radiated light and the electric dipole $\hat{\mathbf{p}} = -e\hat{\mathbf{r}}$ of the defect [1]:

$$\mathbb{H}_{\text{dipole}} = -\hat{\mathbf{p}}\cdot\mathcal{E}_0 = e\left(\hat{x}\mathcal{E}_x + \hat{y}\mathcal{E}_y + \hat{z}\mathcal{E}_z\right). \tag{2.38}$$

The electric field amplitude $\mathcal{E}_0$ is a constant external property which does not influence the symmetry of the defect system. The electric dipole $\hat{\mathbf{p}} = (\hat{p}_x, \hat{p}_y, \hat{p}_z)$ acts like an operator with respect to the group of Schrödinger's equation, thus we are interested in the matrix elements $\langle\hat{\mathbf{p}}\rangle = e\langle\psi_j|\hat{\mathbf{r}}|\psi_i\rangle$. According to the basis functions for the D_{3d} character table, the dipole operator transforms as irreducible representations $A_{2u}+E_u$, where A_{2u} accounts for the $\hat{p}_z$-component and E_u for the pair $(\hat{p}_x, \hat{p}_y)$. We note that both representations have odd parity, hence they only couple states of different parity. For example, according to Tab. 2.8 for $\psi_i = e_u$ we obtain

$$\hat{p}_x|\psi_i\rangle = \hat{p}_x|e_u\rangle \cong E_u \otimes E_u = A_{1g} + A_{2g} + E_g, \tag{2.39}$$

and only if the final state transforms as either A_{1g}, A_{2g} or E_g, the matrix element $\langle\psi_j|\hat{p}_x|\psi_i\rangle$ can be different from zero. For the actual case of the SiV center, the ground and excited state have different parity, so this *selection rule* is readily fulfilled. We denominate the values $\mu_{\mathbf{ij}} = \langle\psi_j|\hat{\mathbf{p}}|\psi_i\rangle$ the *dipole moment* for the transition $\psi_i \to \psi_j$, thus the Hamilton operator for the dipole transition has the expectation value

$$\langle\mathbb{H}_{\text{dipole}}\rangle_{ij} = -\langle\psi_j|\hat{\mathbf{p}}|\psi_i\rangle \cdot \mathcal{E}_0 = -\mu_{\mathbf{ij}} \cdot \mathcal{E}_0 \tag{2.40}$$

We examine the selection rules for optical dipole transitions in greater detail in Sec. 2.3. As the ground and excited states for the SiV center are two-fold degenerate (without taking into account the spin degree), the dipole operators $\hat{p}_x, \hat{p}_y, \hat{p}_z$ are expressed as 2×2-matrices. The direct product rules which we employed above will also be useful for the determination of these matrices, and the resulting dipole moments offer an important insight in the polarization properties of the SiV fluorescence.

As a summary, we have learned in this section, that the correspondence between electronic states, interactions and irreducible representation allows the simplification of matrix element calculations. After this general introduction to direct products and their calculation, we now determine the relevant interaction terms which account for the lifting of the degenerate states and therefore cause the spectral fine structure of the SiV center. The first step in this calculation will always be the question whether the corresponding direct products contain the totally symmetric representation.

2.2.2 Spin-orbit coupling

As the first interaction which lifts the degeneracy among the ground and excited states, we introduce the spin-orbit (SO) coupling. So far, we have focussed primarily on the orbital part of the wave function. In the group theoretical analysis of Sec. 2.1.4, we showed that the negative charge stated of the SiV center is a spin $S = 1/2$ system. Spin-orbit interaction is a relativistic effect due to the interaction of a single electron with its orbital motion in the potential ϕ of a nucleus. The interaction Hamiltonian is given by [156]

$$\mathbb{H}^{\text{SO}} = \frac{\hbar}{4c^2m}\left(\hat{\boldsymbol{\nabla}}V \times \hat{\mathbf{p}}\right) \cdot \frac{\hat{\mathbf{S}}}{\hbar}, \tag{2.41}$$

where $V = e\phi$ is the potential energy of the electron in the magnetic field created by the nucleus, m is the mass of the electron and $\hat{\mathbf{p}}$ is the momentum of the electron (not to be confounded with the dipole operator above). The spin operator $\hat{\mathbf{S}}$ is expressed in terms of Pauli matrices,

$$\hat{S}_x = \hbar \begin{bmatrix} 0 & 1 \\ 1 & 0 \end{bmatrix}, \quad \hat{S}_y = \hbar \begin{bmatrix} 0 & -i \\ i & 0 \end{bmatrix}, \quad \hat{S}_z = \hbar \begin{bmatrix} 1 & 0 \\ 0 & -1 \end{bmatrix}. \tag{2.42}$$

For a free atom, the SO interaction is usually completely invariant under any rotation, i.e. it belongs to the full rotation group. In a lattice, the crystal field breaks this symmetry, therefore, we now make use of group theory to describe $\mathbb{H}^{\mathrm{SO}}$ in a finite symmetry. We first derive which irreducible representation $\mathbb{H}^{\mathrm{SO}}$ belongs to, then we deduce the non-vanishing matrix elements from the direct product formalism (Sec. 2.2.1).

The nuclear potential ϕ has a spherical symmetry, hence it transforms as the totally symmetric representation A_{1g}. As a result, the gradient of the potential $\hat{\boldsymbol{\nabla}}\phi$ transforms as a vector with the components

$$\hat{\boldsymbol{\nabla}} V = e \begin{pmatrix} \frac{\partial}{\partial x}\phi \\ \frac{\partial}{\partial y}\phi \\ \frac{\partial}{\partial z}\phi \end{pmatrix} \equiv \begin{pmatrix} \partial_x \\ \partial_y \\ \partial_z \end{pmatrix} \cong \begin{pmatrix} \hat{x} \\ \hat{y} \\ \hat{z} \end{pmatrix}. \tag{2.43}$$

The similarity relation in Eq. (2.43) results from the fact, that the gradient along the x, y, z-directions transforms similar to the x, y, z-coordinates themselves. With this similarity, we identify the x, y-components of the potential energy to transform as irreducible representation E_u and the z-component as A_{2u}. The quantum mechanical momentum operator $\hat{\mathbf{p}}$ in position space takes the partial derivatives with respect to the spatial coordinates x, y, z, thus, the momentum operator also transforms as a vector. Taking the vector product between the nuclear potential gradient and the momentum, we obtain

$$\hat{\boldsymbol{\nabla}} V \times \hat{\mathbf{p}} = \begin{pmatrix} \partial_x \\ \partial_y \\ \partial_z \end{pmatrix} \times \begin{pmatrix} \hat{p}_x \\ \hat{p}_y \\ \hat{p}_z \end{pmatrix} \cong \begin{pmatrix} \hat{y}\hat{p}_z - \hat{z}p_y \\ \hat{z}p_x - \hat{x}\hat{p}_z \\ \hat{x}p_y - \hat{y}p_x \end{pmatrix} = \begin{pmatrix} \hat{L}_x \\ \hat{L}_y \\ \hat{L}_z \end{pmatrix}. \tag{2.44}$$

This yields the SO interaction Hamiltonian[1] $\mathbb{H}^{SO}_{g,e} = -\frac{\lambda_{g,e}}{2}\hat{\mathbf{L}} \cdot \hat{\mathbf{S}}$ as we known it from atomic physics, where $\hat{\mathbf{L}} = (\hat{L}_x, \hat{L}_y, \hat{L}_z)$ is the orbital angular momentum operator and $\lambda_{g,e}$ is the SO coupling constant for ground and excited state, respectively. When the SO interaction is included, the wave functions consist of a spatial part and a spin part. This means that the irreducible representations that classify the states in a solid must depend on the spin angular momentum. As spin has half-integer angular momentum, it can be shown that it changes the sign under a 360° rotation. This is commonly accomplished with the concept of double groups, in which a new group element (the 360° rotation) is added to the existing symmetry elements. Double groups are extensively treated in group theory textbooks (e.g. in Ref. [155, page 337]). For the present discussion, it is sufficient to note that we can construct the matrix elements for $\hat{\mathbf{L}}$ and $\hat{\mathbf{S}}$ separately in terms of

---

[1] Note, that we introduce a minus sign for $\mathbb{H}^{SO}_{g,e}$; this sign accounts for the fact that we are treating an electron hole instead of an actual electron [157].

2×2-matrices, which we then combine using a direct product (see below). The matrix elements for the spin are given in the $\{m_s = +1/2, m_s = -1/2\} = \{\uparrow, \downarrow\}$ basis by the Pauli matrices (2.42).

Therefore, we search the matrix elements of the orbital angular momentum operator which are of the form $\langle e_g|\hat{\mathbf{L}}|e_g\rangle$ and $\langle e_u|\hat{\mathbf{L}}|e_u\rangle$. The operator $\hat{\mathbf{L}} = (\hat{L}_x, \hat{L}_y, \hat{L}_z)$ generates rotations (R_x, R_y, R_z), therefore it transforms as the irreducible representations $(E_g^{(x)}, E_g^{(y)}, A_{2g})$. To identify the non-vanishing matrix elements of its components, we check whether the corresponding direct products contain the totally symmetric representation A_{1g}. As a first rule, we state that $\hat{\mathbf{L}}$ only couples states of the same parity, i.e. within the ground state or excited state manifold. For example, the matrix element $\langle e_{ux}|\hat{L}_x|e_{ux}\rangle$ transforms as the direct product (cf. Tab. 2.8

$$\begin{aligned} E_u^{(x)} \otimes \left(E_g^{(R_x)} \otimes E_u^{(x)}\right) &= E_u^{(x)} \otimes \left(A_{1u} + A_{2u} + E_u^{(x)}\right) \\ &= E_g + E_g + A_{1g} + A_{2g} + E_g \supset A_{1g}, \end{aligned}$$

and the matrix element $\langle e_{ux}|\hat{L}_x|e_{ux}\rangle$ does not vanish for symmetry reasons. While group theory identifies which elements are zero, it does not tell the value of those matrix elements which are non-zero. For this task, we employ another strategy, which we present for the e_u excited states. The ground states only differ from the excited states by their response to symmetry operations including the inversion, and those operations leave the matrix elements invariant. The excited states e_{ux}, e_{uy} have similarities to the p_x, p_y orbitals of an atom (cf. page 45); the p_z orbital would belong to the A_{2u} representation, which however is far in energy. The p-orbitals of an atom are combined to form the spherical harmonics $Y_l^{m_l}$, with $l = 1$ and $m_l = -1, 0, 1$, thus

$$Y_l^{m_l} = \begin{cases} Y_1^{+1} = -\frac{1}{\sqrt{2}}(p_x + ip_y) \\ Y_1^0 = p_z \\ Y_1^{-1} = \frac{1}{\sqrt{2}}(p_x - ip_y) \end{cases} \tag{2.45}$$

In analogy to the spherical harmonics, we introduce the states $e_+ = -\frac{1}{\sqrt{2}}(e_x + ie_y)$ and $e_- = \frac{1}{\sqrt{2}}(e_x - ie_y)$, where we omit the subscript u, as we will talk exclusively about the excited state. According to the similarity to the spherical harmonics, these states are eigenstates of the $\hat{L}_z$-operator as $\hat{L}_z e_\pm = \pm\hbar \cdot e_\pm$ and $\hat{L}_z a_{2u} = 0 \cdot a_{2u}$. Hence, we already know the matrix elements of $\hat{L}_z$ in the $e_\pm$ basis:

$$\begin{array}{c|cc} \hat{L}_z & |e_+\rangle & |e_-\rangle \\ \langle e_+| & 1 & 0 \\ \langle e_-| & 0 & -1 \end{array}. \tag{2.46}$$

The off-diagonal terms are zero because $\langle e_-|\hat{L}_z|e_+\rangle = \hbar\,\langle e_-|e_+\rangle = 0$ as e_+ and e_- are orthogonal. The bases $\{e_+, e_-\}$ and $\{e_x, e_y\}$ are connected by a simple transformation T,

$$\begin{pmatrix} e_+ \\ e_- \end{pmatrix} = \underbrace{\begin{bmatrix} -1 & -i \\ 1 & -i \end{bmatrix}}_{\hat{T}} \begin{pmatrix} e_x \\ e_y \end{pmatrix}, \tag{2.47}$$

hence, the operator $\hat{L}_z^{(e_{x,y})}$ is transformed according to $\hat{L}_z^{(e_{x,y})} = \hat{T}^{-1}\hat{L}_z^{(e_\pm)}\hat{T}$. In addition to $\hat{L}_z$, we define the ladder operators $\hat{L}_\pm = \hat{L}_x \pm i\hat{L}_y$, where

$$\begin{aligned} \hat{L}_+ Y_l^{m_l} &= \hbar\sqrt{(l-m_l)(l+m_l+1)}\; Y_l^{m_l+1} \\ \hat{L}_- Y_l^{m_l} &= \hbar\sqrt{(l+m_l)(l-m_l+1)}\; Y_l^{m_l-1}. \end{aligned}$$

The operators $\hat{L}_\pm$ couple the $e_\pm$ states to the a_{2u} state, since $\hat{L}_+ e_- = \hbar\sqrt{2}a_{2u} = \hat{L}_- e_+$, but they do not cause any direct coupling between e_+ and e_-. As a result, the matrix elements of $\hat{L}_\pm$ in the $e_\pm$ basis are all zero – although from group theory, they would be allowed to be non-zero. Consequently, the operators $\hat{L}_x$ and $\hat{L}_y$ also vanish in the e_x and e_y basis. Together, the orbital angular momentum operators are given by (with $\hbar$ set to 1)

$$\begin{array}{ccc} \hat{L}_x & |e_{gx}\rangle & |e_{gy}\rangle \\ \langle e_{gx}| & 0 & 0 \\ \langle e_{gy}| & 0 & 0 \end{array} \qquad \begin{array}{ccc} \hat{L}_y & |e_{gx}\rangle & |e_{gy}\rangle \\ \langle e_{gx}| & 0 & 0 \\ \langle e_{gy}| & 0 & 0 \end{array} \qquad \begin{array}{ccc} \hat{L}_z & |e_{gx}\rangle & |e_{gy}\rangle \\ \langle e_{gx}| & 0 & i \\ \langle e_{gy}| & -i & 0 \end{array}. \tag{2.48}$$

It is an important result that both the operator $\hat{L}_x$ and $\hat{L}_y$ are identical to zero. With it, the SO Hamiltonian simplifies to

$$\mathbb{H}_{g,e}^{SO} = -\frac{\lambda_{g,e}}{2}\hat{L}_z\hat{S}_z = -\frac{\lambda_{g,e}}{2}\begin{bmatrix} 0 & i \\ -i & 0 \end{bmatrix} \otimes \begin{bmatrix} 1 & 0 \\ 0 & -1 \end{bmatrix}, \tag{2.49}$$

where the direct product between $\hat{L}_z$ and $\hat{S}_Z$ accounts for the spin double group. Apart from the coupling constant $\lambda_{g,e}$, the SO interaction is the same for ground and excited state, thus using the basis vectors (2.27), we obtain for the ground state

$$\begin{array}{ccccc} \mathbb{H}_g^{SO} & |e_{gx}\uparrow\rangle & |e_{gx}\downarrow\rangle & |e_{gy}\uparrow\rangle & |e_{gy}\downarrow\rangle \\ \langle e_{gx}\uparrow| & 0 & 0 & -i\lambda_g & 0 \\ \langle e_{gx}\downarrow| & 0 & 0 & 0 & i\lambda_g \\ \langle e_{gy}\uparrow| & i\lambda_g & 0 & 0 & 0 \\ \langle e_{gy}\downarrow| & 0 & -i\lambda_g & 0 & 0 \end{array}, \tag{2.50}$$

and for the excited state, we simply replace the subscripts.

Once we know how the SO interaction acts on the basis states, we can determine its effect on the SiV levels. In perturbation theory, we calculate the eigenvalues and -vector of the perturbation Hamiltonian in the basis (2.27) of the unperturbed system. Diagonalizing the SO Hamiltonian (2.50) yields two two-fold degenerate eigenvalues $\pm\lambda$ with the eigenvectors

$$+\lambda \rightarrow \begin{cases} |e_+\uparrow\rangle = -\frac{1}{\sqrt{2}}\left(|e_x\uparrow\rangle + i|e_y\uparrow\rangle\right) \\ |e_-\downarrow\rangle = \frac{1}{\sqrt{2}}\left(|e_x\downarrow\rangle - i|e_y\downarrow\rangle\right) \end{cases} \tag{2.51a}$$

$$-\lambda \rightarrow \begin{cases} |e_+\downarrow\rangle = -\frac{1}{\sqrt{2}}\left(|e_x\downarrow\rangle + i|e_y\downarrow\rangle\right) \\ |e_-\uparrow\rangle = \frac{1}{\sqrt{2}}\left(|e_x\uparrow\rangle - i|e_y\uparrow\rangle\right), \end{cases} \tag{2.51b}$$

where we omitted again the subscripts for ground and excited state. Hence, the formerly four-fold degenerate ground and excited state each splits into two states (Fig. 2.8). The state splitting is proportional to the coupling constant $\lambda_{g,e}$.

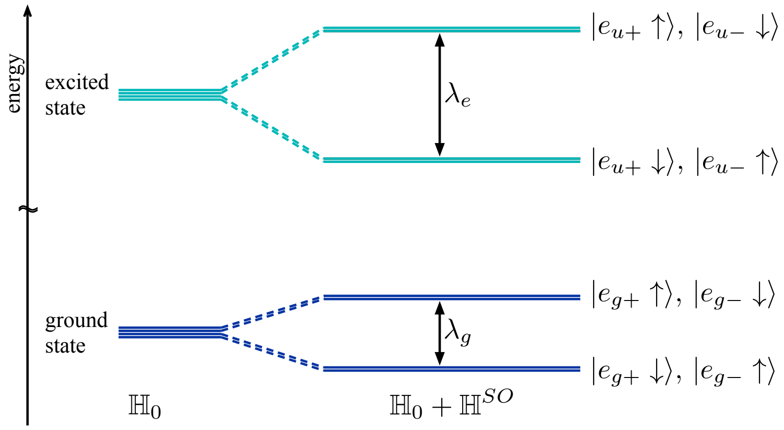

Figure 2.8: Spin-orbit splitting of the ground and excited state. For both manifolds, the formerly four-fold degenerate ground and excited state each splits into two states. The resulting eigenvectors under the perturbation of $\mathbb{H}^{SO}$ are defined in Eq. (2.51).

We expect a stronger coupling in the excited state for the following reason: The SO interaction depends on the gradient of the Coulomb potential of the nucleus. In the case of the SiV center, this potential is created by the Si nucleus. We have seen in Sec 2.1.4, the e_u excited state mixes with the atomic orbitals of the Si impurity, whereas the ground state shows no such coupling. Due to this mixing, the probability of finding the electron hole in proximity to the Si nucleus is higher for the excited state than for the ground state. Therefore, the excited state is more susceptible to the nuclear potential gradient and spin orbit mixing is expected to be larger (cf. Sec. 4.1.4).

It will be convenient to present the eigenvectors in a graphical way, especially when we add multiple perturbations. Therefore, we introduce probability distribution graphs for them. Each eigenvector $|\psi^{(i)}_{g,e}\rangle$ can be expressed as a linear combination of the basis vectors (2.27), i.e. for an eigenstate of the ground state manifold we have

$$|\psi^{(i)}_g\rangle = \tilde{\alpha}|e_{gx}\uparrow\rangle + \tilde{\beta}|e_{gx}\downarrow\rangle + \tilde{\gamma}|e_{gy}\uparrow\rangle + \tilde{\delta}|e_{gy}\downarrow\rangle, \tag{2.52}$$

with $\tilde{\alpha},\ldots,\tilde{\delta}$ being complex coefficients for this superposition. For example, for the eigenstate $|e_+\uparrow\rangle$, we have $\tilde{\alpha}=-1/\sqrt{2}$ and $\tilde{\gamma}=-i/\sqrt{2}$. We graphically represent an eigenstate by plotting the absolute squares $|\tilde{\alpha}|^2,\ldots,|\tilde{\delta}|^2$, which corresponds to the probability of a given state to be detected in the corresponding basis states. The states are normalized, such that $|\tilde{\alpha}|^2+\ldots+|\tilde{\delta}|^2=1$. We consistently label the four ground states of the SiV center with $|1\rangle,|2\rangle,|3\rangle,|4\rangle$ and the excited states with $|A\rangle,|B\rangle,|C\rangle,|D\rangle$, where this labeling is ascending in energy. Figure 2.9 shows the ground state eigenvectors $|1\rangle,\ldots,|4\rangle$ under the influence of spin orbit coupling.

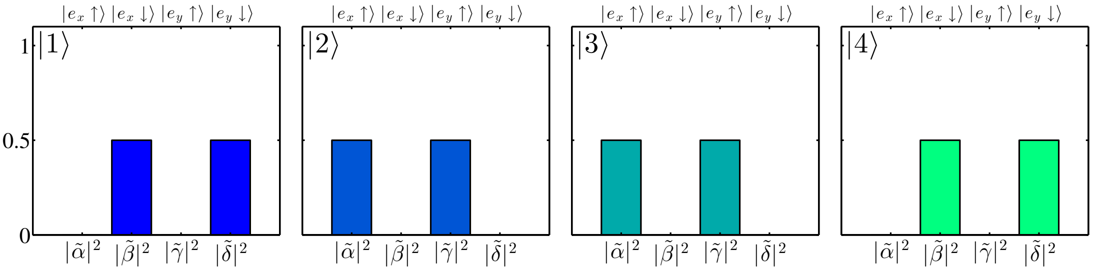

Figure 2.9: Eigenvectors $|1\rangle, |2\rangle, |3\rangle, |4\rangle$ of the SiV ground state under the perturbation of SO coupling. For each eigenstate, we plot the absolute squares $|\tilde{\alpha}|^2, \ldots, |\tilde{\delta}|^2$, which corresponds to the probability of a given state to be detected in the basis states (2.27).

It is straightforward to express the eigenvectors in the "eigenbasis" $|e_\pm \uparrow, \downarrow\rangle$ of the SO Hamiltonian. The two bases are related by a 4×4 transformation matrix, which is equal to the direct product $\hat{T} \otimes \mathbb{I}_2$ of the matrix $\hat{T}$ of Eq. (2.47) and the 2×2 identity matrix $\mathbb{I}_2$. We obtain the eigenvector in a linear combination of the type

$$|\psi_g^{(i)}\rangle = \alpha|e_{g+}\uparrow\rangle + \beta|e_{g+}\downarrow\rangle + \gamma|e_{g-}\uparrow\rangle + \delta|e_{g-}\downarrow\rangle. \tag{2.53}$$

Displaying the SO eigenvectors in their eigenbasis is trivial, as shown in Fig. 2.10. We see in Chap. 4, that the SO coupling remains the strongest perturbation throughout all experiments, therefore we always plot the eigenstates in the $|e_\pm \uparrow, \downarrow\rangle$ basis of the SO Hamiltonian.

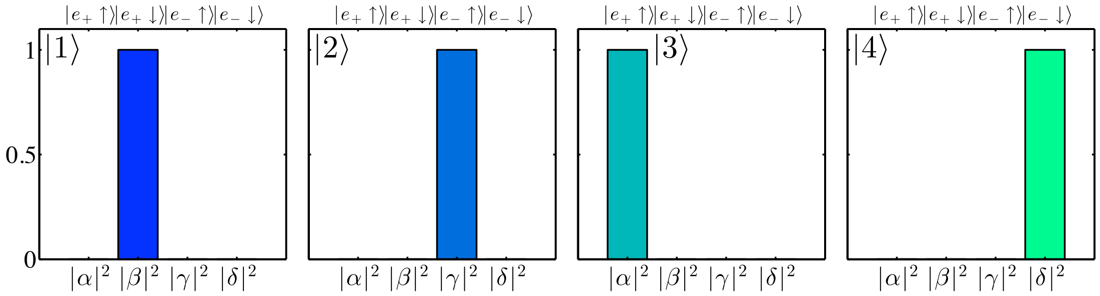

Figure 2.10: Eigenvectors $|1\rangle, |2\rangle, |3\rangle, |4\rangle$ of the SiV ground state under the perturbation SO coupling in the basis states $|e_\pm \uparrow, \downarrow\rangle$. The presentation of the states is equal to Fig. 2.9.

From Figs. 2.9 and 2.10, we infer that there is no spin mixing due to the SO coupling. This particularity is due to the absence of $\hat{L}_x\hat{S}_x$ and $\hat{L}_y\hat{S}_y$ in the SO operator (2.41) which, in turn, results from the vanishing $\hat{L}_x, \hat{L}_y$ terms for the orbital angular momentum operator $\hat{\mathbf{L}}$. This important result explains the observation of spin-tagged fluorescence in Sec. 4.2. We conclude that SO coupling is – in the special case of the SiV center – a purely *orbital* interaction. In the following section, we investigate another purely orbital interaction, the Jahn-Teller effect.

2.2.3 The Jahn-Teller effect

We have seen in Sec. 2.1.4 that both the ground and excited states of the SiV center are energetically degenerated. This degeneracy is lifted partly by the spin-orbit coupling. For the following discussion, we however ignore the SO-interaction, and introduce another effect which also lifts the orbital degeneracy.

In 1936, following a hypothesis of Lev Landau, Hermann Jahn and Edward Teller proved that a molecule in an orbitally degenerate electronic state would be inherently unstable with respect to distortions of its nuclear configuration which lower the orbital symmetry [158]. The only two exceptions of this theorem are linear molecules, where no orbital degeneracy can be lifted, and Kramer's degeneracy for spins.

The Jahn-Teller effect follows from a coupling of the electronic states to vibration modes of the nuclear configuration. Using group theory, we can assign the vibrational modes to irreducible representations and employ the direct product computation rules (Tab. 2.8) to verify which electronic states they couple to. To identify the modes, we employ the following procedure: First, we define a *trivial* representation for the vibration modes using the atomic displacements from the equilibrium positions of the atoms. This trivial representation is then decomposed into a linear combination of irreducible representation, as we have done for dangling bond representation in Sec. 2.1.4. Finally, we write the modes in normal coordinates Q_k, which are linear combinations of the atomic displacements.

To construct the trivial representation, we denote the position of each atom using three mutually orthogonal unit vectors, i.e. atom i has the coordinates x_i, y_i, z_i (Fig. 2.11a). This leaves us with $3N$ degrees of freedom, which is why we term this trivial representation $\Gamma^{(3N)}$. For the SiV center, we take into account the six neighboring carbon atoms and the Si impurity, thus $N = 7$. As the next step, we would track how each of the $3N = 21$ coordinates changes under each respective symmetry operation. This would require a 21×21 matrix for each symmetry operation and is a very tedious procedure. However, as we have seen for the decomposition of the dangling bond representations (2.16), it is sufficient to know the characters $\chi^{(3N)}(R)$ for the trivial representation under the symmetry operation R.

To determine the characters for a given operation R, the following simple rules have been shown. If an atom is moved to another position under R, and with it its unit vectors $x_i \xrightarrow{R} x_j$, with $i \neq j$, then the coordinates do not contribute to the character $\chi(R)$. Thus, we only have to investigate the "χ per unshifted atom" [154]: If a coordinate of an atom i is invariant under a symmetry operation R, i.e. $x_i \xrightarrow{R} x_i$, then we add 1 to the character $\chi(R)$. If the coordinate is reversed $x_i \xrightarrow{R} -x_i$ then, we subtract 1 from $\chi^{(3N)}(R)$. A special case are the C_3 and S_6 rotations, because they transform the unit vectors x_{Si}, y_{Si} of the Si impurity into linear combinations of each other. The characters $\chi^{(3N)}(C_3)$ and $\chi^{(3N)}(S_6)$ can be acquired from the cartesian transformation matrices (2.1). We note, that the characters for all elements of a class are identical.

We apply this procedure to every one of the N atoms and count the contributions of each unshifted atom to the characters. For example, the reflection σ_d'' (Fig. 2.11b) leaves the x and z coordinates of three atoms (two neighboring carbon atoms and the Si atom)

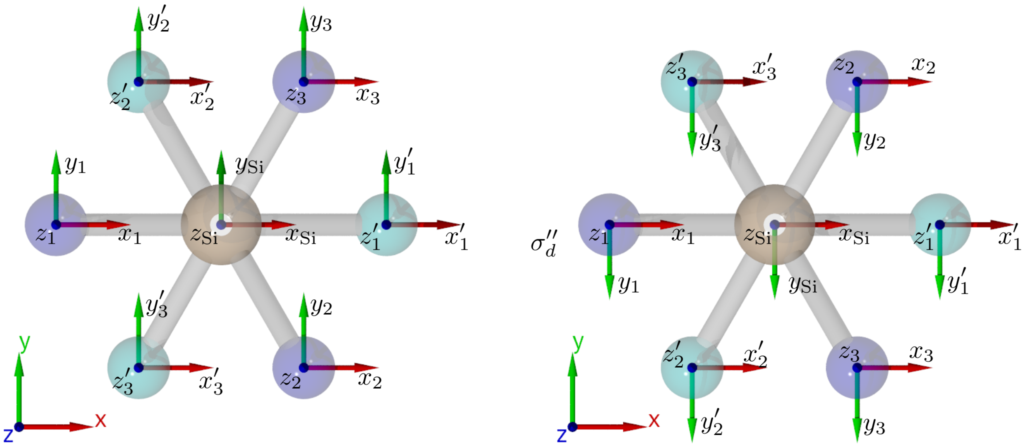

(a) (b)

Figure 2.11: The $3N$ degrees of freedom for the Si-impurity and all next-neighboring carbon atom, denoted by unit vectors x_i, y_i, z_i (panel a). When we apply the symmetry operation σ_d'' (panel b), only the Si atom, and the carbon atoms 1 and $1'$ are unshifted and contribute to the character. For these three atoms, the x and z unit vectors stay invariant, whereas the y vector is reversed.

invariant, thus we add 6 to $\chi(\sigma_d'')$. The y coordinates of the three atoms are reversed, hence we again subtract 3 from $\chi(\sigma_d'')$, and obtain $\chi(\sigma_d'') = 3$. We list the characters $\chi^{(3N)}(R)$ in the second row of Tab. 2.9.

Clearly, the trivial representation is reducible, and we can apply the decomposition formula (2.19) to find the coefficients a_i, which denote how often irreducible representation $\Gamma^{(i)}$ is included in $\Gamma^{(3N)}$ (Tab. 2.9). We obtain for the $3N$ degrees of freedom,

$$\Gamma^{(3N)} = 2A_{1g} + A_{2g} + 3E_g + A_{1u} + 3A_{2u} + 4E_u. \tag{2.54}$$

The non-linear molecule or defect has 3 translational and 3 rotation degrees of freedom. These 6 contributions are included in the decomposition (2.54), and in order to find the vibrations, we need to subtract them from (2.54). The translations in x, y, z direction transform as $A_{2u} + E_u$ and the rotations as $A_{2g} + E_g$, as we can infer from the generating functions in the D_{3d} character table 2.3. Hence, for the $3N - 6 = 15$ vibrational degrees of freedom, we obtain

$$\Gamma^{(3N)}_{\text{vib}} = 2A_{1g} + 2E_g + A_{1u} + 2A_{2u} + 3E_u. \tag{2.55}$$

Before we address the actual directions of these modes, we check which of them couples to the e_g and e_u states of the SiV. We assume, that Jahn-Teller effect only couples states from the same manifold, i.e. ground states do not couple to excited states. According to Jahn and Teller, we verify whether the totally symmetric representation A_{1g} is contained in the

Table 2.9: The character table for the $3N$ representation. The decomposition into irreducible representations is completely analogous to Tab. 2.4.

$\mathbf{D_{3d}}$	E	$2C_3$	$3C_2$	i	$2S_6$	$3\sigma_d$	$a_i = \frac{1}{h}\sum_i N_k\,\chi_{(i)}\,\chi^{(3N)}$
$\chi^{(3N)}$	21	0	-1	-3	0	3	
N_k	1	2	3	1	2	3	$(h = 12)$
$N_k\,\chi^{A^{1g}}\,\chi^{(3N)}$	21	0	-3	-3	0	9	$\frac{1}{12}(21-3-3+9) = 2$
$N_k\,\chi^{A^{2g}}\,\chi^{(3N)}$	21	0	3	-3	0	-9	$\frac{1}{12}(21+3-3-9) = 1$
$N_k\,\chi^{E^{g}}\,\chi^{(3N)}$	42	0	0	-6	0	0	$\frac{1}{12}(42-6) = 3$
$N_k\,\chi^{A^{1u}}\,\chi^{(3N)}$	21	0	-3	3	0	-9	$\frac{1}{12}(21-3+3-9) = 1$
$N_k\,\chi^{A^{2u}}\,\chi^{(3N)}$	21	0	3	3	0	9	$\frac{1}{12}(21+3+3+9) = 3$
$N_k\,\chi^{E^{u}}\,\chi^{(3N)}$	42	0	0	6	0	0	$\frac{1}{12}(42+6) = 4$

direct product $E_g \otimes \Gamma^{(3N)}_{\text{vib}} \otimes E_g = \Gamma^{(3N)}_{\text{vib}} \otimes [E_g]^2$ for the ground state, and $\Gamma^{(3N)}_{\text{vib}} \otimes [E_u]^2$ for the excited state. The square $[E_u]^2$ of the irreducible representations of the electronic states is according to Tab. 2.8 given by

$$[E_g]^2 = [E_u]^2 = A_{1g} + A_{2g} + E_g. \tag{2.56}$$

The only directs which contains the totally symmetric representation A_{1g} are therefore

$$A_{1g} \otimes [E_g]^2 = A_{1g} \otimes [E_u]^2 = A_{1g} + A_{2g} + E_g \tag{2.57}$$

$$E_g \otimes [E_g]^2 = E_g \otimes [E_u]^2 = A_{1g} + A_{2g} + 3E_g. \tag{2.58}$$

Hence, the only relevant vibrational modes which couple to the electronic states of the SiV center transform as A_{1g} and E_g. The A_{1g} mode is the so-called breathing mode, for which all atoms vibrate along their bond axis. However, this mode does not lower the symmetry of the electronic state, and therefore we do not consider it further.

The final step is now to write these modes symmetry adapted coordinates. These coordinates are the normal coordinates $Q_{x,y}$, which are linear combinations of the unit vectors x_i, y_i, z_i. Having expressed the vibrational modes in dependence of $Q_{x,y}$, we call them normal modes. The calculation of normal modes is performed using a projection technique similar to Sec. 2.1.4 and is not explicitly shown here. Jäger derives the normal modes in Ref. [159], and we display them in Fig. 2.12. To distinguish the modes from electronic states, we denote their representations with the greek letter ϵ_g instead of E_g from now on. For each of the two ϵ_g representations, there are two degenerate, normal modes $Q_{x,y}$.

To illustrate *how* the electronic states couple to the $Q_{x,y}$-vibrations according to the Jahn-Teller (JT) effect, we partly follow the argumentation of O'Brien and Chancey [160]. It is common for JT systems to employ the Born-Oppenheimer- or adiabatic approximation: The electron, which has considerable smaller mass than the nuclei, follows the motion

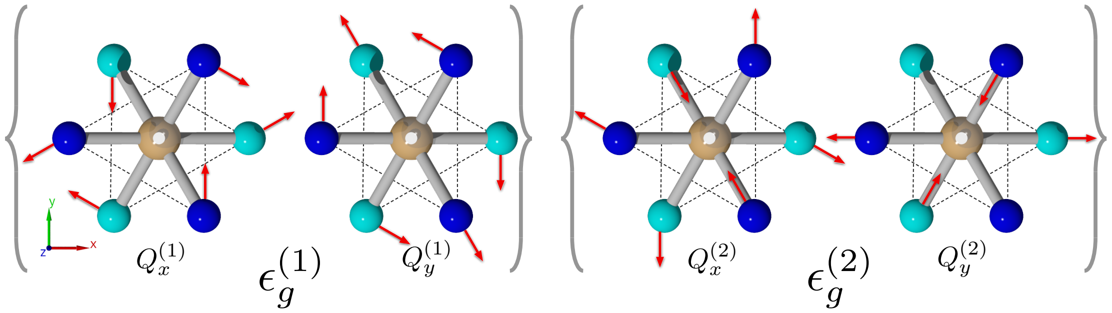

Figure 2.12: Vibrational normal modes transforming as the E_g irreducible representation. To distinguish the modes from electronic states, we denote the representations with the greek letter ϵ_g instead of E_g.

of the nuclei adiabatically. As a result, the Born-Oppenheimer approximation assumes that the state function may be written as the product of electronic and nuclear wave function [161]. The nuclei create an effective potential (the so-called adiabatic potential energy surface) in which the electrons move. First, we consider a simple case: If there was only one mode with normal cordinate Q coupled to a two-fold degenerate electronic state, then the potential energy due to JT interaction would be

$$\mathbb{H}_{\mathrm{Q}}^{JT} = \frac{1}{2}Q^2 + F\begin{bmatrix} Q & 0 \\ 0 & -Q \end{bmatrix}, \tag{2.59}$$

where neglected the kinetic energy contribution. The term $\frac{1}{2}Q^2$ accounts for the vibronic potential of the nuclear configuration (in an harmonic oscillator approximation) and F denotes the strength of the JT coupling. If we had no JT-coupling ($F = 0$), then the $\mathbb{H}_{\mathrm{Q}}^{JT}$ operator would be a simple harmonic oscillator potential, which we would draw as a parabola with its minimum at $Q = 0$. Hence, there would be two degenerate wave functions in a symmetric configuration with their energy minima $E_{min} = 0$ at $Q = 0$. For $F \neq 0$, the Hamiltonian (2.59) can be separated into two equations:

$$\mathbb{H}_{1\text{ mode}}^{JT} = \frac{1}{2}Q^2 \pm FQ. \tag{2.60}$$

These harmonic oscillator potentials describe two parabolas with their minimal energies $E_{min} = -F^{1/2}$ situated at $Q = \pm k$. Hence, the JT-interaction breaks the symmetry of the electronic system, it results in a lower symmetry configuration with two displaced minima, and it lowered the total energy. In this particular example, the wave functions are still degenerate – both have the same minimum energy.

Now, we return to the $E \otimes \epsilon$ coupling: The JT interaction with the normal modes $Q_{x,y}$ is usually developed as a series of powers of $Q_{x,y}$. Developing $\mathbb{H}^{JT}$ to $Q_{x,y}^2$, we obtain the quadratic $E \otimes \epsilon$ Hamiltonian [162]

$$\mathbb{H}^{JT} = \frac{1}{2}K(Q_x^2 + Q_y^2) + F\begin{bmatrix} Q_x & Q_y \\ Q_y & -Q_x \end{bmatrix} + G\begin{bmatrix} (Q_x^2 - Q_y^2) & 2Q_xQ_y \\ 2Q_xQ_y & -(Q_x^2 - Q_y^2) \end{bmatrix}, \tag{2.61}$$

where F denotes the linear vibronic coupling coefficient, G the quadratic coefficient and K the elastic force constant. The solution of Eq. (2.61) in polar coordinates $\rho = \sqrt{Q_x^2 + Q_y^2}$ and $\phi = \arctan(Q_y/Q_x)$ is given by [162]

$$E(\rho,\phi) = \frac{1}{2}K\rho^2 \pm \rho\left[F^2 + G^2\rho^2 + 2FG\rho\cos(3\phi)\right]^{1/2}. \tag{2.62}$$

For $G = 0$, have a linear vibronic coupling similar to the example of one vibrational mode (Eq. 2.59) and the resulting adiabatic potential energy surface is a “mexican-hat” potential, depicted in Fig. 2.13a (with $K = 14.5$ and $F = -0.74$ as given in [162] for the NV center). In this potential there is a continuous number of minima in the coordinate space (Q_x, Q_y) and there is still some energetic degeneracy which can be lifted by another interaction, e.g. spin-orbit coupling. In contrast to the interaction with a single vibrational mode, there is now a coupling between the degenerate electronic states due to the off-axis terms in the linear coupling matrix in Eq. (2.61).

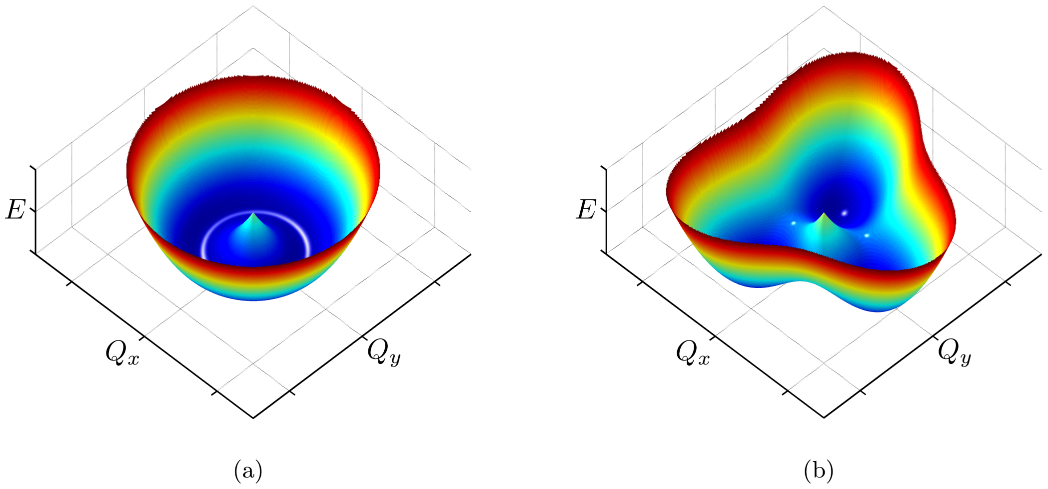

(a) (b)

Figure 2.13: Adiabatic potential energy surface which results from the Jahn-Teller Hamiltonian (2.61) for (a) linear Jahn-Teller coupling, a “mexican-hat” potential, and (b) for quadratic coupling. We employ the parameters $K = 14.5$ and $F = -0.74$ as given in [162] for the NV center.

The addition of a quadratic coupling ($G \neq 0$) results in three distinct minima in the adiabatic potential surface (Fig 2.13b), situated at multiples of $\phi = 120°$. The three wells are due to the three tetragonal distortions along the three cubic axes of a crystal [160]. Energetically, these minima are separated by a barrier. If the kinetic energy of an electronic system is too low to overcome this barrier, then the wave function is strongly localized in one of the three minima. We then think of equally probable, non-interacting ground states with vanishing overlap [160], and we speak of a *static* Jahn-Teller system. When the temperature of the system is raised, the system jumps from well to well, and an averaging over the different ground states is observed.

If the barrier between the wells is small, then there is a significant tunnel probability from one minimum to another. As a result, the wave functions will be delocalized over the different wells. We call this situation a *dynamic* Jahn-Teller effect. If we only consider the linear JT coupling (Fig. 2.13a), then the system is by itself dynamic as there are no distinct minima and the wave function will spread over the coordinate space. We limit the discussion in this work to the linear JT coupling, as it is usually stronger than the quadratic case.

Before we address the dynamic, linear JT coupling in more detail, we already state an important consequence: With the electronic wave function delocalized over the coordinate space (Q_x, Q_y), the electronic properties are changed as well. One example is the coupling of the orbital part of the wave function to an external magnetic field, which we investigate in more detail in Sec. 2.2.6. The interaction strength is defined by the g-factor (or g-tensor depending on the symmetry of the problem). The Zeeman interaction is strictly electronic and does not depend *directly* on the normal modes (Q_x, Q_y) of the nuclear configuration. However, the electronic wave functions show a different response to the external field, depending on where they are localized in the nuclear configuration. Hence, the delocalization of the wave functions due to the dynamic Jahn-Teller effect influences *indirectly* the g-factor (and other properties). Ham introduces reduced matrix elements (later called "Ham"-factors) to account for this indirect coupling [163]: In the adiabatic approximation, we separated the total wave function $\Psi = u(\mathbf{r}, \mathbf{Q})\xi(\mathbf{Q})$ into a purely electronic part $u(\mathbf{r}, \mathbf{Q})$, which depends directly on the electronic coordinates $\mathbf{r}$ and parametrically on the vibrational coordinates $\mathbf{Q}$, and into a vibrational part $\xi(\mathbf{Q})$ with depends only on the nuclear configuration. The reduced matrix element of an operator $V(\mathbf{r})$ is then given as [160]

$$\frac{\int \xi^*(\mathbf{Q})\ \langle u(\mathbf{r}, \mathbf{Q})|V(\mathbf{r})|u(\mathbf{r}, \mathbf{Q})\rangle\ \xi(\mathbf{Q})\ \mathrm{d}Q}{\langle u(\mathbf{r}, \mathbf{Q_0})|V(\mathbf{r})|u(\mathbf{r}, \mathbf{Q_0})\rangle}, \tag{2.63}$$

where $u(\mathbf{r}, \mathbf{Q_0})$ is the uncoupled electronic wave function. This reduced matrix element can be seen as an averaging of the electronic operation $V(\mathbf{r})$ over the vibrational configurations. When there is no vibronic coupling $[\xi(\mathbf{Q}) = \delta(\mathbf{Q} - \mathbf{Q_0})]$, the reduced matrix element simplifies to 1.

With the JT Hamiltonian (2.61) and the respective vibrational modes at hand, we are able to study the effect of the JT coupling on the electronic states of the SiV center. As we stated earlier, we restrict the discussion to linear JT coupling, and define new variables $\Upsilon_{x,y}$ as the products $\Upsilon_{x,y} = FQ_{x,y}$. Furthermore, we drop the harmonic potential $\frac{1}{2}K(Q_x^2 + Q_y^2)$ because it acts equally on all states and simply causes a global energy shift. Hence, in the $\{e_x, e_y\}$ basis of SiV states (where we omit the subscripts g, u), we obtain

$$\mathbb{H}^{JT} = \begin{bmatrix} \Upsilon_x & \Upsilon_y \\ \Upsilon_y & -\Upsilon_x \end{bmatrix}. \tag{2.64}$$

Similar to spin-orbit interaction Hamiltonian (2.50), we extend this operator in order to include the spin degrees of freedom. The JT interaction is a purely orbital operator, hence to include the spin states we take the direct product with the 2 × 2 identity matrix, and obtain the Jahn-Teller Hamiltonian in the basis states (2.27)

$$\mathbb{H}^{JT} = \begin{bmatrix} \Upsilon_x & \Upsilon_y \\ \Upsilon_y & -\Upsilon_x \end{bmatrix} \otimes \begin{bmatrix} 1 & 0 \\ 0 & 1 \end{bmatrix} = \begin{bmatrix} \Upsilon_x & 0 & \Upsilon_y & 0 \\ 0 & \Upsilon_x & 0 & \Upsilon_y \\ \Upsilon_y & 0 & -\Upsilon_x & 0 \\ 0 & \Upsilon_y & 0 & -\Upsilon_x \end{bmatrix}. \tag{2.65}$$

Although the matrix form (2.65) is the same for ground and excited state, the values $\Upsilon_{x,y}$ can be different for both states; for the sake of brevity we however omit the subscripts in Eq. (2.65). Diagonalizing Eq. (2.65) results in the eigenvalues $\pm\Upsilon = \pm\sqrt{\Upsilon_x^2 + \Upsilon_x^2}$ and in the following eigenstates:

$$+\Upsilon \rightarrow \begin{cases} |\cos(\frac{\phi}{2})e_x + \sin(\frac{\phi}{2})e_y\rangle|\uparrow\rangle \\ |\cos(\frac{\phi}{2})e_x + \sin(\frac{\phi}{2})e_y\rangle|\downarrow\rangle \end{cases} \tag{2.66}$$

$$-\Upsilon \rightarrow \begin{cases} |\cos(\frac{\phi}{2})e_x - \sin(\frac{\phi}{2})e_y\rangle|\uparrow\rangle \\ |\cos(\frac{\phi}{2})e_x - \sin(\frac{\phi}{2})e_y\rangle|\downarrow\rangle \end{cases} \tag{2.67}$$

where $\tan(\phi) = \Upsilon_y/\Upsilon_x$. It is important to note, that the eigenvalues $\pm\Upsilon$ do not depend on the x, y components of the JT splitting but only on their quadratic mean value. We schematically display the level splitting caused by JT interaction in Fig. 2.14.

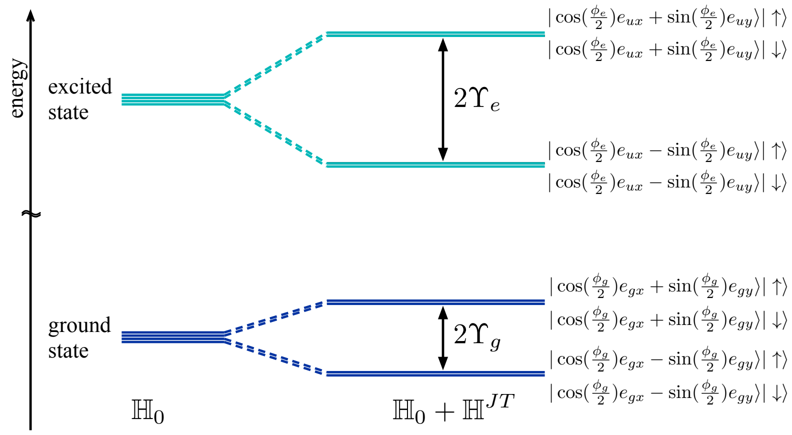

Figure 2.14: Jahn-Teller splitting of the ground and excited state. Similar to spin-orbit coupling, the formerly four-fold degenerate ground and excited state each splits into two states.

Similar to the spin-orbit interaction, the linear JT effect reduces the four-fold degeneracy to a two-fold (spin) degeneracy and it yields superpositions of e_x and e_y. However, the difference to the SO coupling is that in the resulting superpositions do not introduce the phase term $i = \mathrm{e}^{i\pi/2}$. Hence, if we visualize the JT eigenstates (2.67) in the basis $\{|e_\pm \uparrow, \downarrow\rangle\}$ according to Eq. (2.53), we obtain a mixture of orbital states (Fig. 2.15 using a value of $\phi = \pi/2$).

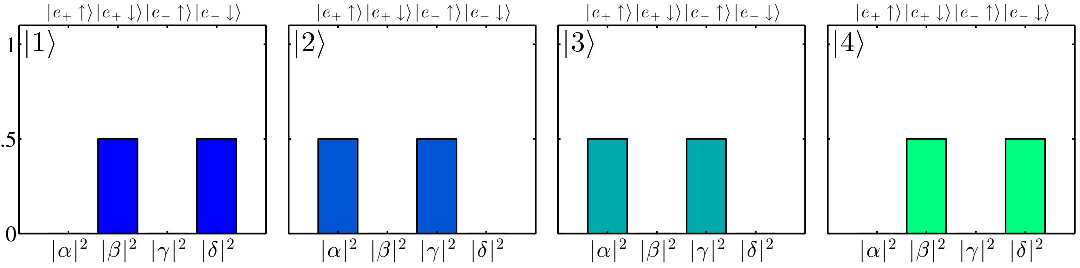

Figure 2.15: Eigenvectors $|1\rangle, |2\rangle, |3\rangle, |4\rangle$ of the SiV ground state under the perturbation of the JT-effect in the basis states $|e_\pm \uparrow, \downarrow\rangle$. The presentation of the states is equal to Fig. 2.9.

As we have stated earlier, we do not consider a quadratic JT coupling, thus, from the continuous minima in the potential surface, the electronic system is *open* to other distortions. One of these other distortions is the SO coupling. We apply SO coupling and JT interaction separately as two, *a priori* equally possible perturbation terms for the four-fold degenerate energy levels of the SiV center. We consider the joint effect of SO and JT interaction in the following section.

2.2.4 Joint effect of spin-orbit and Jahn-Teller interaction

As we have seen in the previous sections, both the spin-orbit (SO) coupling and the Jahn-Teller (JT) effect lift the orbital degeneracy of the e_g, e_u states. Owing to the particular constellation of the SiV symmetry and its electronic configuration, the SO coupling can be considered as a purely orbital interaction, as it does not induce spin mixing. Hence, it is reasonable to investigate the joint effect of the two interactions. Together, they split the formerly four-fold degenerate states into two sets of two-fold degenerate levels, hence we obtain two degenerate ground states and two excited states (Fig. 2.16a).

We define the parameter ΔE_g as the change in energy of the ^2e_g ground state due to a combination of spin orbit coupling λ_g and Jahn-Teller interaction Υ_g. One of the former degenerate orbitals is lowered by $\Delta E_g/2$, the other one is raised by $\Delta E_g/2$. The same applies to the excited state, where one orbital is lowered by the energy $\Delta E_e/2$, whereas the energy of the second orbital is increased.

The two ground and two excited electronic states of the SiV center give rise to four optical transitions – the typical spectral fine structure of the defect, which is observed at low temperature. Figure 2.16b shows the spectral fine structure for an ensemble of SiV defects in relative frequency units measured at 6.4 K (see also Sec.1.3.2). The parameters $\Delta E_{g,e}$ can be obtained from the fine structure spectrum by measuring the difference of the peak frequencies. With $\Delta E_{g,e}$ known, we parameterize the joint contribution of SO and JT interaction using the pseudo-polar coordinates $\theta_{g,e}$ and set the spin orbit coupling term

$$\lambda_{g,e} = \Delta E_{g,e} \cos(\theta_{g,e}). \tag{2.68}$$

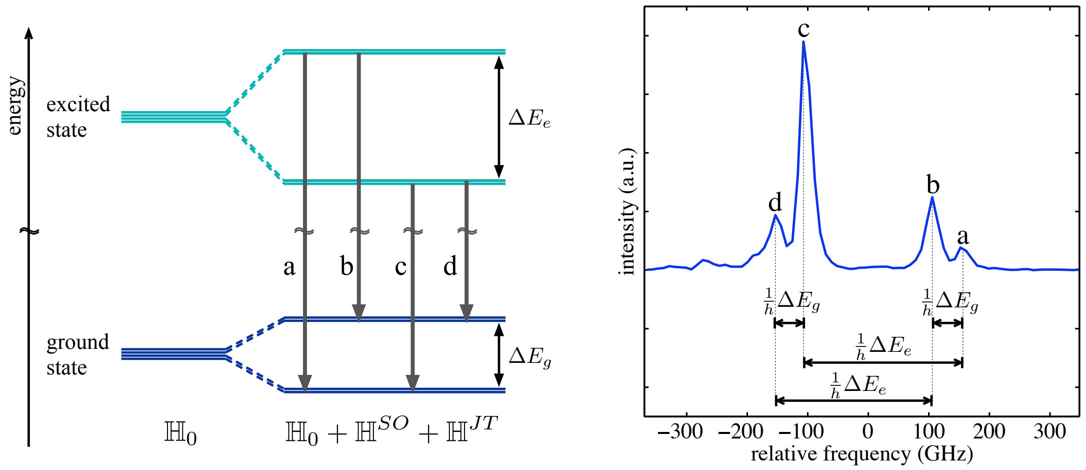

(a) (b)

Figure 2.16: The spin-orbit and Jahn-Teller interactions both lead to an orbital splitting in ground and excited state (panel a). We sum the joint effect of the two interactions in the parameters $\Delta E_{g,e}$. Panel b shows the spectral fine structure for an ensemble of SiV defects in relative frequency units measured at 6.4 K. The parameters $\Delta E_{g,e}$ are obtained from the fine structure spectrum of SiV centers by measuring the difference of the peak frequencies.

Additionally, the contributions $\Upsilon_{x,g,e}$, $\Upsilon_{y,g,e}$ of the Jahn-Teller effects along the x and y directions are also coupled using the parameters $\phi_{g,e}$ to keep their joint contribution to the level splitting constant:

$$\Upsilon_{x,g,e} = \tfrac{\Delta E_{g,e}}{2} \sin(\theta_{g,e}) \cos(\phi_{g,e}) \tag{2.69}$$

$$\Upsilon_{y,g,e} = \tfrac{\Delta E_{g,e}}{2} \sin(\theta_{g,e}) \sin(\phi_{g,e}). \tag{2.70}$$

This yields the total Jahn-Teller contribution $\Upsilon_{g,e}$, with $\Upsilon_g^2 = \Upsilon_{x,g}^2 + \Upsilon_{y,g}^2 = \frac{\Delta E_g}{4} \sin^2(\theta_g)$ (and analoguous for Υ_e) , and the overall ground and excited state splitting can be expressed by

$$\Delta E_{g,e} = \sqrt{\lambda_{g,e}^2 + 4\Upsilon_{g,e}^2}. \tag{2.71}$$

The complete orbital splitting, as it visible in low temperature spectra (Chap. 4), can therefore be calculated using only two parameters (θ_g and θ_e). Hence, we avoid over-parameterization of the simulation. To express the joint effect of SO and JT in more convenient manner, we calculate the fraction

$$r_{g,e} = \frac{\lambda_{g,e}}{\Upsilon_{g,e}}. \tag{2.72}$$

As we have seen, SO and JT interaction imply the electronic level splitting of the SiV defect and preserve the spin degeneracy. Hence, they readily describe the low temperature fine structure at zero magnetic field. However, the zero field fine structure spectra of the defect depend on $\sqrt{\lambda_{g,e}^2 + 4\Upsilon_{g,e}^2}$ and they do not indicate of the ratios $r_{g,e}$, so there would be a large ambiguity in the choice of the parameters. Furthermore, other theoretical models have been proposed to describe the fine structure, e.g. the tunnel-coupling model by Moliver [123], which in principle provides an equally valid description for the spectral fine structure (cf. Sec. 1.2.3). A key experiment in this work is the exposure of individual SiV centers to magnetic fields. Therefore we describe the effect of magnetic fields in the electronic states in Sec.2.2.6. The Zeeman effect splits magnetic sub-levels and it acts directly on the spin degree of freedom. Indirectly, the Zeeman effect also depends on the SO/JT-ratio $r_{g,e}$ as we will see later. Therefore, it helps to identify the ratio $r_{g,e}$ in good approximation and to clarify the electronic structure of the defect

Before we discuss the Zeeman effect and its spin dependent interactions, we mention a third, purely orbital interaction, which is crystal strain. There are large similarities between the JT interaction Hamiltonian $\mathbb{H}^{JT}$ and the Hamilton operator accounting for crystal strain, hence we discuss crystal strain first.

2.2.5 The effect of crystal strain

The interaction terms for spin-orbit and Jahn-Teller coupling, which we encountered in the previous sections, are assumed to be an "indigenous" part of the SiV electronic structure. In contrast, we consider the effect of crystal strain only in particular situations: Strain is defined as the deformation of a solid due to stress, where stress is given as a force per area. First, other imperfections can be present in the diamond. These imperfections distort the lattice, thus they create an internal stress which leads to a deformation (strain) of the crystal. In this first case, the resulting strain can also be considered as an intrinsic perturbation of the electronic states. It is one of the main objectives of the present work, to observe individual SiV centers *free* of this intrinsic strain. In addition, we discuss individual SiV centers subjected to strained environments in diamond nanocrystals in Sec. 4.3.

Second, crystal strain can be present on purpose: The application of uniaxial stress – which leads to crystal strain – is a very common technique to identify the symmetry of a defect and thus, draw conclusions on the electronic structure. Therefore, there exists a large number of both theoretical and experimental reports on defects in solids exposed to uniaxial stress (see e.g. [38]). We need to distinguish between two effects, when stress is applied: The individual centers of an ensemble are often oriented along different equivalent directions in the host crystal lattice, say along [111], [$\bar{1}$11], [1$\bar{1}$1] and [11$\bar{1}$]. All these sub-ensembles *a priori* have the same electronic properties as their environments are equivalent. We call this effect an *orientational degeneracy.* When crystal strain is applied along certain directions, it modifies these sub-ensembles differently and lifts the orientational degeneracy. This effect has been discussed e.g. by Kaplyanskii *et al.* [136].

In the present work, we restrict the discussion to one individual defect, hence, there is no orientational degeneracy. In addition to the orientational degeneracy, crystal strain can lift the orbital degeneracy, and it is this effect which we elucidate in more detail in this section. We assume in the discussion, that also intrinsic crystal strain can be explained in the framework of uniaxial strain. The effect of uniaxial stress on the degeneracy of orbital states has been discussed using group theory in many references (see the introduction of Ref. [164] for further information).

The perturbation $\mathbb{H}^{\text{strain}}$ of the electronic states of a defect under the influence of stress is given by a sum of the stress tensor components $\{\sigma_{ij}\}$ and electronic operators A_{ij} [164], i.e.

$$\mathbb{H}^{\text{strain}} = \sum_{ij} A_{ij}\sigma_{ij}. \tag{2.73}$$

Alternatively, the perturbation $\mathbb{H}^{\text{strain}}$ can also be written in terms of the strain tensor $\{\epsilon_{kl}\}$,

$$\mathbb{H}^{\text{strain}} = \sum_{kl} B_{kl}\epsilon_{kl}, \tag{2.74}$$

where stress creates strain, and the respective electronic operators A_{ij} are related by the elastic constants c_{ijkl} of the crystal according to

$$B_{kl} = \sum_{ij} A_{ij}c_{ijkl}, \tag{2.75}$$

with c_{ijkl} being a tensor of fourth rank, which is given in Ref. [165] for the diamond lattice. Both the stress and strain tensors are symmetric, hence $\epsilon_{kl} = \epsilon_{lk}$, and there are six B_{kl} (A_{ij}) operators. We define the suffixes i, j and k, l to run over the "internal" coordinates x, y, z of the defect (Fig. 2.1). These directions correspond to the unit vectors

$$\hat{x} = \frac{1}{\sqrt{2}}\begin{pmatrix}-1\\1\\0\end{pmatrix}, \qquad \hat{y} = \frac{1}{\sqrt{6}}\begin{pmatrix}-1\\-1\\2\end{pmatrix}, \qquad \hat{z} = \frac{1}{\sqrt{3}}\begin{pmatrix}1\\1\\1\end{pmatrix} \tag{2.76}$$

If uniaxial stress is applied externally, then we convert the components of the strain or stress tensor accordingly (see below). In the internal coordinate frame, we write the strain tensor as

$$\epsilon = \begin{bmatrix}\epsilon_{xx} & \epsilon_{xy} & \epsilon_{xz}\\ \epsilon_{xy} & \epsilon_{yy} & \epsilon_{yz}\\ \epsilon_{xz} & \epsilon_{yz} & \epsilon_{zz}\end{bmatrix}. \tag{2.77}$$

To calculate the energy shifts of the SiV levels, we calculate the matrix elements of $\mathbb{H}^{\text{strain}}$ between the e_g and e_u states. We remember that $e_{g,u}$ belong to irreducible representations of the D_{3d} point group. The idea for the calculation of the matrix elements is to express $\mathbb{H}^{\text{strain}}$ in a symmetry adapted form by choosing linear combinations of the ϵ_{ij}, such that the resulting sets ϵ_r belongs to the rth row of the the irreducible representation $\Gamma_{\text{IR}}^{(r)}$ [164]. The components ϵ_{ij} transform as the quadratic generating functions of the representations. For example, the sum $\epsilon_{xx} + \epsilon_{yy}$ transforms as $x^2 + y^2$ and therefore, as the totally symmetric representation A_{1g} in D_{3d} (cf. Tab. 2.3). Hence, we can rewrite Eq. (2.74) as

$$\mathbb{H}^{\text{strain}} = \sum_r \mathcal{B}_r \epsilon_r, \tag{2.78}$$

where the orbital operator $\mathcal{B}_r$ now also transforms as the irreducible representation $\Gamma^{(r)}$.

The linear combinations are calculated by projecting the ϵ_{ij} components onto the irreducible representations, similar to the projection of basis vectors which we showed in Sec. 2.1.4. As ϵ is a matrix in the basis of the spatial coordinates x, y, z, the projection formula is slightly different from Eq. (2.20). If ϵ_{ij} are the general components of the strain tensor (2.77), then we obtain the symmetry adapted linear combinations of strain components ϵ_r together with the operators $\mathcal{B}_r$ according to [157] as:

$$\mathcal{B}_r \epsilon_r = \frac{l_r}{h} \sum_R \chi^{(r)}(R)\ R^\dagger \,\epsilon\, R, \tag{2.79}$$

where R are the 3×3 transformation matrices (2.1) for the symmetry operations E, C_3^1, $C_3^2, \ldots$ applied to the unit vectors x, y, z, l_r is the dimension of the irreducible representation $\Gamma_{\text{IR}}^{(r)}$ and h is the order of the group. The characters $\chi^{(r)}(R)$ of these symmetry operations for the D_{3d} point group are listed in Tab. 2.3.

Application of Eq. (2.79) on ϵ with the operations R taken from matrices (2.1), yields that only $\epsilon_{A_{1g}}$ and ϵ_{E_g} are different from zero. Hence, the strain tensor in D_{3d} transforms as the irreducible representations $A_{1g} + E_g$. The symmetry adapted, electronic operators $\mathcal{B}_r$ are still 3×3 matrices which are written in the basis $\{|e_x\rangle, |e_y\rangle, |a\rangle\}$ [157]. Therefore, we omit the third row and column because we only consider the coupling between e-states [157], and we obtain the strain Hamiltonian:

$$\mathbb{H}^{\text{strain}} = \epsilon_{A_{1g}} \mathcal{A}_{1g} + \epsilon_{E_{gx}} \mathcal{E}_{gx} + \epsilon_{E_{gy}} \mathcal{E}_{gy} \tag{2.80}$$

with

$$\epsilon_{A_{1g}} = \tfrac{1}{2}(\epsilon_{xx} + \epsilon_{yy}) \qquad \epsilon_{E_{gx}} = \tfrac{1}{2}(\epsilon_{xx} - \epsilon_{yy}) \qquad \epsilon_{E_{gy}} = \epsilon_{xy} \tag{2.81}$$

and the matrices for the operators $\mathcal{B}_r$

$$\mathcal{A}_{1g} = \delta \begin{bmatrix} 1 & 0 \\ 0 & 1 \end{bmatrix} \qquad \mathcal{E}_{gx} = \alpha \begin{bmatrix} 1 & 0 \\ 0 & -1 \end{bmatrix} \qquad \mathcal{E}_{gy} = \beta \begin{bmatrix} 0 & 1 \\ 1 & 0 \end{bmatrix}. \tag{2.82}$$

The factors α, β, δ are scaling factors which describe the response of the SiV center to a strain contribution belonging to the representations A_{1g}, E_{gx}, E_{gy}, respectively. It is important to note, that the scaling factors are empirical and can be different for ground and excited state; for the sake of brevity, we omit the subscripts g, e for ground and excited state. For the further analysis, we ignore the A_{1g} term, as it leads to a global shift of the energy levels. Under this condition, the strain Hamiltonian transforms as the irreducible representation E_g alone.

The matrices in Eq. (2.82) are valid both for ground and excited state. Hence, to couple it to the electronic ground and excited state of the SiV center, we calculate the matrix elements $\langle e_{g,u}|\mathbb{H}^{\text{strain}}|e_{g,u}\rangle$ which correspond to direct products $E_{g,u} \otimes E_g \otimes E_{g,u}$. These direct products only contain the totally symmetric representation A_{1g} if the states exhibit the same parity. Consequently, the strain Hamiltonian couples the ground and excited states among each other, but there is no coupling between ground and excited state.

When strain is an intrinsic property of the diamond hosting a given SiV center, we have no means to determine the strength of the strain components ϵ_{ij} in Eq.(2.80). In this case, it is reasonable to omit these components and to fit the parameters α, β to the given data. We apply this procedure in Sec. 4.3 and obtain a high agreement between the strain model presented here and the experimental spectra.

If strain is created in uniaxial stress measurements, where the pressure applied to the sample is well calibrated, then the scaling parameters α and β can be deduced from the response of the defect to the strain field. We have stated above, that the strain components are given in the internal reference frame of the SiV center (Fig. 2.1). It is worth to briefly outline how the $\mathbb{H}^{\text{strain}}$ matrix elements are transformed, when we work in the "external" coordinate frame defined by the primitive cubic directions $\hat{e}_x = [1, 0, 0]$, $\hat{e}_y = [0, 1, 0]$, $\hat{e}_z = [0, 0, 1]$. In this case, we first perform a coordinate transformation, and then we apply Eq. (2.79). In this external coordinate frame, the SiV symmetry axis is rotated about 54.7° around the y-axis and about 45° around the z-axis. Hence for the coordinate transformation, we apply the rotation matrices $R_y(54.7^\circ)$ and $R_z(45^\circ)$ to ϵ, with

$$R_y(\theta) = \begin{bmatrix} \cos(\theta) & 0 & \sin(\theta) \\ 0 & 1 & 0 \\ -\sin(\theta) & 0 & \cos(\theta) \end{bmatrix} \qquad R_z(\phi) = \begin{bmatrix} \cos(\phi) & -\sin(\phi) & 0 \\ \sin(\phi) & \cos(\phi) & 0 \\ 0 & 0 & 1 \end{bmatrix}. \tag{2.83}$$

While the resulting operators $\mathcal{A}_{1g}$ and $\mathcal{E}_g$ remain unchanged, the symmetry adapted linear combinations of strain components are different. We refer to the SALCs in the external coordinate frame as $\tilde{\epsilon}_r$ and obtain:

$$\begin{aligned} \tilde{\epsilon}_{A_{1g}} &= A_1(\epsilon_{xx} + \epsilon_{yy} + \epsilon_{zz}) - 2A_1'(\epsilon_{xy} + \epsilon_{yz} + \epsilon_{xz}) \\ \tilde{\epsilon}_{E_{gx}} &= B(-\epsilon_{xx} - \epsilon_{yy} + 2\epsilon_{zz}) + C(-2\epsilon_{xy} + \epsilon_{yz} + \epsilon_{xz}) \\ \tilde{\epsilon}_{E_{gy}} &= \sqrt{3}B(\epsilon_{xx} - \epsilon_{yy}) + \sqrt{3}C(\epsilon_{yz} - \epsilon_{xz}). \end{aligned} \tag{2.84}$$

The pre-factors are chosen according to Hughes and Runciman [164], who obtain the same linear combinations. The same result has been obtained for the $E \to E$ transitions of a defect causing the 594 nm band in diamond [166]. We will make use of Eqs. (2.84) for the interpretation of the uniaxial stress measurements of Sternschulte *et al.* [133] in Chap. 5.

The strain Hamiltonian does not act on the spin degree of freedom. To express the matrix $\mathbb{H}^{\text{strain}}$ in the basis set (2.27) which includes the spin subspace, we calculate the direct product of the matrices in Eq. (2.82) with the 2 × 2 identity matrix:

$$\mathbb{H}^{\text{strain}} = \begin{bmatrix} \alpha & \beta \\ \beta & -\alpha \end{bmatrix} \otimes \begin{bmatrix} 1 & 0 \\ 0 & 1 \end{bmatrix} = \begin{bmatrix} \alpha & 0 & \beta & 0 \\ 0 & \alpha & 0 & \beta \\ \beta & 0 & -\alpha & 0 \\ 0 & \beta & 0 & -\alpha \end{bmatrix}. \tag{2.85}$$

To express $\mathbb{H}^{\text{strain}}$ in the eigenbasis of the spin-orbit Hamiltonian $\mathbb{H}^{SO}$ [Eq. (2.50)], we apply the transformation $(\hat{T}\otimes\mathbb{I}_2)\mathbb{H}^{\text{strain}}(\hat{T}\otimes\mathbb{I}_2)^{-1}$, where $\hat{T}$ is the transformation matrix of Eq. (2.47). In the $\{e_\pm\uparrow\downarrow\}$ basis, we obtain

$$\mathbb{H}_{\pm}^{\text{strain}} = \begin{bmatrix} 0 & 0 & -(\alpha+i\beta) & 0 \\ 0 & 0 & 0 & -(\alpha+i\beta) \\ -(\alpha-i\beta) & 0 & 0 & 0 \\ 0 & -(\alpha-i\beta) & 0 & 0 \end{bmatrix}, \tag{2.86}$$

which is identical to the strain Hamiltonian calculated for the E excited state of the 1.4 eV nickel defect in diamond, given in Ref. [167].

We return to the matrix representation $\mathbb{H}^{\text{strain}}$ in the $\{e_{x,y}\uparrow\downarrow\}$ basis set (Eq. (2.85). The eigenvalues and eigenvectors of $\mathbb{H}^{\text{strain}}$ are

$$+\zeta \rightarrow \begin{cases} \frac{1}{\zeta-\alpha}\left[\beta|e_x\downarrow\rangle + (\zeta-\alpha)|e_y\downarrow\rangle\right] = |u_+\downarrow\rangle \\ \\ \frac{1}{\zeta-\alpha}\left[\beta|e_x\uparrow\rangle + (\zeta-\alpha)|e_y\uparrow\rangle\right] = |u_+\uparrow\rangle \end{cases} \tag{2.87a}$$

$$-\zeta \rightarrow \begin{cases} -\frac{1}{\zeta+\alpha}\left[\beta|e_x\downarrow\rangle - (\zeta+\alpha)|e_y\downarrow\rangle\right] = |u_-\downarrow\rangle \\ \\ -\frac{1}{\zeta+\alpha}\left[\beta|e_x\uparrow\rangle - (\zeta+\alpha)|e_y\uparrow\rangle\right] = |u_-\uparrow\rangle, \end{cases} \tag{2.87b}$$

where $\zeta = \sqrt{\alpha^2+\beta^2}$. The resulting level splitting is depicted in Fig. 2.17, where we observe that the strain perturbation reduces the initial four-fold degeneracy to a two-fold degeneracy. The splitting constant ζ depends on the empirical parameters α and β, which can be different for ground and excited state. In consequence, the strain splitting in ground and excited can be different as well. We emphasize this point by writing ζ_g and ζ_e in Fig. 2.17. In case that $\zeta_g \neq \zeta_e$, we observe that the optical transitions do not only split with increasing strain but they also shift in frequency. This shift is increased when the factor δ for the A_{1g} strain term [cf. Eq. (2.82)] is also different for ground and excited state. Fig. 2.17 shows the effect of the strain splitting alone, a more detailed analysis, which takes into account the SO, the JT and the strain interaction, can be found in Sec. 5.1.1.

For the investigation of SiV center in strongly strained nanodiamonds, the strain interaction will be the leading perturbation (instead of the SO coupling) and it will be convenient to express the eigenvectors of the SiV electronic states in the basis vectors $\{u_\pm\uparrow,\downarrow\}$ of the strain Hamiltonian $\mathbb{H}^{\text{strain}}$. Equations (2.87) provide the transformation from the $\{e_{x,y}\uparrow,\downarrow\}$ to the $\{u_\pm\uparrow,\downarrow\}$ basis.

In this section we have covered the strain interaction as the third orbital perturbation. A fourth orbital perturbation – which however is beyond the scope of this work – would be the response to external electric fields, the Stark shift. It can be shown that the Stark shift acts on the same matrix elements as crystal strain does. Therefore, the Stark shift can compensate internal strain fields and re-establish optimum environments for individual defects in diamond. Electric fields help to tune the transition frequency of

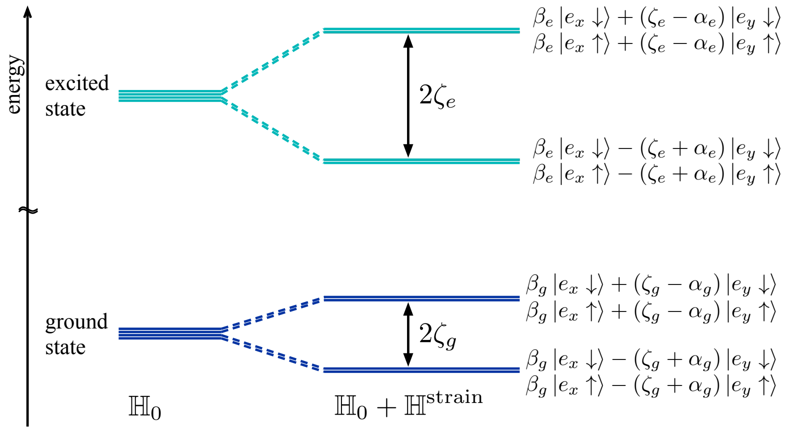

Figure 2.17: Strain splitting of ground and excited state. Similar to the spin-orbit and Jahn-Teller interaction, crystal strain splits the formerly four-fold degenerate levels into two two-fold degenerate branches. The splitting can be different for ground and excited state, thus we label the parameters α, β, ζ with the subscripts g, e. For the sake of brevity, we omit the global factors $\frac{1}{\zeta \pm \alpha}$ from Eq. (2.87).

individual defects [157, 168–170]. This technique has also been applied to tune emitters into resonance with either emitters to produce indistinguishable photons [49]. For the SiV center however, the linear Stark shift only couples states of opposite parity, i.e. it couples the excited states to the ground states in first order. Therefore, this coupling is expected to be small [171]. Very recently, indistinguishable single photons very obtained using two distant SiV centers [61], however, this experiment required a careful preselection of the SiV centers and no Stark shift tuning was employed.

In the following section, we investigate the perturbation caused by magnetic fields as a final interaction term present in the experiments of this work.

2.2.6 Magnetic Fields and the Zeeman effect

None of the interactions, which we discussed in the previous sections, introduced spin mixing to electronic states. In this section we cover the Zeeman effect, which as the only perturbation in this model causes superpositions of different spin projections. A key experiment in this work is the spectroscopy of individual SiV defects in magnetic fields. Exposed to a magnetic field, the Zeeman effect lifts the degeneracy of magnetic sublevels. The SiV center exhibits two magnetic moments, one created by the orbital angular momentum $\hat{\mathbf{L}}$, the other one the spin $\hat{\mathbf{S}}$. As we have seen in Sec. 2.2.2, the x- and y-components of the orbital angular momentum are zero and $\mathbb{H}^{SO} \propto L_z S_z$. We consider the Zeeman interaction for spin $\mathbb{H}^{Z,S}_{g,e}$ and orbit $\mathbb{H}^{Z,L}_{g,e}$ separately.

Therefore, the perturbation term for the Zeeman interaction is given by

$$\mathbb{H}^{Z}_{g,e} = \mathbb{H}^{Z,L}_{g,e} + \mathbb{H}^{Z,S}_{g,e} = \gamma_L \hat{\mathbf{L}} \cdot \mathbf{B} + \gamma_S \hat{\mathbf{S}} \cdot \mathbf{B}, \tag{2.88}$$

where $\gamma_{\mathrm{L}} = \mu_B/\hbar$, $\gamma_{\mathrm{S}} = 2\mu_B/\hbar$ are the orbital and electron gyromagnetic ratios, $\mu_B = 14.1$ GHz/T is the Bohr magneton, and the magnetic field $\mathbf{B} = (B_x, B_y, B_z)$, expressed in the internal reference frame of the SiV (Fig. 2.1). The spin operator $\hat{\mathbf{S}} = \frac{\hbar}{2}(\sigma_x, \sigma_y, \sigma_z)$ is expressed using Pauli spin matrices (2.42). As we have stated earlier, the orbital operator is $\hat{\mathbf{L}} = (0, 0, \hat{L}_z)$, and we can again simplify the orbital contribution to $\mathbb{H}^{Z,L}_{g,e} = \gamma_L \hat{L}_z B_z$.

In Sec. 2.2.2, we have derived that the orbital operator $\hat{L}_z$ transforms as irreducible representation A_{2g}. From the computational rules for the direct product (Tab. 2.8), we infer that the both direct products $E_g \otimes A_{2g} \otimes E_g$ (for the ground state) and $E_u \otimes A_{2g} \otimes E_u$ (for the ground state) contain the fully symmetric representation A_{1g}. Hence, group theory allows for non-vanishing matrix elements in ground and excited state. For many Zeeman measurement in the literature, the electron g-factor, which determines the gyromagnetic ratio, is set as a tensorial scaling factor, which then includes also the effect of the spin-orbit interaction [167]. In our case, we set the gyromagnetic ratios to 1 for the orbital part and to 2 for the spin part, because we treat the spin-orbit interaction as a separate perturbation. Therefore, the Zeeman perturbation $\mathbb{H}^{Z}_{g,e}$ is identical for ground and excited state.

We have seen in Sec. 2.2.3 that the linear, dynamic Jahn-Teller coupling leads to a delocalization of the electronic wave function in the adiabatic potential surface. We have introduced the Ham reduction factor to account for a quenching of electronic properties such as the orbital momentum or the orbital g-factor [163, 172]. To account for this effect, we introduce a quenching factor q which however only acts on γ_L and not on the spin-orbit coupling constant $\lambda_{g,e}$. It is possible that the present SO coupling constant $\lambda_{g,e}$ is already diminished because of a quenched orbital momentum, and $\lambda_{g,e}$ would be even larger without quenching present.

Taking into account all these issues, we write $\mathbb{H}^{Z}_{g,e}$ in the basis $\{e_{x,y} \uparrow, \downarrow\}$ given in Eqs. (2.27):

$$\begin{aligned}
\mathbb{H}^{Z}_{g,e} &= q\gamma_L \hat{L}_z B_z + \gamma_S \hat{\mathbf{S}} \cdot \mathbf{B} \\
&= q\gamma_L \begin{bmatrix} 0 & 0 & iB_z & 0 \\ 0 & 0 & 0 & iB_z \\ -iB_z & 0 & 0 & 0 \\ 0 & -iB_z & 0 & 0 \end{bmatrix} \\
&\quad + \gamma_S \begin{bmatrix} B_z & (B_x - iB_y) & 0 & 0 \\ (B_x + iB_y) & -B_z & 0 & 0 \\ 0 & 0 & B_z & (B_x - iB_y) \\ 0 & 0 & (B_x + iB_y) & -B_z \end{bmatrix}
\end{aligned} \tag{2.89}$$

An important consequence of the Zeeman Hamiltonian (2.89) is the mixing of $\uparrow, \downarrow$ spin projections due to the terms $B_x \pm iB_y$ on the off-diagonal matrix elements. However, if we align the magnetic field with the high symmetry axis of the SiV center, i.e. along the $\langle 111 \rangle$ crystal axis, then $B_x = B_y = 0$ and no spin mixing is expected. We verify these predictions in Secs. 4.1.4 - 4.2.2.

The four eigenvalues of $\mathbb{H}^{Z}$ are $E^{Z} = \pm q\gamma_L B_z \pm \gamma_S B$, where $B = \sqrt{B_x^2 + B_y^2 + B_z^2}$ is the absolute value of the magnetic field. As we expect it, the Zeeman effect splits all magnetic sublevels and this splitting is linear in B. In the experimental geometry in Chap. 4, the magnetic field is aligned along the [001] crystal axis and the SiV high symmetry axis is oriented in [111] direction, hence $B_x = B_y = B_z = \frac{B}{\sqrt{3}}$. In Fig. 2.18a, we depict the $\mathbb{H}^Z$ eigenstates in dependence of the magnetic field for ground and excited state. The graph shows how we expect the energy levels of the SiV to split when exposed to a magnetic field. With the perturbation $\mathbb{H}^Z$ alone, we have not included any orbital splitting, therefore all ground and excited states in Fig. 2.18a start to split from one point.

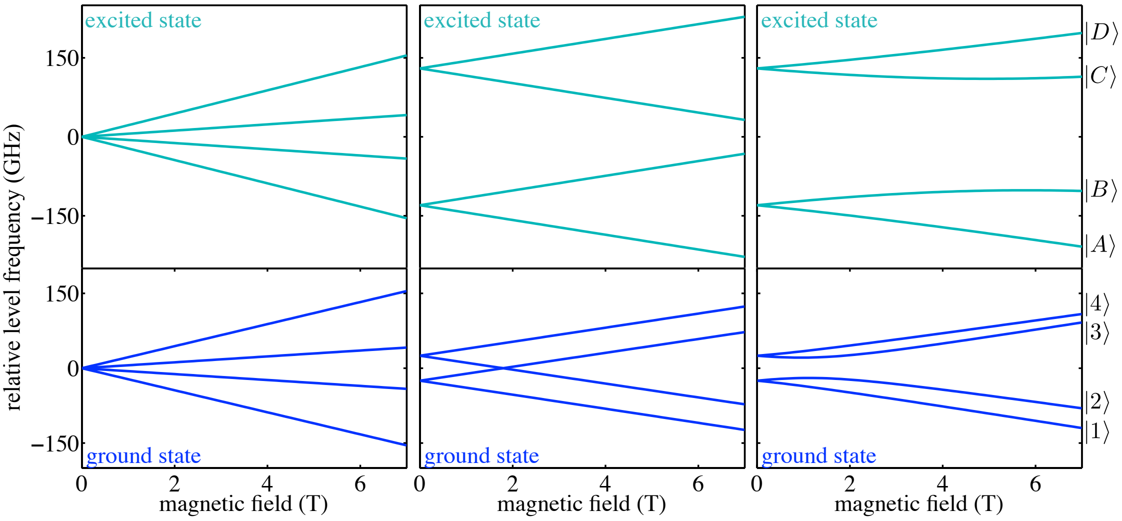

(a) Zeeman interaction only (b) Zeeman and JT interaction (c) Zeeman and SO interaction

Figure 2.18: The energy levels for ground and excited state as resulting from (a) the Zeeman effect only, (b) the Zeeman effect in combination the JT interaction and (c) the Zeeman effect with SO coupling. The zero-field splittings in (b),(c) correspond to the typical fine structure splitting. In panel (a), we set the quenching factor of the orbital magnetic moment to $q = 1$. In panels (b),(c), q is set to the value observed in the experiment ($q = 0.1$) and the magnetic field has a relative angle of 54.7° to the SiV high symmetry axis.

However, we know that the SiV center exhibits an orbital splitting which is caused by a combination of the SO coupling and the JT effect. Thus, it is interesting to calculate the eigenstates of the Zeeman Hamiltonian together with the SO and JT interaction. We consider two border cases here: First, if the JT interaction is much stronger than the SO coupling, then their ratio is $r = \frac{\lambda}{\Upsilon} \ll 1$, and the orbital splittings are $\Delta E_{g,e} \approx 2\Upsilon_{g,e}$ (c.f.

Sec. 2.2.4). The four eigenvalues of $\mathbb{H}^Z + \mathbb{H}^{JT}$ (without the subscripts g, e) are given by

$$\begin{aligned}
E_1^{Z,JT} &= \gamma_S B + \sqrt{\tfrac{1}{3}\,(q\gamma_L B)^2 + \Upsilon^2} \\
E_2^{Z,JT} &= \gamma_S B - \sqrt{\tfrac{1}{3}\,(q\gamma_L B)^2 + \Upsilon^2} \\
E_3^{Z,JT} &= -\gamma_S B + \sqrt{\tfrac{1}{3}\,(q\gamma_L B)^2 + \Upsilon^2} \\
E_4^{Z,JT} &= -\gamma_S B - \sqrt{\tfrac{1}{3}\,(q\gamma_L B)^2 + \Upsilon^2}
\end{aligned}$$

where we wrote the B-field as shown above, and neglected the SO coupling constant λ. We illustrate the resulting level splitting for ground and excited state in dependence of the magnetic in Fig. 2.18b. As we expect it, the JT coupling constant $\Upsilon_{g,e}$ in Fig. 2.18b leads to a zero-field splitting proportional to $\Upsilon_{g,e}$. In Fig. 2.18 we have employed the actual experimental values for the zero-field fine structure splitting which are within our experimental resolution $\Delta E_g = 2\Upsilon_g \approx 50$ GHz and $\Delta E_e = 2\Upsilon_e \approx 260$ GHz. For the quenching of the orbital magnetic momentum, we employed the value $q = 0.1$ which we determine from the experimental spectra in Chap. 4. We observe that the level splitting in Fig. 2.18b is still linear in B and that the ground states cross at about $B = 2$ T in this simulation.

Second, we investigate the other border case, with the SO coupling being much stronger than the JT effect. Hence, we set $r = \frac{\lambda}{\Upsilon} \gg 1$, and the orbital splittings are $\Delta E_{g,e} \approx \lambda_{g,e}$. Now, we neglect the JT coupling constant Υ and obtain the eigenvalues of $\mathbb{H}^Z + \mathbb{H}^{SO}$,

$$\begin{aligned}
E_1^{Z,SO} &= -\tfrac{1}{3}\,q\gamma_L B_z - \sqrt{\gamma_S^2 B^2 + \tfrac{2}{\sqrt{3}}\,\gamma_S \lambda B + \lambda^2} \\
E_2^{Z,SO} &= \tfrac{1}{3}\,q\gamma_L B_z - \sqrt{\gamma_S^2 B^2 - \tfrac{2}{\sqrt{3}}\,\gamma_S \lambda B + \lambda^2} \\
E_3^{Z,SO} &= \tfrac{1}{3}\,q\gamma_L B_z + \sqrt{\gamma_S^2 B^2 - \tfrac{2}{\sqrt{3}}\,\gamma_S \lambda B + \lambda^2} \\
E_4^{Z,SO} &= -\tfrac{1}{3}\,q\gamma_L B_z + \sqrt{\gamma_S^2 B^2 + \tfrac{2}{\sqrt{3}}\,\gamma_S \lambda B + \lambda^2}
\end{aligned}$$

The diagonalization of $\mathbb{H}^Z + \mathbb{H}^{SO}$ shows some similarities to the Breit-Rabi formula for the atomic Zeeman effect [173], however, the conclusions are less obvious than in atomic physics. The square-root with the term $\pm\frac{2}{\sqrt{3}}\,\gamma_S \lambda B$ also appears for spin-orbit coupled atoms, and it corresponds to interactions between atomic states of the same total momentum projection number m_J. It is responsible for the so-called *avoided crossings*. We depict the eigenstates $E_i^{Z,SO}$ for ground and excited state in Fig. 2.18c, where we now set the SO coupling constant $\lambda_{g,e}$ to 50 GHz and 260 GHz, respectively. Again, the orbital coupling (now λ instead of Υ) leads to a zero-field splitting. In contrast to the dominant JT interaction, the "inner" levels $|2\rangle, |3\rangle$ and $|B\rangle, |C\rangle$ do not cross anymore, but show avoided crossings. The two cases we illustrated above the indirect dependence of the Zeeman spectra on the purely orbital interactions: From the slopes of the level splittings, we can clearly distinguish the relative coupling strengths of SO and JT interaction. This tremendously reduces the amount of ambiguity in the choice of the orbital constants λ and Υ. Hence, comparing the response of the SiV energy levels to an actual magnetic field with the simulated eigenvalues allows for a clear assignment of the free parameters in the simulation.

Summary of the interaction terms

The preceding sections have introduced all relevant interaction terms acting on the degenerate e_g and e_u levels of the SiV center. The total Hamiltonian is written:

$$\mathbb{H}_{g,e} = \mathbb{H}^0_{g,e} + \mathbb{H}^{SO}_{g,e} + \mathbb{H}^{JT}_{g,e} + \mathbb{H}^{Z,L}_{g,e} + \mathbb{H}^{Z,S}_{g,e} (+\mathbb{H}^{\text{strain}}), \tag{2.90}$$

where $\mathbb{H}^0_{\text{g,e}}$ is the non-perturbed Hamiltonian, the spin-orbit Hamiltonian $\mathbb{H}^{\text{SO}}_{\text{g,e}}$ is given in Eq. (2.50), the Jahn-Teller matrix $\mathbb{H}^{JT}_{g,e}$ in Eq. (2.65) and the Zeeman terms $\mathbb{H}^{Z,L}_{g,e} + \mathbb{H}^{Z,S}_{g,e}$ in Eq. (2.89). The coefficients α, β in the strain Hamiltonian $\mathbb{H}^{\text{strain}}$ [given in Eq. (2.85)] are set to zero for SiV centers in low-strain environments, but will be non-vanishing for emitters in strained nanodiamonds.

Hence, Eq. (2.90) defines the secular matrix for the SiV center. Calculating the eigenvalues of this matrix yields the energies of all SiV levels in the given perturbation. The eigenvectors will be given in the $\{e_\pm \uparrow, \downarrow\}$ basis set of the SO eigenvectors, defined in Eq. (2.51). The free parameters, which are relevant for the eigenvalues, are the ratios $\theta_{g,e}$ between SO coupling and JT interaction (cf. Sec. 2.2.4) and the quenching factor q for the orbital magneton (cf. Sec. 2.2.6). If we add the effect of crystal strain, then also the parameters α and β are taken into account.

All the perturbation terms in Eq. (2.90) present interactions which act exclusively among states of ground or excited state manifold. For the calculation of optical transitions connecting the ground and excited state, we consider the dipole operator in the following section. The dipole operator imposes selection rules on the optical transitions, which we derive using the same group theoretical considerations as above.

2.3 Transition dipole moments and relaxation

The previous parts of this chapter, we have established the SiV energy levels in the given perturbations. In order to probe these levels, we observe transitions between them. Possible transitions are optical emission lines, which involve electric dipole transitions, or electron paramagnetic resonances, which act on the magnetic moments and relate to magnetic dipole transitions. We will exclusively focus on optical spectroscopy and determine the dipole matrix elements relevant for optical transitions (Sec. 2.3.1). From the selection rules of optical dipole transitions, the polarization of the emitted light is deduced. In the course of this work, we succeed in polarization measurements of single SiV centers, therefore, we introduce here the theoretical foundations to analyze this polarization data (Sec. 2.3.2).

Finally, we briefly investigate the transitions between the four excited states of the SiV centers. This *relaxation* can – from group theoretical considerations – not originate from dipole transitions. Instead, we derive a general orbital matrix which describes the relaxation process (Sec. 2.3.3).

2.3.1 Dipole transitions and selection rules

We have already encountered optical dipole transitions as a brief example in Sec. 2.2.1, and we here repeat the most important properties: The perturbation to the defect in a dipole transition is caused by the electric field amplitude $\mathcal{E}_0$ of the incident or radiated light and the electric dipole $\hat{\mathbf{p}} = -e\hat{\mathbf{r}}$ of the defect [1]:

$$\mathbb{H}_{\text{dipole}} = -\hat{\mathbf{p}} \cdot \mathcal{E}_0 = e\left(\hat{x}\mathcal{E}_x + \hat{y}\mathcal{E}_y + \hat{z}\mathcal{E}_z\right), \tag{2.91}$$

with $\mathcal{E}_0$ being the electric field amplitude of the absorbed or emitted light. The electric dipole $\hat{\mathbf{p}} = (\hat{p}_x, \hat{p}_y, \hat{p}_z)$ acts like an operator with respect to the group of Schrödinger's equation, thus we are interested in the matrix elements $\langle \hat{\mathbf{p}} \rangle = e\langle \psi_j | \hat{\mathbf{r}} | \psi_i \rangle$ (with $\psi_{i,j}$ belonging to the basis states (2.27) for the SiV center in particular). We have already seen in Sec. 2.2.1, that the dipole operator only couples states of different parity, and thus it connects the e_g ground and the e_u excited state of the SiV center.

The dipole operator only acts on the orbital part of the wave function. As the ground and excited states for the SiV center are two-fold orbitally degenerate, the dipole operators $\hat{p}_x, \hat{p}_y, \hat{p}_z$ are expressed as 2×2-matrices in the basis $\{e_{gx}, e_{gy}\}$ and $\{e_{ux}, e_{uy}\}$, i.e. we search matrix elements of the type

$$\begin{bmatrix} \langle e_{gx}|\hat{p}_x|e_{ux}\rangle & \langle e_{gx}|\hat{p}_x|e_{uy}\rangle \\ \langle e_{gy}|\hat{p}_x|e_{ux}\rangle & \langle e_{gx}|\hat{p}_x|e_{uy}\rangle \end{bmatrix}, \tag{2.92}$$

and similar for $\hat{p}_y, \hat{p}_z$. We employ group theory to determine which elements of this matrix are vanishing by symmetry considerations. According to the character table 2.3, the first row E_{gx} of the E_g representation, is generated by the basis orbital $e_{gx} \sim x^2 - y^2$ and the second row by $e_{gy} \sim xy$. The odd representation E_u is generated by $e_{ux} \sim x$ and by $e_{uy} \sim y$. Application of the $\hat{p}_x$-component of the dipole operator on e_{ux} yields $\hat{p}_x|e_{ux}\rangle \sim x^2$. A property depending on x^2 transforms as the first partner function e_{gx} of representation [2] E_g, hence the matrix element $\langle e_{gx}|\hat{p}_x|e_{ux}\rangle$ can be non-zero, while the matrix element $\langle e_{gy}|\hat{p}_x|e_{ux}\rangle$ involving the orthogonal basis function yields zero. Similarly, form the application of $\hat{p}_x$ on the second basis function of E_u, we obtain $\hat{p}_x|e_{uy}\rangle \sim xy$, which transforms as the second basis function e_{gy} of E_g, and the matrix element $\langle e_{gx}|\hat{p}_x|e_{uy}\rangle$ must again vanish. Hence, the $\hat{p}_x$-component of the dipole operator written in the form of matrix (2.92) is

$$\hat{p}_x = \begin{bmatrix} a & 0 \\ 0 & b \end{bmatrix}.$$

The exact values a, b depend on the precise choice of the coordinate frame and are given in various references [50, 174, 175]. We obtain the dipole operator in the $e_{x,y}$ basis:

$$\begin{array}{ccc} \hat{p}_x & |e_{ux}\rangle & |e_{uy}\rangle \\ \langle e_{gx}| & e & 0 \\ \langle e_{gy}| & 0 & -e \end{array} \quad \begin{array}{ccc} \hat{p}_y & |e_{ux}\rangle & |e_{uy}\rangle \\ \langle e_{gx}| & 0 & -e \\ \langle e_{gy}| & -e & 0 \end{array} \quad \begin{array}{ccc} \hat{p}_z & |e_{ux}\rangle & |e_{uy}\rangle \\ \langle e_{gx}| & e & 0 \\ \langle e_{gy}| & 0 & e \end{array}. \tag{2.93}$$

---

[2] Strictly speaking, x^2 transforms as the representations $E_{gx} + A_{1g} \sim x^2 - y^2 + x^2 + y^2$.

In order to add the spin degree of freedom to Eq. (2.93), we take the direct product of $\hat{p}_x, \hat{p}_y, \hat{p}_z$ with the 2×2 identity matrix, as we have done it previously for the strain Hamiltonian (Sec. 2.2.5). We consider the SiV defect to exhibit three separate, orthogonal dipoles X, Y, Z, which in our model are chosen along the vectors (2.76) in the diamond unit cell (cf. the red, green blue arrows in Fig. 2.19). The dipole strength of X, Y, Z is directly proportional to the expectation values $\langle \hat{p}_x \rangle, \langle \hat{p}_y \rangle, \langle \hat{p}_z \rangle$ which are calculated independently using Eq. (2.93) between the eigenstate $|A\rangle, \ldots, |D\rangle$ and $\langle 1|, \ldots, \langle 4|$ of the SiV center.

The probability P for an optical transition between the initial state φ_i and the final state φ_f is given by Fermi's golden rule

$$P = 2\pi\rho \left|\langle \varphi_f | e \cdot \hat{\mathbf{r}} | \varphi_i \rangle\right|^2 , \tag{2.94}$$

with ρ being the final density of states which we set to $\rho = 1$. With the dipole strength being directly proportional to the dipole matrix elements $\langle \hat{\mathbf{p}} \rangle$, the intensity for the respective dipole transition is therefore proportional to the probability P.

Using Eq. (2.94), we model the intensity of an optical transition between the states φ_i and φ_f. As we see later, the comparison of both the simulated polarization (Sec. 4.1.2) and the Zeeman spectra (Sec. 4.1.4) with the experimental data shows that the Z dipole strength $\langle \hat{p}_z \rangle$ is about an empirical factor of 2 larger than the dipole strength $\langle \hat{p}_x \rangle$, $\langle \hat{p}_y \rangle$ of the X, Y dipoles, respectively. Since the detected intensity scales with $|\hat{p}_z|^2$, this results in a factor of 4 for the Z dipole contribution in the polarization measurements. This factor of 4 was confirmed independently by measurements on a large number of SiV defects [176].

The empirical factor for the Z dipole strength can be explained as follows: The SiV center has D_{3d} symmetry (cf. Fig. 2.19). Without the perturbation terms from Secs. 2.2.2 - 2.2.6, the absolute values of the electron densities in the x- and y-direction are expected to be equal owing to the symmetry (cf. Sec. 2.1.4), and the XY dipoles have equal strength. However, the molecular shape of the SiV defect allows that the electron density is different along the z-direction, thus the Z dipole can have *a priori* a different strength. Group theory does not take into account the actual electron density, hence, we require this additional empirical factor for the Z dipole strength in the present case.

The preceding discussion yielded the relative intensity of an optical transition which gives rise to an emission line in a photoluminescence spectrum. The emitted electromagnetic wave is polarized, and this polarization is related to the dipole matrices (2.93). In the following section, we show explicitly which polarization components are contained in the emitted fluorescence of a given transition. For this discussion, we anticipate the results of the electronic state simulation which we obtain from the Zeeman spectra in Sec. 4.1.4.

2.3.2 Polarization of fluorescence light

As we will see later throughout this work, the spin-orbit interaction is the dominant perturbation for the SiV electronic structure at zero magnetic field. We have derived in Sec. 2.2.2, that the eigenvectors of the SO Hamiltonian are $e_\pm = \frac{1}{\sqrt{2}}(e_x \pm i e_y)$ (disregarding the spin degree). These states are depicted – together with the spin projections – in Fig. 2.8 on page 57. Hence, at zero magnetic field, we observe optical transitions between $e_{g\pm}$ ground and $e_{u\pm}$ excited states, and it stands to reason to transform the dipole operator matrix elements (2.93), which given are in the $e_{x,y}$ basis, into the $e_\pm$ basis. For simplicity, we omit the elementary charge e and obtain,

$$\begin{array}{c|cc|} \hat{p}_x & |e_{u+}\rangle & |e_{u-}\rangle \\ \hline \langle e_{g+}| & 0 & 1 \\ \langle e_{g-}| & 1 & 0 \end{array} \quad \begin{array}{c|cc|} \hat{p}_y & |e_{u+}\rangle & |e_{u-}\rangle \\ \hline \langle e_{g+}| & 0 & -i \\ \langle e_{g-}| & +i & 0 \end{array} \quad \begin{array}{c|cc|} \hat{p}_z & |e_{u+}\rangle & |e_{u-}\rangle \\ \hline \langle e_{g+}| & 2 & 0 \\ \langle e_{g-}| & 0 & 2 \end{array}, \tag{2.95}$$

where we scaled the matrix elements of $\hat{p}_z$ with the empirical factor 2 (cf. previous section). Hence, for an $e_{u\pm} \rightarrow e_{g\pm}$ optical transition, only the Z dipole is involved, and for this optical transition, the SiV center emits linearly polarized light. In a simple Hertzian dipole approximation, this linearly polarized light is emitted in directions perpendicular to the $z = \langle 111 \rangle$ high symmetry axis. In contrast, for an $e_{u\pm} \rightarrow e_{g\mp}$ transition we obtain a combined emission of $X \pm iY$ dipoles, which corresponds to $\sigma^\pm$ circularly polarized light. This circular polarization is emitted along the high symmetry axis.

As soon as we start to consider perturbation terms other than SO coupling, these simple polarization rules are not valid anymore. However, calculating the dipole matrix elements between the electronic states numerically is always possible. We note, that the X, Y, Z dipoles are given in the internal coordinate system [cf. Fig. 2.1 and Eq. (2.76)] of the SiV defect. In the experimental configuration employed in Chap. 4, the diamond sample is cut along the primitive $\{100\}$ planes, and the polarization is measured along the [001] direction.

Therefore, it is necessary to transform the emitted field amplitudes A_x, A_y, A_z of the transition dipoles X, Y, Z into the laboratory coordinate frame, in which we observe the sample from the (001) surface (Fig. 2.19b). We denote the projections of the dipoles in the laboratory frame as A_x^l and A_y^l. This transformation it consists of three matrices:

$$\begin{pmatrix} A_x^l \\ A_y^l \end{pmatrix} = \begin{bmatrix} 1 & 0 & 0 \\ 0 & 1 & 0 \end{bmatrix} \begin{bmatrix} \cos(\theta) & 0 & \sin(\theta) \\ 0 & 1 & 0 \\ -\sin(\theta) & 0 & \cos(\theta) \end{bmatrix} \begin{bmatrix} \cos(\phi) & -\sin(\phi) & 0 \\ \sin(\phi) & \cos(\phi) & 0 \\ 0 & 0 & 1 \end{bmatrix} \begin{pmatrix} A_x \\ A_y \\ A_z \end{pmatrix}. \tag{2.96}$$

First, we rotate the emitter reference frame into the lab coordinate system using a rotation of ϕ about the (internal) y-axis and a rotation of θ about the (internal) z-axis [cf. Eq. (2.83)]. Subsequently, we omit the third component of the field amplitude, as we only detect the transverse components A_x^l, A_y^l.

The angle θ denotes the polar angle between the external z axis (the optical axis) in the [001] direction and the internal z axis (the high symmetry axis of the emitter) along [111]. In cubic crystal symmetry, θ amounts to 54.7°. The angle ϕ is the azimuth angle between the main axis of the emitter and the external x axis. In our experiment we use diamond substrates with [110] edges, and therefore ϕ amounts to 0° (since the [110] crystal direction is the projection of the [111] direction onto the (001) plane). To calculate the signal measured by the polarization analyzer, we use the Jones calculus [177]. In this formalism the polarization of the light after traveling through a set of optical elements is calculated by multiplying the initial field amplitudes A_x^l and A_y^l with a specific transformation matrix for each optical element. The polarization analyzer used in this work consists of a rotating half-wave-plate in front of a fixed linear polarizer with a horizontal axis of transmission.

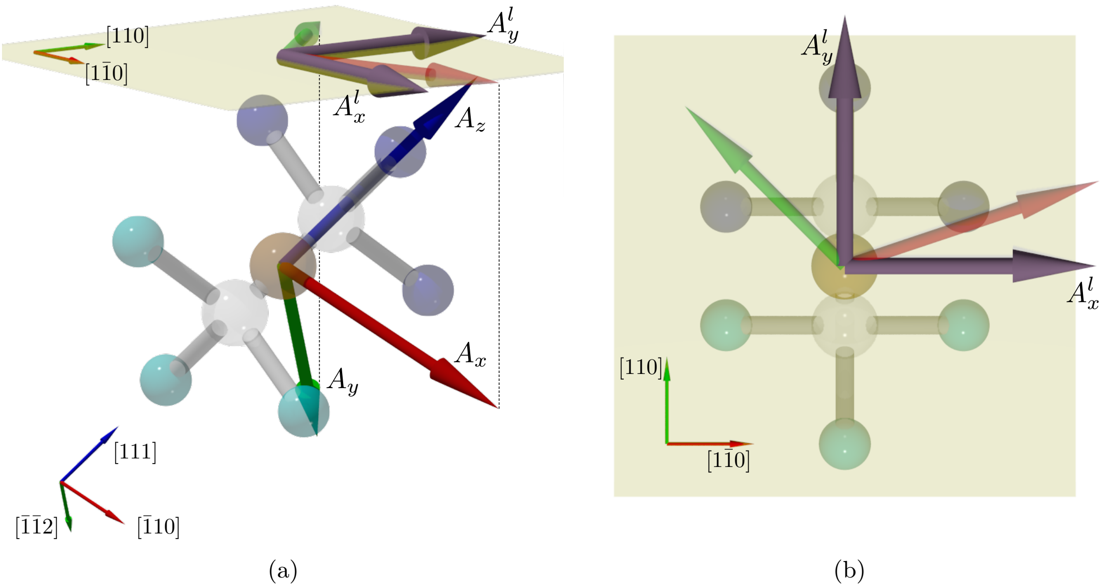

Figure 2.19: (a) The field amplitudes A_x, A_y, A_z of the dipole components X, Y, Z need to be projected from the internal reference frame to the external laboratory reference frame (A_x^l, A_y^l). The axes x, y, z are chosen according to Fig. 2.1. (b) Dipole components as seen in the laboratory frame.

The corresponding transformation is given in Eq. (2.97) in which the first matrix accounts for the linear polarizer, whereas the second matrix corresponds to the half-wave-plate, which is rotated about an angle φ.

$$\begin{pmatrix} A_x^f \\ A_y^f \end{pmatrix} = \begin{bmatrix} 1 & 0 \\ 0 & 0 \end{bmatrix} \begin{bmatrix} \cos(2\varphi) & \sin(2\varphi) \\ \sin(2\varphi) & -\cos(2\varphi) \end{bmatrix} \begin{pmatrix} A_x^l \\ A_y^l \end{pmatrix} \tag{2.97}$$

A plot of the sum of the absolute squares of the final field amplitudes A_x^f and A_y^f for a varying angle φ ($0^\circ < \varphi < 360^\circ$) yields the simulated polarization curve. We use this technique to explain the experimentally observed polarization curves of each fine structure line at zero magnetic field (Sec. 4.1.2).

The radiation of the X, Y, Z dipoles for an emitter close to the surface of a bulk diamond sample is not isotropic. In addition, the collection efficiency of the employed optical system is not uniform over all emitted wave vectors. Therefore, we employ a numerical method, briefly explained in Sec. 4.1.2 and Ref. [117], which introduces weighting factors for the different dipole contributions.

After having derived the selection rules for dipole transitions, we now have all elements available to simulate the spectroscopic experiments on the SiV fine structure. This includes measurements with or without magnetic fields and low- and high-strain samples. When we optically excite the SiV center, then the electron thermalizes among the excited state. This thermalization has been observed in optical spectra at zero-magnetic field in

Refs. [62, 137], and it is discussed briefly in Sec. 1.3.2. When we apply a magnetic field and lift the degeneracy of the spin states (Sec. 4.1.4), we observe that the thermalization shows a selectivity which we express in an relaxation operator in the following section.

2.3.3 Relaxation within the excited state

While we derived matrix representations for well-known perturbations in the previous sections, we now *propose* an interaction which we observe in the experiment, but whose origin in not yet determined. In Sec. 4.2, we show the systematic population of a given excited state. We observe that – prior to the radiative decay – the population thermalizes to other excited states. This thermalization is highly spin-dependent, i.e. states of opposite spin-projection do not thermalize among each other. A similar relaxation has been predicted for the nitrogen vacancy center in diamond. Doherty and Manson refer to this exchange of population among the ^3E excited states of the NV center as an *orbital averaging* [42]. They state, that this averaging is mediated by electron-phonon coupling and the thermalization is purely of orbital nature. However, they do not indicate the physical background of this coupling. Possible mechanisms are local vibration modes of the defect, as we have discussed them in Sec. 2.2.3, or the coupling to optical or acoustic phonons of the host lattice. Very recently, the population dynamics and the temperature dependence of the NV orbital averaging have been determined experimentally [178]. The authors of Ref. [178] state, that the observed temperature dependence agrees well with a two-phonon process. We briefly discuss in Sec. 4.2.2 which of these mechanisms might be likely to cause the thermalization for the SiV center. All the vibrational coupling terms have in common that they are operators acting exclusively on the orbital part of the wave function.

We have encountered two purely orbital interactions in this chapter – the Jahn-Teller effect and crystal strain. The resulting representations $\mathbb{H}^{JT}$ (2.65) and $\mathbb{H}^{SO}$(2.85) exhibit similar matrix elements. This similarity is by no means accidental, but is an expression of the Wigner Eckart theorem [132]: The matrix elements of a general tensor operator can be expressed in terms of a set of *reduced* matrix elements. The expressions for the reduced matrix elements are identical for all orbital tensor operators of the same symmetry [42], hence any orbital operator will always be constituted of the same "basis" elements. For example, the vibronic interaction $\mathbb{H}^{JT}$ of the Jahn-Teller effect transforms as the irreducible representation E_g, hence, we can express its matrix elements in the $\{e_{gx}, e_{gy}, e_{ux}, e_{uy}\}$ basis (2.27) of the SiV center as

$$\langle e_{g,x}|\mathbb{H}^{JT}|e_{g,x}\rangle = c[E||E_g||E], \tag{2.98}$$

with $[E||E_g||E]$ being the reduced matrix element and $c = c(g, x, y)$ being a factor (the Clebsch-Gordan coefficient). The Clebsch-Gordan coefficients have been tabulated in many group theory textbooks (see e.g. [132]), which simplifies the calculation of matrix elements to the trivial task of assigning the operators to irreducible representations. For the JT effect and the strain interaction, we had introduced scaling factors which implicitly contained the Clebsch-Gordan factors, therefore we did not mention them further. For a more general operator, we need to take them into account.

A general orbital operator $\hat{O}$ would – with the knowledge that we acquired in this chapter – transform as the irreducible representations $A_{1g} + E_g$, with the generating functions z^2 for A_{1g} and $(x^2 - y^2, xy)$ for E_g, respectively (cf. Tab. 2.3). The Clebsch-Gordan coefficients c can be calculated (if they are not given in a table) by the action of the operators $\hat{x}, \hat{y}, \hat{z}$ on the fundamental wave functions, i.e. the dangling bond orbitals σ_i (Fig. 2.5). We think of $\hat{x}, \hat{y}, \hat{z}$ as projections on the respective axes, i.e. $\langle \sigma_1 | \hat{x} | \sigma_1 \rangle = 1 = -\langle \sigma_1' | \hat{x} | \sigma_1' \rangle = -2 \langle \sigma_2 | \hat{x} | \sigma_2 \rangle$ and so on. The matrix elements depend on the choice of the coordinate system for x, y, z. In Sec. 2.1.4, we have derived the dependence of the basis functions a_{1g} and $e_{gx,y}$ on the σ_i (see Tab. 2.7), which determines the transformation for the operators $\hat{x}, \hat{y}, \hat{z}$ into the $\{a_{1g}, a_{2u}, e_{gx}, e_{gy}, e_{ux}, e_{uy}\}$ basis set. From this point, we can calculate the matrix representations for $\hat{z}^2, \hat{x}^2 - \hat{y}^2$ and $\hat{x}\hat{y}$ explicitly by simply multiplying the matrices for $\hat{x}, \hat{y}, \hat{z}$. Due to the 6×6 space, in which we calculate the representations $\hat{z}^2, \ldots$, this procedure is much more cumbersome than the determination of matrix elements using group theory, and it testifies the big advantages which we have drawn from group theory.

We obtain for the orbital operator in the subspace $\{|e_{ux} \uparrow\rangle, |e_{ux} \downarrow\rangle, |e_{uy} \uparrow\rangle, |e_{uy} \downarrow\rangle\}$:

$$\hat{O} = \hat{z}^2 + \hat{x}^2 - \hat{y}^2 + \hat{x}\hat{y} = \begin{bmatrix} 0.25 & 0 & -0.25 & 0 \\ 0 & 0.25 & 0 & -0.25 \\ -0.25 & 0 & 0.75 & 0 \\ 0 & -0.25 & 0 & 0.75 \end{bmatrix}. \tag{2.99}$$

The numbers in Eq. (2.99) appear somewhat arbitrary but they result from the particular choice of the x, y, z coordinate system (Fig. 2.1). Transformed into the spin-orbit coupled basis $\{|e_{u+} \uparrow\rangle, |e_{u+} \downarrow\rangle, |e_{u-} \uparrow\rangle, |e_{u-} \downarrow\rangle\}$, we denote the resulting matrix as the relaxation operator $\mathbb{P}^R$,

$$\mathbb{P}^R = \begin{bmatrix} 1 & 0 & \frac{1}{2}(1+i) & 0 \\ 0 & 1 & 0 & \frac{1}{2}(1+i) \\ \frac{1}{2}(1+i) & 0 & 1 & 0 \\ 0 & \frac{1}{2}(1+i) & 0 & 1 \end{bmatrix}. \tag{2.100}$$

Clearly, $\mathbb{P}^R$ does not couple any spin states, as we had constructed it. In Secs. 4.2.2 and 4.3.3, we calculate the matrix elements of $\mathbb{P}^R$ for the simulated SiV electronic states and compare them to the spin-selective relaxation mechanism. We stress that this comparison is rather qualitative as the origin of the internal mechanisms causing the relaxation are subject to debate. Still, we can draw important conclusion from it, as it also explains the excited state relaxation for strained defects (Sec. 4.3.3).

Summary of the theoretical considerations

With the relaxation operator, we have identified the last interaction which we consider relevant for the description of the SiV electronic structure as far as it concerns the experimental measurements in Chap. 4. We briefly summarize the most important results derived from the theoretical considerations of this chapter:

- The SiV center in the split vacancy configuration belongs to the D_{3d} point group. In this point group, the maximum orbital degeneracy of states is two (for the E_g and E_u representations).
- The electronic orbitals of the SiV defect are formed by symmetry adapted superpositions of the dangling bond orbitals. Group theory provides the mathematical background to determine these superpositions and to verify whether they couple to the atomic orbital of the central Si impurity.
- When filling the electronic states with electrons, we end up with even parity e_g ground states and odd parity e_u excited states. Furthermore, we identify the SiV center as a fermionic ($S = 1/2$) system. Both ground and excited state initially show a four-fold energetic degeneracy.
- The orbital degeneracy is lifted by the spin-orbit and the Jahn-Teller interaction. The spin degeneracy is lifted when we apply a magnetic field. We calculated explicit matrix representations for these interactions, and in addition, for the influence of crystal strain. The free parameters for these interactions are fitted to the experimental results of Sec. 4.
- From the comparison of the simulation with the experimental data, we obtain the eigenvalues and eigenvectors of the total Hamiltonian.
- The ground and excited states are connected via optical dipole transitions. From the matrix elements of the dipole operator $\hat{\mathbf{p}}$ linking the eigenvectors of the states, we can predict the polarization of a given optical line.
- When we excite the electron to the excited state, a thermalization takes place between the excited states. We introduced a phenomenological Hamiltonian to account for this relaxation.

An important part in the description of the molecular interactions is the contribution of crystal strain. We have seen, that strain acts on the orbital part of the wave function. When interpreting experimental results of samples where crystal strain is present, it is difficult to distinguish the strain contribution from the other orbital interactions. Thus, a central task in the course of this work was the fabrication of individual SiV centers in low strain diamond which showed sufficient brightness to be detected on a single emitter level. We will therefore investigate the sample fabrication and design of the confocal microscope in the following chapter.

Chapter 3

Experimental setup and sample preparation

This chapter covers the experimental setups utilized for measuring the low temperature optical spectra in Chap. 4. To locate and spectrally analyze individual SiV centers, we employ confocal microscopy. Therefore, we briefly review the concept of this microscopy technique in Sec. 3.1 and name the main figures of merit. Confocal microscopy has been realized in two experimental setups, which we characterize in Sec. 3.1.3.

After introducing both setups, we describe the fabrication of the diamond samples utilized in this work. Most of the research has been carried out using individual SiV defects in bulk diamond created by ion implantation. Hence, we explain the concept of ion implantation and specify the relevant figures of merit in Sec. 3.3. As defect centers in bulk diamond are known to feature relatively modest fluorescence count rates due to refraction effects and total internal reflection, we fabricated solid immersion lenses using focussed ion beam milling. Again, we briefly outline the technique, and subsequently present the fabricated structures as well as the resulting enhancement in collection efficiency.

3.1 Confocal microscopy

The basic idea, which distinguishes confocal microscopy from conventional microscopy, is to focus the excitation light tightly onto the sample, instead of illuminating the whole sample. As we will show in this section, this increases both the lateral and the axial resolution of a microscope. Although the main concepts are valid for all the different confocal techniques, we here consider confocal fluorescence microscopy, where we excite a sample to subsequently collect fluorescence photons. This section only gives a very brief summary over the technique. For a more comprehensive discussion, the reader is referred to the works of Webb [179] and Novotny, Hecht [180].

3.1.1 Principles of confocal microscopy

Figure 3.1 illustrates the very basic difference of confocal microscopy from ordinary microscopy. In an ordinary microscope, we uniformly illuminate the sample. The light being emitted from a point-like emitter A, situated in the focal plane (the object plane) of a lens, is imaged onto A' in the *image plane* of the lens (Fig. 3.1a). Emitter B, which is placed outside the focal point, is imaged to another point B' behind the image plane. Hence, in a conventional microscope, A' is observed as a sharp point whereas B' is blurry. If one places an aperture or a pinhole at a position conjugate to the focal point, all the light from A passes the pinhole, but the light of B is mostly rejected. This pinhole defines the *detection volume.* If we illuminate the sample with the focused light of a point source L such that only emitter A is excited and emits fluorescence, then the light of B is even weaker. The focused illumination defines the *excitation volume.* Hence, the point-like illumination L, the object A and the pinhole are said to be mutually confocal, and the case of Fig. 3.1c corresponds to a confocal microscope. The light of objects outside of the focal point is suppressed in two respects: First, these objects are less excited and even if they are excited, they are not imaged onto the pinhole. As a consequence, only a single point of the sample is detected behind the pinhole with a resolution superior to a conventional microscope. As a trade-off, the measurement of a two- or three-dimensional image requires the beam to be scanned over the sample (see below).

In an experimental realization, one often employs an infinity corrected objective lens instead of a single lens (Fig. 3.2). The fluorescence light is collimated and then focused onto the pinhole using a second lens. It is more convenient to focus the excitation light through the objective lens from the detection side. The excitation light is coupled onto the optical axis using a beamsplitter (either a glass plate or dichroic mirror). When exciting the sample with non-resonant wavelengths, the reflected laser light can be conveniently suppressed using optical bandpass filters. When employing laser excitation, the illumination point-source is often realized by sending the laser through an optical fiber. The narrow fiber core represents a very good spatial filtering for the laser mode. Similarly, the detection pinhole can also be implemented using an optical fiber.

3.1.2 Spatial resolution

In order to quantify the resolution of a confocal microscope, we introduce the notion of the *point-spread-function* or short *psf.* It determines the image pattern of a point-like object in the image plane of a microscope. For cylindrically symmetric optics and apertures, the *psf* is rotationally symmetric around the optical axis. To describe the functional dependence of the *psf* in cylindrical coordinates (z, r), we introduce the reduced (unit-less) variables $\zeta(z)$ and $\rho(r)$, which are defined by [179],

$$\zeta(z) = \frac{2\pi}{n\lambda} NA^2\, z, \qquad \text{and} \qquad \rho(r) = \frac{2\pi}{\lambda} NA\, r, \tag{3.1}$$

where $\zeta(z)$ describes the scaling along the optical axis and $\rho(r)$ the scaling transverse to it. The numerical aperture NA of the objective lens is defined as $NA = n \sin\vartheta$, where n is the refractive index of the medium (for us usually air, $n = 1$) and ϑ is the half angle of the cone of light diverging from point A into the first lens of the microscope. The reduced variables $\zeta(z)$ and $\rho(r)$ are both scaled to the wavelength λ of the emitted light. In the

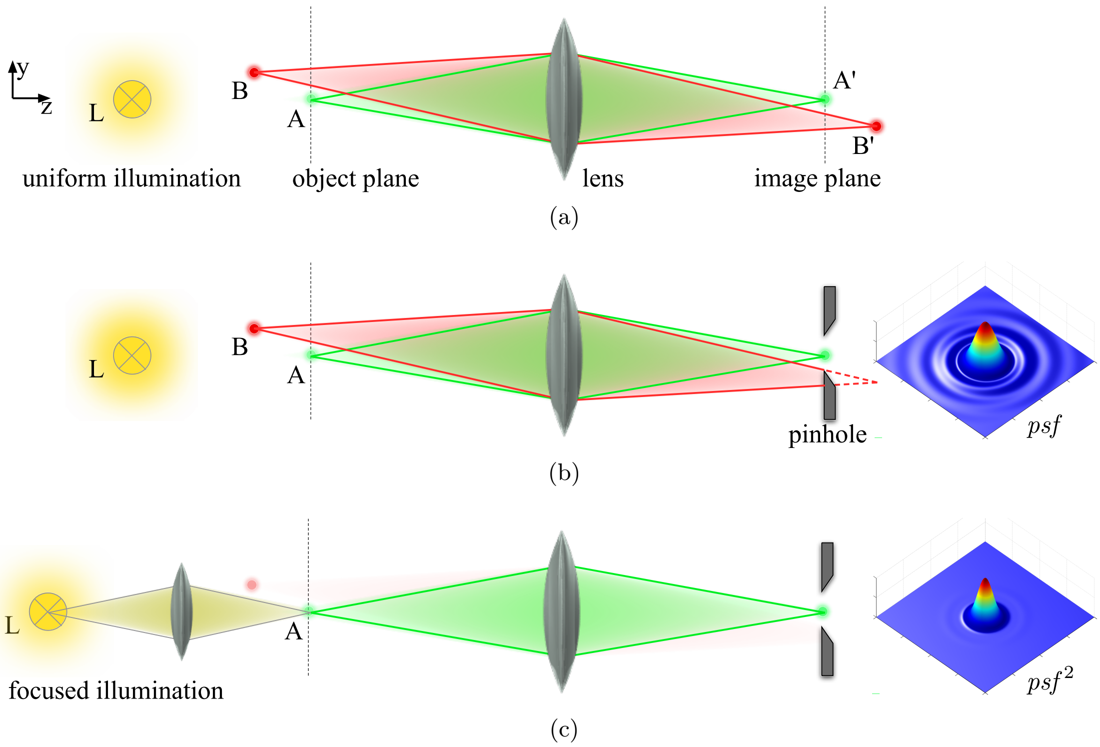

Figure 3.1: Image of two point-like emitters A and B on the image plane of a single lens resulting in the images A' and B'. In panels (a) and (b), both emitters are excited using a uniform illumination. In panel (b), we place a pinhole in the image plane, defining the *detection* volume on A'. In panel (c), the illumination is focused by an additional lens, defining the excitation volume. The insets on the right show the point-spread-functions for conventional (panel b) and confocal microscopy (c).

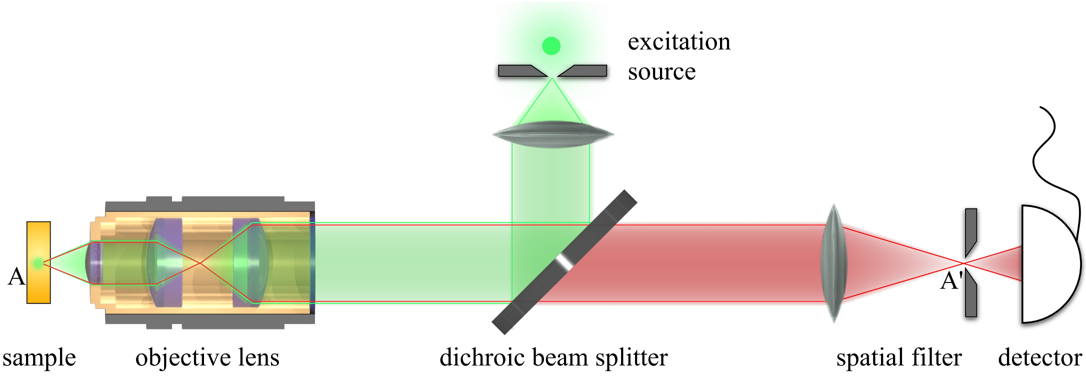

Figure 3.2: Schematic experimental realization of a confocal microscope in reflection geometry. The excitation light is reflected onto the optical axis of the microscope objective using a semitransparent or a dichroic mirror.

focal plane $\zeta = 0$, the *psf* is given by

$$\mathrm{psf}(\zeta = 0, \rho) = 2\left[\frac{J_1(\rho)}{\rho}\right]^2, \tag{3.2}$$

where $J_1(\rho)$ is a first order Bessel function [177]. The central maximum in Eq. (3.2) describes the so-called *Airy disc*, which has a radius ρ_{Airy} of

$$\rho_{\mathrm{Airy}} = 3.83 \qquad \text{or} \qquad r_{\mathrm{Airy}} = 0.61\frac{\lambda}{NA}. \tag{3.3}$$

Strictly speaking, the *psf* in Eq. (3.2) is only valid in the paraxial approximation, which usually is not satisfied when using high *NA* objective lenses. Yet, the overall form of the *psf* also remains valid in the general case [179]. In addition, the discussion above assumes that the pupil of the lens is fully filled with uniform irradiance. This criterion is usually not satisfied when exciting the sample with laser beams which exhibit a Gaussian transversal mode. Nevertheless, it can be shown, that for an excitation beam waist which overfills the lens aperture, the loss in resolution is very small [179]. Therefore, we employ the ideal shape of the *psf* [Eq. (3.2)] throughout the discussion.

Lateral and axial resolution for conventional microscopes Two luminescent point-like objects imaged from the object plane of a microscope give rise to two *psfs* in the image plane. We can resolve the two points, if their *psfs* are spatially separated. The minimum separation is given by the Rayleigh criterion, which states that the *psf* maximum of the second object needs to be at least in the minimum of the *psf* of the first object, i.e. the two *psfs* need to be displaced more than $\Delta r_{\mathrm{trans}} = r_{\mathrm{Airy}}$ from each other. It is equivalent to say, that the two *psfs* require to have a dip of 26 % of the maximum intensity between them. This defines the lateral resolution of a conventional microscope.

In a similar way, we can define the axial resolution of a conventional microscope. Along the optical axis, i.e. in ζ-direction, the *psf* depends of the sinc^2 of ζ,

$$\mathrm{psf}(\zeta, \rho = 0) = \left[\frac{\sin(\zeta/4)}{\zeta/4}\right]^2, \tag{3.4}$$

which corresponds to the diffraction pattern of a slit. When an aperture with a diameter of the (lateral) *psf* is placed in the image plane of a microscope (Fig. 3.1b), then two objects on different positions of the optical axis can also be distinguished, if their axial spacing amounts to

$$\Delta\zeta_{\mathrm{axial}} = 4\pi \qquad \text{or} \qquad \Delta z_{\mathrm{axial}} = 2\frac{n\lambda}{NA^2}. \tag{3.5}$$

However, this is called a “depth of focus criterion”, as the light of the second object will always contribute to the overall signal although it might be defocused [179]. Hence, this spurious light adds to the noise in the measurement and reduces the contrast in a microscope image. Confocal microscopy picks up at this point. We now analyze the resolution criteria as they result in a confocal geometry and state the actual differences to conventional microscopy.

Resolution for confocal microscopes In confocal microscopy (Figs. 3.1c, 3.2) , the excitation light is focused into a small volume of the sample. Only objects positioned in this *excitation volume* contribute to the fluorescence of the sample. The fluorescence is imaged by the microscope optics onto a pinhole in the image plane, which defines the *detection volume*. Hence, the excitation and detection volume are mutually confocal, thus they are summed up in the term *confocal volume*.

Analogous to the imaging of a point-like object onto the observation plane, the image of the excitation source onto the sample is also determined by a *psf*. When we consider the resolution of a confocal microscope, the *psf* for the excitation and the detection volume are convoluted [180]. If the excitation path uses the same optics as the detection path, then the *psf* for the confocal volume is simple the excitation or detection *psf* squared,

$$\mathrm{psf}_{\mathrm{conf}}(\zeta, \rho) = [\mathrm{psf}(\zeta, \rho)]^2. \tag{3.6}$$

Equation (3.6) can be seen as the product of the independent probabilities to focus light onto the excitation volume and to image this light out of the excitation volume onto the pinhole. As a result, the lateral resolution of a confocal microscope is given by,

$$\Delta\rho_{\mathrm{conf}} = 2.76 \qquad \text{or} \qquad \Delta r_{\mathrm{conf}} = 0.44\,\frac{\lambda}{NA}, \tag{3.7}$$

where we assume that the excitation wavelength λ_{exc} and the wavelength of the emitted fluorescence λ_{fluor} are approximately equal. The increased resolution is only part of the advantage of confocal microscopy. We display the confocal *psf* in the inset on the right of Fig. 3.1c. In the direct comparison to the simple *psf* created by the diffraction of a conventional microscope (Fig 3.1b), we observe that the higher order fringes are strongly suppressed in the confocal geometry. As a consequence, a dim object inside the confocal volume is better distinguishable from a brighter object just outside the confocal volume, because the bright one is less excited. Hence, while the resolution is only slightly increased, the contrast of the image tremendously improves when using confocal microscopy.

In addition, there is a “true” axial resolution for confocal microscopy. With the Rayleigh criterion above, we obtain the axial resolution, i.e. the distance $\Delta\zeta_{\mathrm{axial}}$ between two emitters to be separated,

$$\Delta\zeta_{\mathrm{axial,conf}} = 0.2\pi \cong 0.6 \qquad \text{or} \qquad \Delta z_{\mathrm{axial,conf}} = 1.5\,\frac{n\lambda}{NA}. \tag{3.8}$$

In contrast to the depth of focus for a conventional microscope, Eq. (3.8) is an actual resolution criterion. This means, an object e.g. $3\Delta\zeta_{\mathrm{axial}}$ away from the confocal volume is not just blurry (see above) but it is really suppressed, and thus does not spoil the signal-to-noise ratio. Hence, confocal microscopy can also be used to optically isolate objects inside a transparent sample. When scanning the beam over the sample, “slices” of the sample at different depths can be visualized this way. We will show in the following section, how confocal microscopy is realized in the experiments of this work.

3.1.3 Experimental setups

In this work, we employed two home-built confocal microscopes, one situated at the Saarland University in Saarbrücken, and the second one situated in the Cavendish Laboratory at the University of Cambridge. The former setup employs a liquid helium flow cryostat, whereas the setup in Cambridge employs a bath cryostat combined with a superconducting magnet. Hence, the apparatus in Saarbrücken is also denoted as the “flow cryostat setup”.

The flow cryostat setup

First, we describe the setup in Saarbrücken, which is depicted in Fig. 3.3.

Excitation light source The diamond samples are excited using a continuous-wave (cw) titanium-sapphire laser (ti:sapph, Sirah Matisse TX) which is tunable between 690 and 1000 nm. Throughout the experiments, the laser was tuned to 690 nm. The ti:sapph laser can be frequency stabilized using a Pound-Drever-Hall scheme [181], and achieves a line width of ≈ 50 kHz. The laser is pumped utilizing a cw, diode-pumped Nd:YVO4 solid state laser (DPSS) emitting at 1064 nm. The DPSS is internally frequency-doubled to 532 nm using a beta-barium borate (BBO) non-linear crystal, and operates at a maximum output power of 15 W at $\lambda = 532$ nm. With 10 W pump power, the ti:sapph laser at $\lambda = 690$ nm exhibits an output power of 500 mW. Using a combination of half-wave plates and polarizing beamsplitters (PBS), the DPSS pump laser can also be sent to another ti:sapph-laser (Spectra Physics Tsunami), which emits femtosecond pulses using an active mode-locking scheme. This laser can be employed to measure the fluorescence lifetime of SiV centers [182] which, however, is beyond the scope of this work.

Behind its Pound-Drever-Hall stabilization, the cw ti:sapph laser passes a neutral density filter wheel for the coarse adjustment of the laser intensity. Subsequently, a combination of a half-wave plate and a PBS allows the fine adjustment of the laser intensity. The laser is coupled into a single-mode optical fiber (SMF, core diameter ≈ 5 µm, Thorlabs SM600), using an aspheric lens of focal length $f = 11$ mm. As we stated above, the SMF acts as a spatial filter to suppress higher transverse laser modes, and we approximate the laser excitation to form a point-like illumination source, which we image onto the confocal volume.

Confocal microscope The light is guided to the confocal microscope part of the setup using the SMF mentioned above. The laser light emerging from the SMF is collimated to a beam waist of about 2.8 mm, using an aspheric lens of $f = 13.86$ mm focal length. This beam waist matches the entrance aperture of the microscope objective employed (see below). The excitation light first passes a PBS which transmits linearly polarized light (s-polarized, cf. Fig. 3.3), and a spectral bandpass filter (transmitting wavelengths between 685 and 695 nm). The bandpass acts as a clean-up filter to remove light which is shifted in frequency due to Raman scattering while traveling through the excitation SMF [183]. Behind the bandpass filter, the excitation light is sent to a glass plate inserted under 45° into the beam. The glass plate is a 90 : 10 beamsplitter which reflects 10 % of the excitation light onto the optical axis of the objective lens. It might appear disadvantageous to loose the vast majority of the excitation light, however, this loss can be compensated by simply increasing the laser power. Conversely, when sending the fluorescence light

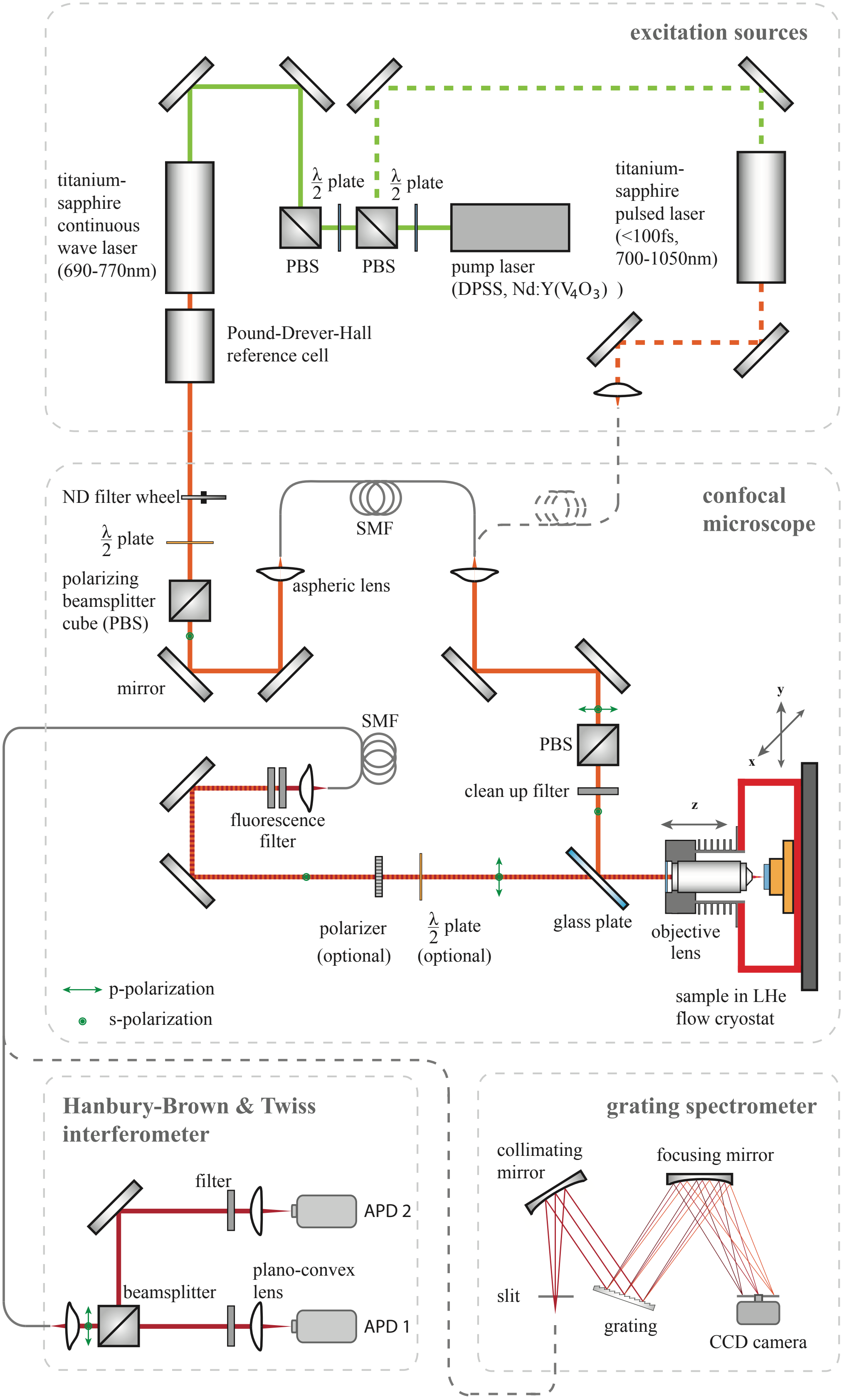

Figure 3.3: Schematic sketch of the flow cryostat setup located in Saarbrücken (taken from Ref. [169]). The beam path is described in the main text.

through the glass plate, the high transmission is an asset to maintain a high overall detection efficiency.

The objective lens (Olympus LMPLFLN100x) exhibits a magnification of a factor 100, a numerical aperture of $NA = 0.8$, and a working distance of 3.4 mm. The lens is mounted behind a sapphire window inside a flexible bellow in the isolation vacuum of a liquid helium flow cryostat. It is advantageous to place the lens inside the vacuum, as we avoid a loss in resolution, which typically occurs when focussing through the cryostat window. The objective lens sits on a linear translation stage (driven by stepper motors of 50 nm minimum step size) to change the distance between the objective lens and the sample, and thus, to vary the axial focus position in the sample. The sample is mounted on the cold finger of a liquid helium flow cryostat (Janis Research, ST-500LN). We move the whole cryostat in xy-direction using two linear translation stages. In this manner, the sample is scanned under the excitation laser beam to provide two-dimensional fluorescence images of the sample.

The emitted fluorescence of the sample is collected using again the objective lens, and is sent through the glass plate to the detection path of the confocal microscope. Using a second aspheric lens of $f = 13.86$ mm focal length, the fluorescence light is coupled into another SMF (SM600), in which it is guided to the grating spectrometer or the Hanbury-Brown & Twiss interferometer. To suppress laser light, which is reflected or scattered on the sample surface, we employ two dielectric longpass filters, which transmit wavelengths above $\lambda = 720$ nm. Optionally, a polarization analyzer can be placed before these longpass filters in the detection arm. The polarization analyzer consists of a half-wave plate in a motorized rotation mount, combined with a fixed polarization filter (Thorlabs LPVIS). The polarization analyzer is described in more detail in Ref. [184].

Grating spectrometer The fluorescence light emitted by the defects in the diamond sample is spectrally analyzed using a grating spectrometer (Horiba Jobin Yvon, iHR 550). The optical fiber which guides the fluorescence light to the spectrometer, is attached to a "fiber-port" which features two concave metal mirrors to focus the fluorescence onto the entrance slit of the fiber. The spectrometer is an imaging spectrometer, i.e. it images the entrance slit onto its detector. The focal length of this imaging corresponds to 550 mm. The detector is a charge-coupled device (CCD) with 1024 × 256 pixels (pixel width 50 µm). To decrease the noise-level of the recorded spectra, the CCD is cooled using liquid-nitrogen. The CCD camera is specified by the manufacturer to provide a detection efficiency of 90 % at a wavelength of 740 nm.

The spectrometer comprises three interchangeable diffraction gratings with 600, 1200 and 1800 grooves/mm, respectively. The resulting maximum resolution for the three gratings are approximately 0.22 nm for 600 grooves/mm, 0.1 nm for 1200 grooves/mm and 0.04 nm for 1800 grooves/mm. For details on the optical alignment of the spectrometer and the determination of its response function, we refer the reader to Ref. [73].

Hanbury-Brown Twiss interferometer Instead of sending the fluorescence light to the grating spectrometer, it can also be guided to the Hanbury-Brown Twiss (HBT) interferometer. The fluorescence is coupled into the HBT setup using an aspheric lens.

Subsequently, it is split into two beams by a non-polarizing 50 : 50 beamsplitter. The two beams are focused onto the active areas of two avalanche photon diodes (APDs, Perkin Elmer, SPCM-AQRH-14), using plano-convex lenses with $f = 50$ mm. A photon impinging on an APD creates an electron-hole pair in a semiconductor material, which in turn is multiplied in an avalanche process [185]. This electric signal ("click") is amplified to a TTL pulse which is registered using a fast time-correlated single photon counting system (PicoQuant PicoHarp). These electronics save the arrival times of the TTL pulses in a "click-list", which subsequently can be evaluated in order to calculate the photon count rate or the correlation between the two detector channels. The timing resolution of the photon arrival time is limited by the timing jitter of the APDs, which was measured to show a mean value of 354 ps per APD [73].

The APDs work similar to a Geiger-counter, i.e. they exhibit a dead time after an avalanche (typically 50 ns) in which no further photons can be detected. Furthermore, they cannot distinguish between one and several photons arriving at the same time. The APDs typically feature a quantum efficiency[1] of 65 % at 740 nm according to manufacturer specifications [73]. The detection efficiency is wavelength dependent, but besides this spectral dependence, the APDs do not discriminate different wavelengths. Hence, the detection window can be limited to a spectral interval by placing bandpass filters in front of each APD.

The HBT has two functions: On the one hand, it is used to record the intensity autocorrelation $g^{(2)}(\tau)$. For the principle of the $g^{(2)}$ function, we refer the reader to Sec. 1.3.3. On the other hand, the two APDs are utilized to record two-dimensional fluorescence images or "maps" of the sample. For this purpose, the sample is scanned in x- and y-direction while recording the photon count rates for each point of the scan. By putting two different bandpass filters in front of the APDs, two different spectral images of the same sample region can be acquired simultaneously (multispectral imaging, cf. Sec. 4.1.2).

The optical resolution of the flow cryostat setup At the beginning of this chapter, we have discussed the resolution of a confocal microscope, expressed in lateral and axial *psfs*. We now investigate the optical resolution of the flow cryostat setup and compare the experimental value to the theoretical limit. To obtain the lateral, experimental *psf*, we measure the fluorescence image of a fluorescent nanodiamond in x, y-direction (Fig. 3.4a). The nanodiamonds have a mean diameter of 130 nm, thus they are smaller than the wavelength of the emitted light (~ 740 nm). Hence, the nanodiamonds can be considered as point-like emitters, and their image produced by the optics corresponds to the experimental *psf*.

The fluorescence map in Fig. 3.4a shows two nanodiamonds positioned in proximity to each other. We draw cuts along the white dashed lines in x- and y-direction (blue dots in Fig. 3.4b,c). We add the theoretical *psfs* for the two emitters to the cross section graphs (red solid lines), where the confocal *psf* is given by the square of Eq. (3.2) using $\lambda = 0.73$ µm and $NA = 0.8$. Instead of using the Rayleigh criterion (Eq. (3.7)) for the

---

[1] Quantum efficiency is defined as the probability that an impinging photon is converted into an electric pulse by the APD.

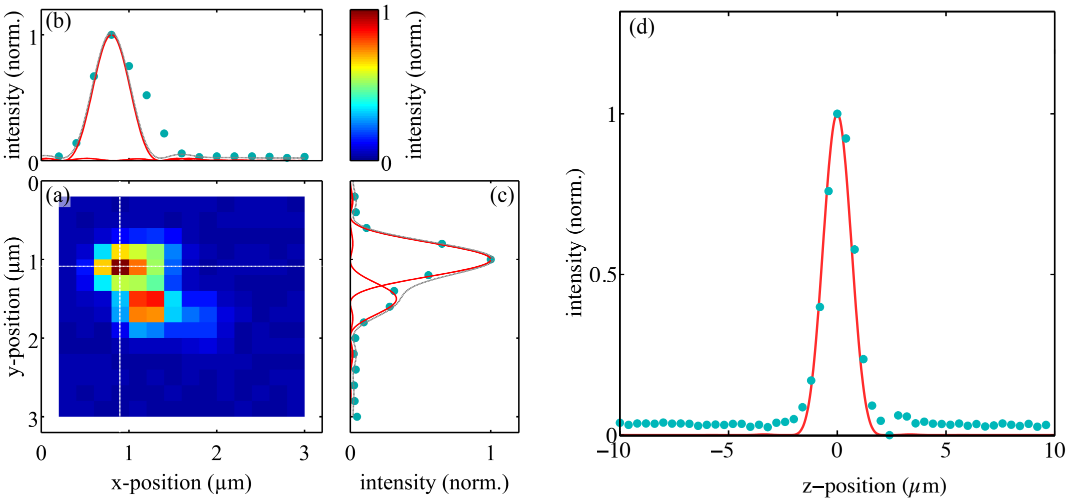

Figure 3.4: Fluorescence scans of a nanodiamond sample in order to specify the experimental *psf* (step size 200 nm). Two closely positioned nanodiamonds are imaged in x, y-direction (a) with a cross section cut along the white dashed lines through the x- (b) and the y-direction (c) as light blue dots. In panels (b,c), the red solid lines denote the theoretical *psf* for the two emitters in the confocal case [Eq. (3.2) squared]. The grey dashed line is the sum of the *psfs* for the two emitters. Panel (d) shows a scan of the laser focus of the top left nanodiamond, along the z-direction (step size 400 nm); the red solid line denotes the axial *psf* [Eq. (3.4) squared].

lateral resolution, it is more convenient to employ the FWHM of the theoretical *psf*, which is given approximately by $FWHM(psf_{\text{theo}}) = 340$ nm. For the y-direction, the theoretical *psf* agrees well with the measured data points, whereas in x-direction, the experimental *psf* is slightly larger than the theoretical limit. This deviation can arise from a slight misalignment along the x-direction. From Fig. 3.4a-c, we infer a lateral, experimental resolution of ~ 470 nm in x- and ~ 400 nm in y-direction, respectively. The values correspond to the FWHM of the data peaks in the cross section graphs.

For the resolution along the z-direction, the excitation laser was focussed onto the top left nanodiamond in Fig. 3.4a and scanned along the z-direction (Fig. 3.4d). The theoretical *psf* in z-direction is given by Eq. (3.4) squared (red solid line), and amounts to a FWHM of 1.48 μm. There is a high agreement between the theoretical and experimental *psf*. Figure 3.4 reflects the typical situation of two closely positioned objects, which however can be resolved to a high degree using confocal microscopy.

The bath cryostat setup

The second setup, situated at the Cavendish Laboratory in Cambridge, employs the very same principles as the first one. The main difference is the sample being placed in a helium bath cryostat, which also features a superconducting magnet. While the all principles of confocal microscopy, which we have introduced above, remain valid, this configuration has some technical consequences. A schematic view of the bath cryostat setup is depicted in Fig. 3.5.

Excitation light source Two different excitation lasers are employed: For non-resonant excitation and similar to the flow cryostat setup, a tunable titanium-sapphire laser (Coherent Mira), pumped again by a 532 nm DPSS laser (Coherent Verdi, set to 5 W) is utilized. The ti:sapph laser can either be operated in cw- or pulsed-mode (3 ps pulses at a repetition rate of 76 MHz). For the measurements presented here, operation at 700 nm in cw-mode was employed. For resonant excitation of the SiV zero phonon line, an external cavity diode laser (ECDL, Toptica, DL pro) at 737 nm is used. The diode laser employs a grating in Littrow configuration to select a single mode. It is tuned in wavelength using two mechanisms: For coarse tuning, the grating is rotated manually using a fine-threaded screw. For fine tuning, the grating is rotated by a piezo while simultaneously modulating the laser current ("feed forward"). The diode laser is frequency-stabilized to a wavelength meter (Highfinesse WSU10, 10 GHz absolute frequency resolution). Depending on the experiment, one of the two excitation lasers is coupled into a SMF and guided to the confocal microscopes.

Confocal microscope Similar to the flow cryostat setup, the excitation light passes a linear polarizer followed by a clean-up filter [(700 ± 5) nm bandpass] and is reflected towards the sample using a glass plate which is mounted at an angle of 45°. The excitation light which is transmitted through the glass plate is sent to a calibrated photodiode, which allows to measure the excitation power.

The sample is placed inside a tube, which is first evacuated to pressures below 10^{-5} mbar, then filled with approximately 50 mbar of dry helium for thermal contact. Subsequently, this exchange gas tube is lowered into a isolated vessel filled with liquid helium. This requires the first lens to be placed inside the exchange gas, which imposes high durability requirements on the lens. Therefore, no microscope objective is utilized, as the optical components inside the objective would deteriorate when being cooled to liquid helium temperatures. Instead, a single aspheric lens with a numerical aperture $NA = 0.6$ is employed. Due to the lower NA, we expect the fluorescence count rates from individual defects to be inferior as compared to the flow cryostat setup. Furthermore, an aspheric lens is susceptible to chromatic aberrations which necessitates a careful realignment when changing laser wavelengths. To accurately position the sample in the focus of the excitation laser, a set of XYZ translation stages (Attocube ANP) is used. The piezo-driven positioners employ the inertial sliding principle [186].

In addition, the cryostat features a superconducting magnet, capable of magnetic flux densities up to 7 T. The magnet coils are mounted such, that the magnetic field is aligned with the direction of the incoming excitation laser, the so-called Faraday configuration.

The fluorescence light is collected using the aspheric lens and transmitted through the glass plate. The glass plate under 45° induces a slight beam displacement, which is compensated using a second glass plate which is mounted perpendicular to the first on, i.e. under $-45°$. At this second glass plate, a fraction of the excitation laser is reflected towards a CCD camera. The CCD image of the reflected beam allows for a

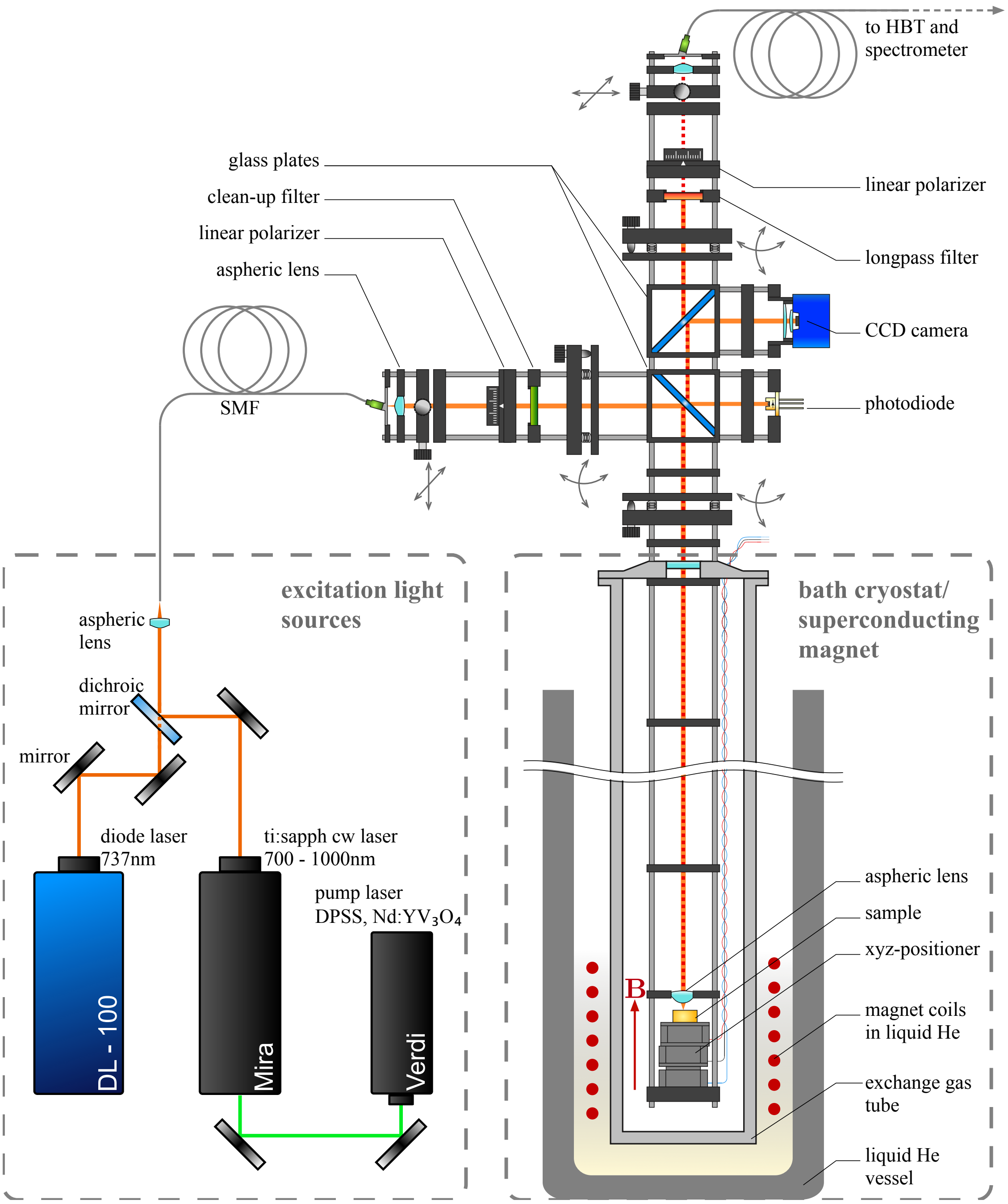

Figure 3.5: Schematic picture of the bath cryostat setup located in Cambridge. A further description is given in the text.

coarse positioning of the laser spot on the sample. When using non-resonant excitation of the SiV center at a wavelength of 700 nm, the remaining reflected laser is suppressed using a longpass filter, which transmits wavelengths $\lambda > 720$ nm. For resonant excitation, a second linear polarizer is placed in the beam path, which is set perpendicular to the incoming excitation beam and thus rejects the reflected laser light. For details on the crossed polarizer laser suppression see Ref. [64].

The fluorescence light is coupled into a single fiber and guided to either a grating spectrometer (PI Acton SpectraPro 2750 with Spec10 LN-cooled CCD camera) or to a Hanbury-Brown & Twiss interferometer. The two detection devices are analogous to the one in the flow cryostat setup, except that the spectrograph exhibits a focal length of 750 mm and thus features a higher spectral resolution (5 GHz measured using a grating with 1800 grooves/mm).

As we stated above, the two microscopy setups only differ in technical aspects. However, these technical differences suggest to dedicate the setups for complementary tasks: The flow cryostat shows a relatively high collection and detection efficiency and, in addition, can be extended to automated polarization measurements. Hence, we employ it for zero magnetic field spectroscopy and fluorescence polarization analysis. Furthermore, the measurement of the intensity autocorrelation $g^{(2)}(\tau)$ of individual SiV defects is performed using this setup. The bath cryostat setup provides magnetic fields to split magnetic sublevels and thus, is used to measure Zeeman spectra of SiV centers (Sec. 4.1.4). In addition, the bath cryostat setup is utilized to perform resonance fluorescence measurements.

3.2 Diamond samples

This section covers the diamond samples which host the SiV centers analyzed throughout this work. Afterwards, we review the creation of individual SiV centers in bulk diamond using ion implantation (Sec. 3.3) and the fabrication of solid immersion lenses to enhance the collection efficiency (Sec. 3.4).

All diamond samples in this work were fabricated using chemical vapor deposition (CVD). For the CVD process, a more detailed discussion can be found in Ref. [74]. In short, methane is dissociated using a reactive hydrogen plasma, and adsorbs covalently bound to existing carbon atoms. Due to the reaction kinetics, the process leads to a preferential creation of diamond, because other carbon modifications, such as graphite or diamond-like-carbon, are selectively etched. The degree of this selectivity is determined by the process parameters, which are the gas pressure, the substrate-temperature and the relative methane content. In addition, the choice of the substrate plays an important role: To date, single crystalline diamond can only be grown homoepitaxially, i.e. on existing single crystalline diamond substrates. Defects in the diamond lattice of the substrate, such as dislocations, stacking faults, point or line defects, are translated into the adsorbed diamond, and create crystal strain in the growth layer.

3.2.1 SIL sample

Impurities in CVD-grown diamonds emerge from contaminations of the process gases utilized, as well as from the contact of the reactive CVD plasma with parts inside the CVD

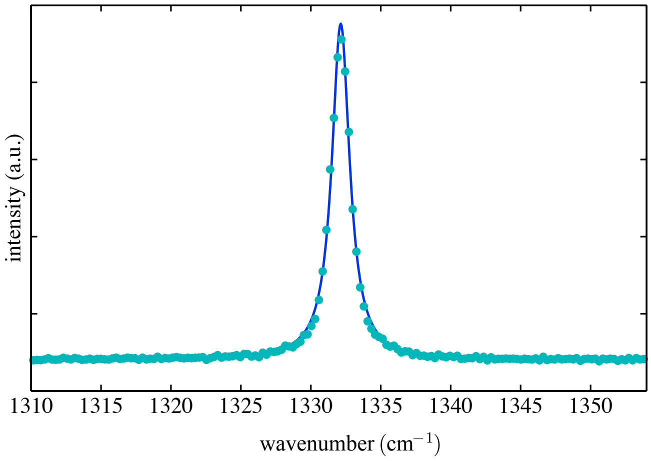

Figure 3.6: First-order Raman spectrum of the SIL sample. The light blue dots denote the experimental data, measured with the flow cryostat setup and the blue solid line is a fit using a Lorentzian peak function with a full width at half maximum of 1.55 cm^{-1}.

reactor. Using purified gas sources and minimizing the contact to the growth chamber, CVD diamonds can achieve high purity levels. One of the three diamonds which we present here was grown commercially (Element Six "electronic grade"), and is specified to contain substitutional nitrogen levels below 5 parts per billion (ppm) and a boron concentration of below 1 ppb according to the manufacturer. No other specifications on impurity levels of the diamond, such as Si contents, are given by the manufacturer and no information is provided on the growth process. However, preliminary experiments on the as-grown diamond using the flow cryostat setup showed no presence of SiV centers in the material. Hence, this sample is well suited for a controlled creation of individual SiV centers using ion implantation (cf. next section). An enhancement of the collection efficiency using solid immersion lenses (SILs) on this sample is presented in Sec. 3.4, thus, we term this sample the "SIL sample".

To reveal the electronic structure of the SiV center without the influence of crystal strain in the host diamond, we require diamond samples of high crystalline quality. One figure of merit for the crystalline quality of diamond is the width of the first order Raman peak. The Raman effect occurs as a consequence of inelastic scattering of the excitation laser in the diamond. For first-order Raman scattering, the excitation laser creates a vibrational quantum (a phonon) in the diamond, thus a part of the laser energy is absorpted by the phonon creation and the scattered light is shifted to longer wavelengths. Perfect diamond shows one optically active vibration mode, which is located at the center of the first Brillouin zone. Hence, for high crystalline quality diamond, the first order Raman spectrum consists of a single line shifted by a wavenumber of 1332.5 cm^{-1} with respect to the excitation laser [36]. This line can be broadened by the presence of defects in the lattice, resulting in an asymmetric peak shape [187]. Natural and synthetic HPHT diamonds show line widths between 1.7 cm^{-1} and 2.2 cm^{-1}, and high quality CVD diamonds were reported to lie in the range of 2.3 cm^{-1} [187]. The Raman spectrum of the SIL sample, given in the intensity of the scattered line versus the wavenumber, is depicted in Fig. 3.6. The spectrum was measured at $T = 30$ K using the flow cryostat setup (1800 grooves/mm grating in the spectrometer). The first-order Raman peak is fitted using a Lorentzian function with a full width at half maximum equal to FWHM $= 1.55\ \mathrm{cm}^{-1}$, which even surpasses the results in Ref. [187].

3.2.2 Ensemble sample

For the SIL sample, we imposed the condition that no defects are present in the as-grown diamond to provide a "pure" host material for implantation. For the two other samples presented in this work, we use the contamination inside the growth chamber on purpose to create SiV centers. The second sample is a thin CVD film, grown on a (001) high-pressure-high-temperature (HPHT) substrate of type Ib (Sec. 1.1). The HPHT substrate was preselected for low crystal strain and high surface quality to provide an ideal, unstrained environment for defects. The CVD layer was grown in a hot-filament CVD chamber, using a H_2:CH_4-ratio of 0.26 % and a slow growth rate (approximately 10 nm/h). It has been shown in Ref. [188], that a low methane concentration is advantageous for homoepitaxial growth, resulting in smooth sample surfaces and high crystalline quality. The sample showed a first order Raman peak width of 2.6 cm^{-1} [73], proving the high crystalline quality of the diamond.

The CVD growth chamber for the fabrication of the sample showed a contamination with silicon, as diamond growth on silicon was frequently performed in this chamber. The silicon atoms are etched by the reactive hydrogen plasma, and incorporated into the diamond layer. Hence, we observe an *in situ* doping of the thin film, resulting in an ensemble of SiV defects. For the sake of brevity, we simply call this sample the "ensemble sample". As neither the degree of the contamination, nor the efficiency of the doping process are unknown, a quantization of the Si concentration remains challenging for this sample. More details on the ensemble sample can be found in Ref. [189], [73] and [115].

3.2.3 Nanodiamonds

Nanodiamonds are a promising system for several applications of color centers. Their main advantage over bulk diamond is the enhanced extraction of fluorescence from the defects inside them. In bulk diamond, a large fraction of the emitted light is not irradiated towards the objective. This has two reasons (see also Sec. 3.3.4): First, the dipole emission pattern of a defect close to the interface of two dielectrics is not isotropic, but shows a preferential emission towards the higher index material [190]. Hence, most of the fluorescence is emitted away from the diamond surface. Second, total internal reflection at the surface limits the collection angle of the emission (cf. Sec 3.4).

Typically, nanodiamonds are smaller than the wavelength of the emitted light and can be considered as point-like emitters. As a result, they do not exhibit total internal reflection, which greatly improves the collection efficiency. However, placed on a high refractive index substrate, much of the radiation is still directed towards the substrate.

Nevertheless, placing the nanodiamonds on a reflective substrate, this light can partly be recovered.

Owing to the resulting brightness and the relatively modest complexity in their fabrication, nanodiamonds show a high potential for applications as room-temperature single photon sources. In addition, luminescent defects – in particular the SiV center – have been reported to show stable emission in nanodiamonds of sizes down to 2 nm [191]. In combination with their non-toxicity, the are promising candidates for fluorescence labeling of biological samples. The SiV center placed in nanodiamonds appears to be particularly promising because its emission at about 740 nm lies in the "biological window" where many biological tissues are transparent.

Nanodiamonds often originate from detonation diamond or from milled polycrystalline films [66]. Using centrifugation, different nanodiamond sizes can be separated. We here employ an advanced nanodiamond fabrication [56]: Synthetic detonation nanodiamonds are utilized as seeds to start the diamond growth in a CVD process. During the growth, an *in situ* doping with silicon creates individual SiV centers.

The nanodiamonds are grown on a stratified substrate, consisting of a 150 nm thin iridium layer, which was deposited on a 40 nm buffer layer of yttrium-stabilized zirconia (YSZ) on a silicon wafer [192]. Prior to the growth, the seed-diamonds, which are diluted in water, are spin-coated onto the substrate. We employ seed diamonds with a mean diameter of 17 nm (Microdiamant Liquid Diamond MSY). The seed density amounts to approximately 2.5 seed crystals per μm^2. The seeded substrates were subjected to a microwave-plasma-assisted CVD process for 25 min. The relative methane concentration is chosen to be 1% at a gas pressure of 30 mbar, and a microwave power of 2000 W was employed. Size characterization of the isolated nanodiamonds using scanning electron microscopy (SEM) showed a median of 130 ± 30 nm.

The silicon source for the *in situ* creation of SiV centers, is the silicon substrate employed for the growth of the nanodiamonds. As the surface of the substrate is covered with iridium and consequently, is not exposed to the CVD plasma, we assume the substrate edges as the main source of silicon. Nanodiamonds grown directly on silicon without a cover layer typically showed ensembles of SiV defects, whereas the nanodiamonds created in this process exhibited single SiV centers or none at all. The SiV centers created using this method showed the highest single photon count rates for color centers centers in diamond. A series of reports on individual SiV centers has been published by Neu *et al.* using these samples [56, 58, 73, 114–117].

Fluorescence properties of the nanodiamond sample We verified that the nanodiamond sample, employed in this work, shows fluorescence properties similar to the samples in the reports of Neu *et al.*. A typical fluorescence map of the sample, acquired at room temperature using the confocal microscope in Saarbrücken (cf. Sec. 3.1.3), is shown in Fig. 3.7. The sample was excited using 690 nm laser light, and the emitted fluorescence light was detected utilizing the HBT-setup with a 730 – 750 nm band pass filter in front of every APD. Nanodiamonds containing SiV centers are observed as bright, point like objects on the fluorescence map. The sample has been structured in order to provide position markers to relocate individual nanodiamonds. Circular Ag-markers (10 µm diameter, 100 nm height, 30 × 30 µm spacing) have been fabricated in a conventional lift-off process using photolithography.

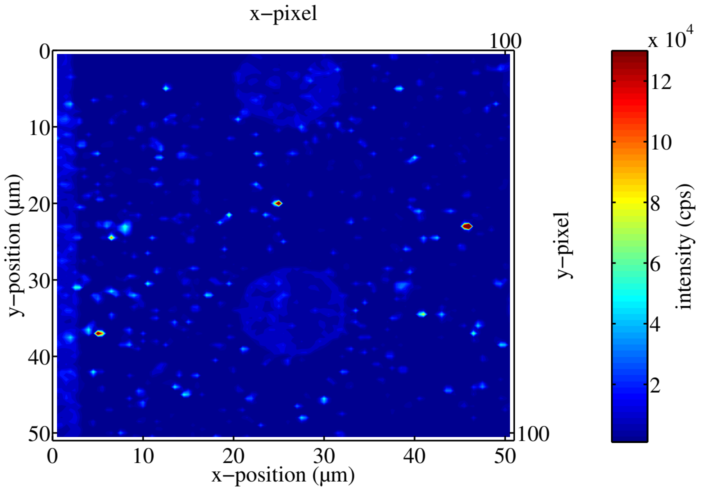

Figure 3.7: Fluorescence image of the nanodiamond sample, excited with 0.1 mW, 690 nm laser light and detection at 730 − 750 nm using the flow cryostat setup. The measurement was performed at room temperature. The sample has been structured with circular position markers.

The typical count rates observed in Fig. 3.7 are on the order of $10^4 - 10^5$ photons per second. Several emitters were investigated in more detail, revealing narrow zero phonon lines at ∼ 740 nm and saturation count rates in the range of 10^6 photons per second (not shown). Hence, the nanodiamond sample, employed in the present work shows properties comparable to earlier studies [56].

We employ the nanodiamonds in this work as a "test bench" for strained SiV centers. The crystalline quality of fabricated nanodiamonds depends – as for bulk diamond – on the choice of the growth parameters. The process parameters mentioned above were optimized to produce well-faceted crystallites. However, inherent defects in the seed diamond give rise to twinning and other faults of the grown crystal. These defects originating from the seed diamond lead to residual strain in the nanodiamond. As we will see later, strain results in a shift of the SiV zero phonon line (ZPL). For nanodiamonds similar to the ones used in this work, a statistical variation of the ZPL for different emitters was observed [56]. We make use of this strain to probe the SiV electronic structure in the presence of crystal strain to verify the theoretical model presented in the preceding chapter.

For individual defects without crystal strain, we create SiV centers using ion implantation in the SIL sample mentioned above. The method of ion implantation is described in the following section.

3.3 Ion implantation

We speak of ion implantation, when charged impurity atoms are accelerated onto a sample (a target) with a sufficiently high energy such that the ions enter the target and are incorporated at a given depth. On their trajectory through the material, the impurities collide with the target atoms and create lattice vacancies. Using thermal annealing after the implantation, the mobility of these lattice vacancies can be sufficiently increased to migrate to the impurities where defect complexes are formed. The most important parameters for ion implantation are the *fluence* which defines the resulting density of the impurities incorporated in the material, and the *ion energy* which mainly defines the stopping range and which is directly proportional to the acceleration voltage.

In the previous section, we discussed the *in situ* doping of samples during their growth. For this doping method, the incorporation mechanism, i.e. the addition of doping materials during growth, can also influence the growth mechanism and lead to e.g. different morphologies of the diamond sample. In contrast, ion implantation offers the possibility to characterize a given sample *before* and *after* incorporation of defects and therefore provides a highly deterministic way to incorporate defects. In addition, the resulting density of impurities is challenging to control for *in situ* doping and often requires to repeat the growth procedure with widely varying parameters. As the fluence of an ion beam can be measured from the charge deposited on the sample, the number of impurities is a well controllable parameter. Hence, ion implantation is a useful technique to deterministically place impurities in a well controlled environment. We briefly review a few theoretical concepts for implantation in diamond in the following paragraph and subsequently summarize the actual implantation experiment conducted in the RUBION institute in Bochum, Germany.

The downside of ion implantation is the occurrence of radiation damage in the sample. For diamond samples, this can lead to a graphitization of the irradiated surface. Hence, ion implantation requires a post-treatment of the sample in order to remove this residual damage. We discuss radiation damage and suitable annealing strategies in Sec. 3.3.3.

3.3.1 Calculation of the stopping range

When an charged particle penetrates a solid material, the ion gradually loses its energy due to scattering events in the target. We follow the argumentation outlined in Ref. [83]. The deceleration of the ion results from Coulomb interaction and can be divided into two contributions: The first one is the electronic energy loss which involves an interaction between the ion and the electrons of the target. The second interaction is between the ion and the nuclei of the target material.

In general, the effect of slowing down the ion is quantified using the *stopping power* ($\mathrm{d}E/\mathrm{d}x$), which is defined as the loss in energy $\mathrm{d}E$ per distance $\mathrm{d}x$, and which is given by

$$\frac{\mathrm{d}E}{\mathrm{d}x} = N \int T \mathrm{d}\sigma. \tag{3.9}$$

In Eq. (3.9), $\mathrm{d}\sigma$ denotes the collision cross section, T the loss of energy per collision event and N the density of scattering centers in the target [83]. Equation (3.9) relates to a stopping cross section $\mathcal{E}$ given by $\mathcal{E} = N^{-1}(\mathrm{d}E/\mathrm{d}x)$. As the total stopping of the ion depends on an electronic and a nuclear contribution, we write the total stopping power as

$$\frac{\mathrm{d}E}{\mathrm{d}x} = \left(\frac{\mathrm{d}E}{\mathrm{d}x}\right)_e + \left(\frac{\mathrm{d}E}{\mathrm{d}x}\right)_n = N(\mathcal{E}_e + \mathcal{E}_n), \tag{3.10}$$

with $\mathcal{E}_e, \mathcal{E}_n$ being the electronic and nuclear stopping cross sections, respectively. For the electronic contribution $\mathcal{E}_e$, the electrons are considered as a free electron gas which experiences a perturbation by the charge of the penetrating ion and in turn, exhibits a stopping force on the ion. This approach was published by Lindhard, Scharf and Schiøtt in 1963 [193] and hence is referred to as the LSS theory. The electronic stopping power is directly proportional to the velocity of the ion, or in other words, proportional to the square-root $\sqrt{E}$ of the kinetic energy E of the ion. The electronic stopping is dominant for higher ion energies, and has its maximum for the implantation of carbon in diamond at $E \approx 2$ MeV [83]. The LSS theory does not predict a deviation of the ion on its way through the crystal.

The nuclear contribution on the stopping power is dominant for lower energies (on the order of 10 keV). This interaction is provoked by the Coulomb interaction of the (positively charged) ion with the positive nuclei, where the ion and the scatter center are both approximated as point-like objects. As a result, the stopping cross section relates to a Rutherford scattering process. In contrast to the electronic contribution, the nuclear stopping leads to a change of the ion direction when scattered. In addition, it gives rise to the target atoms leaving their lattice site, thus creating vacancies.

The loss rate in Eq. 3.9 enables the calculation of the ion range R which can be considered as the mean track length of the ion before being completely stopped,

$$R = \int_{E_0}^{0} \frac{\mathrm{d}E}{(\mathrm{d}E/\mathrm{d}x)}, \tag{3.11}$$

where the integral limits range from the initial ion energy E_0 to zero. The ion range R is closely related to projected range R_p, i.e. the predicted depth below the surface of an ion. This range is not a sharp peak, but shows a statistical distribution owing to the statistical nature of the scattering events. The *implantation density* $n(z)$ along the direction of the beam is a Gaussian distribution centered at R_p and showing a width of σ_d:

$$n(z) = \frac{\phi}{\sigma_p\sqrt{2\pi}} \exp\left[-\frac{(z-R_p)^2}{2\sigma_p^2}\right]. \tag{3.12}$$

The implantation density $n(z)$ is directly proportional to the fluence ϕ, given in the number of ions per cm^2. Hence, we deduce that the main parameters, the fluence ϕ and the ion energy E, determine the density and the mean depth of the implantation, respectively.

Equation (3.12) provides an intuitive model of the underlying physics to understand the implantation profile, but it neglects e.g. channeling [83]. Therefore, the calculation of the integral in Eq. (3.11) and the resulting density is usually replaced by more sophisticated, numerical simulations. We employ the TRIM software (TRansport of Ions in

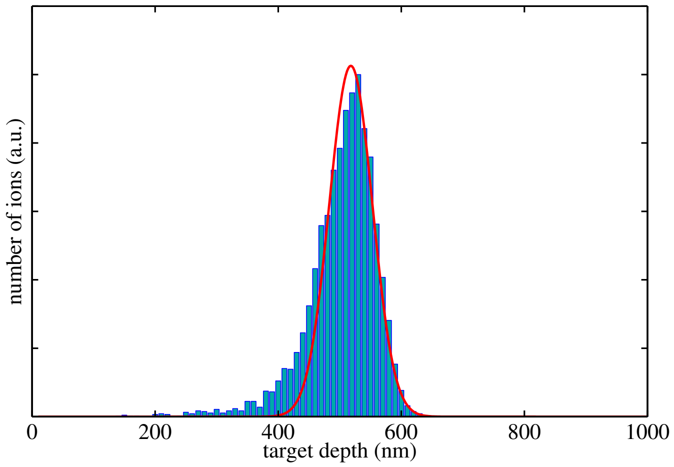

Figure 3.8: Ion implantation density profile $n(z)$ along the path of the ion in a diamond sample (blue histogramm), simulated with the SRIM algorithm [194], using 5000 ^{28}Si ions at an energy of 900 keV and an angle of incidence of 8° to prevent channeling. The red solid line shows a fit according to Eq. (3.12) with parameters $R_p = 518$ nm, $\sigma_d = 35$ nm. Both curves are normalized to 1.

Matter), which was developed by Ziegler *et al.* [194]. TRIM is a Monte-Carlo simulation, which numerically follows the path of an ion through the target. The target is approximated as a homogeneous material of a given density and the scattering events thus occur probabilistically. In addition, the program infers the mean number of vacancies created per ion. This is a figure of merit for both the creation yield of vacancy-related defects, such as the SiV center, and for the damage induced by the ion (see below). Figure 3.8 shows a TRIM simulation for the implantation profile of Si atoms into diamond using Si ions at an energy of 900 keV. The density profile is fitted using a Gaussian peak function according to Eq. (3.12). The mean depth of the Si ions amounts to 500 nm with an uncertainty ("straggle") of $\sigma = 54$ nm. The simulation predicts that each ion creates a mean number of about 1344 vacancies. We note that the density profile is slightly asymmetric, hence a fit with a Gaussian peak function according to our simplified model above [Eq. (3.12)] does not perfectly reproduce the simulation.

We employed these parameters for the implantation of the SILs sample at the RUBION institute. In the following section, we briefly give an overview, how an ion implanter as present at the RUBION is technically realized.

3.3.2 Technical realization of the ion implantation

The implantation on the SIL sample (cf. Sec. 3.2) was carried out at the RUBION located at the Ruhr-Universität in Bochum. The institute disposes over a 4 MeV Tandem Dynamitron accelerator (Radiation Dynamics Inc., see Ref. [195]) which provides ion currents up to several 100 µA at energies from 300 keV to 50 MeV (depending on the charge state of the ion). Figure 3.9 shows a schematic overview over the facility.

First, the ions – in our case silicon – are extracted from a Cs sputter source [196] and preaccelerated at 20 keV. Using a 90° analyzer magnet, ions of the desired mass and charge are preselected and enter the main acceleration beam line. The Tandem Dynamitron is a linear accelerator and follows a principle which is described e.g. by Van der Graaf [197]: The injected ions, which are negatively charged, enter the accelerator at a ground potential and are accelerated towards a positive high-voltage terminal. In this terminal, the ions pass a stripper gas which strips the electrons off the ions. Being positively charged, the ions are repulsed by the positive terminal and are further accelerated to a second ground terminal where they leave the accelerator. Hence the high-voltage is utilized twice for the acceleration. The ions are steered towards the sample, using additional sector magnets. In front of the sample, a quadrupole lens focusses the ion beam. Subsequently, the beam is scanned over the sample using two pairs of plate capacitors driven by a function generator, resulting in a homogeneous density of ions over the sample.

For the SIL sample, we employed an acceleration voltage of 900 keV on singly negative Si ions. The stopping range is predicted to be 500 ± 50 nm (cf. Fig. 3.8). During the implantation, the sample was masked with a circular metal aperture. Different fluences ($10^8 - 10^{11}$ ions per cm^2) where applied to different positions on the sample (cf. Fig. 3.10). Before a series of implantations, the ion current is measured using a picoampere meter. The fluence ϕ is then given by the ratio of the current times the exposure time over the area of the sample holder. The area is defined by an aperture inserted before the sample and the irradiation is assumed to be homogeneous over the target holder. In addition to the Si implantation, nitrogen has been implanted on a central region of the sample for test purposes which are beyond the scope of this work (fluence: 10^{13} ions per cm^{-1}, energy: 600 keV).

3.3.3 Radiation damage and post-treatment

While the ion penetrates the target atom and is gradually slowed down, the nuclear collisions of the ion lead to a displacement of the atoms in the material. This results in the formation of lattice vacancies and interstitials. One ion on its way through the crystal can create several vacancies, and additionally, the displaced atoms can create other vacancies, resulting in a damage cascade. We stated above, that the nuclear interaction is related to a Rutherford scattering process which in turn depends on $1/E^2$ of the ion energy E. Hence, the slower the ion moves through the crystal, the more vacancies are created, until the energy of the ion is not sufficient anymore to displace the atoms of the target. The overall number of vacancies created per ion depends on the energy and on the mass of the ion.

For the removal of these lattice defects, the crystal is usually heated in vacuum or stabilizing gas atmospheres (e.g. forming gas) to prevent oxidation of the diamond surface. Lattice vacancies in diamond become mobile at temperatures of approximately 800°C and start to mutually annihilate with the interstitials. During the thermal annealing, the radiation damage can lead to graphitization of the material [198], as broken sp^3 bond orbitals can be replaced by sp^2 orbitals which are thermodynamically more stable. The threshold fluence for an irreversible graphitization was found to be 10^{15} ions per cm^2 [199].

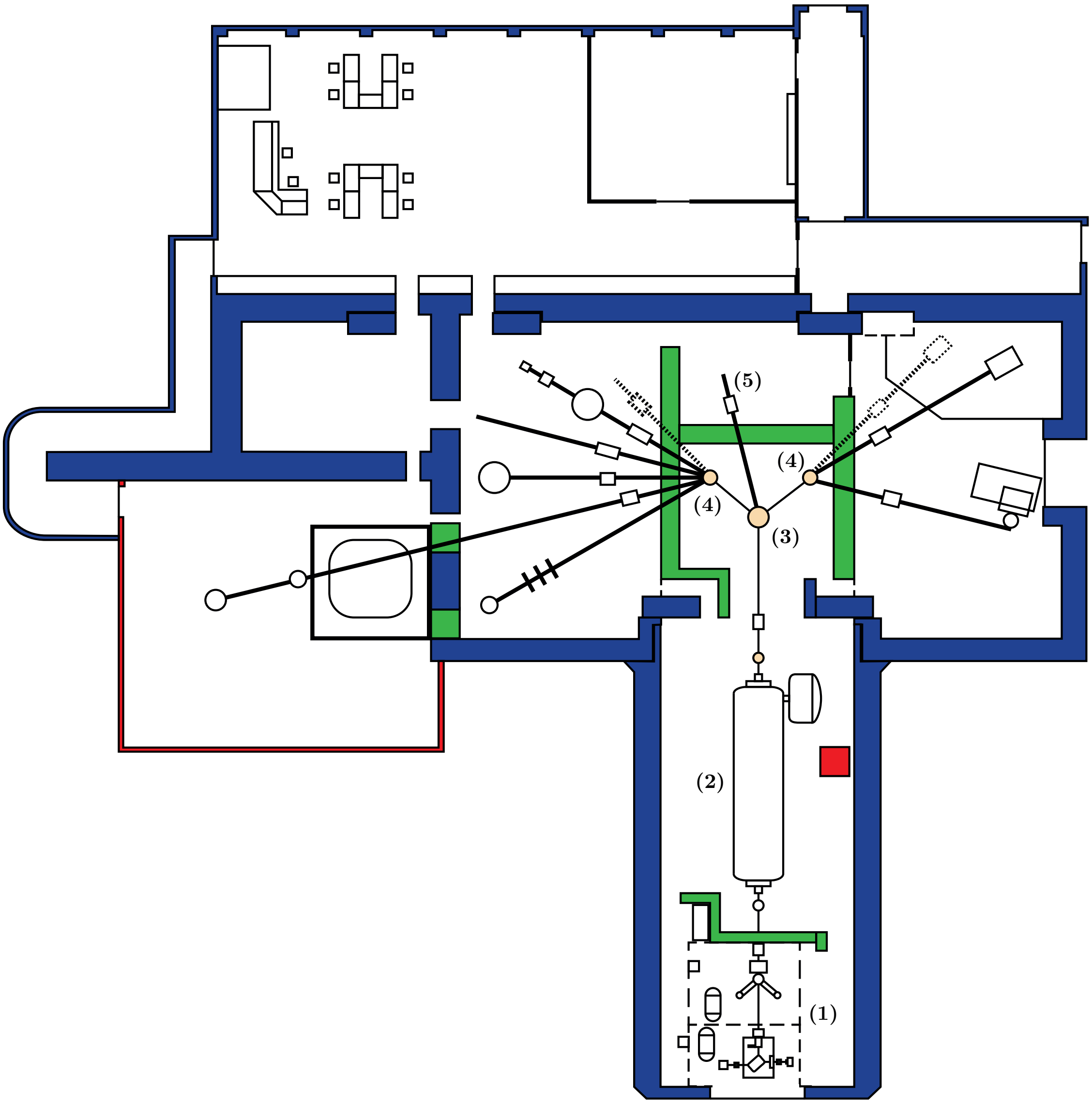

Figure 3.9: Overview over the RUBION accelerator facility. The negatively charged ions are extracted from the ion sources (1) in the lower part of the picture and enter the Tandem Dynamitron accelerator beam line (2) in which they are stripped of electrons and subsequently carry a positive charge. The accelerated ions are then guided to a an analyzer magnet (3). There, the ion beam is split up towards bending magnets (4) from where it is distributed to various beam lines. An additional heavy ion beam line (5) is directly attached to the analyzer magnet and was used for silicon implantation during this work (after Ref. [169] and www.rubion.rub.de).

The SiV center constitutes of an Si impurity and a vacancy, thus the creation of vacancies during the implantation is necessary for creating the defect complexes. To promote a coalescence of impurity and vacancy, and to anneal the radiation damage, the SIL sample is heated to 1000°C for two hours in vacuum to assure a sufficiently high vacancy mobility. After the annealing process, the sample surface shows a graphitization, which is observed in a grey-shaded surface. To remove the graphite layer, the sample is cleaned in peroxymonosulphuric acid ($H_2SO_4 : H_2O_2$, 1 : 1) for 30 minutes and afterwards heated to approximately 460°C in air for two hours. This process has been employed to remove residual damage from diamond which has been structured using focussed ion beam milling [86].

3.3.4 Preliminary results of the ion implantation

Figure 3.10 shows a fluorescence image of the whole SIL sample, measured at room temperature with a setup similar to the flow cryostat setup. The sample was excited using 1 mW of 660 nm laser light, and the detection was in the spectral interval of 730 - 750 nm. Out of the four implantation sites in the corners of the sample (marked by blue circles), the region with 10^{11} ions per cm^{-2} is clearly observable and the area with 10^{10} ions per cm^{-2} shows a slightly elevated count rate. The regions with 10^8 and 10^9 ions per cm^{-2} are not discernible form the background fluorescence of the diamond. The spectrum in the region with 10^{11} ions per cm^{-2} shows emission of an ensemble of SiV centers, and no individual defects could be isolated in this region.

Single SiV centers were found in the area with 10^{10} ions per cm^{-2} (cf. Sec. 4.1.2), with an average density of approximately 3 SiV centers per 10×10 µm^2. One defines the creation efficiency or yield of an implantation as the probability to convert one implanted Si atom into an SiV center. At a dose of 10^{10} ions per cm^{-2} and with a creation efficiency equal to unity, we would expect $\sim$ 100 SiV defects per µm^2. With the result above, we estimate our creation efficiency to be slightly below 1‰.

We compare these results with the ion implantation experiments carried out by Wang *et al.* [57,198]. They implanted ^{28}Si ions at an energy of 10 MeV and a fluence of 10^9 ions per cm^{-2}. Confocal microscopy revealed single SiV defects at these conditions. It is noticeable that the dose of Si ions to create individual centers was an order of magnitude smaller than in our studies. A simulation of the SRIM software reveals that at 10 MeV implantation energy, one ion creates about 2000 vacancies, thus 50 % more vacancies than at the 900 keV in our experiment. Thus, we assume that, in our case, the creation efficiency is limited by the number of vacancies available to pair up with the Si impurities. As a result, providing more vacancies in the diamond would result in a higher creation efficiency. When the diamond is structured using a focused gallium beam, additional vacancies are produced, which can form further SiV centers with unpaired Si impurities present in the material. In Sec. 4.1.2, we show that structured regions exhibit a higher number of SiV defects, which is consistent with the hypothesis above.

Similar to the results of Wang *et al.*, the individual SiV centers in the implanted diamond showed modest count rates in the range of a few 1000 cps. These low count rates render the follow-up experiments of Chap. 4 challenging. At this point it is interesting to discuss the reason why SiV centers in nanodiamonds (cf. Sec. 3.2.3) show fluorescence

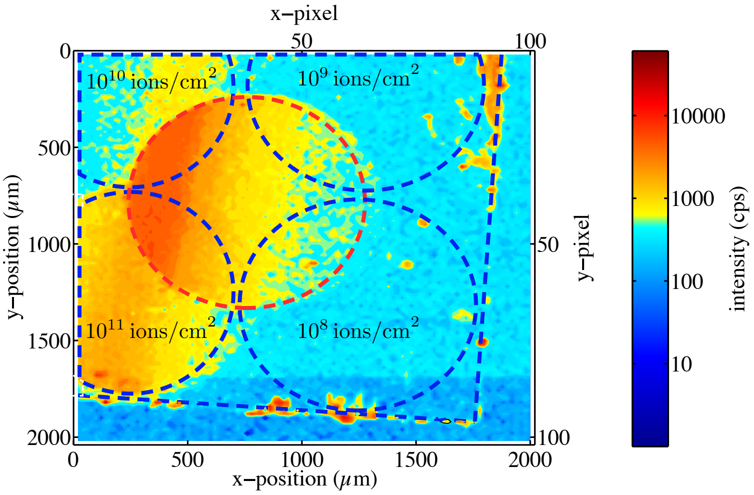

Figure 3.10: Fluorescence image of the SIL sample after implantation, excited with 1 mW, 660 nm laser light and detection at 730 − 750 nm (setup similar to flow cryostat setup, cf. [200]). The four blue dashed circles mark ^{28}Si implantation sites with fluences of $10^8 - 10^{11}$ ions per cm^{-2} at an energy of 900 keV. The blue rectangle marks the sample edges. The red dashed circle in the middle of the sample was implanted with nitrogen for test purposes and shows fluorescence of the NV center.

count rates, which are more than two orders higher than individual defects in bulk diamond. The collection of the emission light for defects in bulk diamond is limited due to three reasons: First, the orientation of the defects in the (001) oriented bulk diamond is disadvantages, because the main dipole emission comes from the Z dipole, which however has a fairly large angle of 54.7° to the diamond surface (cf. Sec. 2.3.1). In Ref. [201], it is shown that the collection efficiency for emitters oriented perpendicular to the surface is about ten times lower than for emitters parallel to it. Nanodiamonds grow from randomly oriented seed diamonds, thus the angle of the SiV Z dipole to the substrate can be arbitrary. Hence, in the optimal case, the Z dipole of an individual defect is oriented parallel to the surface, leading to collection efficiencies of up to 80 %. Second, the radiation pattern of a dipole, i.e. the angular distribution of the irradiated light intensity, is modified by the photon density of states in the surrounding material. As a consequence, an electric dipole placed at the diamond-air interface shows a dominant emission towards the higher index material [190]. On the other hand, the metallic Ir-surface of the nanodiamond sample has proved to be advantageous, since it can channel the emission towards smaller angles, thus enhancing the collection efficiency. As a drawback, the collection efficiency depends strongly on the distance of the SiV dipole to the metallic surface, ranging from below 20 % to approximately 80 %. Third and finally, the refraction and the total internal reflection at the diamond-air interface limits the angle at which fluorescence light can leave the material. An improvement of the collection efficiency can be obtained by using photonic structures, such as solid immersion lenses, which we discuss in the following section. In contrast, nanodiamonds are smaller than the wavelength of the emitted light and can be considered as point-like emitters. As a result, they do not exhibit total internal reflection, improving the collection efficiency.

3.4 Solid immersion lenses

To enhance the collection efficiency on the implanted SiV center, we fabricate solid immersion lenses (SILs) into the diamond surface. First, we discuss the limitations of the collection angle for emitters placed below a flat diamond surface, and then we show how SILs inhibit these refraction effects. Subsequently, we outline the fabrication process of the SILs and briefly discuss the enhancement of the collection.

3.4.1 Collection efficiency for emitters in bulk diamond

We consider a single SiV defect placed in proximity to the diamond air interface (Fig. 3.11a). In a preliminary approximation, we assume the emission of the defect to be isotropic. The emitted light is refracted at the surface according to Snellius' law,

$$n_1 \sin(\theta_1) = n_2 \sin(\theta_2), \tag{3.13}$$

where for the diamond-air interface $n_1 = 2.4$ and $n_2 = 1$. The maximum collection angle $\theta_{2,\mathrm{max}}$ is limited in two aspects: First, light reaching the surface at an angle $\theta_1 > 24.6°$ is reflected back into the diamond due to total internal reflection (dashed lines in Fig. 3.11a). This imposes one limitation on the maximum angle under which light can be collected.

The second limitation is the numerical aperture NA of the objective lens, which defines the maximum collection angle $\theta_{2,\mathrm{max}}$ in the upper hemisphere of Fig. 3.11a via the relation $NA = n_2 \sin(\theta_{2,\mathrm{max}})$. For the flow cryostat setup, the numerical aperture has a value of $NA = 0.8$. Due to refraction at the diamond surface [Eq. (3.13)], the maximum emission angle inside the diamond $\theta_{1,\mathrm{max}}$ is then given by [202]

$$\theta_{1,\mathrm{max}} = \arcsin\left[\frac{n_2 \sin\left(\theta_{2,\mathrm{max}}\right)}{n_1}\right] = \arcsin\left[\frac{NA}{n_1}\right] = 19.5°. \tag{3.14}$$

Hence, light emitted at an angle of more than 19.5° inside the diamond is not collected by the finite NA lens. We define the collection efficiency η_{bulk} for the emitter as the ratio of the collected light over the total emission. This fraction is equal to the ratio of the solid angle Ω defined by the opening angle $\theta_{1,\mathrm{max}}$ over the emission into the whole space (4π), where we remember that the emission was assumed to be isotropic,

$$\eta_{\mathrm{bulk}} = \frac{\Omega}{4\pi} = \frac{2\pi[1-\cos(\theta_{1,\mathrm{max}})]}{4\pi} \approx 0.029. \tag{3.15}$$

Thus, the collection efficiency is on the order of 3 %, which imposes a serial limitation on the brightness of an individual defect in bulk diamond. Strictly speaking, this efficiency is only valid for emitters with their dipole oriented parallel to the sample surface. For emitters perpendicular to the surface, the collection efficiency is about an order of magnitude lower [201]. We have already discussed, that these effects do not account when the

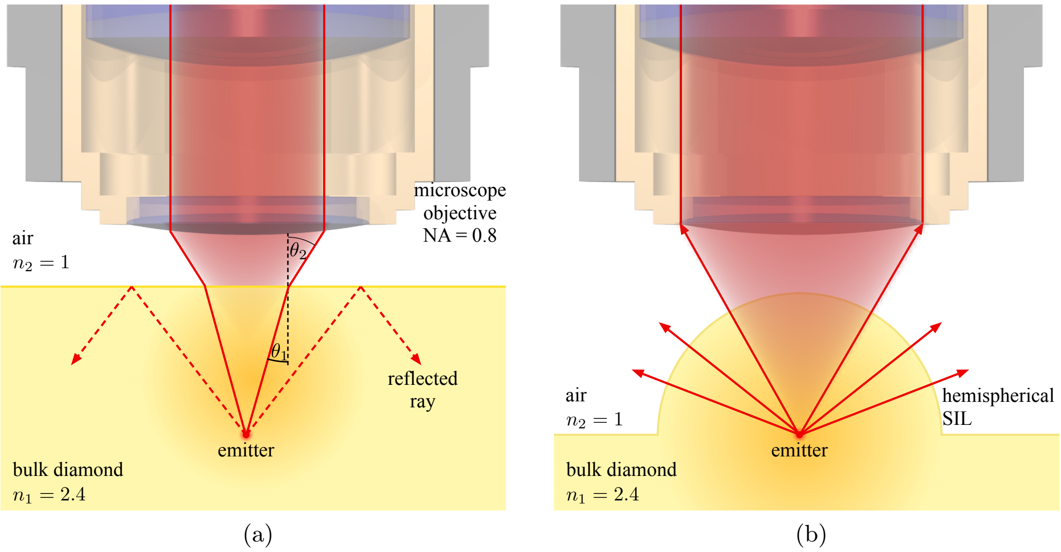

Figure 3.11: Collection angles for an individual defect in diamond placed (a) under a flat diamond surface and (b) at the center of a hemispherical SIL. The maximum collection angle (a) without the SIL is limited to 19.5° (red solid lines). With the SIL (b), no refraction occurs at the surface and the possible collection angle increases to 53.1° (angles not to scale). The red shaded areas denote the light collected by the objective lens.

diamond itself is smaller than the wavelength of the emitted light, i.e. when we employ nanodiamonds (cf. Sec. 3.2.3). However, nanodiamonds show other limitations, such as crystal strain or spectral diffusion [58].

3.4.2 Improvement of the collection efficiency using SILs

An alternative method to enhance the collection efficiency is to use solid immersion lenses (SILs) which partly inhibit the refraction at the surface. A SIL is a truncated sphere, made of a dielectric material with a high refractive index, such as zirconia ($n = 2.17$). We distinguish between the hemispherical and the Weierstrass geometry for SILs [203]. Often, SILs are macroscopic optics placed onto the surface of a solid sample. However, when placing such a macroscopic SIL onto the sample, one faces three problems: First, there is typically a remaining index mismatch between e.g. a zirconia SIL and the diamond. Second, the possible air-gap between SIL and diamond surface can again lead to refraction and spoil the positive effects of the SIL. Third, the SIL decreases the excitation focus size inside the material. While this can be beneficial for some applications [204], it limits the usable field of view for a microscope objective which is disadvantageous in our case.

Hence for us, it is preferential to fabricate the SILs directly into the material, where we restrict ourselves to hemispherical SILs as these are easier to manufacture. Before we outline their fabrication in the next section, we derive the improvement in collection efficiency when using SILs. We consider an emitter placed at the center of a hemispherical

SIL, and again we simplify the problem by assuming that the emitter radiates isotropically (Fig. 3.11b). As every ray exits the surface at a normal angle, we obtain $\theta_1 = \theta_2 = 0$ and no total internal reflection occurs. Since the angle of the beam does not change at the diamond-air interface, the collection angle determined by the NA of the objective lens becomes

$$\theta_{1,\max} = \theta_{2,\max} = \arcsin\left(\frac{NA}{n_2}\right) = \arcsin(0.8) = 53.1^\circ. \tag{3.16}$$

As a consequence, the collection angle has considerably improved when using a SIL. The collection efficiency is calculated similarly to Eq. (3.15), which yields

$$\eta_{\mathrm{SIL}} = \frac{\Omega}{4\pi} = \frac{2\pi[1-\cos(\theta_{1,\max})]}{4\pi} \approx 0.2. \tag{3.17}$$

Thus, the SIL would improve the collection efficiency by a factor of approximately 7. This is only valid for an isotropic emission of the emitter, which is hardly the case. First, the emission is proportional on the photonic density of states ρ_{phot} which is larger inside the diamond [190], thus a large fraction of the light is emitted inside the material. Second, the emission of an electric dipole exhibits an angular dependence and is usually polarized. For the directional emission of a dipole, one typically employs numerical simulations [94, 202]. Hadden *et al.* employ a finite-difference time-domain method to compare an emitter centered under a 5 µm hemispherical SIL with the same emitter in bulk diamond, assuming a numerical aperture of $NA = 0.9$. The simulation predicts an enhancement by a factor of 5, which is even outperformed in their experimental realization – factors between 8 and 10 were achieved [94, 205].

The SILs which we consider are smaller than the SILs produced by Hadden *et al.*. Their size is predetermined by the implantation depth of the SiV centers. As the defects require to be positioned in the center of the SIL, the radius of the SIL must be equal to the implantation depth, which we deduced to 500 nm below the diamond surface (Sec. 3.3.1). For small SILs, the improvement of the collection efficiency is more sensitive to fabrication tolerances and to the defect position with respect to the SIL focal point, thus we expect a slightly lower enhancement. The following section outlines the fabrication procedure and provides the parameters for the SIL fabrication.

3.4.3 Fabrication of the SILs using focussed ion beam milling

To fabricate the SILs in the diamond material, we employ focussed ion beam milling (FIB), similar to the approaches of Hadden *et al.* [94, 205]. First, we give a brief introduction on the function principle of a FIB before we name the parameters. A FIB bases on the same principles as a scanning electron microscope (SEM). A beam of charged particles, i.e. ions for the FIB and electrons for the SEM, is extracted from a source, accelerated, and focused onto the sample. When the beam hits the sample surface, secondary electrons are emitted and are guided to a detection device. To form an image of the sample surface, the ion or electron beam is scanned over the surface. In contrast to the electrons, the ions sputter the surface of the specimen which – in combination with a sophisticated beam steering – enables a high resolution structuring of the sample.

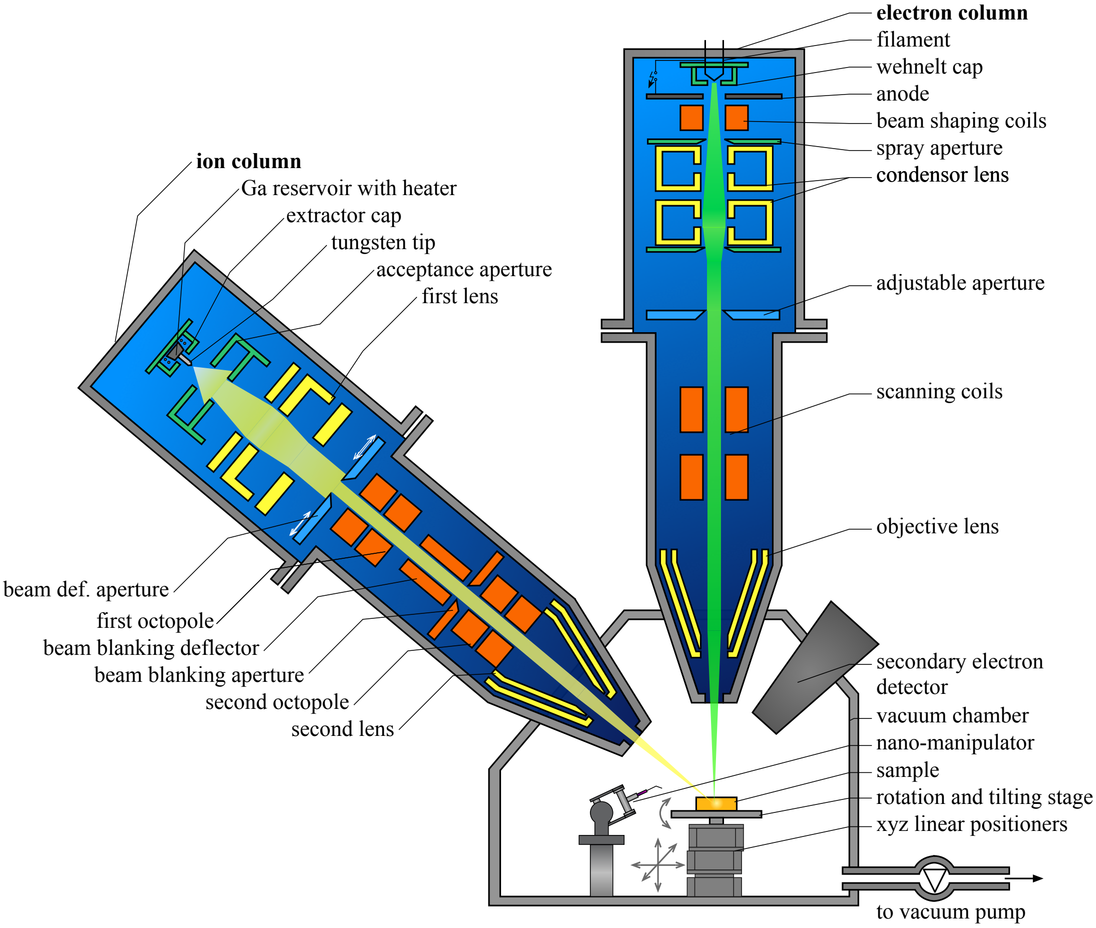

Figure 3.12: Illustration of the dual beam focussed ion beam setup. The ion/electron optical elements and their function principles can be found e.g. in Ref. [206].

We employ a so-called dual beam FIB (FEI Helios Nanolab 600), which comprises both an ion and an electron beam, situated in different columns of the setup (Fig. 3.12). Utilizing the electron microscope, we monitor the fabrication process and pre-align the sample.

In the ion column, Ga^{3+} ions are extracted from a liquid metal ion source (LMIS). Among other convenient properties [207], Ga exhibits a low melting point (29.8°C) and therefore is kept liquid via heating slightly above room temperature. The resolution of the ion beam, i.e. the diameter one can focus the beam to, depends on the size of the ion source. Hence, the smaller the LMIS, the better the resolution. A reservoir of liquid Ga is positioned in close contact with a tungsten needle with a tip of $2-3$ µm [206]. Due to capillary forces, the tip is wetted with liquid Ga. When applying an electric field (on the order of 10^{10} V/m) between the tungsten tip and the extraction electrode, the electric field imposes a force against the surface tension of the Ga. At equilibrium, the liquid Ga forms a Taylor cone, which shows a cusp of down to 5 nm, hence we satisfy the criterion of a small ion source. This results in structuring resolutions down to 10 nm [207].

The ion beam is shaped using apertures and at least two lens systems, a condensor and objective lens (referred to as first and second lens in Fig. 3.12). The focussing strength of an electromagnetic lens depends on the charge-to-mass ratio for a particle beam, hence electromagnetic lenses for ions would be very large. Instead, it is more convenient to employ electrostatic lenses. Further beam shaping is accomplished using a number of apertures. In addition, the beam defining aperture controls the beam current, ranging typically between a few pA and ~ 1 µA. Further components, such as cylindric octopole lenses, beam blankers and stigmators, provide additional control for scanning and blanking the beam and correct possible aberrations. The sample is typically mounted on 5-axis stage (x, y, z, rotation and tilt) in the focal point of both the ion and the electron beam. A number of imaging detectors are placed inside the sample chamber. To manipulate parts of the sample, e.g. to lift out transmission electron microscope samples, a nano-manipulator is placed inside the vacuum chamber.

We have discussed the radiation damage from ion implantation in Sec. 3.3.3, and the same effects are utilized for the FIB milling of the sample surface. Due to nuclear energy loss, the impinging Ga ions displace the atoms of the target. In turn, the primary recoil atoms successively displace secondary atoms, giving rise to a damage cascade. Atoms displaced at the surface can leave the crystal and are sputtered. The typical energies of the Ga ions are on the order of 30 keV, which corresponds to a stopping range of 10 to 100 nm depending on the target material. In the course of the sputtering, Ga ions are implanted into the sample, which necessitates a post-treatment procedure, similar to ion implantation experiments (Sec. 3.3.3).

3.4.4 Lens fabrication on the SIL sample

To enhance the emission of individual color centers, different strategies have been used. Marseglia *et al.* fabricated SILs over nitrogen vacancy centers, which were created 4 µm below the diamond surface using ion implantation [205]. Prior to SIL fabrication, they etched position marks into the sample to correlate fluorescence microscopy images with the SEM images in the FIB. Consequently, they could produce a single SIL positioned accurately over an individual emitter. The larger the SIL is, the less sensitive it is to the emitter being positioned in its center [94]. Hence, the approach of Marseglia *et al.* works especially well when using emitters buried deep in the diamond.

As this is not the case for the SIL sample presented in this work, we employed an alternative method: Arrays of SILs have been produced on the sample using the FIB apparatus described in the previous section. Each of the arrays features 10×10 SILs, closely packed in a hexagonal pattern (Fig. 3.13c). In total, we fabricated 9 of these SIL arrays on the sample (Fig. 3.13d). Statistically, some of these SILs should exhibit individual SiV defects at their center. The arrays were placed in the region of the sample where Si atoms where implanted at a fluence of 10^{10} ion per cm^2 and where individual SiV center were located before.

We employed 30 keV Ga ions at a beam current of approximately 300 pA. The sample was covered with a approximately 60 nm Cr layer to provide sample conductivity and inhibit charging of the sample during the fabrication. The ion optics were used to create a

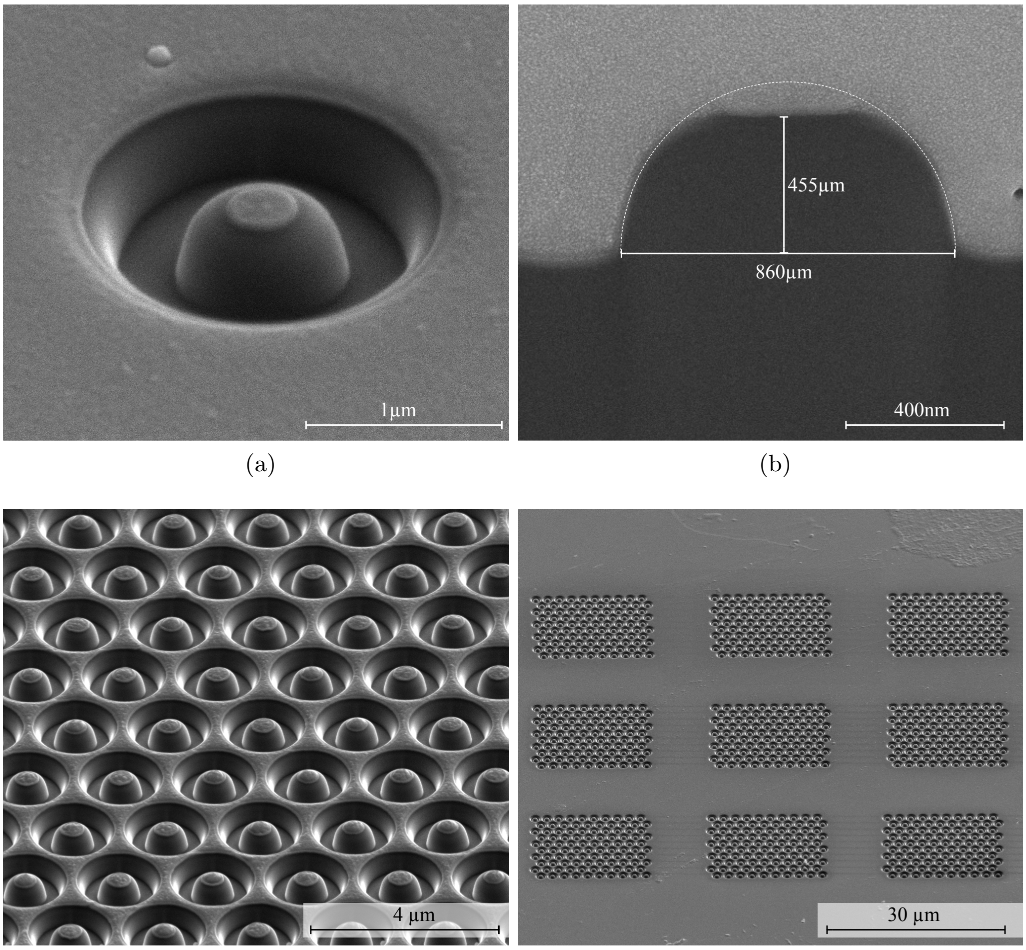

(a) (b)

(c) (d)

Figure 3.13: A single SIL fabricated in diamond using focused ion beam milling in (a) top and (b) cross sectional view. The sample surface in (a) still shows a Cr cover layer which was applied to prevent charging up the sample. In panel (b) the upper part of the image shows platinum which was sputtered over the SIL to prevent uncontrolled damage during the cross section cut. The SILs were fabricated in 9 arrays of 10 × 10 lenses (c,d)

donut shaped beam which was intentionally “blurred”, i.e. slightly defocused. As result, we milled trenches into the diamond with an inner diameter of 0.9 µm and an outer diameter of 1.4 µm. Owing to the blurred ion beam, the edges of these trenches are rounded off giving the central feature a hemispherical shape (Fig. 3.13a) which corresponds to a SIL. Deviations from the ideal spherical shape are investigated from the cross section of the SIL. To obtain a cross sectional view, a large rectangular trench is cut from one side. Before this cut, a line of platinum is sputtered *in situ* over the SIL to prevent ion damage and spurious sputtering [206]. Subsequently, the sample can be tilted to view the cross section (Fig. 3.13b). Besides a slight truncated top, the SIL appears in a well-defined spherical shape.

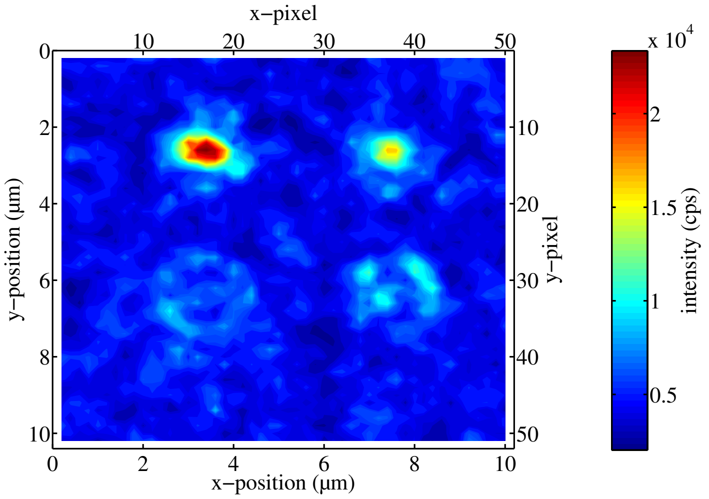

Figure 3.14: Fluorescence image of four test SILs, produced over homogeneously distributed SiV ensembles, and measured with 660 nm laser excitation at 1.7 mW and detection in the spectral interval from 730 - 750 nm. For the two rows, we varied the intentional blur of the ion beam. For top (bottom) row, the blur was chosen to be 100 nm (75 nm).

The SILs are fabricated sequentially in a total writing time of approximately 5 hours was needed. Following the FIB milling, the Cr coating was removed using a mixture of acetic acid, water and ceric ammonium nitrate (in a mass concentration of $8.75mg$: $240mg$: $50g$). Subsequently, the sample is subjected to the same annealing steps as the ones following the ion implantation.

To quantify the improvement of the collection efficiency when using SILs, we fabricated a SIL test array of lenses in the region of the sample where 10^{11} Si ion per cm^2 were implanted and consequently, ensembles of SiV centers have been observed. We assume that the SiV centers in this region are homogeneously distributed such that each test SIL has the same number of SiV centers in its focal point. Figure 3.14 shows a confocal fluorescence image of the region. The fluorescence of SiV ensemble appears as a constant fluorescence exhibiting a mean count rate of 4200 cps. Four of the SILs are observed as point-like objects in the fluorescence scan. The two rows of SILs visible in 3.14 were fabricated using different blur parameters for the ion beam, given roughly in the FWHM of a Gaussian beam broadening. The top row SILs with a FWHM of 100 nm showed the highest increase in fluorescence count rates of a factor between 4 and 6. Hence, we employed this blur parameter throughout the fabrication of the SIL arrays described above.

After this preliminary quantification, it is more interesting to investigate the enhancement of the collection efficiency for SILs over single emitters. This is discussed in the following chapter on experimental results. We stress, that the SILs have been a key element to achieve sufficient fluorescence count rates from individual SiV centers for the spectral investigations in this work.

This concludes the experimental preparations to investigate the electronic structure of the SiV center. Combined with the advantages from the SILs, the elaborate microscopy technique discussed in this chapter enables the measurement of the spectral properties of individual SiV centers. With the diamond samples presented in this chapter, we have access to low and high strain SiV centers to probe the influence of crystal strain on the electronic structure.

Chapter 4

Experimental Results

In this chapter, we summarize the experimental results of low temperature spectroscopic experiments on ensembles and single SiV defects. In the first part, we discuss the “ideal” SiV electronic structure based on Zeeman spectra of low strain SiV defects found in single crystalline diamond (Sec. 4.1). This discussion is founded on the theoretical considerations of Chap. 2. Having established a faithful description of the electronic structure of the defect, Sec. 4.2 relates these results to recent resonant excitation experiments on SiVs in low strain defects where spin selective population of electronic states is observed. The third and last part of this chapter (Sec. 4.3) focusses on the effect of crystal strain on the electronic structure. In particular, we will return to spin resolved measurements again, and compare the predictions of a strain perturbed electronic system with the experiments.

4.1 Unstrained defects in single crystalline diamond

In order to identify the unperturbed electronic nature of the SiV center, we investigate the defect in low strain environments found in single crystalline diamond. As we will see throughout this chapter, the figure of merit for crystal strain is the spectral position and splitting of the zero phonon line fine structure of the SiV center. These two parameters are given in the literature for reference samples (Chap. 1). In addition, we investigate an ensemble of SiV centers in a homoepitaxial diamond film (fabrication, cf. Sec. 3.2). The fine structure splitting of this sample is in perfect agreement with the one reported in Refs. [62, 133, 137]), hence the sample will be considered as a reference sample. In order to prevent ensemble effects such as inhomogeneous broadening and the contribution of equivalent orientations, the analysis is extended to single SiV centers (Sec. 4.1.2). It has so far been challenging to have optical access to single SiV centers with low environmental strain, not obscuring the center’s true electronic nature. This goal has been attained using solid immersion lenses, fabricated directly into the single crystalline diamond (Sec. 3.4 and Ref. [61]). The creation of these sample types enables polarization measurements of all fine structure lines, yielding first hints towards the electronic structure of the SiV.

A more distinct understanding of the SiV electronic structure is obtained by measuring the fine structure splitting in magnetic fields (referred to as “Zeeman spectra”, Sec. 4.1.4). The analysis of the Zeeman spectra with the theoretical framework developed in Chap. 2

enables the calculation of internal parameters, such as spin-orbit coupling strength and leads to conclusions about spin state purity (Sec. 4.1.5).

4.1.1 Low temperature spectroscopy on silicon vacancy ensembles

In the first part of this section, we investigate the low temperature spectrum of the SiV center. A crucial prerequisite to observe the SiV fine structure is a low strain crystal environment. Clark *et al.* [62] and Sternschulte *et al.* [133, 137] showed that in homoepitaxial CVD films of high crystalline quality, the zero phonon line of the SiV splits into four fine structure peaks at liquid helium temperatures. This spectral fine structure is seen as the "fingerprint" of the SiV center and provides an unambiguous way to identify this defect. To introduce the main properties of the spectral fine structure, we investigate it in an approximately 100nm thick homoepitaxial CVD diamond film, containing an ensemble of SiV defects (the sample is denominated "ensemble sample" throughout this work and details are found in Chap. 3.2).

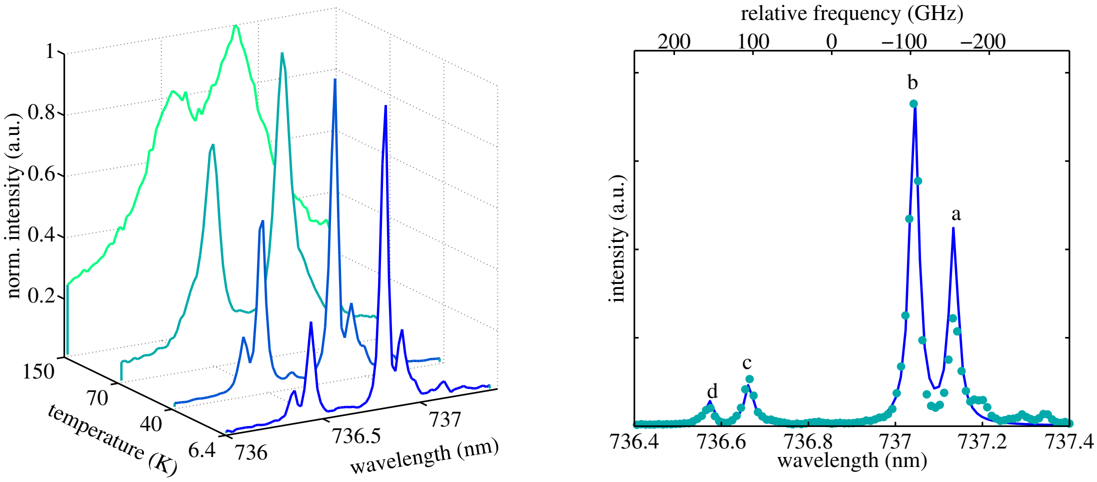

(a) (b)

Figure 4.1: The fine structure of the SiV center. When cooling down SiV defects, the zero phonon line splits into four fine structure lines (a). Panel (b) displays the fine structure splitting at $T = 4.7K$ (green dots). We denominate the four strongest peaks of the fine structure line from a to d in accordance with Ref. [133]. These peaks have been simulated using the SiV model described in the text (blue lines).

Figure 4.1a displays how the zero phonon line of the SiV ensemble narrows down with decreasing temperature. Below 70 K, a splitting into four components is observed. The temperature dependent broadening of the fine structure, which is observed together with a shift of the zero phonon line, is treated in detail in Ref. [115]. We focus here on the spectral properties at liquid helium temperature. Figure 4.1b shows a spectrum of the ensemble sample at 4.7 K. We note that the spectrum in 4.1a and 4.1b are displaced in wavelength by 0.2 nm. We have used different experimental setups for the measurements in Figs. 4.1a and 4.1b and this absolute shift is due to a difference in spectral calibration for the two setups. Throughout the discussion of this section, this displacement is however irrelevant as the figure of merit is exclusively the relative fine structure splitting. We therefore add an upper axis to all spectra indicating the relative frequency of the fine structure peaks making all the spectra comparable.

The low temperature spectrum of SiV centers usually show a total number of 12 peaks [62] of which we fitted the main four peaks in Figure 4.1b . These 12 peaks can be grouped in three sets. The relative intensities of the three groups are proportional to the natural abundance of the ^{28}Si, ^{29}Si and ^{30}Si isotope, respectively [62]. The four most intense lines are therefore attributed to the ^{28}Si isotope, and labeled from a to d according to Ref. [133]. Former investigations (cf. Chap. 1 and Refs. [62, 133]) deduced a phenomenological level scheme from the fine structure. The level scheme exhibits both a split ground and excited state, with the ground state splitting $\Delta\nu_g = \nu_d - \nu_c = \nu_b - \nu_a$ and excited state splitting $\Delta\nu_e = \nu_d - \nu_b = \nu_c - \nu_a$, with ν_i being the frequency of the i-th peak. From Fig. 4.1b, we obtain $\Delta\nu_g = 50 \pm 5$ GHz and $\Delta\nu_e = 260 \pm 5$ GHz. Clark *et al.* determine the ground state splitting to be 0.2 ± 0.01 meV (48 ± 2 GHz) and the excited state splitting to 1.07 ± 0.01 meV (259 ± 2 GHz) which is in agreement within our measurement resolution. For a further comparison to single emitters, Tab. 4.2 at the end of the section sums up the fine structure splittings.

We use these splittings as starting values for the simulation of optical transitions for an "ideal" SiV defect. The simulation is described in detail when we analyze Zeeman spectra (Sec. 4.1.4), but since it also yields the center frequencies ν_j of optical transitions j for zero magnetic field, we use it already here to fit the fine structure splitting. We therefore mention here already the most important points: Each optical transition is modeled individually using a Lorentzian line shape centered at the simulated transition frequency ν_j. Consequently, the Lorentzian peak functions are superimposed to form the spectrum in Fig. 4.1b (blue solid line). To account for the width of each peak, the Lorentzian line width has been set to 10 GHz (see below). The intensity of each peak is calculated from dipole transition moments and weighted with the collection efficiency η_x, η_y, η_z for the respective dipole emission. The expectation values of the dipole matrix elements can be directly calculated using group theory (cf. Sec. 2.3.1). The collection efficiencies η_x, η_y, η_z for X-, Y- and Z-dipoles are numerically calculated using the algorithm of Ref. [117], assuming the Z dipole oriented along the equivalent $\langle 111 \rangle$ directions and the XY-dipole perpendicular to these axes (cf. Sec. 2.1.4). From the numerical analysis, we obtain a ratio of $\eta_x : \eta_y : \eta_z = 1 : 0.64 : 0.82$ for X, Y, Z-dipoles, respectively. Finally, we simulate a thermalization among the excited states, which follows a Boltzmann distribution (cf. 2.3.3 and Ref. [62]). For this Boltzmann distribution, we assume a temperature of 5 K.

The line widths of peaks a - d in Fig. 4.1b are close to the resolution limit of the spectrometer employed. To investigate the line widths in further detail, a scanning Fabry-Perot interferometer (FPI) was used (the FPI is described in closer detail in Ref. [208]). Figure 4.2 shows the resulting high resolution spectrum. Each peak $a, \ldots, d$ has been preselected separately using a 50 GHz etalon band pass filter and has been subsequently plotted over a spectrum acquired with a grating spectrometer to illustrate the correspondence to each peak [115]. The peaks are fitted using Gaussian line shapes. The resulting line widths

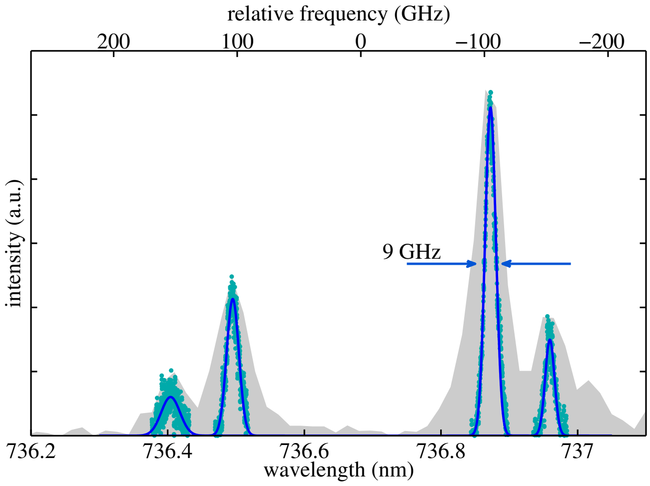

Figure 4.2: High resolution spectrum of SiV ensemble using a scanning Fabry-Perot interferometer (green dots). The four peaks have been measured individually and are placed in correspondence to the spectrum acquired with a grating spectrometer (grey shaded area). Each peak has been fitted using Gaussian peak functions (blue lines).

range from 9 to 19 GHz. Related measurements on the line width of the ensemble sample using photoluminescence excitation (PLE) and resonance fluorescence [65] confirm these values. This width is about an order of magnitude larger than the expected lifetime limited line width [61], assuming a lifetime of $\sim$ 4 ns [137]. This deviation can be explained by an inhomogeneous broadening which is present due to slightly varying crystal environments for individual SiVs. We consider this small inhomogeneous broadening as a proof of the relatively high crystalline quality of the ensemble sample. Moreover, the absolute wavelength of the fine structure peaks as well as their relative splitting are in good agreement with the literature values, which confirms this assumption. Consequently, the ensemble sample will be treated as a reference sample throughout the discussion which we compare single SiV center to. Single SiV centers in a similar quality diamond are covered in the following section.

4.1.2 Single defect spectroscopy

The following part of the section covers spectroscopy on single SiV centers. While general spectral properties can in principle also be deduced using *ensembles* of color centers, single defect spectroscopy shows certain advantages over ensemble measurements: As we have seen in the preceding section, an ensemble of color centers in diamond is susceptible to ensemble related broadening effects. Together with presence of other Si-isotopes, this broadening limits the resolution of the fine structure lines and makes a clear assignment of transitions difficult. The investigation of single emitters does not suffer from these inhomogeneous broadening effects.

Furthermore, single emitters are used to measure the polarization of each fine structure transition. In an ensemble there are equivalent orientations of SiV defects along the crystal axes, such that polarization measurements show superimposed contributions of each orientation. A polarization analysis on ensemble samples is in principle still feasible [131, 209]. However, as these techniques rely on polarization contrast (cf. Sec. 4.1.3), they require a carefully defined polarization detection as well as high spatial homogeneity of the investigated ensemble. All these limitations do not apply when studying single defects. We will show later (in Sec. 4.1.3) that the polarization of single emitters are employed as a further verification of our theoretical model of the SiV.

To have access to single defects in a low strain environment, we investigate a high purity single crystalline diamond which has been implanted with ^{29}Si in order to deterministically create single SiV defects. To enhance the collection efficiency, solid immersion lenses (SILs) with a diameter of 1 µm have been fabricated directly into the diamond (details on the sample, see Sec. 3.2). Later throughout this chapter we also study single SiV defects in nanodiamonds, however, these defects usually reside in strongly strained crystals. As outlined in Sec. 2.2.5, crystal strain leads to shifts of the electronic levels, thus it affects the spectral fine structure. Hence, we focus in this first part on single emitters in bulk diamond, where crystal strain is observed to be less prominent.

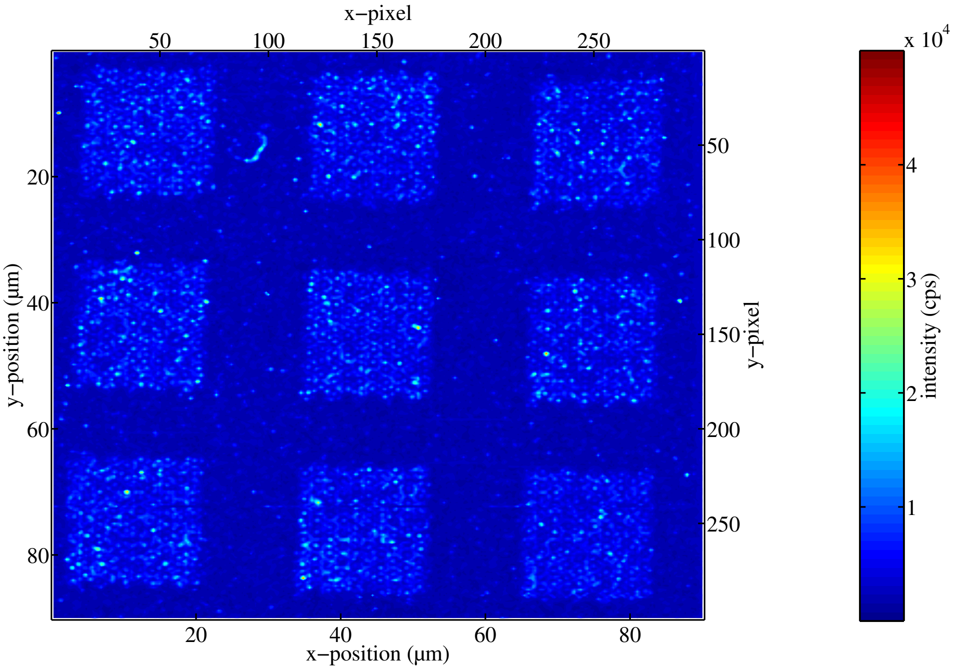

Figure 4.3: Confocal microscopy scan over 3 × 3 arrays of solid immersion lenses on high purity diamond exhibiting single SiV defects, perceivable as brighter spots. Excitation laser tuned to 690 nm at 8 mW (cw), detection in spectral interval 730 − 750 nm. The step size of the confocal scan was chosen to 0.3 µm. The sample temperature was kept constant at 15 K.

To locate single defects, we perform confocal fluorescence scans over the diamond sample, utilizing the avalanche photodiodes (APDs) of the photon correlation setup as fluorescence detectors. All measurements shown in this subsection are performed using the flow cryostat setup (details on the setup are given in Sec. 3.1.3); the sample is excited with 690 nm laser light and kept at a temperature of 15 K. To preselect emitters in a defined spectral interval, band pass filters are mounted in front of each APD, such that two detection channels are possible. In a first step, both channels detect the same spectral interval 730 − 750 nm. Fig. 4.3 shows a fluorescence scan of the nine solid immersion lens arrays. The fields of solid immersion lenses are clearly visible as squares showing the single SILs arranged in hexagonal patterns. The presence of the SILs in the fluorescence maps show a first advantage of this approach, as they provide “markers” to reproducibly locate individual defects. These individual SiV defects are observed as bright spots in the fluorescence scan. Their density is on the order of 3 - 5 isolated defects per $10 \times 10\ \mu m^2$.

We note that centers on the SIL arrays appear brighter than outside the arrays: On average, the emitters in the SIL array exhibit a factor of ≈ 3 higher photon count rate compared to defects outside the SIL arrays. The maximum enhancement observed amounts to a factor of 6. For comparison, Hadden *et al.* show an enhancement of up to 10 for single nitrogen vacancy defects under SILs with a diameter of 5 µm [94]. Numerical simulations reveal that SILs of this size are insensitive to the positioning of the emitter with respect to the focal point of the SIL. In our case, the diameter of the SILs is considerably smaller compared to those in Ref. [94]. Hence, both positioning and fabrication tolerances limit the performance of the SILs employed, explaining the moderate enhancement.

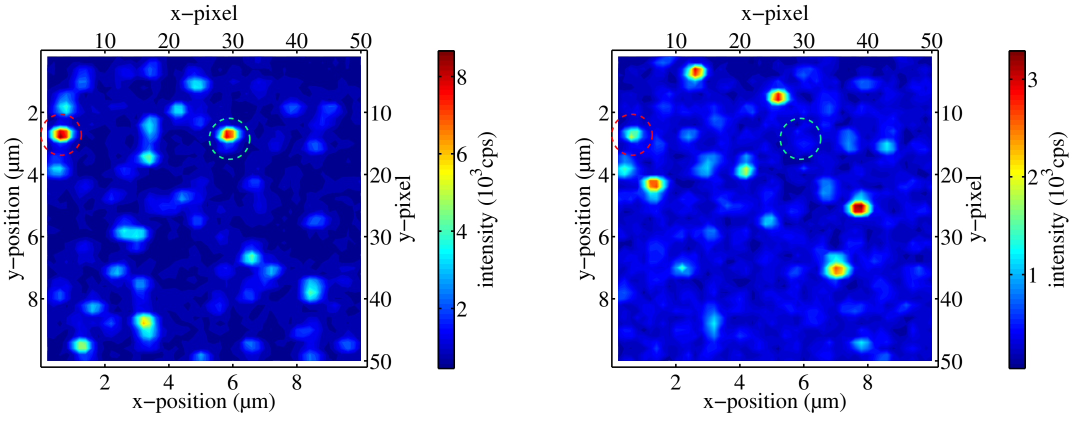

(a) (b)

Figure 4.4: Detailed fluorescence scan of the top left area in the central SIL array, using (a) a 737 ± 1 nm bandpass filter and (b) a 738 ± 1 nm filter. All other parameters are identical to Fig. 4.3.

In a second step, the fluorescence mapping of Fig. 4.3 is repeated using multispectral imaging, i.e. we place two spectrally disjoint filters (transmission intervals 737 ± 1 nm and 738 ± 1 nm, resp.) in front of the two APDs (Fig. 4.4). A similar strategy has been employed earlier [73] to distinguish the narrow emission of nanodiamonds containing individual SiV defects from other nanodiamonds with broad background fluorescence. The narrow transmission intervals of the filters used here facilitate the identification of unstrained SiV centers: Crystal strain shifts the absolute position and changes the splitting $\Delta\nu_{e,g}$ of the SiV fine structure (see also Sec. 4.3). From the reference ensemble sample in Sec. 4.1.1, we know that the zero phonon line of unstrained SiV defects at low temperature is centered around 737 nm. We therefore investigate primarily sites in the sample, that feature high count rates in the corresponding detection window and low count rates in the disjoint interval (green circle in Fig. 4.4a and Fig. 4.4b). We utilize this strategy to also discard emitters with broad emission as they show comparable count rates in both detection windows (red circle in Fig. 4.4a,b).

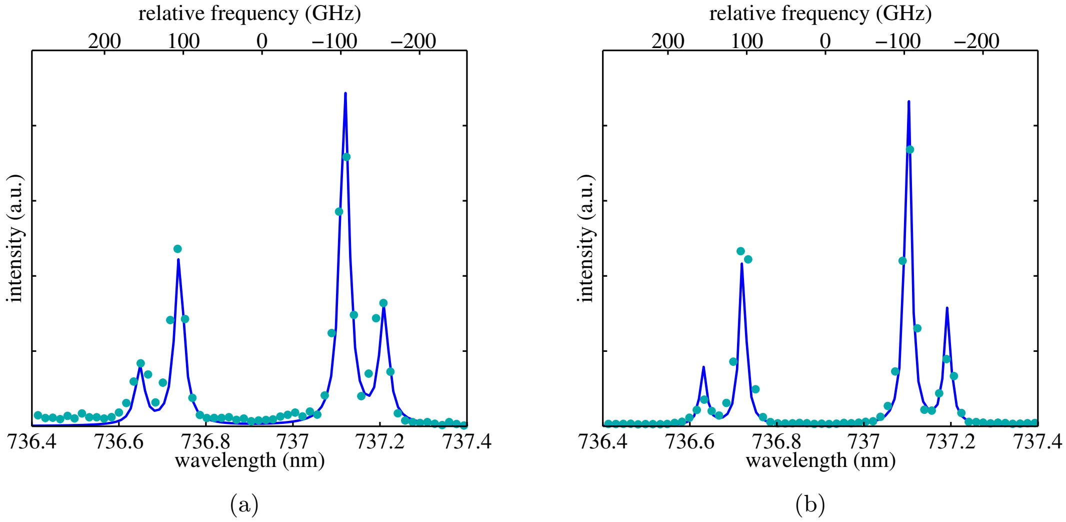

(a) (b)

Figure 4.5: Low temperature spectra of single emitters “SIL1” (a) and “SIL2” (b), excited using the parameters given in Fig. 4.3. Green dots are measurements and the blue solid lines are the result of the simulation for the two emitters.

Figure 4.5a shows the spectrum of emitter “SIL1” encircled in green in Figs. 4.4. A second emitter “SIL2” is depicted in Fig. 4.5b. Using the same procedure as described for Fig. 4.1b, the spectra (green dots) have been simulated using the theoretical model given in Chap. 2.3 (blue solid lines). The relative intensity of the peaks is different from the SiV ensemble which is due to a different temperature and resulting different thermalization [62]. As outlined earlier, the figures of merit to classify single SiV defects are the fine structure splittings $\Delta\nu_{g,e}$ for ground and excited state, respectively. Within our measurement resolution, these values are identical for emitters “SIL1”, “SIL2” and the ensemble sample (cf. Tab. 4.2). This measurement marks the first experimental observation of the low temperature spectrum of single SiV defects in bulk diamond. The high similarity between the two spectra and the fine structure spectrum of the reference SiV ensemble (Fig. 4.1b) proves our ability to deterministically fabricate single SiV defects in an “ideal”, low strain environment.

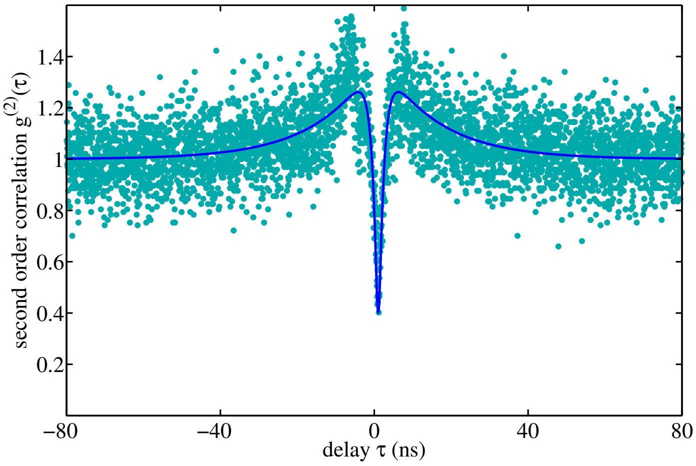

Figure 4.6: Intensity autocorrelation $g^{(2)}(\tau)$ measurement of emitter “SIL1”. The data (green dots) is fitted using a $g^{(2)}$-function for a three-level system, described in the main text. The autocorrelation for zero delay equals $g^{(2)}(\tau = 0) = 0.39$ without and $g^{(2)}(\tau = 0) = 0.26$ with correction for the timing jitter of avalanche photodiodes.

To verify that the emitters are single defects, we measure the intensity autocorrelation $g^{(2)}(\tau)$ of their emitted light using a Hanbury-Brown Twiss interferometer (see Sec.3.1.3). A typical autocorrelation measurement is shown exemplarily for emitter “SIL1” in Fig. 4.6. The data (green dots) has been fitted using the following $g^{(2)}$-function (blue solid line)

$$g^{(2)}(\tau) = 1 - (1 + a) \cdot \mathrm{e}^{-|\tau|/\tau_1} + a \cdot \mathrm{e}^{|\tau|/\tau_2}. \tag{4.1}$$

This function describes the underlying dynamics of a three-level system [56], where the *antibunching* time constant τ_1 is equal to the temporal separation between two consecutive photons. The *bunching* time constant τ_2 relates to a metastable shelving state which gives rise to values of $g^{(2)} > 1$, i.e. correlated emission for certain time delays [198]; the strength of the bunching is quantified by the parameter a. In the course of the fit, we calculate the coefficients to be $a = 0.5$, $\tau_1 = 1.3$ ns and $\tau_2 = 14.8$ ns. To account for the finite time response of the counting electronics used, the $g^{(2)}$-function in Eq. (4.1) has been convoluted with an instrument response function featuring a timing jitter of 354 ps [200, 210].

Deriving the intensity autocorrelation in the framework of quantum optics yields for zero delay $\tau = 0$ the value $g^{(2)}(0) = 1 - \frac{1}{n}$, where n is the expectation value of the photon number operator [149]. In an intuitive picture, this equals the number of emitters contributing to the emission [211]. Consequently, a threshold value of $g^{(2)}(\tau = 0) < 0.5$ indicates the presence of a single emitter. The obtained experimental value for $g^{(2)}(\tau = 0) = 0.26$ after subtraction of the influence of the timing jitter thus clearly identifies emitter “SIL1” as a single SiV center. The deviation from zero can be explained with the presence of an uncorrelated background emission, most likely due to a residual damage in the diamond film either from the focussed ion beam milling or from the implantation of Si atoms. We correct for the background luminescence by renormalizing the measured autocorrelation using a constant $\rho = S/(S+P)$, where S is the fluorescence of the emitter and P the background [117, 212]. The ratio ρ describes the probability that a detected photon originates from the SiV center and not from uncorrelated background source. It is a free parameter in the fit of the $g^{(2)}$-function and was estimated to be $\rho \approx 0.9$.

The measurement of the intensity autocorrelation for different excitation intensities can be used as a valuable tool to provide insight into the dynamics of electronic transitions. Neu *et al.* deduced transition rates for the phenomenological three-level system of single SiV centers in nanodiamonds, investigated both at room temperature and as function of temperature [56, 115, 117]. This requires to excite the emitter under investigation with laser intensities ranging from far below to above saturation power. While SiV defects in nanodiamonds show typical saturation powers between 10 − 100 µW [56], Sipahigil *et al.* recently showed that single SiV centers in bulk exhibit saturation powers of 20 − 30 mW [61]. Due to technical limitations in the current measurement configuration, these powers are challenging to achieve. Hence, we deliberately focus on the “stationary” description of the electronic states here, leaving the dynamics between these electronic states for future research.

Having reliably fabricated single SiV defects in an unstrained environment, we will explore the properties of these emitters in the following paragraphs. To begin with, we investigate the polarization of the four fine structure peaks of emitters “SIL1” and “SIL2”. Although we will anticipate some results from the following studies in magnetic fields (Sec. 4.1.4), the polarization can be used as an independent verification for the electronic structure deduced in Chap. 2.

4.1.3 Emission polarization of single emitters

This paragraph analyses the polarization of single SiV defects “SIL1” and “SIL2” introduced in the previous section. The polarization analysis of single emitter fluorescence gives a first hint towards the orientation and thus the symmetry of the defects. Furthermore, it can reveal the nature of dipole transitions. While former investigations on SiV polarizations exclusively studied the zero phonon line polarization at room temperature [58, 134], we here study for the first time the polarization of all fine structure lines individually. We already use some implications taken from the next section on Zeeman spectra (Sec. 4.1.4). However, a simplified level scheme for zero magnetic field will be sufficient for the discussion of the results. To measure the polarization, we use a combination of a rotating half-wave-plate and a fixed linear polarizer placed in the detection arm of the confocal microscope described in Sec. 3.1.3. For each angular setting of the half-wave plate, we acquire a photoluminescence spectrum using a grating spectrometer and integrate over the area of each fine structure peak. The integrated intensity is plotted in a polar diagram versus twice the angle of the half-wave-plate. Figures 4.7 and 4.8 show the polarization graphs for emitters “SIL1” and “SIL2”, respectively. The diamond sample has been mounted such that the crystallographic [110] axis coincides with the 0°-setting of the polarization detection. We therefore relate the angular axis of the polar diagrams directly to the crystallographic directions. The excitation laser (690 nm, 8 mW) was polarized

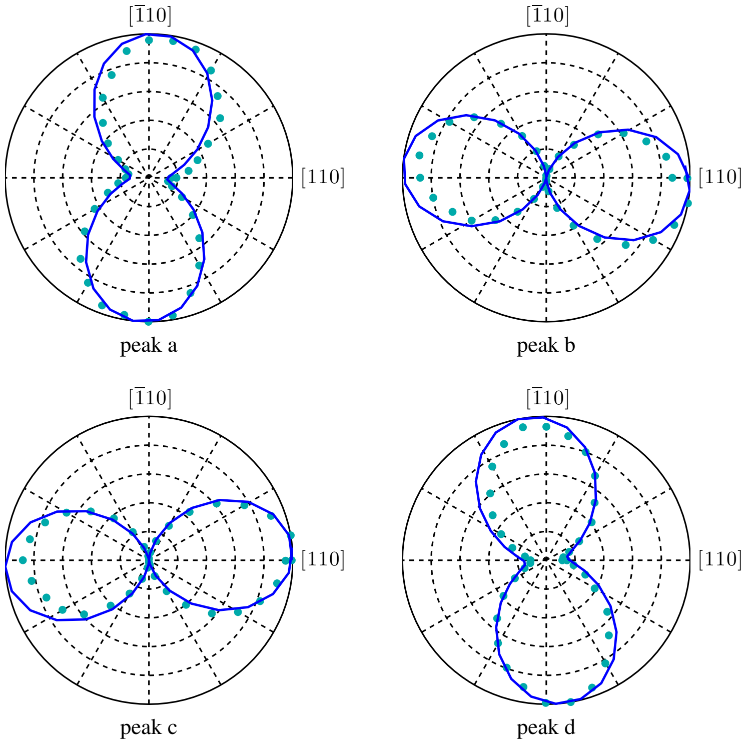

Figure 4.7: Emission polarization of emitter “SIL1”, individually measured for all four fine structure peaks at a temperature of $T = 15$ K and at zero magnetic field. The excitation laser (690 nm, 8 mW) was polarized along the [110] axis throughout all measurements. The data is depicted as cyan blue dots, the solid blue line is a simulation of the polarization described in the main text.

along the [110] axis throughout all measurements.

First, we focus on emitter “SIL1” (Fig. 4.7): The polarization of the fine structure lines can be grouped in two subsets. The inner transitions are polarized parallel to each other and perpendicular to the outer ones, where all polarization axes are parallel to the equivalent ⟨110⟩ directions. To further characterize the polarization graphs, we calculate the visibility

$$V = \frac{I_{max} - I_{min}}{I_{max} + I_{min}} \tag{4.2}$$

from the maximum (minimum) intensities I_{max} (I_{min}) of each polar diagram. The results for both emitters are given in Tab. 4.1. As it is evident from Tab. 4.1, the visibilities of the outer peaks a, d are inferior to those of the inner peaks b, c. Furthermore, we observe that peaks a and b are tilted by $8 \pm 4°$ away from the ⟨110⟩ direction. For emitter “SIL2”, we note that all peaks are turned by approximately 90°. The outer peaks a and d have a lower visibility, and they are tilted by $8 \pm 4°$ away from the ⟨110⟩ direction.

To compare the experimental data to the theoretical model of the SiV defect, developed in Chap. 2, we simulate optical dipole transitions and their resulting polarizations. While

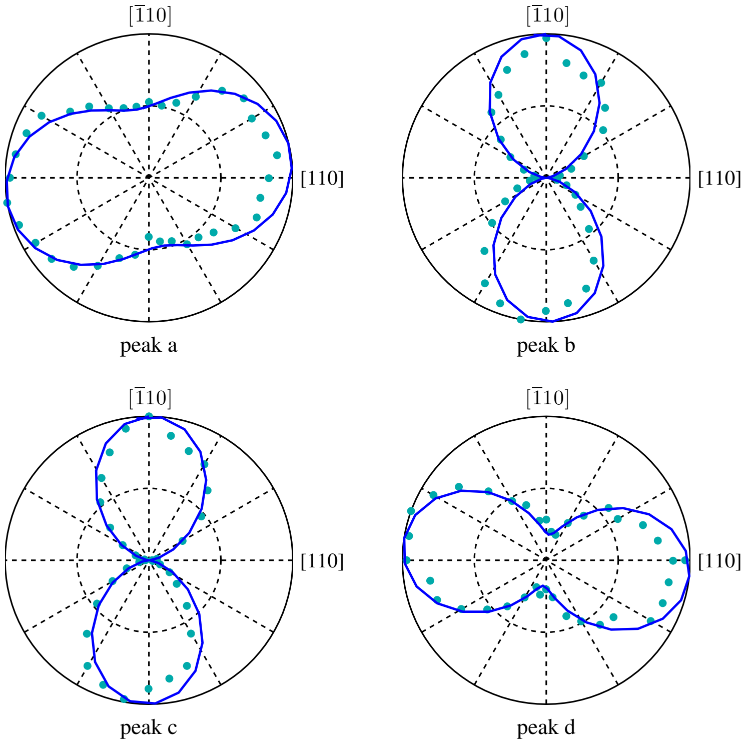

peak a

peak b

peak c

peak d

Figure 4.8: Emission polarization of emitter “SIL2”, individually measured for all four fine structure peaks. Excitation cf. Fig. 4.7. The data is depicted as cyan blue dots, the solid blue line is a simulation of the polarization described in the main text.

details on the calculation can be found in Sec. 2.3.1 and 2.3.2, we here outline briefly the major steps of the simulation. First, we calculate the eigenvectors for unstrained SiV defects at zero magnetic field. From the comparison of Zeeman spectra with the simulation in the following section, the leading electronic interaction on the orbital part of the SiV wave function is spin-orbit (SO) coupling (see Sec. 2.2.2). In a first approximation, we therefore only apply SO interaction as perturbation on the $e_{g,u}$ basis states of the unperturbed SiV center (see Sec. 2.1.4). This leads to the new eigenstates[1] depicted in Fig. 4.9a, where the orbital part can be expressed $|e_{\pm}\rangle = |e_x \pm i e_y\rangle$.

To characterize the dipole transitions, we calculate the expectation values $\langle \mathbf{p} \rangle$ of the dipole operator $\mathbf{p} = e\mathbf{r}$ for all optical transitions, where e is the elementary charge and $\mathbf{r} = (x, y, z)$ is the position operator. The resulting expectation values $\langle p_x \rangle, \langle p_y \rangle, \langle p_z \rangle$ are directly proportional to the respective field amplitudes A_x, A_y, A_z of the emitted light, and therefore relate to the polarization of the SiV fluorescence. The matrix elements of $\mathbf{p}$ and the calculation of expectation values are given explicitly in Sec. 2.3.1. It is important to note, that the expectation values are calculated always between an excited state e_u and a ground state e_g of the same spin projection, because the dipole operator only links

---

[1] We omit here the subscripts “g” and “u” designating the parity for ground and excited state, respectively, as their assignment in the graph is unambiguous.

Table 4.1: Visibilities for the polarization measurements of emitters “SIL1” and “SIL2”, given by Eq. (4.2).

emitter	Peak a	Peak b	Peak c	Peak d
SIL1 (exp.)	0.83	0.97	0.98	0.80
SIL1 (theor.)	0.75	1.00	1.00	0.78
SIL2 (exp.)	0.42	0.88	0.96	0.68
SIL2 (theor.)	0.35	1.00	1.00	0.70

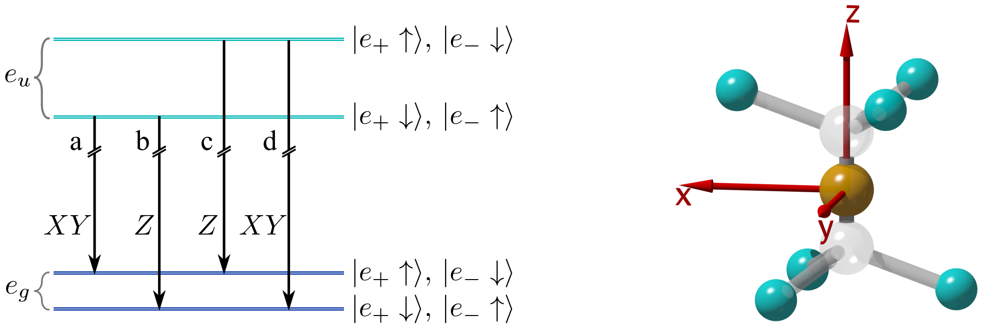

(a) (b)

Figure 4.9: (a) Simplified level scheme for zero magnetic field, taking into account only spin-orbit interaction. The orbital part of the wave function is expressed as $|e_\pm\rangle = |e_x \pm ie_y\rangle$. (b) Internal x, y, z axes of the SiV center as assumed in our model.

states of different parity and equal spin state ($\Delta m_s = 0$). The calculation shows that either $\langle p_x\rangle$ and $\langle p_y\rangle$, or $\langle p_z\rangle$ is non-zero. Hence in the approximation of pure SO coupling, a transition originates either from a Z-dipole and is linearly polarized, or it stems from an XY-dipole and is circularly polarized (when looking along the z-axis). The vertical arrows in Fig. 4.9a sum up the resulting dipole characters for the four transitions visible at zero magnetic field in this simplified picture.

The labels X, Y, Z for the dipole transitions refer to the internal coordinate axes x, y, z of the SiV center (cf. Fig. 4.9b). We project the electric field amplitudes onto orthogonal components in the (001) plane (Sec. 2.3.2). We then use a Jones calculus [177] to calculate the electronic field amplitudes measured by the combination of half-wave-plate and linear polarizer (all transformations matrices are given in Sec. 2.3.2). Finally, we calculate a normalized intensity for each transition by taking the absolute square of the respective field amplitudes.

With this procedure we simulate the polarization curves, depicted as blue solid lines in Figs. 4.7 and 4.8. We note the following remarks and results:

- The linear emission of the Z-dipole along the [111] z-axis of the SiV center appears

- due to the projection in the (001) plane - in $\langle 110\rangle$ direction. The projection does not reduce the visibility of this emission. Furthermore, it gives rise to our observation of two orientations separated by 90° (Figs. 4.7, 4.8). The XY-dipoles emit circularly polarized light in z-direction; in this direction one would observe a vanishing visibility $V = 0$ for a linear polarization analysis. Perpendicular to the z-axes, the circular components appear linearly polarized. As we observe the XY-dipoles from a finite angle, we see a superposition of linear and circular components, yielding a visibility V ranging from 0.35 to 0.78. The calculated directions and visibilities (cf. Tab. 4.1) are in good agreement with the experimental polarization measurements.

- While the discussion above serves as an intuitive explanation, it neglects the effects from the JT interaction. For a realistic description of the experimental data, we therefore calculate the eigenvectors taking into account the full interaction Hamiltonian, including Jahn-Teller (JT), interaction (Sec. 2.2.3). JT interaction lifts the orbital degeneracy by energetically favoring an alignment of the wave function in x- or y-direction. For a pure SO interaction, the resulting eigenstates consist of a *symmetric* superposition of e_x and e_y orbitals (e.g. $|e_+\rangle = |e_x\rangle + i|e_y\rangle$). Adding JT to the perturbation leads to a stronger contribution of either e_x or e_y in the eigenstates. This lowered orbital symmetry leads to deviations from a perfect XY-dipole emission.

- The main free parameters in this simulation are the coupling energies $\Upsilon^{JT}_{g,e}$ and $\lambda_{g,e}$ of JT and SO interactions and the spatial coefficients Υ_x, Υ_y of the JT interaction. The starting parameters for this simulation are obtained from Zeeman spectra for SiV ensemble and single emitter “SIL3” (cf. Sec. 4.1.4). The analysis of the Zeeman spectra shows that the SO coupling is about an order of magnitude stronger then the JT interaction, which justifies our simplified model above. The variation of Υ_x and Υ_y leads to a tilt of the peaks and a change in the polarization visibility for the outer peaks a and d. This is observed in particular for emitter “SIL2” which shows a relatively low visibility for peak a (Fig. 4.8).

- As we simulate the collection of XY- and Z-dipoles, we need to take into account their emission and collection through the microscope objective. We therefore weight the relative contributions from the three dipoles according to their orientation in the diamond lattice. The weighting factors η_x, η_y, η_z are directly proportional to the collection efficiency which we numerically calculate using the algorithm outlined in Ref. [117] (cf. Sec. 2.3.2). The weighting factors influence the relative peak height in the simulated spectra (Figs. 4.1b, 4.5a, 4.5b) and the visibility in the simulated polarization curves (Figs. 4.7, 4.8). Our analysis shows that, for a X-, Y- and Z-dipole under a flat diamond surface, the relative collection efficiencies scale as $1 : 0.6 : 0.8$. The numerical procedure employed does not allow to simulate the collection efficiency for emitters under solid immersion lenses. Yet, we observe similar relative peak heights for single emitters under SILs (Figs. 4.5a, 4.5b) and for the SiV ensemble under a flat surface. As a consequence, we assume that the influence of the SILs on the relative collection of the three dipole components is small.

The results of the polarization analysis have been published in Ref. [213], together with the results of the following section. Shortly after this publication, Rogers *et al.* published a similar study on the polarization of single SiV centers in (111) oriented single crystalline diamond [176]. We here summarize briefly their results and analyze them in the framework of the discussion above.

Rogers *et al.* also show room temperature measurements: First, they observe one possible alignment of the defect parallel to the (111) surface normal. Integrating over all fine structure lines, the polarization graph for this orientation shows almost zero visibility, which is consistent with our model: In this direction, only the XY dipoles contribute theoretically to the emission (the Z dipole does not emit in the direction of its axis). Looking in the z-direction, they therefore observe exclusively a circular polarization. Second, Rogers *et al.* observe two out of three orientations[2] at the tetrahedral angle 109.5° to the surface normal, separated from each other by 120°.

At low temperature and analyzing each fine structure peak separately, they also observe an almost unity visibility for the inner peaks b, c, and a slightly reduced visibility for the outer peaks a and d ($V_a = 85\%$ and $V_d = 71\%$). This is again consistent with our model as the authors of Ref. [176] observe the XY-, Z-dipoles also under a finite angle. Compared to our measurements, this angle is closer to 90°, therefore the outer peaks show a higher visibility than our measurements.

As a second reference, Brown and Rand investigated the polarization of SiV ensembles in mosaic type diamond on silicon at room temperature [134]. The technique employs a rotation of the incident polarization while keeping the sample and detection polarizer fixed, and in a second step, turning the sample while fixing incident and detected polarization. The measured polarization graphs are then compared with a theoretical model [136]. From the orientation and the contrast of their data in polarization graphs, they derived a orientation of SiV centers along $\langle 110\rangle$ crystal axes. The theoretical polarization curves for $\langle 110\rangle$ and $\langle 111\rangle$ oriented defects however only differ in the polarization contrast. The diamond film employed by Brown and Rand was grown on a silicon, which shows a considerable lattice mismatch. Hence, it stands to reason, that the SiV centers in their films are subject to crystal strain. We assume, that this strain field follows a statistical distribution. In Sec. 5.1.2, we show that crystal strain significantly modifies the polarization properties of the SiV center, and we tentatively suggest this to be an alternative explanation for the results of Brown and Rand.

In this section, we have shown that the polarization of unstrained, single SiV defects in bulk diamond can be successfully modeled using the theoretical description of the SiV in Chap.2. The polarization of single SiV centers has formerly been investigated by Neu *et al.* [117]. These studies have been carried out on isolated nanodiamonds at room temperature. A second publication by Riedrich-Möller *et al.* reports on the polarization of single SiV defects in heteroepitaxial diamond films on iridium [214]. Both investigations treat SiV centers in strained environments. As we have shown in Sec. 2.2.5, the theoretical

---

[2] The authors of Ref. [176] explain the absence of the third orientation, by a preferential creation of SiV centers along the other three orientations during growth. Preferential alignment of SiV defects during diamond growth has been reported earlier [63].

model of the SiV present in this work can be extended to strained SiV defects. These strained defects will be discussed in the next chapter (Sec. 5.1.2). In the following section, we investigate the effect of magnetic fields on SiV ensembles and single defects. We show that these measurements can be utilized as a further verification of the theoretical model.

4.1.4 Zeeman spectra of ensemble and single defects

In the preceding sections, we introduced the spectroscopic results on single SiV centers and on an SiV ensemble in low strain diamonds - the "workhorse" of this first part of the chapter. The results, we have already presented, give a first hint about the orbital part of the SiV electronic structure. In particular, polarization measurements on single defects are well consistent with an orbital splitting dominated by spin-orbit interaction.

In this section, we investigate the application of magnetic fields onto ensembles and single centers. These experiments represent the "heart" of the analysis of the electronic structure. As we will see, the Zeeman interaction lifts the spin degeneracy of the electronic states, providing a powerful tool to verify the theoretical assumptions of Chap. 2. While this section covers the Zeeman spectra and - for direct comparison - their simulation, the implications for the electronic levels will be discussed in the following section.

The experiments involving magnetic fields have all been carried out in the bath cryostat setup described in Sec. 3.1.3. They took place at the Cavendish Laboratory (group of Prof. Atatüre) at the University of Cambridge, United Kingdom, and were published in collaboration with the members of the Atatüre group [213]. With the sample being cooled to 4.7 K, we measure photoluminescence (PL) spectra for the ensemble sample (cf. Sec. 4.1.1) and single SiV defects in the sample with solid immersion lenses (cf. Sec. 4.1.2) in dependence of the applied magnetic field. The magnetic field is generated using a superconducting magnet and it is oriented in a Faraday configuration. The samples are mounted such that the magnetic field is collinear with the crystallographic [001] direction. The excitation laser for PL measurements is tuned to 700 nm, at an average excitation power of 2 mW (measured before the objective lens consisting of a single aspheric lens with $NA = 0.66$). We display the PL spectra in dependence of the magnetic field as a two-dimensional color plot (called a "Zeeman spectrum"), where the intensity of the peaks is always plotted in logarithmic scaling.

Figure 4.10a displays the Zeeman spectrum for the SiV ensemble. We focus our attention solely to the four fine structure peaks of the ^{28}Si isotope, which are visible as the four strongest peaks at zero magnetic field. Each of the four peaks splits into several components. To facilitate the counting of the lines, we display the Zeeman spectrum together with the theoretical prediction of optical transitions as a guide to the eye (white lines in Fig. 4.10b). We count a total number of 16 peaks (numbered from $A1$ to $D4$) which points towards a spin 1/2 system: If each doubly degenerate level is split into two by the magnetic field, then there are 16 possible transitions at finite field. Furthermore, there are several lines "bending away" from each other, predominantly between 2 and 3 Tesla. These *avoided crossings* are a sign of spin-orbit interaction (cf. Sec. 2.2.2). Finally, we observe that the relative intensity of the split peaks are different and change with increasing magnetic fields. This points towards towards a change in the dipole transition moments for the optical transitions.

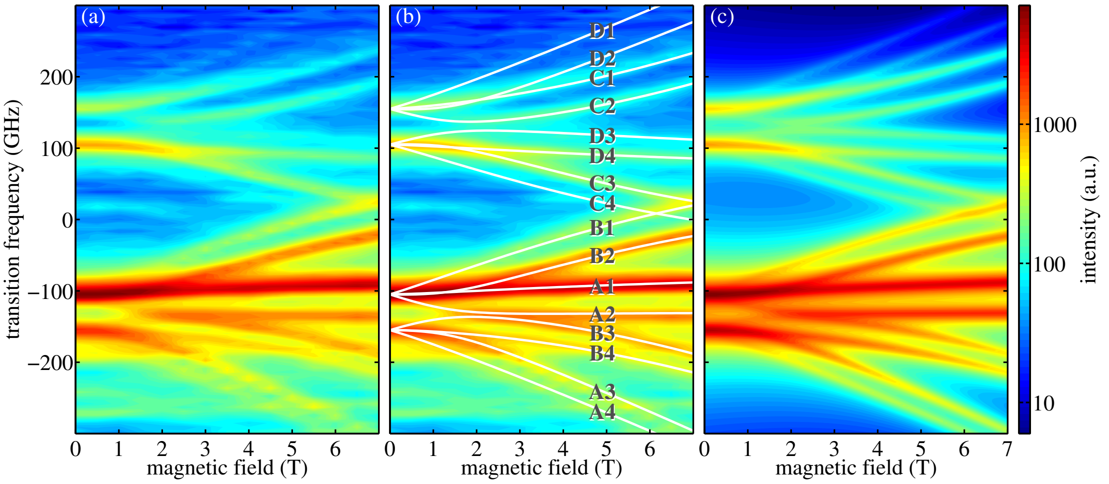

Figure 4.10: Measured Zeeman spectrum of an SiV ensemble (a,b), shown as photoluminescence spectra (in relative frequency units) in dependence to the applied magnetic field. The color (from blue to red) indicates the peak intensity in logarithmic scaling. Optical transitions calculated from the theoretical model described in the text are shown as solid white lines in panel (b) over the experimental data. For comparison, panel (c) shows the simulated intensity in the same color scale as panels (a,b).

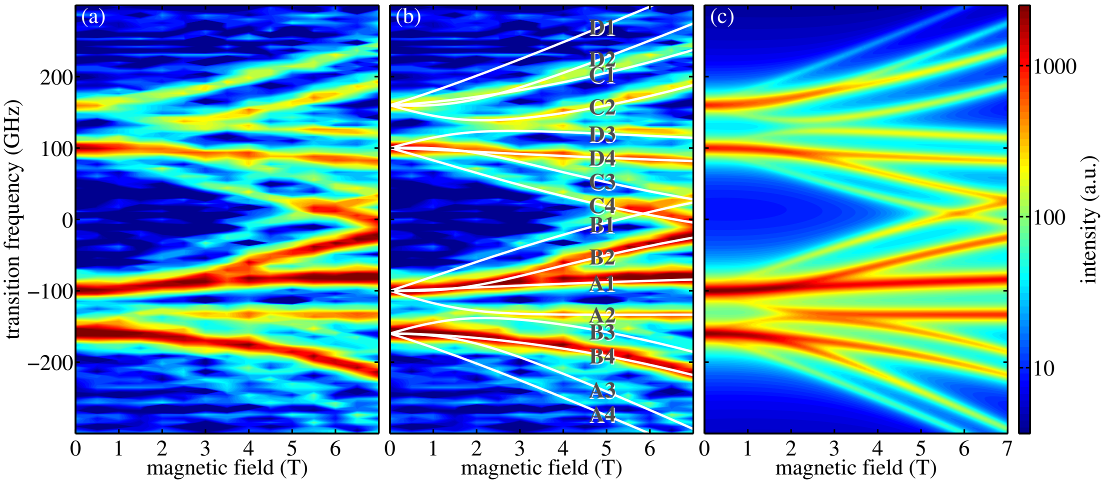

Figure 4.11: Measured Zeeman spectrum of single SiV defect “SIL3”. The presentation of the data and simulation is equal to the one in Fig. 4.10.

Before we describe the measured Zeeman spectra with our theoretical model of the SiV center, we compare the ensemble spectra of Fig. 4.10 with the Zeeman spectrum of another single emitter "SIL3", depicted in Fig. 4.11. The splitting pattern of single center "SIL3" shows a high similarity to the splitting of the ensemble sample. Consistent with the other single centers "SIL1" and "SIL2", the spectrum of "SIL3" shows a smaller line width than the SiV ensemble and therefore makes the assignment of optical transitions easier. We note that the "branch" starting from the lowest frequency peak (at ≈ -150 GHz, corresponding to peak d at 0 T) has relatively high intensity. This can be successfully modeled by adjusting the relative collection efficiencies from the X, Y, Z dipole contributions (see below).

In the following part, we briefly describe the main points of the theoretical approach used in order to simulate the Zeeman spectra of both single emitter and ensemble. We recall the SiV center's molecular structure belonging to the D_{3d} symmetry group in our model. In this approach, the high symmetry axis of the defect is along the $\langle 111 \rangle$ crystal directions. Therefore, all equivalent orientations of the defect have same relative angle 54.7° between the magnetic field and their symmetry (z) axis. This explains why ensemble and single SiVs split into the same number of peaks under exposure of magnetic fields, and in turn proves thes assumption of the $\langle 111 \rangle$ orientation of the defect.

To take into account the effect of the magnetic field, we add a Zeeman perturbation term $\mathbb{H}^{Z}_{g,e}$ to the interaction Hamiltonian (cf. Sec. 2.2.6)

$$\mathbb{H}^{Z}_{g,e} = \mathbb{H}^{Z,L}_{g,e} + \mathbb{H}^{Z,S}_{g,e} = \gamma_L \mathbf{L} \cdot \mathbf{B} + \gamma_S \mathbf{S} \cdot \mathbf{B}, \tag{4.3}$$

with the orbital and electron gyromagnetic ratios $\gamma_{\mathrm{L}} = \mu_B/\hbar$, $\gamma_{\mathrm{S}} = 2\mu_B/\hbar$ (μ_B Bohr magneton) and the magnetic field $\mathbf{B} = (B_x, B_y, B_z)$, expressed in the internal reference frame of the SiV (Fig. 4.9b). We note, that due to the off-axis alignment of the magnetic field, all three components B_x, B_y, B_z are non-zero. The spin operator $\mathbf{S} = \frac{\hbar}{2}(\sigma_x, \sigma_y, \sigma_z)$ is expressed using Pauli spin matrices. The perturbation $\mathbb{H}^{Z}_{g,e}$ is identical for ground and excited state (subscripts g, e).

As shown in Sec. 2.2.6, the orbital Zeeman interaction can be simplified to $\mathbb{H}^{Z,L}_{g,e} = \gamma_L L_z B_z$, as the transverse terms L_x, L_y of the orbital momentum operator $\mathbf{L}$ only couple to a_{1g} and a_{2u} states which are far in energy. In the presence of dynamic Jahn-Teller coupling, defect centers in solids often show a quenching of the orbital momentum which results also in a quenching of the orbital gyromatic ratio [163, 172]. To account for this effect, we introduce a quenching factor q which however only acts on γ_L.

Adding the Zeeman effect to the perturbation terms, the overall interaction Hamiltonian is given by

$$\begin{aligned} \mathbb{H}_{\mathrm{g,e}} &= \mathbb{H}^{0}_{\mathrm{g,e}} + \mathbb{H}^{\mathrm{SO}}_{\mathrm{g,e}} + \mathbb{H}^{\mathrm{JT}}_{\mathrm{g,e}} + \mathbb{H}^{\mathrm{Z,L}}_{\mathrm{g,e}} + \mathbb{H}^{\mathrm{Z,S}}_{\mathrm{g,e}} \\ &= \mathbb{H}^{0}_{\mathrm{g,e}} + \lambda_{\mathrm{g,e}} L_{\mathrm{z}} S_{\mathrm{z}} + \Upsilon^{\mathrm{JT}}_{g,e} + q\gamma_{\mathrm{L}} L_{\mathrm{z}} B_{\mathrm{z}} + \gamma_{\mathrm{S}} \mathbf{S} \cdot \mathbf{B}. \end{aligned} \tag{4.4}$$

$\mathbb{H}^{0}_{\mathrm{g,e}}$ is the non-perturbed Hamiltonian, $\mathbb{H}^{\mathrm{SO}}_{\mathrm{g,e}} = \lambda_{\mathrm{g,e}} L_{\mathrm{z}} S_{\mathrm{z}}$ models SO interaction with the coupling constant $\lambda_{\mathrm{g,e}}$ (cf. Sec. 2.2.2), and $\Upsilon^{\mathrm{JT}}_{g,e}$ accounts for Jahn-Teller interaction (cf. Sec. 2.2.3). All operators are expressed in the basis states

$$\{|e_{\mathrm{gx}} \uparrow\rangle, |e_{\mathrm{gx}} \downarrow\rangle, |e_{\mathrm{gy}} \uparrow\rangle, |e_{\mathrm{gy}} \downarrow\rangle\} \text{ for the ground state and} \tag{4.5a}$$

$$\{|e_{\mathrm{ux}} \uparrow\rangle, |e_{\mathrm{ux}} \downarrow\rangle, |e_{\mathrm{uy}} \uparrow\rangle, |e_{\mathrm{uy}} \downarrow\rangle\} \text{ for the excited state.} \tag{4.5b}$$

Solving the secular equation defined by the Hamiltonian in Eq. (4.4) yields the energies E_i of each state i at a given magnetic field value. We note, that the fine structure at zero magnetic field is given by the SO and JT interactions only and is equal to $\left(\lambda_{\mathrm{g,e}}^2 + 4\Upsilon_{\mathrm{g,e}}^2\right)^{1/2}$. This quantity is set equal to the experimentally observed ground and excited state splittings $\Delta\nu_{g,e}$ and we use the ratios between SO and JT $r_{\mathrm{g,e}} = \lambda_{\mathrm{g,e}}/\Upsilon_{\mathrm{g,e}}$ as free parameters. These ratios dictate the slopes of split fine structure lines and the presence or absence of avoided crossings.

We calculate the optical transition frequencies $\nu_j = \frac{1}{\hbar}(E_i - E_f)$, $j = A1 \dots D4$, between the electronic levels E_f, E_i in ground and excited state, and compare them with the peak positions in the Zeeman spectra. In this procedure, we vary only $r_{g,e}$ and the quenching factor q, such that we iteratively fit transition frequencies ν_j to the experimental data. It is important to note that the outer lines $A4$ and $D1$ are not affected by r_g, r_e and thus provide an independent control for the quenching factor q which minimizes potential mutual dependences of the parameters. We observe that $A4$ and $D1$ can only be fit using a strong quenching ($q \in [0.1; 0.2]$) of the orbital magnetic moment. Subsequently, r_g and r_e are adjusted to fit all inner lines. In a first step, this fit is obtained without taking into account transition probabilities and peak shapes. The resulting optical transition are shown as solid white lines in Figs. 4.10b and 4.11b, and we list parameters involved in Tab. 4.2.

Table 4.2: Resulting parameters for SiV ensemble and single SiV defects "SIL1" - "SIL3" depicted above.

emitter name	$\Delta\nu_g$	$\Delta\nu_e$	λ_g	$\Upsilon_{g,x}$	$\Upsilon_{g,y}$	λ_e	$\Upsilon_{e,x}$	$\Upsilon_{e,y}$	f
				(GHz)					(-)
ensemble	50	260	45	11		257	20		0.1
SIL1	50	260	40	14	5	210	75	12	0.1
SIL2	50	260	48	7	2	257	20	0	0.1
SIL3	60	260	53	14		257	20		0.1

As a second step, we calculate intensity of the optical transitions. Similar to the proceeding for the polarization analysis, we calculate the dipole transition moments p_x, p_y, p_z for all optical transitions j. The probability of each transition is proportional to the absolute square of the respective expectation value of the dipole matrix elements $|\langle \mathbf{p} \rangle|^2 = |\langle \varphi_f | \mathbf{p} | \varphi_i \rangle|^2$, with φ_i (φ_f) being an eigenvector for the excited (ground) state (Sec. 4.1.5). In the course of acquiring the Zeeman spectra, no polarization optics are placed in the detection path, therefore all polarization components are detected. Hence, we sum up the X, Y, Z dipole contributions for each transition.

In this process, we again take into account the collection and emission efficiencies η_x, η_y, η_z of each dipole component (X, Y, Z). For the SiV ensemble in bulk diamond (Fig. 4.10), the collection efficiencies can be calculated numerically with high accuracy [117]. For single emitter "SIL3", the parameters η_x, η_y, η_z are fitted to the Zeeman spectra.

Furthermore, the relative intensity of an optical transition starting from excited state

i is proportional to the occupation n_i of state i. For acquiring the Zeeman spectra in Figs. 4.10 and 4.11, we excite the SiV centers using a non-resonant laser (tuned to 700 nm). We assume that this non-resonant excitation populates a higher lying level which decays via a non-radiative transition into the excited states (with equal branching ratio) [176]. For zero magnetic field, Clark *et al.* showed that the excited states thermalize among each other [62]. Due to this thermalization, the probability of occupation n_i of state i is given by a Boltzmann distribution

$$n_i(T) = n_A \exp\left(-\frac{E_i - E_A}{k_B T}\right). \tag{4.6}$$

Here, T is the sample temperature, n_A the population of the lowest energy excited state with energy E_A, E_i the energy of state i and k_B the Boltzmann constant. When applying magnetic fields, the excited states thermalize following spin-preserving selection rules (Sec. 4.2). We will show later that the Boltzmann distribution in Eq. (4.6) however yields an approximative agreement for non-resonant excitation.

In summary, each optical transition j is expressed by a Lorentzian peak function

$$L_j(\nu) = \frac{2}{\pi} \frac{I_j \Gamma}{2(\nu - \nu_j)^2 + \Gamma^2}, \tag{4.7}$$

centered at frequency ν_j which we calculated above. The intensities I_j are proportional to the dipole transition moments weighted with the respective collection efficiency, i.e.

$$I_j = n_i \left(\eta_x \left|\langle\varphi_f|p_x|\varphi_i\rangle\right|^2 + \eta_y \left|\langle\varphi_f|p_y|\varphi_i\rangle\right|^2 + \eta_z \left|\langle\varphi_f|p_z|\varphi_i\rangle\right|^2\right). \tag{4.8}$$

The full width at half maximum Γ for the Lorentz peaks is set equal to the line widths observed for single center "SIL3" ($\Gamma = 5$ GHz) and SiV ensemble ($\Gamma = 10$ GHz), respectively. We note, that the resolution of the line width for "SIL3" is limited by the spectral resolution of the grating spectrometer used.

The resulting simulations for the overall intensity of the optical transitions are depicted in Figs. 4.10c and 4.11c. We describe correctly all crossings and avoided crossings, and reproduce all line intensities to a high degree of accuracy. A particular example is transition $D1$, which has a low transition dipole moment as it is spin forbidden. This selection rule is weakened by transverse spin components S_x, S_y in the Zeeman term $\mathbb{H}_{g,e}^{Z,S}$. The resulting low intensity of $D1$ is clearly visible both in the experimental data (Fig. 4.10) and the simulation. At high magnetic fields, the dipole moments for optical transitions are changed by the increasing influence of the Zeeman interaction. This effect is also correctly predicted by our theoretical simulation.

The impressive agreement between simulation and experimental data is an important validity check for the theoretical model that forms the basis of this simulation. It is worth repeating, that – although the simulation process outlined above has a certain complexity – we restrict the number of free parameters to a minimum in this simulation and assure that the resulting parameter set (Tab. 4.2) is unambiguous. In the following section we now discuss the level scheme resulting from the simulations above.

4.1.5 Discussion of the electronic structure of unstrained silicon vacancy centers

For all SiV emitters investigated in the previous sections, we have shown a high consistence between the experimental data and the theoretical model which we introduced in Chap. 2. In this paragraph, we study the implications that arise from the actual set of parameters which was presented in the Tab. 4.2. Hereby, we again treat the SiV ensemble as the reference case.

For all emitters, the quotient of the spin-orbit (SO) coupling constant $\lambda_{g,e}$ over the Jahn-Teller (JT) interaction strength $\Upsilon_{g,e}$ is considerably larger than one, both for ground and excited state. The Zeeman interaction scales linear with the magnetic field strength $\mathbf{B}$; the proportionality factor is given by the gyromagnetic ratios γ_L and γ_S of orbit and spin. As the orbital magnetic moment is observed to be strongly quenched, the spin splitting is the leading term, scaling at ≈ 14 GHz/T. This implies, that the SO coupling is the leading perturbation for the measurements presented here.

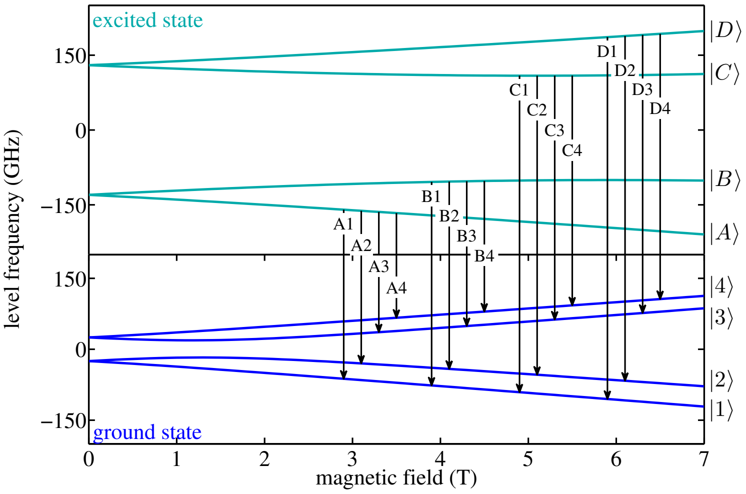

Figure 4.12: Calculated splitting of SiV electronic levels for increasing magnetic field. Ground and excited state labeled according to the letters and numbers at the right of the panel. Optical transitions between all levels indicated by black arrows and correspond to white solid lines in Fig. 4.10b. The curves represent the simulation parameters for the SiV ensemble.

When analyzing Zeeman spectra and polarization graphs, we diagonalize the full interaction Hamiltonian (Eq. (4.4)) and calculate its eigenvalues and eigenvectors of each electronic state. The eigenvalues are equal to the energies of the electronic ground and excited states (Fig. 4.12). The numerical calculation of eigenvalues makes an explicit assignment of optical transition frequency possible. We display the optical transitions as vertical arrows linking the electronic states in Fig. 4.12.

We observe that all energy levels split in two components as the magnetic field is applied. While this appears to be consistent with a spin $S = 1/2$-system as predicted by the theoretical model, we need to keep in mind that we deal with a strongly SO coupled system. The manifestation of SO coupling is the strong avoided level crossings visible in the ground state at $B \approx 2$ T and in the excited state at $B \approx 5$ T.

In addition to the eigenvalues, diagonalizing Hamiltonian (4.4) allows to calculate the eigenvectors of the system. We label the eigenvectors in the ground state with $|1\rangle, \dots, |4\rangle$ and in the excited state with $|A\rangle, \dots, |D\rangle$; this also explains the labels of the optical transitions, e.g. $A1$ denotes a transition from states $|A\rangle$ to $|1\rangle$. As the Hamiltonian (4.4) is expressed in the basis of the many-electron SALCs of type $|e_{x,y}\rangle| \uparrow, \downarrow\rangle$ (basis states in (4.5)), the diagonalization of Hamiltonian (4.4) yields eigenvectors in linear combinations of these basis vectors. Since the leading perturbation of the electronic states is SO coupling, it would stand to reason to transform the eigenvectors to the basis $e_\pm = e_x \pm i e_y$ which are the eigenfunctions of the SO coupled system. The spin part of the eigenstates is not affected by this transformation.

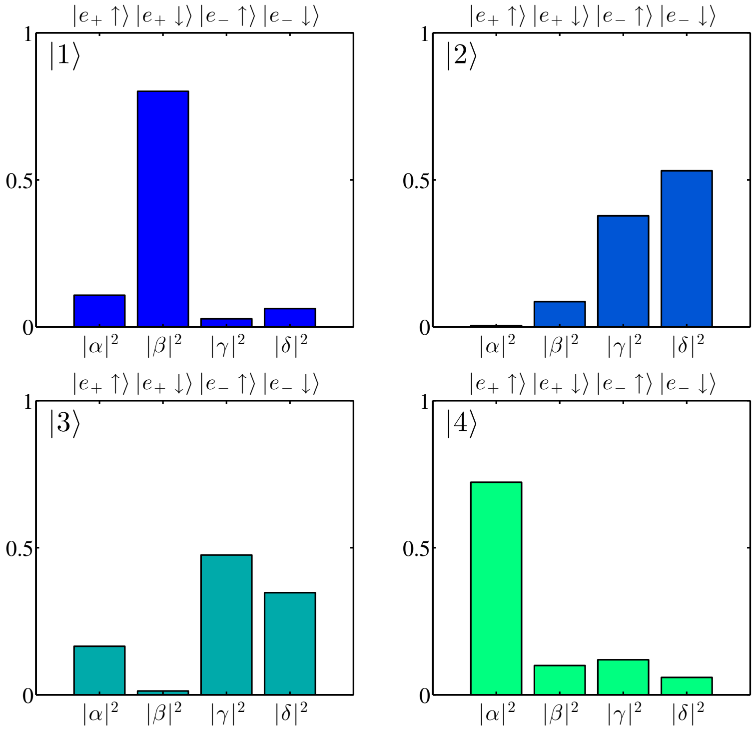

Figure 4.13: Ground state eigenvectors $|1\rangle, \dots, |4\rangle$ of the SiV center at a magnetic field of $B = 4$ T, resulting from the numerical analysis of the SiV ensemble. We plot the absolute squares of the coefficients $\alpha, \beta, \gamma, \delta$ for the linear combination of basis vectors (depicted over each bar graph). This corresponds to the probability of finding the electronic states in the respective orbital state $|e_\pm\rangle = |e_x\rangle \pm i|e_y\rangle$ and spin state $|\uparrow, \downarrow\rangle$.

The eigenvectors are then written as linear combinations of type (cf. Sec. 2.2.2)

$$|\varphi\rangle = \alpha|e_+\uparrow\rangle + \beta|e_+\downarrow\rangle + \gamma|e_-\uparrow\rangle + \delta|e_-\downarrow\rangle, \tag{4.9}$$

where $\varphi = A, \ldots, D, 1 \ldots, 4$, and $\alpha, \beta, \gamma, \delta$ are in general complex coefficients of the linear combinations. In Fig. 4.13 and 4.14, we display the absolute squares $|\alpha|^2, \ldots, |\delta|^2$ for all ground and excited states at $B = 4$ T, respectively. The absolute squares of the coefficients are equal to the probability of finding the electronic states in a given orbital and spin state. We observe, that the excited states are dominated each by one particular basis state, and therefore also by one particular spin state. We now quantify this spin "purity" in an explicit manner.

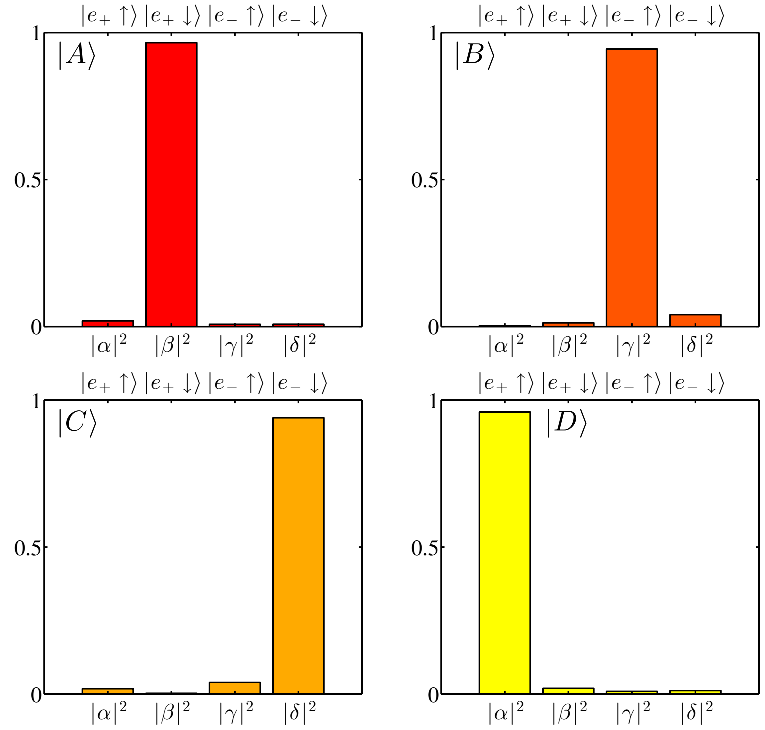

Figure 4.14: Excited state eigenvectors $|A\rangle, \ldots, |D\rangle$ of the SiV center at a magnetic field of $B = 4$ T, resulting from the numerical analysis of the SiV ensemble. We use the same plotting scheme as in Fig. 4.13.

Having obtained the eigenvectors of each state, we build the density matrix for a particular state, e.g. $\rho_A = |A\rangle\langle A|$. The diagonal elements of this density matrix then correspond to the absolute squares plotted in Figs. 4.13 and 4.14. As a second definition, we set the term *spin polarization* P equal to the expectation value of the spin projection[3] σ_z along the z-axis $P_A \equiv \langle \sigma_z \rangle = \mathrm{Tr}(\rho_A \sigma_z)$. The phrase spin polarization originally stems from the description of an ensemble of particles where "polarization" refers to the fraction of particles having their spin aligned to a certain axis (e.g. Stern-Gerlach-type experiments). This notion has been generalized to describe single particles where spin polarization is the degree to which the spin of the single particle is aligned with a reference

---

[3] The spin projection σ_z is expanded in our case to a 4×4-matrix (to fit the dimensions of the Hilbert space) by the direct product of the known Pauli σ_z-matrix with a 2×2-identity matrix.

axis [215]. We note that $|P| \leq 1$ and that for $P = \pm 1$, the eigenvalue of the spin z-projection σ_z is ± 1. For $P = 0$, we observe a spin mixture that has no defined projection whatsoever.

Table 4.3: Spin polarizations P for ground and excited states.

gnd. states	$\|1\rangle$	$\|2\rangle$	$\|3\rangle$	$\|4\rangle$
P	-0.73	-0.23	0.28	0.68
exc. states	$\|A\rangle$	$\|B\rangle$	$\|C\rangle$	$\|D\rangle$
P	-0.95	0.89	-0.89	0.94

The calculation of the spin polarization P for all four ground and excited states (Tab. 4.3) confirms the spin properties of the states already apparent from Figs. 4.13, 4.14: While all excited states exhibit a high spin polarization $|P| \geq 0.89$, the ground states show a non-uniform result: The outer levels $|1\rangle$ and $|4\rangle$ still evidence a moderate spin polarization $|P| \approx 0.7$, but the levels $|2\rangle$, $|3\rangle$ are strongly mixed with $|P| \leq 0.28$.

The reason for the difference on spin mixing for ground and excited state lies in the complex interplay of the different perturbation terms: Coming from an atomic physics background with the picture of a simple hydrogen atom in mind, it is already counterintuitive that the strong SO coupling does not mix spin states. The reason for this particularity is the (finite) D_{3d} symmetry of the SiV defect – in contrast to the full rotation symmetry of an atomic system. Owing to this symmetry, $\mathbb{H}_{SO}$ only acts on the S_z-component and neither on S_x nor S_y. The only interaction acting on S_x and S_y is in fact the spin part of the Zeeman interaction $\mathbb{H}^{Z,S} = \gamma_S(B_xS_x + B_yS_y + B_zS_z)$. Against them, SO coupling even acts as a "shielding" mechanism: A strong SO coupling separates states in energy which would be mixed via transverse Zeeman terms B_xS_x, B_yS_y. Therefore the overlap of these states is small and there is no spin mixing.

Hence, in the excited state, the SO coupling strength $\lambda_e \approx 260$ GHz (Tab. 4.2) is considerably larger than the transverse Zeeman contributions $\gamma_S(S_xB_x + S_yB_y) \leq 55$ GHz (for a maximum field strength of $B = 7$ T). In contrast, the transverse Zeeman terms are comparable to the ground state SO coupling $\lambda_g \approx 45$ GHz, which explains the stronger mixing in ground state. A further experimental evidence of spin mixing in the ground state is the observation of all 16 possible transitions in the Zeeman spectra: If the ground state had a spin polarization similar to the excited state, then the selection rule $\Delta m_S = 0$ for optical dipole transitions would suppress spin forbidden transitions and we would observe less lines in the Zeeman spectra. As the ground states $|1\rangle$ and $|4\rangle$ exhibit a moderate spin polarization, these selection rules are visible in the spectra (Figs. 4.10, 4.11): Transitions $A1$ and $B4$ are spin allowed and show a high intensity; transitions $A4$ and $B1$ are forbidden and show a low intensity as we have discussed earlier.

All the arguments presented in this section yield a consistent picture of the SiV electronic structure. Unfortunately, there is little literature on the SiV defect to compare our results to: As discussed in Sec. 4.1.3, the results on polarization of single SiV centers are confirmed by a very recent publication from Rogers *et al.* [176]. For the Zeeman spectra, to the best of our knowledge, there is only one measurement conducted by Sternschulte *et al.* [133]: Their investigations comprise Zeeman spectra on a homoepitaxial CVD diamond containing an ensemble of SiV centers, similar to the reference ensemble we present here. The magnetic field was aligned parallel to the crystallographic axes [001], [110], [111] (details of this paper are discussed in Chap. 1). The characteristics of the Zeeman spectrum in [001]-direction are comparable to the spectrum shown in Fig. 4.10, however the line width of the ensemble is larger than in our measurement. This obviously make a clear assignment of optical transitions challenging for the authors. In conclusion, Sternschulte *et al.* do not establish a theoretical model to describe the Zeeman spectra, but infer from the appearance of the splitting pattern and the number of split components an SiV orientation along the $\langle 100 \rangle$ axis. This orientation would give rise to a monoclinic symmetry of the SiV center, in which no orbital degeneracy [132] exists. Hence, the explanation of the four level fine structure at zero magnetic field would require different mechanisms, such as tunnel-coupling [62]. The authors of Ref. [133] however state that other models are feasible to explain their findings. We will analyze the experimental results of Sternschulte *et al.* in Sec. 5.1.1 in the framework of the theoretical model presented here.

Furthermore, it would be interesting to measure the polarization properties of the split fine structure components in a magnetic field for emitter “SIL3”, similar to the measurements shown in Sec. 4.1.2. However, due to the limited collection efficiency of the experimental setup employed for the Zeeman spectra, most of the split fine structure components show an insufficient signal-to-noise ratio for a detailed polarization analysis.

Coming back to the results presented here, we conclude for the first part of this chapter that we achieved the fabrication of SiV centers both on ensemble and single emitter level. All SiV centers created respond with the same spectral properties to all experiments we conducted on them. In particular, we have seen that the four excited state eigenvectors show a distinct spin polarization. In the following part of this chapter, we investigate the spin polarization in greater detail and show that we can distinguish the different spin states via a selective optical excitation of the excited state levels.

4.2 Spin tagged fluorescence using resonant excitation

This second part of the experimental chapter covers follow-up experiments that base upon the experimental confirmation of the theoretical model of Chap. 2. We present a direct readout scheme for the spin projection in the SiV excited state. This scheme uses spectroscopy of the SiV zero phonon line while performing resonant optical excitation (so-called resonance fluorescence). We briefly explain the experimental procedure and the main results on the SiV ensemble in Sec. 4.2.1.

The experiments of this section have again been achieved together with Tina Müller and Benjamin Pingault at the Cavendish Laboratory of the University of Cambridge, United Kingdom, and have been published in Refs. [65] and [64]. We stress however, that the discussion in these references employs another, slightly more phenomenological level scheme for the SiV center. We present here a rigorous analysis of the experiments, and prove that the level scheme of the SiV center obtained from Zeeman spectra correctly predicts the results of spin readout (Sec. 4.2.2).

4.2.1 Experimental results for resonant excitation of single fine structure lines

In the previous section, we discussed measurements using non-resonant optical excitation. For color centers in diamond, such a non-resonant excitation is common practice because the electronic excited states couple to vibrational states forming higher lying vibronic states. These states can be populated when exciting non-resonantly and relax quickly to their vibrational ground state [216]. For SiV centers, it has been shown that an excitation with laser light in a broad spectral range (down to 480 nm [141]) is possible. As we have seen in Sec. 4.1.4, non-resonant excitation populates *all* excited states of the SiV center, and they all contribute to the optical emission. If we want to populate a *particular* excited state, we therefore need to perform resonant optical excitation. At the same time, we probe the fluorescence from optical zero-phonon transitions. When using a confocal reflection microscope, this fluorescence is overlain by the excitation laser with up to 7 orders of magnitude higher intensity. Hence, we here suppress the excitation laser by placing a linear polarizer in the microscope collection arm that is perpendicular to the incoming linearly polarized laser field, providing an extinction of the laser greater than $2 \cdot 10^6$ [64]. This technique has been demonstrated successfully on single quantum dots [217] and is called resonance fluorescence.

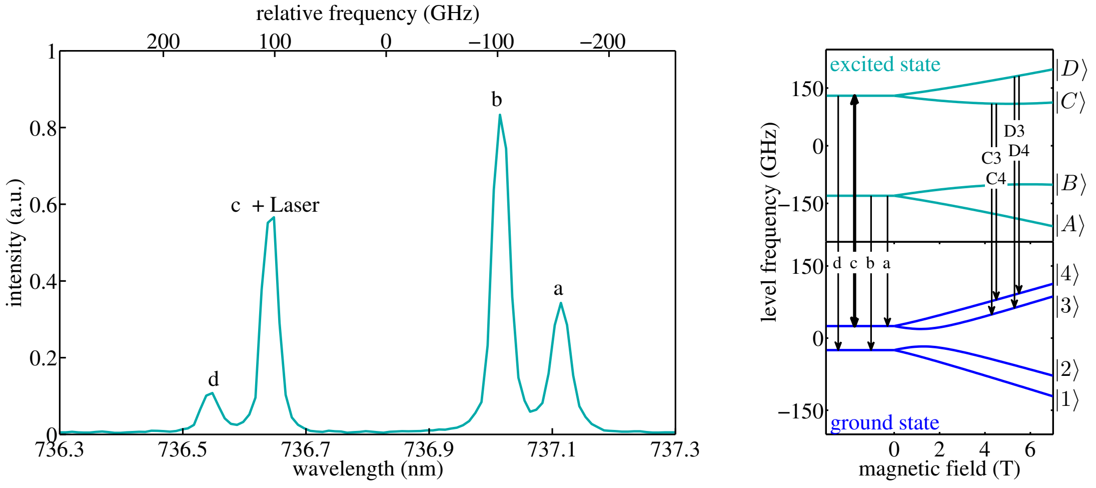

(a) (b)

Figure 4.15: Resonant excitation of an ensemble of SiV defects at zero magnetic field. The excitation laser is brought into resonance with transition c (panel (b), thick double-headed arrow), and is suppressed in the detection arm using crossed polarizers. The fluorescence spectrum (a) shows residual laser light overshadowing luminescence from transition c, and emission from the SiV centers for transitions a, b, d [64].

To show the potential of this technique, we display exemplarily a resonance fluorescence spectrum of the SiV ensemble in Fig. 4.15a. For this measurement, we operate a zero magnetic field giving rise to the simple four line SiV fine structure. The excitation laser is brought into resonance with transition c of the fine structure. The residual laser light after suppression with crossed polarizers is weak enough to be separated in wavelength from the SiV emission on the spectrometer and no additional spectral filters are needed. Although this suppression is highly dependent on the laser wavelength and needs to be re-aligned for the excitation of each transition, we stress that it is feasible to drive the SiV on all four fine structure lines.

When comparing the resonance fluorescence spectrum in Fig. 4.15a with the non-resonant spectra at 0 T (Fig. 4.1b), we observe that all four optical transitions of the ^{28}Si isotope are visible. Resonant excitation does not lead to fluorescence from the ^{29}Si and ^{30}Si isotopes. The absence of the two isotopes proofs that we excite the subset of SiV defects which is resonant to the excitation laser. We have shown in Ref. [65] that resonance fluorescence can probe the optical line width of a transition, yielding line widths between 4 and 11 GHz which is comparable to the spectral line widths obtained for non-resonant excitation (Sec. 4.1.1).

It is important to note, that an excitation resonant to transition c gives rise to all other fine structure lines in Fig. 4.15a. At zero magnetic field, the ground states $(|1\rangle, |2\rangle)$, $(|3\rangle, |4\rangle)$ and excited states $(|A\rangle, |B\rangle)$, $(|C\rangle, |D\rangle)$ are pairwise degenerate (Fig. 4.15b). In our complete level scheme, transition c passes from ground states $(|3\rangle, |4\rangle)$ to the excited states $(|C\rangle, |D\rangle)$, thus comprising transitions $C3, C4, D3, D4$. As we shall see in the following discussion, there is spin preserving relaxation among the excited states. An absorption at zero magnetic field on transition c populates excited states $|C\rangle$ and $|D\rangle$, which contain spin up and down components. Therefore, it is plausible that a relaxation to states $|A\rangle, |B\rangle$ (giving rise to transitions a, b) is possible.

In Ref. [64], it is observed that when exciting transition d, the relative intensities of transitions a and b match the intensity ratio of a non-resonant excitation. In contrast, when exciting transition c, the relative intensity of line a becomes larger then line b. This change in relative intensities has been interpreted as a first sign of "selectivity". While our theoretical model does not account for such a selectivity, we cannot exclude it. Still, we tentatively suggest that in this case an alternative effect can be responsible for the apparent selectivity: Transition c is excited using resonant, linearly polarized light. It is plausible to assume, that this laser light only excites a subset of SiV centers having the z dipole of transition c parallel to the excitation polarization. The emitted polarization of transition b will be parallel to this excitation will be suppressed by the polarizer in the detection arm together with the laser. In contrast, transition a is polarized perpendicular to b and will be transmitted through the polarizer. When exciting transition d, the effect would be reversed.

As a consecutive step, the resonance fluorescence experiment is repeated with magnetic field applied in [001] crystallographic direction in order to lift the two-fold spin degeneracy. At magnetic field $B = 4$ T, we infer from the simulation of the level scheme (Fig. 4.12) that all electronic levels are split by at least 15 GHz and all optical transitions are clearly discernible (Fig. 4.10). The analysis of the eigenvectors in the previous section revealed that all four excited states show a dominant contribution of a distinct spin state, i.e. states $|A\rangle, |C\rangle \propto |\downarrow\rangle$ and $|B\rangle, |D\rangle \propto |\uparrow\rangle$. We now selectively populate a given state $|C\rangle$ via transition $C1$ and measure the resonance fluorescence spectrum (Fig. 4.16a,b).

The spectrum shows the residual excitation laser and 7 further peaks. Using the numbering of Fig. 4.10, we identify exclusively transitions from excited states $|C\rangle$ and $|A\rangle$; the fluorescence of transition $C1$ is covered by the laser line. If we populate the opposite spin state by exciting state $|D\rangle$ (Fig. 4.16d), only peaks related to excited states $|D\rangle$ and $|B\rangle$ are visible in the spectrum (Fig. 4.16e). Hence, we observe that the two excitations give rise to complementary spectra and, together, they form the complete spectrum obtained for non-resonant excitation at $B = 4$ T (Fig. 4.16c).

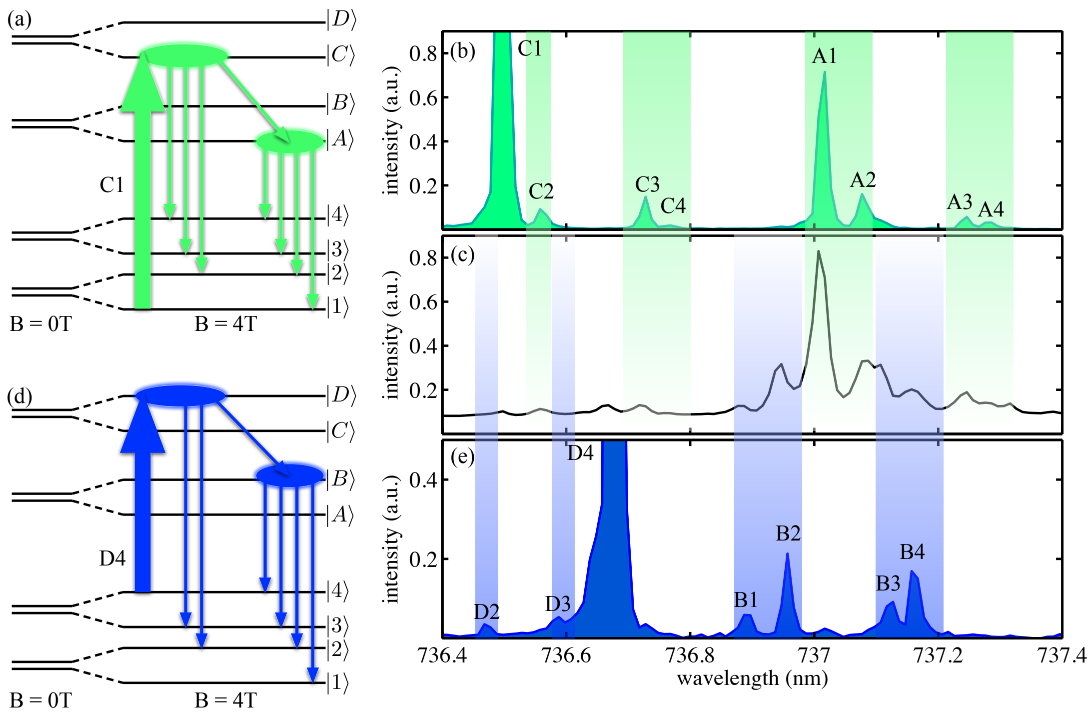

Figure 4.16: Resonance fluorescence on SiV ensemble for magnetic field $B = 4$ T. We selectively populate the excited state $|C\rangle$ via resonant laser excitation of transition $C1$ (a) and observe the fluorescence spectrum (b), which consists of optical transitions from states $|C\rangle$ and $|A\rangle$. In contrast, an excitation of state $|D\rangle$ (panel (d)) gives rise to transitions (e) starting at levels $|D\rangle$, $|B\rangle$. In comparison, we observe that the spectra (b) and (d) are complementary and add up to the complete non-resonant spectrum (c).

The resonant spectra thus show that there is a relaxation among the excited states which is selective between $|A\rangle \leftrightarrow |C\rangle$ and $|B\rangle \leftrightarrow |D\rangle$. This relaxation is according to the spin polarization of the excites states, i.e. it preserves the spin state. We deliberately use here the notion "relaxation" to distinguish this transition from optical transitions which happen between ground and excited states; the "relaxation" is purely between the excited state levels. Furthermore, it is important to stress again that the optical transition to the ground state is in principle also spin-preserving. If the ground states had a spin-polarization similar to the excited states, we would observe a selectivity for the optical transitions, too. Due to the spin-mixing in the ground states which we infer from the state tomography in Fig. 4.13, this selectivity is weak however (cf. discussion at the end of the previous section).

Müller investigated in Ref. [64] almost all resonant optical excitations and unequivocally observed a spin-preserving relaxation. For excitations of the lower excited states $|A\rangle$ and $|B\rangle$, we only observe weak relaxation to higher states $|C\rangle, |D\rangle$. This points towards a thermal activation of the relaxation mechanism, in which a downward relaxation is always feasible whereas an upward relaxation would require thermal energy. We have seen for non-resonant excitation that the population n_i of an excited state i can be described in good approximation by a Boltzmann distribution (4.6). For a more realistic model, we need to extend this simple thermal distribution with additional "selection rules" accounting for the conservation of spin. We suggest such a relaxation mechanism in the following section.

In conclusion, we first note that the selective excitation of two subsets in the excited state is in perfect agreement with the theoretical model which we assumed so far and can be seen as a further verification of this model. The selective excitation can be considered as an optical way to initialize the excited state spin: A selective excitation populates a well-determined spin projection among states $|A\rangle, \ldots, |D\rangle$, which is preserved by any relaxation in the excited state. We discuss the prospects for a subsequent spin manipulation in Chap. 5.

After a possible spin manipulation, spin state read-out is feasible by observing the fluorescence spectrum. As a figure of merit to quantify the spin state, Müller e.g. calculated the intensity ratio between spin-preserving and spin-flipping transitions [64]. While an explicit formula for this measurement will depend on which excitation transition is used, we expect a clear distinction from the high complementarity of resonance fluorescence spectra (Figs. 4.16b,d). For this purpose, it is also helpful that the excited state shows already a relatively high zero magnetic field splitting. This enables us to excite the higher lying states $|C\rangle, |D\rangle$ while detecting conveniently far off resonance on transitions from levels $|A\rangle, |B\rangle$. Hence, instead of using the technique of resonance fluorescence, a sharp spectral filtering provided by e.g. a tunable etalon [218] or a highly dispersive grating would be an alternative. Disregarding the technique behind measuring the spin state, this overall insight marks an important step towards using the spin degree of the SiV center. A central point in this analysis is the spin conserving relaxation in the excited state, which we analyze in detail in the following section.

4.2.2 Application of selection rules for relaxation within the excited state

We now focus our attention to the relaxation process among the excited states $|A\rangle, \ldots, |D\rangle$, for which we have seen that it preserves the spin projection. On the other hand, the orbital part of the wave function, which can in approximation be seen as $|e_\pm\rangle$, is changed in the relaxation process. In this section, we construct a matrix representation, i.e. a tensorial operator, obeying these "selection rules" and compare it to physical mechanisms which are likely to provoke the excited state relaxation.

To construct a matrix representation describing the relaxation process in the excited state, we refer to a similar process for nitrogen vacancy (NV) color centers in diamond: Rogers *et al.* have investigated an NV ensemble by means of magnetic circular dichroism [219] - a method using differential absorption of circularly polarized light with the sample exposed to magnetic fields. This method directly relates to the spin-orbit coupled electronic states $|e_\pm\rangle$, each having an orbital angular momentum of ±1 and giving rise to the absorption of left-hand or right-hand polarized light. Hence, the authors measure the ratio (or variation) of the two circular polarization components which yields the effective orbital magnetic momentum g_{orb} of these states (equivalent to the γ_L in Eq. (4.4)). For the NV center, the orbital magnetic momentum g_{orb} decreases with increasing temperature [219]. Rogers *et al.* interpret this decrease by a *time-averaging* of the orbital states taking place in the excited state. This time-averaging is explained by vibronic coupling of electronic states to vibrational modes, inducing a rapid transfer between electronic states of positive ($|e_+\rangle$) and negative ($|e_-\rangle$) orbital angular momentum. As vibrational modes of higher energy are excited with rising temperature, this time-averaging is stronger for room temperature than for cryogenic temperatures. While changing the orbital state, the vibronic coupling leaves the spin untouched.

Hence, this averaging process on the NV center has the same effect as the relaxation observed in case of the SiV center, i.e. it connects states of different orbital angular momentum projection and equal spin projection. Doherty *et al.* derive that the matrix representation of the NV time-averaging is the same as a general orbital operator O [42]. In fact, the Wigner-Eckart theorem predicts that the matrix elements of *all* orbital operators are directly proportional to each other for a given symmetry. In Sec. 2.3.3, we have deduced a matrix representation $\mathbb{P}^R_{SO}$ (or short the *relaxation operator*,) for a coupling of electronic states to vibrational modes.

The matrix representation $\mathbb{P}^R_{SO}$ is valid for a coupling to both lattice phonons and local vibrations of the defect. We here briefly discuss, which of these processes are possible to cause vibronic coupling: In order to couple two E_u states, i.e. states with equal parity, the vibration mode requires to have even parity. In addition, it needs to show a non-vanishing density of states for energies which roughly match the gap between the excited SiV levels ($\approx$ 100 GHz). It can be shown, that all lattice vibrations in diamond which have even parity, are also Raman-active [220]. If we search for suitable lattice modes, we therefore can restrict our search to Raman-active modes or bands:

- The acoustic branch of the diamond dispersion relation has odd symmetry for phonons at the center of the Brillouin zone [155], therefore (single) acoustic phonons do not couple states of equal parity.
- The only optical phonon with even parity is the dominant diamond Raman peak at 1332 cm^{-1} [36,221], which does not fit to the coupling energies we are interested in.
- Two phonon processes for acoustic and optical modes transform as A_{1g}, E_g and T_{2g} in a O_h symmetry [221] and there is a considerable number of possible two-phonon Raman transitions in diamond [220]. One possible two phonon process leads to so-called difference modes [156], where one phonon can be created and a second phonon of different energy can be destroyed. Since the coupling energy relevant for the SiV vibronic coupling would be rather small, a two-phonon coupling arising

from difference acoustic modes (so called acoustic *overtones* [220]) might be in a suitable energy range [222], and therefore possibly mediates the relaxation among excited SiV states.

- Little is known about local vibrational modes of the SiV center: Sternschulte *et al.* [137] as well as Feng and Schwartz [138] investigate the vibronic sideband of the SiV center, however, their analysis is restricted to modes of energy shifts larger 42 meV (10 THz), which is out of the range we are interested in. Nevertheless, local vibrational modes of the SiV center cannot be excluded.

Determining, which vibration is responsible for the excited state relaxation, requires a deeper investigation of the vibronic spectrum of the SiV center, which is not in the focus of this work. Notwithstanding, group theory assures that the *orbital* operator describing any kind of vibration will always transform similarly to $\mathbb{P}^R_{SO}$ and hence, we employ matrix representation $\mathbb{P}^R_{SO}$ throughout this chapter.

In Sec. 2.3.3, we have seen that the relaxation operator $\mathbb{P}^R_{SO}$ transforms as irreducible representation E_g and thus similar to the strain Hamiltonian $\mathbb{H}^S$ which we will discuss in the next section. As the vibronic coupling so far only involves orbital states, it is expressed as a (reduced) 2×2 matrix in the SO coupled basis $\{|e_+\rangle, |e_-\rangle\}$. In order to express the spin conservation, we expand $\mathbb{P}^R_{SO}$ to the spin space calculating the direct product $\mathbb{P}^R_{SO} \otimes \mathbb{I}_2 \equiv \mathbb{P}^R$, where $\mathbb{I}_2$ denotes a 2×2 identity matrix.

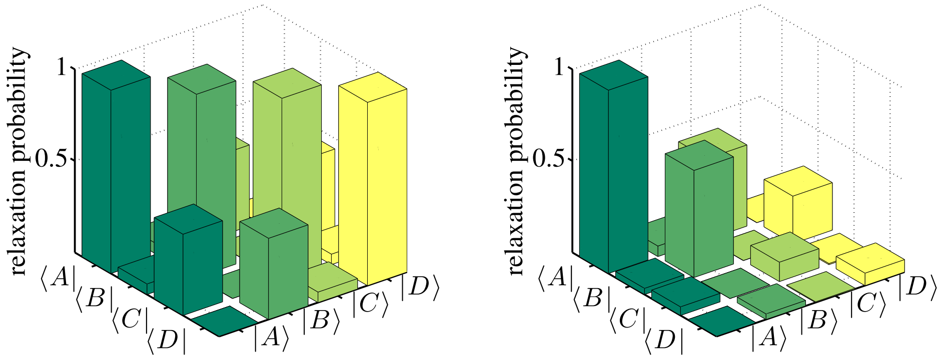

(a) (b)

Figure 4.17: The probability for a relaxation between the excited states $|A\rangle, \ldots, |D\rangle$, expressed as matrix elements $\left|\Gamma^R_{if}\right|^2$ without (a) and with (b) a weighting for thermal effects.

To show the effect of $\mathbb{P}^R$, we calculate matrix elements $\Gamma^R_{if} = \langle \varphi_f | \mathbb{P}^R | \varphi_i \rangle$, with initial state φ_i and final state φ_f belonging to the excited state manifold $|A\rangle, \ldots, |D\rangle$. The absolute squares $\left|\Gamma^R_{if}\right|^2$ (Fig. 4.17a) denote the transition probability from one excited state to another. In agreement with the experimental findings, the relaxation operator

$\mathbb{P}^R$ predicts a transition between states of equal spin projection, i.e. $|D\rangle \leftrightarrow |B\rangle$ and $|C\rangle \leftrightarrow |A\rangle$. In addition, from the large main diagonal elements, we expect a large probability to undergo an optical transition from a given excited state directly to the ground state without relaxing to another excited state.

We have discussed in the preceding paragraph (Sec. 4.2.1), that the relaxation mechanism is strongly "unidirectional" in terms of the energy of the excited states, i.e. we observe a strong downwards relaxation but a weak upwards transfer, which is consistent with a thermal distribution. To model this thermal distribution, we weight the rows of matrix $\left|\Gamma^R\right|^2$ with the Boltzmann coefficients $n_i(T)$ (Eq. (4.6) with $T \approx 5$ K). This has the effect, that a transfer from lower to higher lying states has smaller probability than vice versa (Fig. 4.17b).

It is important to note, that the relaxation operator $\mathbb{P}^R$ has been constructed to be spin conserving in agreement with our experimental results. At vanishing magnetic field, we can drop this prerequisite. Hence, the two spin-degenerate excited states will thermalize according to $\mathbb{P}^R$ where we again need to include the Boltzmann distribution. This means that the relaxation changes to the simple thermalization for zero magnetic field as it has been described in Refs. [62,137]. This also explains why all fine structure peaks are visible in Fig. 4.15.

For non-resonant Zeeman spectra (Figs. 4.10, 4.18b) we stated before, that we neglect the spin-selective relaxation. We here briefly explain how we justify this approximation: When exciting non-resonantly, we first populate a higher lying electronic or vibronic level, which rapidly decays to the four excited states $|A\rangle, \ldots, |D\rangle$. All the experimental evidence and literature ([62,137]) suggests that this rapid decay does not favor a particular spin orientation, hence we assume that all states $|A\rangle, \ldots, |D\rangle$ are *equally* populated after an excitation. From this point on, it is plausible that a spin-selective relaxation is happening which connects $|D\rangle$ with $|B\rangle$ and $|C\rangle$ with $|A\rangle$. Hence, the population will *pairwise* follow a thermal distribution which we approximate by a full thermalization for all states.

We have seen in this section that the population transfer among excited states is consistent with an orbital relaxation operator $\mathbb{P}^R$. This relaxation operator yields qualitatively correct predictions for the relaxation in the excited state and is taken as another verification of our theoretical model of the SiV center. So far, the spin selective excitation has only been shown on the SiV ensemble sample. We will extend the technique to single SiV emitters in the following part. To date, single SiV centers under solid immersion lenses such as SIL1 - SIL3 have been impractical for resonance fluorescence experiments, because the surface of the microscopic solid immersion lenses deteriorates the beam profile of the reflected excitation laser; this makes an effective laser suppression very challenging. We therefore present here experiments on single SiV centers in nanodiamonds. As nanodiamonds usually exhibit crystal strain, we employ these measurements also to describe the effect of strain on the level structure of the SiV defect.

4.3 Strained defects in nanodiamonds

Individual SiV centers in nanodiamonds offer a large potential for room-temperature single photon sources [56,58,117,182], but also for fluorescence-labeling of biological specimens

[73,191,223]: They show bright and stable single photon emission with narrow zero phonon lines already at room temperature. A statistic distribution of the zero phonon line position [58] and variations in the low temperature fine structure [73,115] have however indicated, that SiV defects are prone to crystal strain effects in nanodiamonds. Therefore, we use strained nanodiamonds on purpose as a "test bench" for the influence of crystal strain on individual SiV centers. We will see, that the addition of a strain Hamiltonian consistently describes the measurements while retaining all other parameters introduced in the theory. A disadvantage of nanodiamonds is however that they grow from randomly oriented seed diamonds which introduces some uncertainty when determining the orientation of the defects.

There have been a few publications on the electronic properties of SiV defects which were placed in strained environments: Neu *et al.* measure emission polarization of single SiV centers at room temperature in (001) oriented heteroepitaxial diamond on iridium [58]. In addition to polarization along the $\langle 110 \rangle$ axis (which would be consistent with $\langle 111 \rangle$ oriented centers projected onto the (001) surface) they measure polarization graphs along directions which coincide with $\langle 100 \rangle$ orientation. This experimental finding is consistent with an alignment of the center along $\langle 110 \rangle$ and hence, the authors deduce a rhombic or monoclinic orientation of SiV defects. The diamond which hosted the SiV centers in Neu's report is however susceptible to crystal strain, as the iridium substrate shows a lattice constant mismatch in relation to the diamond. Neu *et al.* investigate the effect of crystal strain in this sample by measuring the distribution of zero phonon line wavelength of different individual SiV centers: A statistic distribution of the spectral position on the order of 20 nm indicates the presence of strong strain fields in the diamond.

This illustrates the difficulty of working with strained SiV defects: As the influence of crystal strain on the electronic structure is unknown, the resulting conclusion (in this case the orientation) needs to be subjected to discussion. Therefore, we here started with a model for "ideal", unstrained SiV centers and discussed their properties on the basis of the experimental findings in Sec. 4.1. Consequently, we extend this model to also cover strained samples, while keeping the previous parameters and assumptions unchanged. In order to characterize strained samples and compare the extended model, we again measure the fine structure splittings in magnetic fields (Sec. 4.3.1), and investigate the strain effects on spin selective resonance fluorescence (Sec. 4.3.3). In the outlook of this thesis (Sec. 5.1.2), we return to the polarization measurements of Neu *et al.* [58] and show how crystal strain influences the polarization properties of individual SiV centers.

4.3.1 Zeeman spectra for silicon vacancy defects in strained nanodiamonds

The figures of merit for SiV centers in strained nanodiamonds are on the one hand the spectral fine structure splittings $\Delta\nu_{g,e}$ and on the other hand the magnetic field splittings of the fine structure. Before we characterize the effect of strain on the level structure quantitatively using an additional energy term, we qualitatively discuss the effect of strain neglecting the exact values and directions of the strain field. Figure 4.18 show Zeeman spectra for three single SiV centers ND1, ND2, ND3 in nanodiamonds. We will see later that from ND1 to ND3 the crystal strain parameters are increasing. The measurements have been performed on the nanodiamond sample described in Sec. 3.2.3, using non-resonant excitation of the emitters exposed to a magnetic field (cf. Sec. 4.1.4).

First we direct our attention to the spectra at $B = 0$ T (left side of the graphs 4.18(i),(iv),(vii)): With increasing crystal strain the inner fine structure peaks b, c move closer together while the outer peaks a, d move further apart. These typical spectra show a characteristic property of strained defects (cf. simulations in Sec. 2.2.5). We summarize the fine structure splittings $\Delta\nu_{g,e}$ in Tab. 4.4 taking into account the effect of crystal strain. From the color scale we also infer, that the relative intensity of the peaks is different from the reference SiV ensemble of Sec. 4.1.4.

Second, we qualitatively examine the fine structure splitting with increasing magnetic fields: For emitters ND1 and ND2, each fine structure peak clearly splits into four components. For emitter ND3, the middle peaks b, c show a splitting with strongly varying intensity: The lines $A1, B2, C3, D4$ exhibit a high relative intensity while the lines $A2, B1, C4, D3$ show an almost imperceptible intensity. The slopes of the Zeeman splitting indicate avoided crossings for ND1 and ND2, while for ND3 all lines appear to shift linearly.

Now, we analyze quantitatively the effect of strain by again applying a theoretical model to describe the data. Similar to the preceding section, we briefly outline the theoretical assumptions and specify the procedure for fitting parameters of the model to the data. The latter is again important to minimize mutual dependencies of parameters.

To simulate the effect of crystal strain, we add a strain term $\mathbb{H}^S_{g,e}$ to the perturbation Hamiltonian in Eq. (4.4). The strain term $\mathbb{H}^S_{g,e}$ is derived in Sec. 2.2.5 and can be expressed in the basis functions (4.5) as a 4×4-matrix:

$$\mathbb{H}^S_{g,e} = \begin{bmatrix} \delta - \alpha & 0 & -\beta & 0 \\ 0 & \delta - \alpha & 0 & -\beta \\ -\beta & 0 & \delta + \alpha & 0 \\ 0 & -\beta & 0 & \delta + \alpha \end{bmatrix} \tag{4.10}$$

where parameters α, δ quantify the energy shift of the basis states $|e_{x,y}\rangle$ and parameter β marks the mixing between $|e_x\rangle$ and $|e_y\rangle$[4]. Matrix $\mathbb{H}^S_{g,e}$ is deduced for uniaxial stress measurements using group theory (Sec. 2.2.5) and agrees with former theoretical studies on trigonal defects [38,164,166,167]. For uniaxial stress, parameters α, β, δ directly relate to the stress tensor components σ_{ij} $(i, j = x, y, z)$, which are given usually by the direction and strength of the external pressure applied to the sample. In the measurements presented here, strain is an *intrinsic* property, arising most probably from other faults (such as dislocations, stacking faults or grain boundaries) in the vicinity of the SiV center under test. Hence, we use α and β as free parameters; δ can be neglected and is set to zero as it acts equally on the main diagonal for ground and excited state, therefore no spectral shift is expected from it. As we consider strain to be a static perturbation, $\mathbb{H}^S_{g,e}$ acts uniformly on ground and excited state, hence the same α and β are taken for both cases. While it is arguable that intrinsic strain follows solely from uniaxial stress contributions,

---

[4] The choice of using α and β for the strain matrix is perhaps unfortunate as we have used them before for the spin polarization, but we deliberately employ the same notation as Ref. [167] and no confusion should arise from this usage.

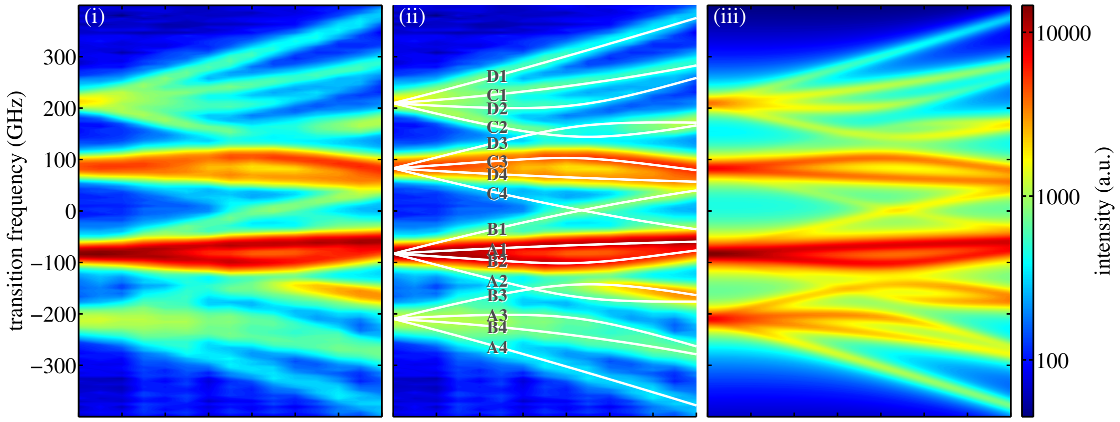

(a) Single emitter ND1

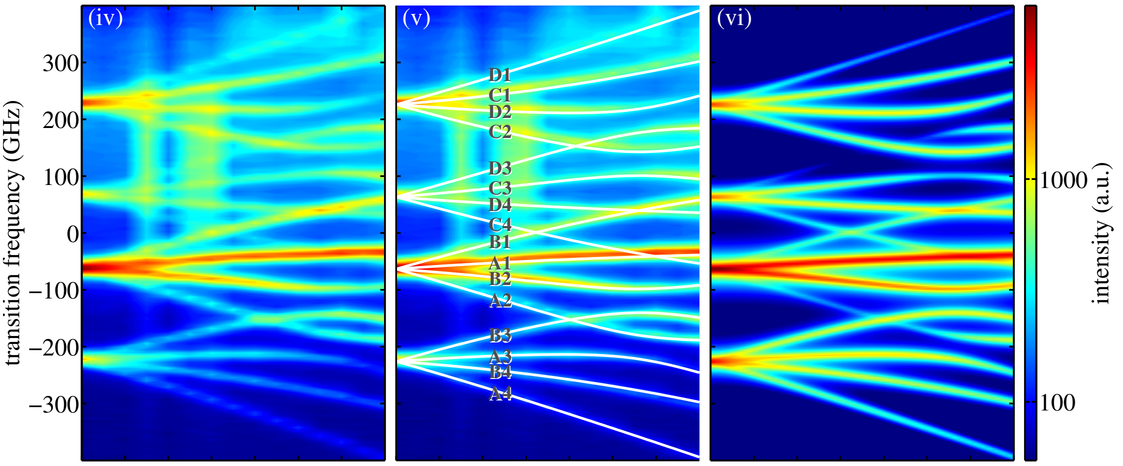

(b) Single emitter ND2

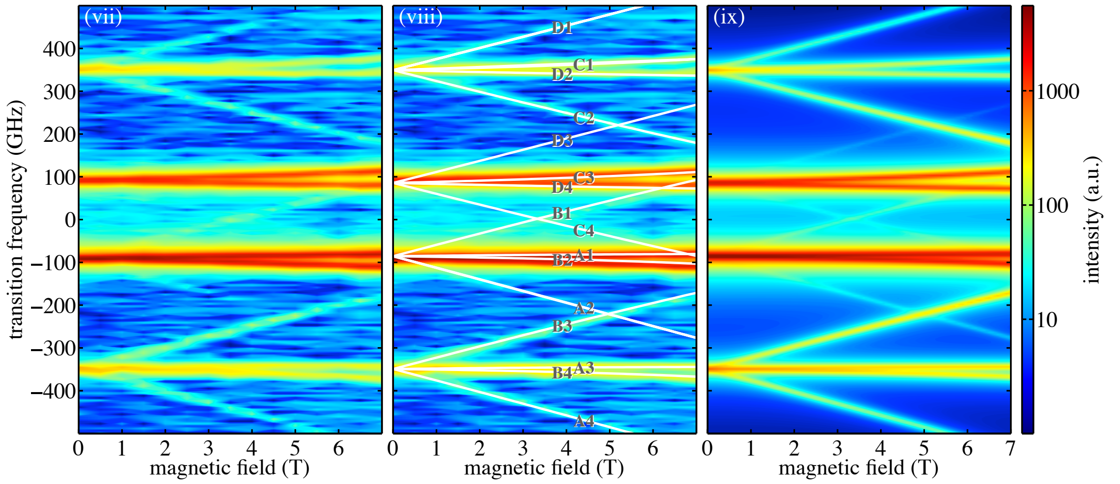

(c) Single emitter ND3

Figure 4.18: Zeeman spectra for three individual SiV centers ND1 (a), ND2 (b) and ND3 (c) in nanodiamonds. The representation of left, middle and right panels is equal to Fig. 4.10 with color scaling in logarithmic, arbitrary units (uniform for each emitter).

the comparison to the data in this section still shows a reasonable agreement, thus we assume this approximation to be justified for our analysis.

When adding the strain Hamiltonian $\mathbb{H}^{S}$ to the other perturbations $\mathbb{H}^{\mathrm{SO}}_{\mathrm{g,e}}$, $\mathbb{H}^{\mathrm{JT}}_{\mathrm{g,e}}$, $\mathbb{H}^{\mathrm{Z,L}}_{\mathrm{g,e}}$, $\mathbb{H}^{\mathrm{Z,S}}_{\mathrm{g,e}}$ (cf. Eq. (4.4)), we set the parameters for SO coupling, JT interaction and Zeeman effect to their values of the SiV ensemble sample (Tab. 4.2) and keep them constant. The only exception is the relative angle θ_B between magnetic field and the z-axis of the SiV defect, which used to be fixed to 54.7° for defects in (001) oriented bulk diamond, but now is variable due to the random orientation of the nanodiamonds on the substrate. The comparison of theory and model is fully identical to the proceeding in Sec. 4.3.1: Diagonalizing the total Hamiltonian, we determine eigenvalues and eigenstates, calculate the 16 optical transitions and compare them to experimental data (middle panels in Fig. 4.18). The proceeding for fitting the free parameters α, β, θ_B is as follows: First, we fit the strain parameters α, β to match the fine structure splitting $\Delta\nu_{g,e}$ at $B = 0$ T; inspecting the spectra at 0 T introduces a cross-check as we can completely neglect the Zeeman terms for this situation. After having determined α and β, we use the slope of optical transitions $A4$ and $D1$ in the Zeeman spectra (Fig. 4.18) to fit the relative angle θ_B between magnetic field and SiV z-axis. These two transitions are mainly dependent on the Zeeman terms, and the only free parameters in the Zeeman terms are the quenching factor q and relative angle θ_B of the magnetic field. As the quenching q is known from the SiV ensemble (Tab. 4.2), the angle θ_B can be identified unambiguously within an error of approximately 5°.

Table 4.4: Resulting parameters for single SiV defects "ND1" - "ND3" and reference SiV ensemble for comparison. α, β indicate the strength of crystal strain, $\Delta\nu_{g,e}$ denote the splitting of ground and excited state (including the energy shift from strain). The remaining parameters λ_g, $\Upsilon_{g,x}$, $\Upsilon_{g,y}$, λ_e, $\Upsilon_{e,x}$, $\Upsilon_{e,y}$, f are identical to the ensemble sample.

emitter	α	β	$\Delta\nu_g$	$\Delta\nu_e$	θ_B
name			(GHz)		(°)
ensemble	0	0	50	260	55
ND1	44	29	127	293	70
ND2	11	66	162	289	70
ND3	51	121	259	396	45

The modeling of optical transitions (white solid lines in Fig. 4.18, parameters in Tab. 4.4) shows an excellent agreement with the measured Zeeman spectra, suggesting that the simple strain term we add is sufficient to describe the changes for strained SiV centers in nanodiamonds. From the resulting splitting of energy levels, i.e. the eigenvalues of the system (Fig. 4.19), we see the orbital splitting for $B = 0$ T for both ground and excited state increases as α, β become larger. This is consistent with the simulations on the energy dependence of strain coefficients in Sec. 2.2.5. It is noticeable that –although the SO-coupling strengths $\lambda_{g,e}$ are the same for all emitters "ND1" - "ND3" – there are no avoided crossings visible for ND3. The reason lies in the simple fact that ground state

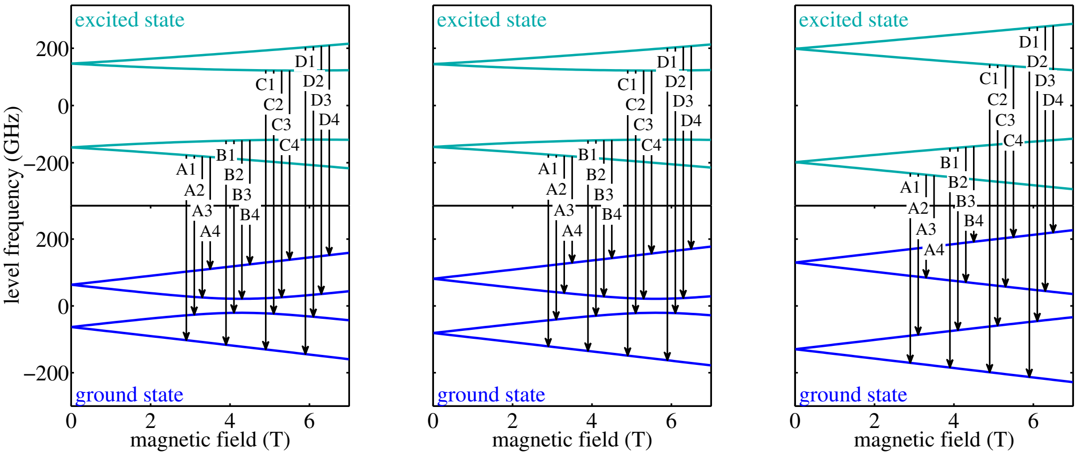

(a) Single emitter ND1 (b) Single emitter ND2 (c) Single emitter ND3

Figure 4.19: Level splitting for three individual SiV centers ND1 (a), ND2 (b) and ND3 (c) in nanodiamonds for increasing magnetic field. The scaling of all frequency (y-)axes is the same.

levels are taken far apart such that even for strong magnetic field, no levels approach each other. As a consequence for emitters “ND1” - “ND3”, the ordering of transitions is different from the ensemble sample and emitter “SIL3”, e.g. lines $A3$ and $B4$ swap positions (Figs. 4.18, 4.10).

We simulate the peak width and intensity of each optical transition in the Zeeman spectra 4.18 using the very same proceeding as in Sec. 4.1.4: We calculate eigenvectors $|1\rangle, \ldots, |4\rangle$ for ground and $|A\rangle, \ldots, |D\rangle$ for excited state (shown exemplarily for “ND2” in Figs. 4.20a, 4.20b in the following section). With these eigenvectors, we determine the X, Y, Z dipole strength of optical transitions from the expectation values $\langle \mathbf{p} \rangle$ of the dipole matrix elements. The resulting intensities of the dipole transitions are again weighted using the collection efficiencies η_x, η_y, η_z for X, Y, Z-dipoles, taking into account the relative orientation of the defect to the observation plane.[5] Optical transitions are expressed as a sum of Lorentzian peaks (Eq. (4.7)) with the intensity of each peak calculated using Eq. (4.8), taking into account also the population probability n_i of each excited state i. The full width at half maximum of the Lorentzian peaks is set equal to the experimentally observed peak width (5 GHz for “ND2”, “ND3” and 10 GHz for “ND1”, resp.). The simulated Zeeman spectra (right panels in Fig. 4.18) match the experimental spectra with excellent agreement, indicating that a faithful simulation of the strained SiV centers is indeed feasible. As next step, we investigate how crystal strain influences the spin polar-

---

[5] While we can determine the polar angle θ_B of the emitter from the slopes of optical transitions in the Zeeman spectra, the azimuth ϕ_B cannot be determined from the Zeeman spectra because the magnetic field acts rotational invariant on the emitter. Hence, the relative collection efficiencies η_x, η_y of the X, Y dipoles are free parameters and we adjust them to fit the data.

ization in the SiV excited states and discuss the consequences in the context of resonance fluorescence spectra.

4.3.2 Electronic state tomography of strained silicon vacancy defects

We discussed for the SiV ensemble sample in Sec. 4.2.2 that a relaxation among excited states preserves the spin state and hence offers an optical read-out of the excited state spin. In this section, we investigate whether crystal strain alters the spin polarization of excited states and verify if these changes can be observed in the relaxation mechanism using again resonance fluorescence in the next section.

The strain term (4.10) in the perturbation Hamiltonian has no *direct* effect on spin states, as the secondary diagonal elements in matrix (4.10) are equal to zero. Hence, it introduces no coupling between states of different spin projection. However, we observe an *indirect* effect: We have seen before, that spin mixing occurs as a consequence from off-axis magnetic field terms $B_{x,y}$. SO coupling (acting only on the S_z component of the spin operator) "shields" the excited states from spin mixing by shifting energy states which are susceptible to spin-mixing far away from each other. The additional strain Hamiltonian $\mathbb{H}^S$ acts on the same matrix elements as SO coupling and thus we expect it to counteract SO coupling and to weaken the "shielding" effect.

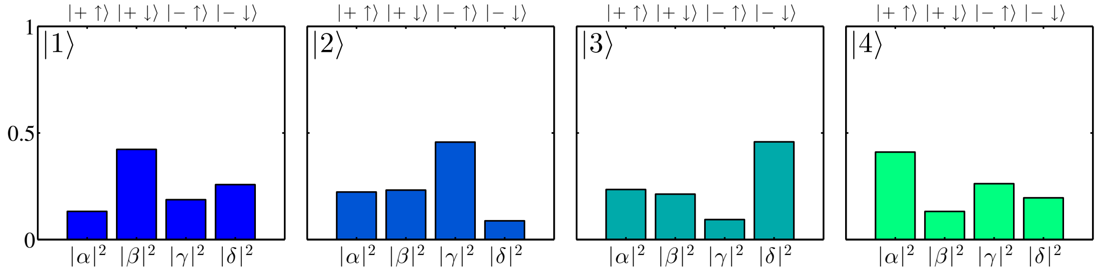

(a) ground state

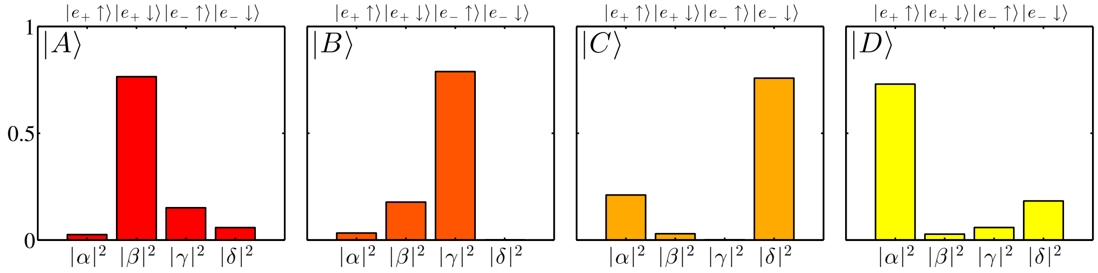

(b) excited state

Figure 4.20: Eigenvectors $|1\rangle, \ldots, |4\rangle$ for the ground (a) and $|A\rangle, \ldots, |D\rangle$ for the excited state (b) of SiV center "ND2" under the influence of crystal strain. We employ the same plotting scheme as in Fig. 4.13. The calculation is performed for $B = 2$ T.

Figures 4.20a and 4.20b depict the eigenvectors of emitter "ND2" exemplarily for a strained emitter, making use of coefficients $\alpha, \beta, \gamma, \delta$ from Eq. (4.9) to express states in a the linear superposition of basis vectors $|e_{\pm} \uparrow, \downarrow\rangle$. We notice that for all ground states $|1\rangle, \ldots, |4\rangle$, spin mixing has considerably increased as almost all basis vectors are contributing to the eigenvectors. For each excited state, besides a dominant basis vector in the linear superposition there is a second contribution. A closer inspection reveals that this second basis vector is opposite to the predominant one both in spin and orbital degree of freedom: For excited state $|A\rangle$ for example, the largest coefficient is $|e_+ \downarrow\rangle$ with $|\beta|^2 \approx 0.75$ and the second largest contribution comes from basis vector $|e_- \uparrow\rangle$ with $|\gamma|^2 \approx 0.2$.

It is straightforward to quantify this spin mixing in terms of spin polarization P as we have done earlier on unstrained SiV centers (cf. page 138). Table 4.5 lists spin polarizations of emitter "ND1" - "ND3" for ground and excited states, respectively.

Table 4.5: Spin polarizations P for ground states $|1\rangle, \ldots, |4\rangle$ and excited states $|A\rangle, \ldots, |D\rangle$ of emitters "ND1" - "ND3" in nanodiamonds.

states	$\|1\rangle$	$\|2\rangle$	$\|3\rangle$	$\|4\rangle$	$\|A\rangle$	$\|B\rangle$	$\|C\rangle$	$\|D\rangle$
P(ND1)	-0.37	0.36	-0.34	0.35	-0.63	0.63	-0.56	0.56
P(ND2)	-0.36	0.36	-0.34	0.34	-0.65	0.64	-0.58	0.58
P(ND3)	-0.71	0.71	-0.71	0.71	-0.81	0.81	-0.77	0.77

We note, that "ND3" shows a surprisingly high spin polarization for ground and excited states. In fact, the graphical representations for the ground state eigenvectors (Fig. 4.21a) reveal that there is large orbital but small spin mixing. Here, the strain term is the leading perturbation (instead of SO coupling) and it leads to a large orbital splitting. This provides a similar "shielding" for transverse magnetic field components as SO coupling, and hence spin remains a good quantum number in ground state for "ND3". With strain being the leading term in the Hamiltonian, the orbital part of the eigenvectors $|1\rangle, \ldots, |4\rangle$ are similar to the eigenvectors $|u_1\rangle, \ldots, |u_4\rangle$ of the strain Hamiltonian $\mathbb{H}^S$ (calculated for a general case in Sec. 2.2.5), hence it is straightforward to apply a basis transformation in order to present the ground state of "ND3" in this basis (Fig. 4.21b).

We observe that this new basis representation is to a good approximation also an eigenbasis for the strained SiV electronic states. We stress, that this is the first observation of large spin polarization in both excited *and* ground state. The consequences of this spin polarization are visible in the Zeeman spectrum (Fig. 4.18c): We stated before, that the intensities for optical dipole transitions of emitter "ND3" are strongly non-uniform, eg. peak $A2$ has vanishing intensity whereas $A1$ is very strong. These different relative intensities arise from the fact, that optical dipole transitions are spin-preserving. Hence, all transitions which would flip the spin projection, eg. $A2, B1, C4, D3$, have a low relative intensity whereas spin-preservation transition, eg. $A1, B2, C3, D4$ have a high intensity. Still, the spin polarization of "ND3" is non-unity (Tab. 4.5, Fig. 4.21b) and thus, these selection rules are weakened for "ND3".

We note this important result, that even in the presence of a strong strain field, the spin polarization of the SiV center can be preserved to a high degree. The spectroscopy

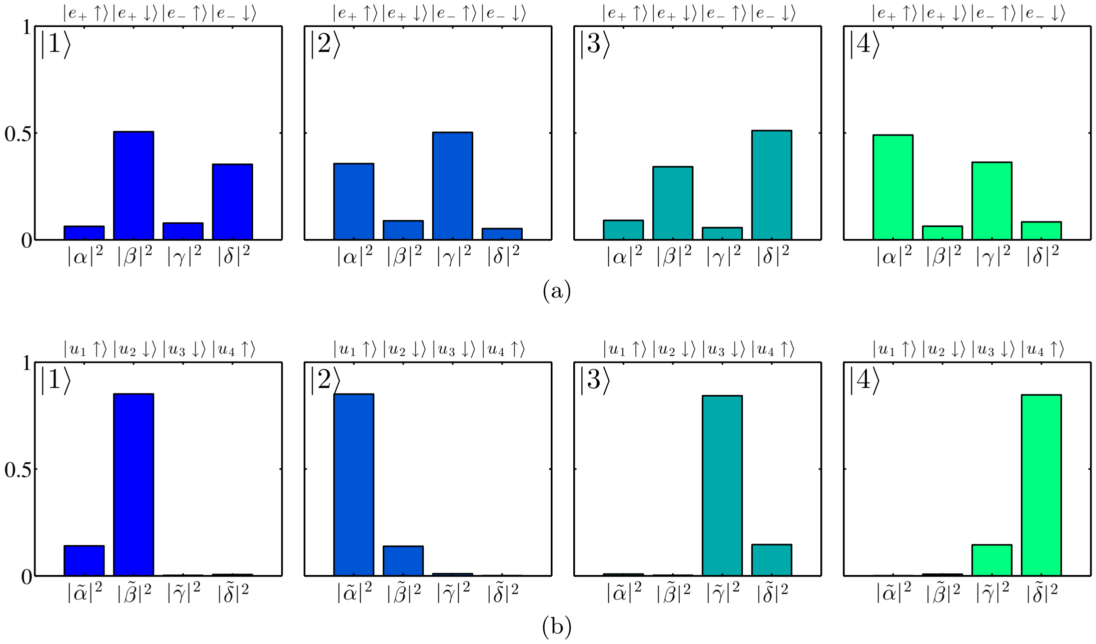

Figure 4.21: Eigenvectors $|1\rangle, \dots, |4\rangle$ for the ground state of SiV center "ND3" under the influence of crystal strain. In panel (a), we express the eigenvectors in the SO coupled basis and employ the same plotting scheme as in Fig. 4.13. In panel (b) we apply a basis transformation to the eigenbasis of the strain Hamiltonian $\mathbb{H}^S$. The calculation is performed for $B = 2$ T.

in magnetic fields which we presented in this section combined with a faithful description of our theoretical model represents a valuable tool to evaluate these spin properties. We show in the following section, that a selective readout in these sample is possible as well.

4.3.3 Strain effects on spin-resolved fluorescence

The promising results on spin polarization of the previous section suggest to apply the resonance fluorescence technique described in Sec. 4.2.1 to individual SiV defects in nanodiamonds. Owing to their high brightness [56, 58], SiV centers in nanodiamonds promise a competitive signal to noise ratio for this sample system. Furthermore, it is helpful, that the nanodiamonds which contain the SiV centers are smaller than the wavelength of the excitation laser. Hence, we expect only a little distortion of the reflected laser beam which should result in an sufficient laser suppression.

Figure 4.22 displays exemplarily the resonance fluorescence measurements of "ND2" at $B = 2$ T. In a first step, we populate the spin up manifold ($|\uparrow\rangle$) by exciting resonantly on transition $D1$ (Fig. 4.22a). The resulting spectrum (Fig. 4.22b) shows a multitude of peaks: In reference to Fig. 4.18b we identify fluorescence of excited states $|D\rangle$, i.e. a direct optical transition to the ground state, and of states $|A\rangle, |B\rangle$, i.e. transition which occur after a relaxation among the excited states. We do not observe any emission arising

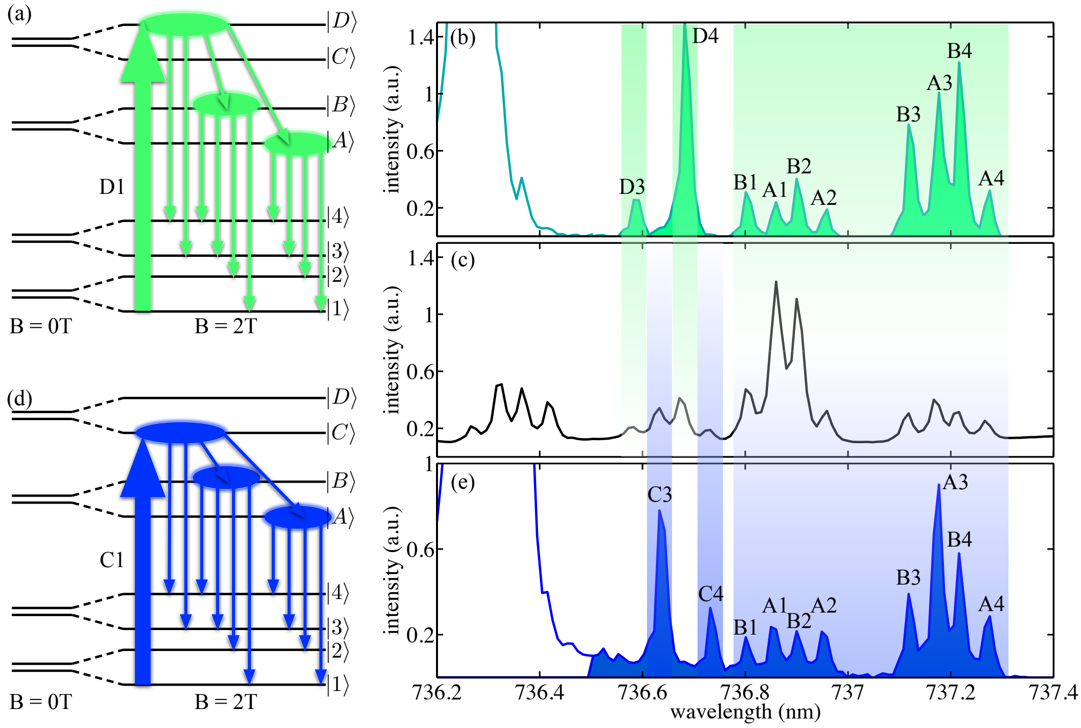

Figure 4.22: Resonance fluorescence on single emitter “ND2” for magnetic field $B = 2$ T. We selectively populate the excited state $|D\rangle$ via resonant laser excitation of transition $D1$ (a) and observe the fluorescence spectrum (b), which consists of optical transitions from states $|D\rangle, |B\rangle$ and $|A\rangle$. Optical excitation of state $|C\rangle$ (panel (d)) gives rise to transitions (e) starting at levels $|C\rangle$, $|B\rangle$ and $|A\rangle$. In comparison to the non-resonant spectrum (c) we observe a partial selectivity of transitions: States $|D\rangle$ and $|C\rangle$ do not show a thermalization into each other, but both decay into states $|A\rangle$ and $|B\rangle$. The large peaks on the left of spectra (b) and (e), respectively, are the residual peaks of the excitation laser, tuned to transition $D1$ (b) and $C1$ (e).

from excited state $|C\rangle$. While the presence of fluorescence from level $|B\rangle$ and the absence of $|C\rangle$ are well expected and consistent with the results presented for the reference SiV ensemble (Fig. 4.16), transitions starting at level $|A\rangle$ are surprising at first glance. As a second step, we populate the spin down manifold ($|\downarrow\rangle$) via transition $C1$ (Fig. 4.22). Now, the resonance fluorescence spectrum reveals transitions starting from $|C\rangle$ but no transitions from $|D\rangle$, and again fluorescence arising from both $|A\rangle$ and $|B\rangle$. In contrast to the resonant fluorescence for the SiV ensemble (Fig. 4.16) where we observe fully complemental spectra, we here encounter a *partial* complementarity: While the upper excited state branch (states $|D\rangle$ and $|C\rangle$) do not thermalize among each other, it appears at first glance that the lower states $|B\rangle, |A\rangle$ show a thermalization.

To check this partial selectivity, we repeat the resonance fluorescence experiment with an excitation of the lower excited state branch (Fig. 4.23): First, we excite resonantly to

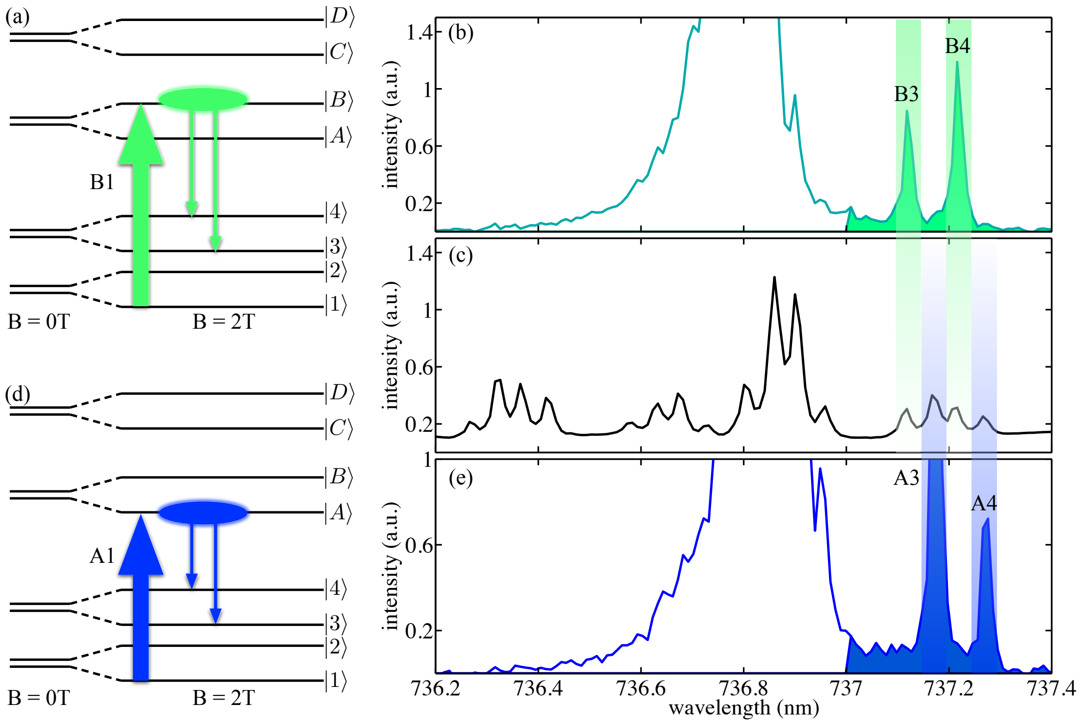

Figure 4.23: Resonance fluorescence on single emitter "ND2" for magnetic field $B = 2$ T. Resonant excitation of state $|B\rangle$ (a) does not lead to relaxation into state $|A\rangle$, as the resonance fluorescence spectrum (b) shows exclusively optical transitions from $|B\rangle$. Similarly, excitation of $|A\rangle$ (d) leads only to fluorescence from $|A\rangle$ itself (e). The large peaks in the middle of spectra (b) and (e), respectively, are the residual peaks of the excitation laser, tuned to transition $D1$ (b) and $C1$ (e).

state $|B\rangle$ ($\propto |\uparrow\rangle$, Fig. 4.23a). The resonance fluorescence spectrum (Fig. 4.23b) shows no optical transitions from state $|A\rangle$, but only direct transitions from $|B\rangle$ itself. Similarly, exciting state $|A\rangle$ resonantly (Fig. 4.23d) leads to no peaks connected to $|B\rangle$ (Fig. 4.23e). This indicated that surprisingly, there is no thermalization between $|B\rangle$ and $|A\rangle$ when they are directly excited. Hence, a direct population of the lower excited state branch restores the selectivity for these states.

In the following section, we take a closer look at the relaxation among excited states for "ND2". For this purpose, we make use of the state tomography outlined in the previous section and we review the relaxation operator $\mathbb{P}^R$ which we introduced in Sec. 4.2.2. The representation of operator $\mathbb{P}^R$ in basis states (4.5) reveals that $\mathbb{P}^R$ only connects states of the *same* spin projection but *different* orbital degree of freedom, e.g. it links $|e_+\uparrow\rangle$ with $|e_-\uparrow\rangle$. The eigenvector $|D\rangle$ of "ND2" is composed mainly of two basis states, viz. $|e_+\uparrow\rangle$ and $|e_-\downarrow\rangle$. When we apply the relaxation operator $\mathbb{P}^R$ to $|D\rangle$, we project state $|D\rangle$ into a superposition of $|e_-\uparrow\rangle$ and $|e_+\downarrow\rangle$. Hence, there is a vanishing overlap with state $|C\rangle$ (which is also composed of $|e_+\uparrow\rangle$ and $|e_-\downarrow\rangle$) and we do not expect a relaxation from

$|D\rangle$ to $|C\rangle$. The same argument holds for state $|C\rangle$ the other way around, although the magnitudes of the coefficients α and δ are swapped.

In contrast, the application of $\mathbb{P}^R$ to $|D\rangle$ leads to a large overlap both with states $|A\rangle$ *and* $|B\rangle$, because both states are composed mainly of $|e_- \uparrow\rangle$ and $|e_+ \downarrow\rangle$. Therefore, the relaxation from $|D\rangle$ into both $|A\rangle$ and $|B\rangle$, which we observe in the resonance fluorescence experiments, is well described by the operator $\mathbb{P}^R$. The same argument holds again for state $|C\rangle$. The direct relaxation between $|B\rangle$ and $|A\rangle$ is again forbidden, because of the same argument as for the forbidden decay between $|D\rangle$ to $|C\rangle$ above.

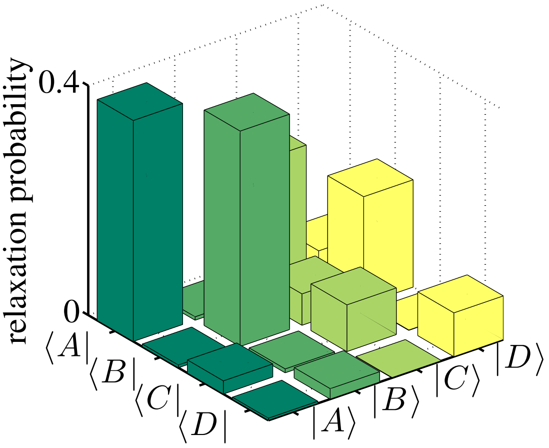

Figure 4.24: The probability for a relaxation between the excited states $|A\rangle, \ldots, |D\rangle$ (cf. Fig. 4.20b) of strained SiV center “ND2”, expressed as matrix elements $\left|\Gamma^R_{if}\right|^2$.

We strengthen these intuitive arguments by calculating the matrix elements $\Gamma^R_{if} = \langle\varphi_f|\mathbb{P}^R|\varphi_i\rangle$ of the relaxation operator between initial state φ_i and final state φ_f, both belonging to the excited state manifold $|A\rangle, \ldots, |D\rangle$ (cf. Sec. 4.2.2). We display the absolute squares $\left|\Gamma^R_{if}\right|^2$ which corresponds to the relaxation probability in Fig. 4.24 and again weight the values with a thermal (Boltzmann) distribution as we have done it in Sec. 4.2.2. A comparison between Fig. 4.24 with the selection rules observed in Figs. 4.22 and 4.23 shows an excellent agreement: The upper states $|C\rangle$ and $|D\rangle$ decay both in the lower states $|A\rangle$ and $|B\rangle$, but a direct relaxation between states of the same “branch” ($|D\rangle \leftrightarrow |C\rangle$, $|B\rangle \leftrightarrow |A\rangle$) is forbidden. It is very important to stress here, that we employ the same relaxation operator, thus the physical mechanism behind the relaxation remains the same for strained SiV defects. Hence, the application of resonance fluorescence on strained SiV centers is feasible although its results might require a more careful discussion.

Conclusion of the experimental results

This closes the chapter on experimental results. We have shown in this chapter that spectroscopy on SiV centers at low temperatures in combination with magnetic fields provides a powerful tool to investigate the electronic structure of the defect. In conclusion, we have been able to explain every experimental evidence using the theoretical model of the SiV center developed in Chap. 2. This includes “ideal” SiV defects which we studied in bulk diamond as well as strained defects in nanodiamonds. Unstrained centers are predominantly governed by spin orbit coupling which “shields” the excited state spin from transverse Zeeman interaction and thus provides access to pure spin states in the excited states. This spin purity has been experimentally verified using the technique of resonance fluorescence. Strained SiV centers have – depending on the strength of crystal strain – a tendency for lower spin polarization but still provide a feasible selectivity when resonantly excited.

We have seen in this chapter that the only terms which theoretically lead to spin mixing are off-axis magnetic field components which give rise to transverse Zeeman terms on the spin operators S_x and S_y. While it was technically not possible in the current experimental setup to apply magnetic fields in directions other than presented here, we can still *simulate* the state tomography if we apply the magnetic field such that the off-axis terms vanish. We will study the implications of this “Gedankenexperiment” in the following chapter and use it as a starting point for a further outlook on the electronic structure of the SiV center.

Chapter 5

Summary and Outlook

This chapter summarizes both the experimental and theoretical results obtained in this work. In addition, we employ the model of the SiV electronic structure to predict the outcome for two types of experiments: First, we return to the influence of crystal strain on the electronic structure (Sec. 5.1). In a previous report by Sternschulte *et al.*, uniaxial stress measurements have been performed on ensembles of SiV centers, but no detailed interpretation has been given. We review these uniaxial measurements using the simulation established before (Sec. 5.1.1). Moreover, we have assumed earlier in this work that crystal strain induces significant changes in the polarization properties of individual SiV centers. In Sec. 5.1.2, we discuss the polarization of an individual SiV center in dependence of a theoretical strain field and relate the results to recent publications.

In a second section, we discuss the application of magnetic fields along the $\langle 111 \rangle$ high symmetry axis of the SiV center. We have seen in Sec. 4.1.5, that transverse magnetic field terms give rise to spin-mixing in the ground and excited states of the SiV center. Consequently, this spin-mixing is not present when aligning the magnetic field with the defect. While this was not possible experimentally during this work, we can still discuss the theoretical predictions for an optimized field geometry, which is covered in Sec. 5.2. Finally, we summarize the results of this thesis in Sec. 5.3.

5.1 Predictions for strain-related measurements

We have already investigated the influence of crystal strain on the electronic structure of the SiV center, both theoretically (Sec. 2.2.5) and experimentally (Sec. 4.3). In the experimental part, strain presented a constant perturbation on the emitter which was predetermined by the local environment in a nanodiamond. While we could describe the effective perturbation by fitting the relevant parameters to the experimental data, the explicit form of the strain tensor was unknown in these measurements.

In this section we simulate a variable strain perturbation using the theory established in Sec. 2.2.5. We assume, that crystal strain is created by external pressure. This corresponds to the situation arising in uniaxial stress measurements. In contrast to Sec. 2.2.5, where we referred to the strain tensor ϵ_{ij} [Eq. (2.77)], we here employ the stress tensor σ_{ij} because it is defined by the external pressure. For the stress Hamiltonian (2.80), we simply exchange the components ϵ_{ij} by σ_{ij}. Strictly speaking, the numerical pre-factors of the interaction terms in Eq. (2.80) change, and we will relate them in the following section to the experimental parameters utilized by Sternschulte *et al.* [133].

In principle, the stress tensor components can have arbitrary values. However, in unaxial stress measurements, stress is usually applied along the cubic vectors $\langle 100\rangle$, $\langle 110\rangle$ and $\langle 111\rangle$. We will consider the most simple case of a stress applied in [100] direction, hence the stress tensor components σ_{ij} are only non-zero for σ_{xx}. The stress is applied in an external reference frame corresponding to the primitive cubic axes, whereas the internal reference frame corresponds to the x, y, z-axes of the SiV defect (cf. Fig. 2.1). Therefore, we employ Eq. (2.84) on page 71 with ϵ replaced by σ, which simplifies to

$$\tilde{\sigma}_{A_{1g}} = A_1\, \sigma_{xx} \qquad \tilde{\sigma}_{E_{gx}} = -B\, \sigma_{xx} \qquad \tilde{\sigma}_{E_{gy}} = \sqrt{3}B\, \sigma_{xx}. \tag{5.1}$$

Again, we neglect the contribution of $\tilde{\sigma}_{A_{1g}}$, as it only leads to global energy shift. As a result, the strain interaction Hamiltonian for external stress applied in [100] direction in the $\{e_{x,y}\}$ basis set (2.27) is given by:

$$\mathbb{H}^{\text{strain}} = B\sigma_{xx} \begin{bmatrix} -1 & \sqrt{3} \\ \sqrt{3} & 1 \end{bmatrix} \tag{5.2}$$

where we restrict ourselves to the matrix for the orbital part of the wavefunction, and neglect the spin degree of freedom since it is not affected by stress in our model. The only free parameter in the operator (5.2) is B, which defines the energy shift of an E state in dependence of the applied pressure σ_{xx}. Hence, B is given in the unit [meV GPa^{-1}] or [GHz GPa^{-1}]. In the general case, we expect the parameter to be different for ground and excited state, thus we introduce $B^{(g)}$ and $B^{(e)}$ for the ground and excited states, respectively. The parameters $B^{(g,e)}$ are not listed in the literature for the SiV center. For the NV center, Davies and Hamer showed that $B^{(\mathrm{NV})}$ is on the order of 1 meV GPa^{-1} or 242 GHz GPa^{-1} [38].

The eigenvalues of the strain Hamiltonian in Eq. (5.2) are given by [cf. Eq. (2.87)]

$$E_{1,2}^{(g,e)} = \pm\zeta = \pm 2B^{(g,e)}\sigma_{xx}. \tag{5.3}$$

If no other perturbation than stress was present for the SiV center, then the E_g, E_e ground and excited states would be orbitally degenerate. In this case, the stress perturbation would lift the orbital degeneracy and it would lead to a linear splitting with a slope of $\pm 2B^{(g,e)}$. This situation is shown in Fig. 5.1a for ground and excited state, respectively.

We know from the previous chapter that the orbital degeneracy of the E_g, E_e states is lifted by the spin-orbit (SO) and Jahn-Teller (JT) interactions, with SO coupling being the leading perturbation. Hence, the stress Hamiltonian adds to these two effects as a third perturbation. For a small value of the applied stress, we encounter a situation where the SO and stress have comparable energies. In this regime, the resulting level splitting is not linear anymore (Fig. 5.1b). For higher values of σ_{xx}, stress becomes the dominant perturbation, thus the level splitting is directly proportional to σ_{xx}. In the high stress regime, the eigenvectors of the ground and excited states are given by Eq. (2.87).

The energy diagrams in Fig. 5.1 have been calculated utilizing the same algorithm which we used for the simulation of the Zeeman spectra in Sec. 4.1.4. In contrast to

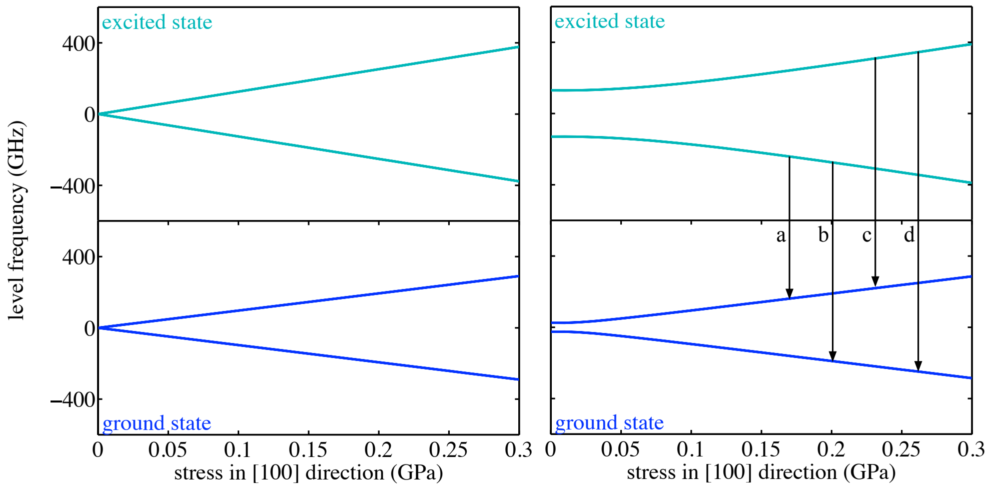

(a) (b)

Figure 5.1: Eigenvalues of the stress Hamiltonian (5.2) for the SiV ground and excited states (a) without and (b) with spin-orbit and Jahn-Teller interaction. Panel (b) also shows the possible optical transitions. The parameters for the simulation are given in the caption of Fig. 5.2.

the previous chapter, we here set the magnetic field equal to zero and vary the stress component σ_{xx}. As a first application, we employ this approach to interpret the uniaxial stress measurements on SiV centers performed by Sternschulte *et al.*

5.1.1 Interpretation of earlier uniaxial strain measurements

In 1995, Sternschulte *et al.* performed uniaxial stress measurements on a (001) oriented CVD diamond film, grown on an HPHT substrate [133]. The sample is comparable with the ensemble sample introduced in the present work. In their measurements, the pressure was applied along the crystallographic [100] axis, and the SiV fluorescence was recorded at 4 K both in PL and PLE (cf. Sec. 1.3.2).

The results of this measurement are shown in Fig. 5.2a, where the photon energies of the fine structure peaks are shown for increasing stress. The peaks are denoted from a to d in ascending energy. The two inner peaks, b and c, are mostly invariant to the increasing stress while the outer peaks a and d split apart with a slope of $\sim 8\,\mathrm{meV\,GPa^{-1}}$. The authors state the following observations: In PL, the highest energy peak d "disappears even at moderate stress values of 0.26 GHz. In PLE (. . .), component d remains fully visible but here the lowest energy component a disappears quickly." Sternschulte *et al.* assume an internal overpressure as the reason for the SiV fine structure, because in their graph, all peaks intersect at a negative stress of −0.06 GPa.

We now employ the theoretical model introduced above to simulate the experiments by Sternschulte *et al.*. We plot the fine structure spectrum (Fig. 5.2b) resulting from optical

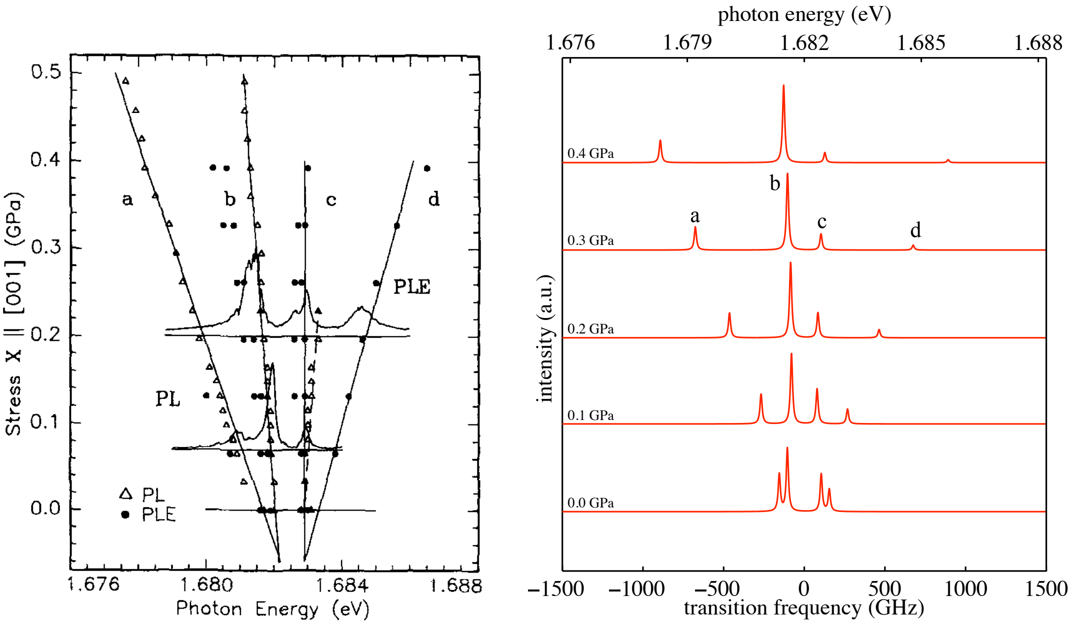

(a) (b)

Figure 5.2: (a) SiV fine structure peak positions in uniaxial stress measurements performed by Sternschulte *et al.* (re-printed from Ref. [133] with permission from Elsevier). In panel (b) we simulate these measurements using the parameters $B^{(g)} = 484$ GHz GPa^{-1} and $B^{(e)} = 630$ GHz GPa^{-1}. Shown are the fine structure spectra for stress increasing from 0 GPa to 0.4 GPa.

transitions between the ground and excited states shown in Fig. 5.1b. The spectrum is simulated in the same way as the theoretical spectra in the previous chapter (e.g. Fig. 1.4a). All parameters for this simulation are equal to those obtained for the ensemble sample (cf. Tab. 4.2); no Zeeman interaction is assumed. The simulated peak energies are compared to the positions in Sternschulte's measurements, where we keep this comparison at a qualitative level. In the simulation, we have the two free parameters $B^{(g)}$ and $B^{(e)}$, which we adjust successively to describe the splitting observed in Fig. 5.2a. Utilizing $B^{(g)} = 484$ GHz GPa^{-1} and $B^{(e)} = 630$ GHz GPa^{-1}, we match the splitting of the outer peaks a, d with the experimentally observed slope while keeping the inner peaks b, c at a constant spacing.

In agreement with the experimental findings, we observe in the simulation that the intensity of peak d vanishes with increasing stress. The intensity of peaks a and c is also reduced, but not as strongly as for peak d. The peak intensities in Fig. 5.2 are determined by three factors: the dipole transition matrix elements, the radiation and collection efficiency for a given dipole contribution and the population of a given state. The calculation shows that the reason for the decrease in intensity for peaks a, c, d is due to the change in population. We have seen in the previous chapter that a thermalization occurs among the electronic states. When no magnetic field is applied, the population in the two ground and the two excited states follows a Boltzmann distribution [Eq. (4.6) on page 135]. With increasing stress the levels in ground and excited state split further apart, and the population of the upper states ($|3\rangle, |4\rangle$ and $|C\rangle, |D\rangle$, cf. Fig. 5.1) decreases exponentially.

This explains why Sternschulte *et al.* observe peak d in PLE but not in PL, and conversely for peak a: The optical transition for the emission of peak d connects the excited state $|C\rangle$ ($|D\rangle$) with the ground state $|1\rangle$ ($|2\rangle$). The excited states $|C\rangle$ and $|D\rangle$ show a vanishing population probability in the high stress regime, thus no PL signal is expected. However, the two ground states $|1\rangle$ and $|2\rangle$ are populated at thermal equilibrium. Hence, for an absorption measurement corresponding to the PLE measurement, we expect non-vanishing absorption. In contrast, the ground states $|3\rangle, |4\rangle$ are not populated when high stress is applied. Therefore, the absorption on transition a, which starts on $|3\rangle, |4\rangle$ is expected to be weak. This is in agreement with the observation of Sternschulte *et al.*

The stress parameters $B^{(g)}$ and $B^{(e)}$, which we assumed for the calculation of Fig. 5.2b, are a factor 2 to 2.6 larger than the parameter $B^{(NV)}$ for the NV-center ($B^{(NV)} = 242\ \mathrm{GHz\,GPa}^{-1}$ according to Ref. [38]). Hence, we tend to assume that the SiV center is slightly more susceptible to crystal strain than the NV center. However, given the qualitative comparison above, a deeper investigation is required to clarify this statement.

Next, we investigate the eigenvectors in the high stress regime. Figure 5.3 displays the ground state eigenvectors $|1\rangle, \ldots |4\rangle$ in the scheme which we introduced in Sec. 2.2.2. We note that the states $|1\rangle$ and $|2\rangle$ as well as the states $|3\rangle$ and $|4\rangle$ are pairwise degenerate (cf. Fig. 5.1). For the visualization, we employ the $\{e_{x,y} \uparrow, \downarrow\}$ basis. The plot in Fig. 5.3 is calculated using the SO and JT parameter for the SiV ensemble sample (cf. Tab. 4.2), $B^{(g)}$, $B^{(e)}$ as given above, and an applied pressure of 0.5 GPa in [100] direction. We note, that for higher stress values, the relative contributions of the basis vectors in Fig. 5.3 remain invariant, since the ratio of the matrix elements in the Hamiltonian (5.2) is constant.

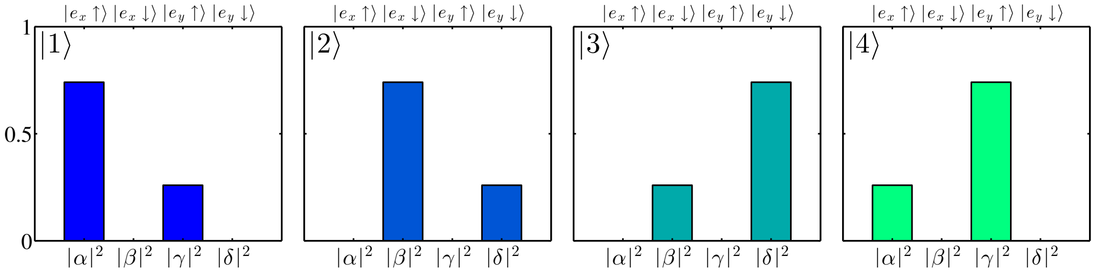

Figure 5.3: Eigenvectors $|1\rangle, |2\rangle, |3\rangle, |4\rangle$ of the SiV ground state under the perturbation of the stress Hamiltonian (5.2) in the basis states $|e_{x,y} \uparrow, \downarrow\rangle$. We employ the SO and JT parameters for the SiV ensemble sample (cf. Tab. 4.2), $B^{(g)} = 484\ \mathrm{GHz\,GPa}^{-1}$ and $B^{(e)} = 630\ \mathrm{GHz\,GPa}^{-1}$, and an applied pressure of 0.5 GPa in [100] direction. The representation of the states is equal to Fig. 2.9.

The off-diagonal terms in the Hamilton operator (5.2) lead to an orbital mixing. If the stress was applied along the internal x axis of the SiV defect, i.e. along the $[\bar{1}10]$ direction, no off-diagonal terms would be present in matrix (5.2) and the stress would not introduce any mixing at all. In the following section, we utilize the eigenvectors in Fig. 5.3 to calculate the dipole matrix elements for optical transitions in order to describe the polarization of a strongly strained emitter.

5.1.2 Strain-induced changes of polarization properties

In this section, we discuss the polarization of strained SiV centers. Using the eigenvectors for ground (Fig. 5.3) and excited state, we calculate the dipole matrix elements for optical transitions using the dipole operator $\hat{\mathbf{p}} = (\hat{p}_x, \hat{p}_y, \hat{p}_z)$. For the calculation of the polarization graphs, we employ the algorithm outlined in Sec. 2.3.2. We consider a single SiV center, located in an (001) diamond sample, thus in the same experimental configuration as in the SIL sample in Sec. 4.1.2. For this configuration, we saw that the polarization graphs showed maxima along the equivalent $\langle 110 \rangle$ directions, which resulted from the projection of a $\langle 111 \rangle$ oriented defect into the (001) sample surface. The simulated polarization curves for this low-strain case are depicted as red dashed lines in Fig. 5.4, where we reprinted the simulated curve for emitter “SIL1” from Fig. 4.7. As we have stated before (cf. Tab. 4.1), the fine structure peaks b and c show high polarization visibilities (close to

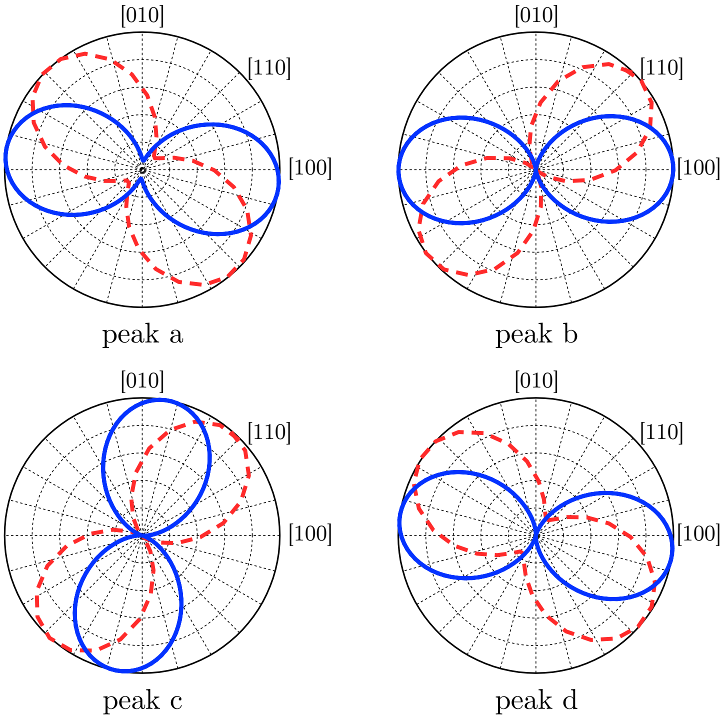

Figure 5.4: Simulated polarization plots for the four fine structure peaks a - d (cf. Fig. 5.2b), for a SiV defect in a low-strain environment (red dashed lines) and with the defect exposed to uniaxial stress of 0.5 GPa along the [100] crystal axis (blue solid lines). The axes labels refer to the primitive crystallographic axes [100] and [010]. The curves are normalized to the maximum of each peak.

unity) whereas the visibilities of peaks a and d are slightly smaller (~ 0.75). This reflects the situation of an SiV defect in an ideal environment, which we now compare to the case of an emitter with uniaxial stress applied.

For the application of uniaxial stress in [100] direction, we assume a measurement geometry according to the experiment of Sternschulte *et al.* [133] discussed in the previous section. The blue solid line in Fig. 5.4 shows the resulting polarization graph for an emitter at an applied pressure of 0.5 GPa. When stress is applied to the sample, the polarization maxima are oriented along approximately 0° and 90°. These directions correspond to the crystallographic axes [100] and [010] direction, thus in comparison to the low-strain case (red dashed line) they are rotated by $\sim 45°$. We observe, that this rotation follows the direction of the applied stress: Stress in the [100] direction leads to a rotation of the polarization lobes, such that their maxima are oriented along the equivalent $\langle 100 \rangle$ directions. Additionally, we observe that the fine structure peaks a and d now also show visibilities close to unity, thus they appear linearly polarized in the simulation. For a single SiV center with strain along these directions, only the fine structure peak b is observed in photoluminescence spectroscopy, because b is the only peak which does not vanish with increasing strain (cf. Fig. 5.2). Hence a strongly strained SiV center can appear in an actual experiment as a single peak, which is linearly polarized along one of the equivalent $\langle 100 \rangle$ direction.

We relate these results to two experimental reports: First, in Ref. [58], the polarization of individual SiV centers in heteroepitaxial "nano-islands" on Ir substrates has been measured (cf. Secs. 1.2.3 and 1.3.3). Owing to the epitaxial growth on an oriented substrate, these measurements allowed to investigate the polarization of individual emitters with respect to the crystal axis of the diamond. Due to the lattice mismatch between the substrate and the diamond nano-islands, the SiV centers in these samples are subject to crystal strain. As a second experimental reference, Riedrich-Möller *et al.* recently published the polarization of individual SiV centers in thin, freestanding diamond films [214]. The films are again grown heteroepitaxially on an Ir substrate, thus, they experience similar strain fields as the nano-islands in Ref. [58]. Both publications report on measurements at room temperature. In the first report, Ref. [58], emitters with linearly polarization fluorescence along [100], [010], [110] and $[\bar{1}10]$ are found. In the second report by Riedrich-Möller *et al.*, two individual SiV defects are discussed which both show polarization graphs along the [100] crystal axis. The room temperature zero phonon lines of the two emitters are shifted in wavelength from the typical value (738 nm) by more than 10 nm, revealing that the diamond film shows considerable crystal strain.

This internal strain field can be present in the samples of Refs. [58, 214] due to the heteroepitaxial growth, which leads to a lattice mismatch for the grown diamond-films. It stands to reason, that certain crystallographic directions are more susceptible to strain than others. Hence, we tentatively suggest that these measurements are performed using samples, which show predominantly stress along the equivalent $\langle 100 \rangle$ crystallographic directions. To date, it is not certain whether the growth conditions favor such an in-plane strain, and more profound investigations are required. Nevertheless, the the theoretical model proposed above provides a consistent explanation for polarization properties observed by Neu *et al.* and Riedrich-Möller *et al.*

In the experimental reports of Neu *et al.* [56, 58] and Riedrich-Möller *et al.* [214], strongly strained SiV defects were investigated which showed spectral shifts of several nanometers, e.g. $\sim 20\,\mathrm{nm}$ (10^4 GHz) in Ref. [214]. In the current theoretical model, a shift of the optical transitions is caused by the different strain response for ground and excited state, i.e. the difference $B^{(e)} - B^{(g)}$ from the previous section and, in addition, the contribution of a totally symmetric stress term $A_1^{(e)} - A_1^{(g)}$ [cf. Eq. (2.84) on page 71]. In the previous section, we showed that these differences are on the order of $\sim 100\ \mathrm{GHz\,GPa^{-1}}$. Hence, the observed line shifts in Refs. [56, 58, 214] would require intrinsic pressures far beyond 50 GPa. It is debatable whether the effect of crystal strain on this order can still be described in terms of a perturbative interaction. When the crystal is subjected to such high strain fields, we expect a lowering of the SiV symmetry, thus, the theoretical model, which we derived in Chap. 2, needs to be re-established starting from a lower symmetry. Nevertheless, the group theoretical concepts outlined in Chap. 2 allow to construct such a model in a similar manner as we have proceeded in the present work.

In summary, we interpreted two experimental findings for the SiV center in this section, using the stress simulation algorithm introduced in the previous sections. Although these predictions reside on a rather qualitative level, they demonstrate the versatility of the theoretical model derived in this work. In the next section, we employ our theoretical model to predict Zeeman spectra for a magnetic field aligned with high symmetry axis of the SiV center, and we discuss the implications for the ground and excited states.

5.2 Optimized magnetic field orientation

In Sec. 4.1.4, we experimentally investigated the response of the SiV center to magnetic fields. Due to the experimental restrictions, the magnetic field was not aligned with the high symmetry axis of the SiV defect. This resulted in transverse magnetic field terms in the Zeeman interaction. These off-axis terms were identified as the reason of spin-mixing. It is interesting to study theoretically, how the properties of the defect are changed when the magnetic field is aligned with the high symmetry axis. We first present the resulting level splitting as well as the resulting Zeeman spectrum for this case. In a second step, we discuss the eigenvectors and the spin polarization in this optimized magnetic field geometry.

We consider a single SiV center in a bulk diamond with a (111) surface, which is placed in the experimental setup, described in Sec. 3.1.3. We simulate the sample to be mounted in Faraday configuration, with the magnetic field being aligned with the z-axis of the SiV defect. To perform this simulation, we take into account the SO coupling ($\mathbb{H}^{\mathrm{SO}}$, cf. Sec. 2.2.2), the JT effect ($\mathbb{H}^{\mathrm{JT}}$, cf. Sec. 2.2.3) and the Zeeman interaction ($\mathbb{H}^{\mathrm{Z}}$, cf. Sec. 2.2.6). We set the relative B-field angle to 0°, hence the transverse magnetic field components $B_x = B_y = 0$. In these simulations, no crystal strain is taken into account.

In the discussion of the ensemble sample (Sec. 4.1.4), we have seen that the SO coupling is the leading orbital interaction. To obtain an intuitive picture for the situation of a [111] aligned magnetic field, we first neglect the JT interaction and only consider the action of $\mathbb{H}^{\mathrm{Z}} + \mathbb{H}^{\mathrm{SO}}$. With $\mathbf{B} = (0, 0, B_z)$, the Zeeman Hamilton operator (2.89) on page 74

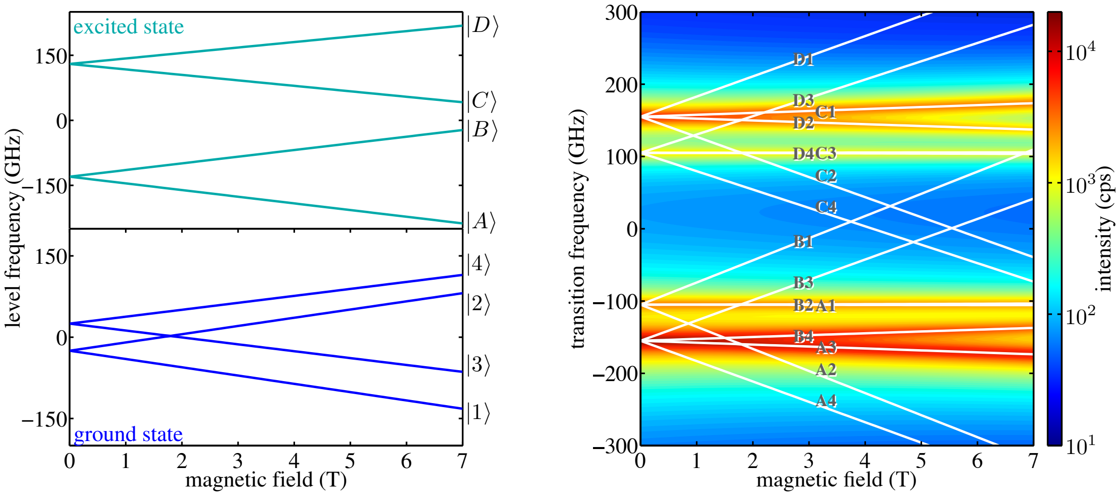

(a) (b)

Figure 5.5: (a) Level splitting in the ground and excited states for a [111] oriented SiV center in dependence of an increasing magnetic field, which is aligned parallel to the high symmetry axis of the emitter. (b) Resulting optical transitions (white lines) and a simulated Zeeman spectrum (color-plot) versus the magnetic field.

becomes diagonal, and the eigenvalues of $\mathbb{H}^{\mathrm{Z}} + \mathbb{H}^{\mathrm{SO}}$ are given by

$$E_1^{Z,SO} = -(q\gamma_L + \gamma_S)B_z - \lambda \tag{5.4a}$$

$$E_2^{Z,SO} = (q\gamma_L + \gamma_S)B_z - \lambda \tag{5.4b}$$

$$E_3^{Z,SO} = (q\gamma_L - \gamma_S)B_z + \lambda \tag{5.4c}$$

$$E_4^{Z,SO} = -(q\gamma_L - \gamma_S)B_z + \lambda \tag{5.4d}$$

Hence, the level splitting scales linearly with the magnetic field B_z when the field is parallel to the [111] direction. This dependence is preserved when adding the JT interaction and the result is the same for ground and excited state. For the relevant interaction terms, we employ the parameters $\lambda_{g,e}$, $Q_{g,e}$ and q of the ensemble sample, indicated in Tab. 4.2 on page 134. The resulting level splitting – including the JT interaction – is shown in Fig. 5.5a for ground and excited. We observe, that the ground states cross at a magnetic field of ~ 2 T.

With the eigenvalues for ground and excited states we simulate the corresponding Zeeman spectrum (Fig. 5.5b). From the energy distance we calculate the resulting frequencies for optical transition between ground and excited states. These transitions are shown as white solid lines in Fig. 5.5b, irrespective of the transition probability. To simulate a realistic spectrum, we use the same approach as for the single emitters presented in Sec. 4.1.4: We calculate the matrix elements $\langle \hat{p}_x \rangle, \langle \hat{p}_y \rangle, \langle \hat{p}_z \rangle$ of the dipole operator $\hat{\mathbf{p}}$ between the eigenvectors of ground and excited state (cf. following section), and take into account the collection efficiencies for the X, Y, Z dipoles. The Z dipole, which is parallel to the [111] crystal direction, is assumed to be perpendicular to the sample surface in the present simulation. Hence, approximately an order of magnitude less of the light is collected in comparison to the X, Y dipoles [73, 201] and we adjusted the collection efficiency coefficients η_x, η_y, η_z accordingly. Furthermore, the intensity of an optical transition depends on the population of the initial state, which we again assume to follow a Boltzmann distribution (Eq. (4.6)). In accordance with Sec. 4.1.4, we model the transition peaks using Lorentzian peak functions (cf. Eq. (4.7), with a full width at half maximum $\Gamma = 10$ GHz). The resulting Zeeman spectrum is shown as a color-plot in Fig. 5.5b.

The Zeeman spectrum for magnetic fields in [111] direction is considerably simpler than for fields aligned with the [001] direction (cf. Fig. 4.10). In the level splitting scheme (Fig. 5.5a), several ground states shift with the same slope as corresponding excited state, e.g. state $|A\rangle$ and state $|1\rangle$. Hence, their energetic difference remains constant and the corresponding optical transitions (e.g. $A1$, $B2$, $\dots$) do not shift when increasing the magnetic field. We further observe, that several transitions indicated by white lines are not visible in the color-plot, e.g. $A4$, $A2$ and others. As we will see in the next section, these transitions would flip the spin of the electron, hence they are forbidden because of the dipole selection rules.

In Ref. [133], Zeeman spectra for ensembles of SiV centers have been measured with the field applied along the [111] axis. In comparison with field applied parallel to the [100] and [110] direction, the Zeeman spectrum in [111] also appears relatively simple. However, for an ensemble of defects, the equivalent orientations of the centers all contribute to the Zeeman spectrum. In contrast, Fig. 5.5b simulates an individual SiV center, hence a quantitative comparison of our simulation with Ref. [133] remains challenging.

For the application of magnetic fields parallel to [111] in an actual experiment, two approaches are feasible which both impose technical challenges. One method would be to cut or cleave a diamond containing SiV centers along a (111) plane and then mount the sample in Faraday configuration. For such a sample, the experimental setup employed in this work could be utilized. However, one faces the problem that (111) diamond surfaces are difficult to polish to an adequate surface smoothness. To date, no high purity diamond with (111) surface is commercially available. Nevertheless, different research groups recently achieved the fabrication of (111) oriented diamond samples for single defect center spectroscopy [121, 224]. Additionally, the light of the Z dipole would be collected with lower efficiency. Hence, the resulting photon count rates are expected to be small. Nevertheless, photonic structures, such as nano-wires, could re-enhance the collection efficiency [93].

An alternative approach would be to mount the sample in a so-called vector magnet, where the magnetic field direction can be aligned in arbitrary directions. For this measurement geometry, any diamond orientation can be employed, thus also the SIL sample presented in this work. Preliminary Zeeman spectra of individual SiV centers in the SIL sample, performed in a vector magnet at the University of Sheffield show a high agreement with the predicted spectrum in Fig. 5.5b [225].

The main reason of aligning the magnetic field with the high symmetry axis of the SiV center is the suppression of the spin mixing, which is caused by the off-axis Zeeman terms. Therefore, we investigate the eigenvectors and the corresponding spin polarization in [111] oriented magnetic fields in the following section.

5.2.1 Spin polarization in [111] aligned magnetic fields

In the previous section, we simulated how the Zeeman spectra change when the magnetic field is aligned with the z axis of the SiV defect. We now discuss the implications for the eigenvectors and the spin purity of the resulting states. We have seen in Sec. 4.1.5, that the transverse magnetic field terms B_x, B_y give rise to spin-mixing $\propto B_x S_x + B_y S_y$, which was particularly dominant in the ground state. When the transverse terms are absent, we expect the spin-mixing to vanish.

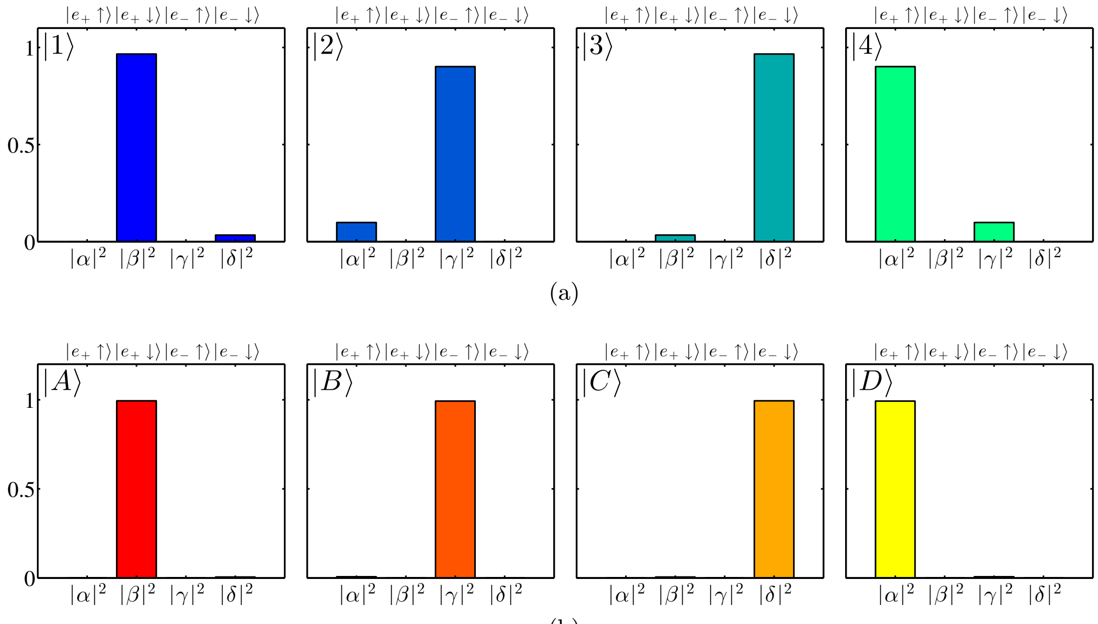

(a)

(b)

Figure 5.6: Eigenvectors (a) $|1\rangle, \dots |4\rangle$ and (b) $|A\rangle, \dots |D\rangle$ of the SiV ground and excited states, respectively. The states are simulated assuming a magnetic field of 5 T aligned parallel to the high symmetry axis of the SiV defect. The states are expressed using the SO coupled basis vectors $|e_\pm \uparrow, \downarrow\rangle$. We employ the parameters for SO, JT and Zeeman interaction of the SiV ensemble sample (cf. Tab. 4.2). The representation of the states is equal to Fig. 2.9.

Figure 5.6a shows the eigenvectors for the ground states $|1\rangle$, $|2\rangle$, $|3\rangle$, $|4\rangle$ at a magnetic field strength of 5 T. The representation of the states is equal to Fig. 2.9, i.e. we plot the absolute squares of the basis vector coefficients $\alpha, \dots, \beta$. The states are given in the SO coupled basis $\{e_\pm \uparrow, \downarrow\}$. We observe that the state-mixing is dramatically reduced both for the ground and excited states. The residual mixing is purely of orbital nature, e.g. we observe a mixture of the $|e_+ \downarrow\rangle$ and $|e_- \downarrow\rangle$ for ground state $|1\rangle$. This orbital mixing is a consequence of the weak, but non-negligible, JT effect. As we have predicted it, no spin-mixing is observed in either ground or excited state. As a trivial consequence, the spin polarization P, defined in Sec. 4.1.5, equals $P = \pm 1$ for all states.

In this optimized B-field configuration, both the ground and excited states offer pure spin states which enable the initialization and manipulation of spin states. In Sec. 4.2, we have selectively populated the $m_S = \pm\frac{1}{2}$ spin manifolds in the excited state and verified this selective excitation using resonance fluorescence. The resonance fluorescence is also feasible in the optimized B-field geometry. For instance, the transitions $B4$ and $A3$ originate from excited states of different spin projection. Hence, we can determine the excited state spin by discriminating which line is visible in the spectrum.

Additionally, a distinguished spin projection in the ground state can now be selectively populated. We assume that, initially, the ground state spin is in a statistical mixture of up and down projections. When shining in a resonant laser, e.g. tuned to the transition $C1$, we populate the $|e_- \downarrow\rangle$ excited state. After the radiative lifetime, the SiV center decays back into the ground states $|e_+ \downarrow\rangle$ or $|e_- \downarrow\rangle$, because the optical dipole transition preserves the spin. Hence, we optically pump the system to a given spin projection, and thus, initialize the spin for further manipulation.

For spin manipulation, it is advantageous that the states $|2\rangle$ and $|3\rangle$ cross at a magnetic field strength of about 2 T. States $|2\rangle$ and $|3\rangle$ have opposite spin projection, but the same orbital wave function. Thus in this regime, the spin could be flipped theoretically using similar microwave techniques as applied for the NV center in diamond [226]. To read out the spin state, resonance fluorescence measurements can then be applied.

Clearly, this has been a very compact proposal on how to perform spin manipulation for the SiV defect. Furthermore, the current theoretical model needs to include higher order effects which govern properties like spin coherence times. However, spin manipulation is beyond the scope of this work, as our primary aim was to understand the electronic structure of the defect. With the results we have obtained, we provide a stable basis for further investigations and a gradual refinement of this model. We have seen in this section, that a tremendous improvement of the spin purity both for ground and excited state should be attainable when optimizing the magnetic field orientation. This closes the section on predictions from the theoretical model. In the upcoming final section, we summarize the results, which we have obtained in this thesis.

5.3 Summary of the results presented in this work

The objective of this thesis was to determine the electronic structure of the SiV defect in diamond. Connected to the electronic structure is the molecular geometry of the defect. We start from the configuration which was predicted theoretically in Refs. [122, 127]. In this configuration, the defect consists of a Si impurity which replaces one carbon atom and a neighboring lattice vacancy. The theoretical considerations showed that the Si atom then moves along the [111] axis towards the vacancy, resulting in a split-vacancy configuration.

As we have seen in the first part of the theoretical chapter, the geometry of the defect defines the orbital symmetries, which in turn, can be conveniently classified using group theory. Hence, as a first definition, we have introduced point groups and their corresponding symmetry elements. The SiV center belongs to the dihedral D_{3d} group, which includes the identity, two three-fold rotations, three two-fold rotations, an inversion center, two improper rotations and three mirror planes.

To derive the electronic states, we have first introduced the notion of irreducible representations. The irreducible representations of a defect belonging to a given point group label the resulting states and specify their degeneracies. This degeneracy is equal to the dimension of the irreducible representation, which is indicated in the character table for a given point group. For the D_{3d} group of the SiV center, there are four one-dimensional representations A_{1g}, A_{2g}, A_{1u}, A_{2u}, and two two-dimensional representations E_g, E_u. Hence, the SiV center has a maximum orbital degeneracy equal to two.

As a consecutive step, we calculated the single electron orbitals in a molecular orbital approach. The electrons can populate orbitals provided by the unsaturated carbon bonds and by the $2s$, $2p$ orbitals of the central Si impurity. These orbitals are superimposed to form symmetry adapted linear combinations (SALCs), applying again group theoretical principles. As a result, we obtain bonding and antibonding superpositions of the orbitals for the A_{1g}, A_{2u}, E_g, E_u representations. Density functional theory calculations yield the energies of the dangling bond SALCs. The center hosts a total number of eleven electrons: six electrons contributed by dangling bonds, four electrons from the Si-atom and one electron trapped from nearby donors to account for the negative charge [63]. Taking into account spin degeneracy, the a (e) orbitals accommodate 2 (4) electrons, i.e. one unpaired electron remains in the e_g orbital. We therefore consider the SiV ground state as $^2E_\mathrm{g}$ and the excited state as $^2E_\mathrm{u}$ where a single hole formalism is equivalent to a single electron state [41].

These two states initially show a fourfold energetic degeneracy, i.e. a twofold orbital and a twofold spin degeneracy. This degeneracy can be lifted by several interaction terms. We model these interactions in a perturbative approach: An unperturbed Hamiltonian $\mathbb{H}_0$ gives rise to fourfold degenerate levels in the ground and in the excited state, respectively. Ground and excited state are separated by 1.68 eV corresponding to the 740 nm zero phonon line transition of the SiV center. The fourfold degeneracy is reflected in four orthonormal basis vectors $\{e_{x,y} \uparrow, \downarrow\}$ for ground and excited state, respectively. Small perturbations result in linear combinations of these basis vectors.

We model four interaction terms: The orbital degeneracy is lifted by the spin-orbit and the Jahn-Teller interaction. Owing to the particular level structure of the SiV center, the spin-orbit interaction only couples the z components of spin and orbit, and consequently does not lead to spin mixing. The Jahn-Teller interaction is caused by vibrations of the nuclear configuration. We identified vibrations of E-type symmetry to couple to the electrons of the SiV center. A third perturbation, which we discussed, was the interaction for crystal strain. Starting from a general strain tensor, we deduced which tensor components couple to the orbital parts of the wave function. The spin degeneracy is lifted when we apply a magnetic field, thus as a fourth interaction, we investigated the Zeeman effect on both spin and orbital part of the wave function. We showed that this interaction depends indirectly on the spin-orbit and Jahn-Teller ratio, which motivated the measurements of Zeeman spectra in the experimental part of the work (see below). For all interaction terms, we calculated the explicit matrix representations and showed theoretically their action on the eigenstates of the SiV center.

While the four perturbations above act on ground and excited state separately, we introduce the dipole operator as a fifth interaction which connects ground and excited states. By calculating explicitly the matrix elements of the dipole operator for all combinations of ground and excited states, we model optical dipole transitions. Hence, the frequency, intensity and polarization of the emitted light depends on the eigenvalues and -vectors of the perturbed electronic system. Consequently, these optical transitions can be compared to ones which we observe in a spectroscopy experiment, and the free parameters in the electronic interaction terms can be fitted to the experimental results (see below).

To provide experimental access to the optical properties of individual SiV centers, we employed confocal microscopy at cryogenic temperatures. In Sec. 3.1, we introduced the concept of confocal microscopy and discussed its advantages over conventional microscopy. Confocal microscopy has been realized in two experimental setups which were characterized in Sec. 3.1.3. Subsequently, we discussed the sample fabrication. The results presented in this work have been obtained using three different CVD diamond samples: One sample – called the ensemble sample – contained an ensemble of SiV centers for preliminary measurements. Single defects have been created in a second and third sample. On the second sample, single SiV are found in isolated nanodiamonds grown on an Ir substrate. These centers are subject to crystal strain and are used as a test-bench for individual centers in strained environments.

Finally, the third sample is a high purity single crystalline diamond which has been implanted with Si ions. We discussed the implantation procedure and defined the stopping range. As a side effect, the ion implantation creates lattices vacancies. Using appropriate thermal annealing we can promote the vacancies to pair with implanted Si atoms and form SiV complexes. After the ion implantation, the sample showed luminescence from individual SiV centers, however at very modest count rates. As the primary cause for the low count rates, we identified the refraction and total internal reflection of the SiV fluorescence at the diamond-air interface. This problem is mostly solved by placing solid immersion lenses (SILs) over the emitter. We fabricate these lenses directly into the diamond surface using focused ion beam milling (FIB). Employing a donut shaped ion beam with an intentional blur, we developed a fast and reliable technique to produce arrays of SILs. The fabricated SILs showed an improvement of the fluorescence count rate by a factor of approximately 5. With this approach, a sufficiently high collection efficiency was obtained with typical single photon count rates of $\sim 2 \cdot 10^4$ photons per second.

This improvement of the collection efficiency enabled a detailed investigation of the spectral fine structure for individual SiV centers, first without a magnetic field applied. The spectral fine structure at 0 T consists of four characteristic peaks spread by 48 GHz and 249 GHz, respectively [62]. As an initial experiment, we compared the spectral fine structure of the ensemble and the SIL sample with reference measurements in the literature, yielding an unprecedented agreement on both the absolute wavelength and the splitting of the fine structure peaks. To the best of our knowledge, it is the first time that the SiV fine structure has been observed for single defects in bulk diamond. This provides access to individual defects in a low strain material, and thus enables the investigation of the SiV electronic structure in an ideal, unperturbed environment. The line width of the fine structure peaks ranges from approximately 1 GHz for individual SiV centers in the SIL sample to 10 GHz for the SiV ensemble. As a first verification of the proposed theoretical model, we measured the polarization of each individual fine structure line. The polarization of the lines can be grouped in two subsets. The inner transitions are polarized parallel to each other and perpendicular to the outer ones. All polarization maxima are parallel to the equivalent $\langle 110\rangle$ directions. The measurements correspond to a projection into the (001) plane, thus the observed polarization direction is consistent with the predicted $\langle 111\rangle$ alignment of the defect. In addition, the visibility for the polarization graphs is predicted correctly using our theory. This result is confirmed by independent measurements on a larger number of SiV defects [176].

The key experiment in this thesis is the application of a magnetic field, which splits the magnetic sublevels of the defect. The measurement has been carried out on both the ensemble sample and single defects under SILs. For both samples, we observe a splitting of each fine structure line into four lines. The splitting is not symmetrical and shows several avoided crossings. The splitting into four components points towards a spin 1/2 system, and the avoided crossings indicate a dominant spin-orbit coupling. As the ensemble spectrum shows a splitting pattern, which is identical to the single defect, we infer that all possible equivalent orientations of the center in the ensemble have the same relative angle to the magnetic field. The only orientation which allows for this fact is along the $\langle 111\rangle$-axes. In combination with the polarization measurements, this shows for the first time experimental evidence of a $\langle 111\rangle$-alignment for SiV centers and establishes a link to theories published so far [122, 126].

Fitting the free parameters of the interaction terms to the experimental data, we obtain an excellent agreement between the theoretical and experimental Zeeman spectra. The fit shows that the spin-orbit interaction is the leading orbital perturbation. In addition, we observe a strong quenching of the orbital gyromagnetic moment, which we attribute to the influence of the Jahn-Teller interaction. The comparison between theory and experiment yields both eigenvalues, i.e. the energy levels, and eigenvectors of the total Hamiltonian, and allows a comprehensive study of the SiV electronic structure. As we expect it for a spin 1/2 system, all energy levels split in two components as the magnetic field is applied. The discussion of the eigenvectors shows, that the each of the four excited states is composed mainly of one of the $\{e_{x,y}\uparrow,\downarrow\}$ basis states, thus the excited state shows a high spin polarization. In contrast, spin mixing is observed for the ground states.

This spin purity motivates the spin selective population of the excited states. We perform this experiment using the technique of resonance fluorescence. While the experiment is described in detail elsewhere [64, 65], our theoretical model provides a straight-forward explanation of the underlying mechanisms. Using resonant optical excitation, we populated a particular spin manifold in the excited state. A thermalization takes place, which however leaves the spin projection invariant while changing the orbital part of the wave function. We discussed physical origins for this relaxation among the excited states and deduced a phenomenological relaxation operator which is in agreement with the observed, spin-dependent relaxation. This experiment can be seen as a first step towards deterministic spin preparation and read-out for individual SiV centers. Our model provides a profound theoretical basis to promote these types of experiments.

To this point, the experiments were all carried out using SiV centers in optimized, low strain samples. In many cases, one faces defect centers which are subject to crystal strain. To compare the influence of crystal strain with the theoretical considerations which we took in Chap. 2, we investigated strained SiV centers in nanodiamonds. In a first step, we discussed again Zeeman spectra of single SiV centers in these nanodiamonds and showed, how the magnetic field splitting is influenced when crystal strain is present. Subsequently, we repeated the spin selective excitation for a strained defect. At first glance, the relaxation mechanism appears to be modified in strained samples, because the spin selectivity is partly lost in the experiment. However, a detailed investigation revealed that this apparent change can be fully explained in the framework of the existing theoretical model.

Hence, in conclusion we could explain every experimental aspect we presented using the theoretical model of the electronic structure, which we established for the SiV center. Furthermore, as an outlook at the beginning of this chapter, we showed that the model also explains uniaxial strain measurements carried out in an earlier publication. As a further outlook, we discussed the consequences of aligning the magnet field parallel to the high symmetry axis of the SiV center. In this *Gedankenexperiment*, the absence of transverse field components prevents a spin mixing. Theoretically, we expect a spin polarization equal to unity which would reveal higher order interaction terms. Performing resonant optical excitation for such an optimized magnetic field geometry is highly interesting for future experiments on spin manipulation on the SiV center.

The main goal of this thesis was to understand the electronic structure of the SiV center, in a sense that we understand the internal physical mechanisms which determine the spectral fine structure of the defect. While the key role of this work was the explanation of the Zeeman spectra, the theory was – without further modifications – extendable to polarization measurements and the effect of crystal strain. At the same time, all the experiments are feasible at a single emitter level, which proves the suitability of the defect for quantum optics experiments. We started this thesis with a discussion of color centers in diamond as spin-photon interfaces, and we raised the question, whether the SiV center provides – besides its excellent optical properties – electronic properties that allow its usage as a qubit. The profound knowledge of the electronic states and of the relaxation mechanism in the excited state, which we acquired in the course of this thesis, have established the foundations, on which future experiments on spin manipulation with the SiV center can be built.

Concluding remark

I hope that the knowledge, which I acquired in the course of studying this fascinating defect, will further increase its prospects for solid-state quantum applications. At the same time, some of the open questions and apparent contradictions from earlier publications could be resolved using the theoretical model shown. We established a link between some theoretical proposals on the SiV center and showed many experimental verifications for them. The upcoming research on the SiV center will reveal whether the model, which we proposed, requires to be refined.

I would like to finish with a few words about the integrity of a physical model, as spoken by Richard Feynman [227]:

“When you have put a lot of ideas together to make an elaborate theory, you want to make sure, when explaining what it fits, that those things it fits are not just the things that gave you the idea for the theory; but that the finished theory makes something else come out right, in addition.”

I tried to elucidate the SiV electronic structure from many possible angles. This way, I hope that I could satisfy Feynman's idea of scientific integrity by proposing a theory which goes beyond its initial purpose. I think that some of these criteria are met when I recollect a few of the consistent phenomena which we observed. For all the problems, which remain to be solved and which might further elucidate the exciting SiV center, I am eagerly looking forward to the experiments to come.

Matlab scripts

The theoretical model developed in Chap. 2 and employed in Chap. 4 has been implemented using Matlab. We here list the core functions for the simulation of the total Hamiltonian (including spin-orbit-, Jahn-Teller-, Zeeman- and stress interaction), of the transition dipole strengths and of the polarization curves. Not shown are the plotting subroutines.

```
function [Eg, Ee, T, Ef, Exp] = SiVModel(G1,G2,tg,pg,te,pe,tB,f,eps)
% G1 and G2 are the spectral splittings in GHz, G1 betw/ peak a and d,
% G2 betw/ peak b and c.
% tg,pg and te,pe are free parameters.
% tg = 0 means, all the splitting corresponds to spin-orbit splitting
% te = pi/2 means, all the splitting is due to the Jahn teller effect.
% tB is theta_B, the relative angle betw/ SiV high symmetry axis and the
% external b-field. f is the factor that diminishes the orbital g-factor
% g_L (c.f. function "Hamiltonian" at the end of this file).
% eps is the value of uniaxial stress in GPa, we employ a scaling factor
% of the NV center as a reference. For arbitrary stress expressed in
% parameters alpha, beta (cf. Sec. 2.2.5), set eps = alpha + i*beta.

% B-field vector, same dimension as the experimental data vector to plot
% the two in the same graph
B = 0:0.1:7;

% Constants and conversions:
t = tB*pi/180;
p = 45*pi/180;
GHz = 1e9;
c = 3E8;
G1 = G1*GHz;
G2 = G2*GHz;
k = 2;
eps = eps.*242.*k.*GHz;
% The value 242 GHz/GPa is the corresponding stress
% response of the NV center, cf. Davies1976. The factor
% k is the free parameter for the SiV center.

% Level splitting in excited (EEe) and ground state (EEg)
EEe = (G1+G2)/4;
EEg = (G1-G2)/4;

% Calculation of the relative contribution of SO- and JT-interaction for
% ground ...
```

```
Dg = 2*EEg*cos(tg);
Qgx = EEg*sin(tg)*cos(pg);
Qgy = EEg*sin(tg)*sin(pg);
Qg = sqrt(Qgx.^2 + Qgy.^2);
DeltaEg = 2*sqrt(Qg.^2 + (Dg.^2)./4)./GHz;

% ... and excited state
De = 2*EEe*cos(te);
Qex = EEe*sin(te)*cos(pe);
Qey = EEe*sin(te)*sin(pe);
Qe = sqrt(Qex.^2 + Qey.^2);
DeltaEe = 2*sqrt(Qe.^2 + (De.^2)./4)./GHz;

%Print the contributions from spin-orbit-coupling and Jahn-Teller, resp.
fprintf('\n Dg = %6.2f Qgx = %6.2f Qgy = %6.2f',Dg/GHz,Qgx/GHz,Qgy/GHz);
fprintf('\n De = %6.2f Qex = %6.2f Qey = %6.2f',De/GHz,Qex/GHz,Qey/GHz);
fprintf('\n Delta_Eg = %6.2f, Delta_Ee = %6.2f ',DeltaEg,DeltaEe);
fprintf('\n'); %CH: added line break


%For printing the eigenfunctions later on
Base1Array = {'|egx>|up>' '|egx>|dn>' '|egy>|up>' '|egy>|dn>'};
Base2Array = {'|+>|up>' '|+>|dn>' '|->|up>' '|->|dn>'};
LabelArray = {'+\uparrow' '+\downarrow' '-\uparrow' '-\downarrow'};
labl = {'A','B','C','D'};

%% Calculate eigenvalues and eigenvectors
for b=1:length(B)
    % B-Field as a vector
    Bv = B(b)*[sin(t)*cos(p), sin(t)*sin(p),cos(t)];
    % Calculate the Hamiltonian matrices, for the uniaxial stress
    % measurements of Sternschulte1995, the results fit best with the
    % excited state stress parameter scaled by 1.3
    Hg = Hamiltonian(Dg,Bv,Qgx,Qgy,f,eps);
    He = Hamiltonian(De,Bv,Qex,Qey,f,1.3.*eps);

    % Calculate the eigenstates and -values for ground state...
    [Vg,Ega ] = eig(Hg);
    Eg(:,b) = diag(Ega);
    % ... and excited state
    [Ve,Eea] = eig(He);
    Ee(:,b) = diag(Eea);

    % Calculate the transition frequencies (the PEAKS in the spectrum)
    % and the peak intensities, ILHWP is for the polarization analysis
    [Ta Tlbla Ia Axa Aya Aza ILHWP] = Transitions(Eg(:,b),Ee(:,b),Vg,Ve);
    T(:,b) = Ta;
    I(:,b) = Ia;
    Ax(:,b) = Axa;
    Ay(:,b) = Aya;
    Az(:,b) = Aza;
    ILHWP = ILHWP';

    % Transformation matrix for eigenstates
    % transform to e+/e- states (eigenbasis for L_z operator)
```

```
    Tv = (1/sqrt(2)) * [-1 0 -i 0; 0 -1 0 -i; 1 0 -i 0; 0 1 0 -i];
    Vg = inv(Tv.')*Vg;
    Ve = inv(Tv.')*Ve;

    % plot the ground and excited state eigenvectors for B = 4.0T
    if (b==40)
        % EVsExcStateB001;
        % EVsGndStateB001;
    end
end

%% This part of the script simulated the experiment

% Constants
dw = 10e9; ... Linewidth of the transition (FWHM = 10 GHz in the exp.)
NE = 1500; ... number of points
minE = -1500*GHz;
maxE= 1500*GHz;

% The frequency axis
Ef = minE:(maxE-minE)/(NE-1):maxE;
% The magnetic field axis
Bf = ones(size(Ef))'*B;

E = Ef'*ones(size(B));
dimension = ones(size(Ef))';
Exp = dimension*ones(size(B));

% Calculate the maximum of matrix I (normalisation to 1)
I=I/max(max(I));

for t = 1:size(T,1)
    % Plot the lines with a lorentzian lineshape
    % E - dimension*T(t,:) gives the "peak position" of the Lorentzian
    % dw is the width. Multiplied by 3.7E3 to compare it
    % with bulk ensemble data
    ExpT = dimension*3.7e+03*I(t,:)./(1+(E - dimension*T(t,:)).^2/dw^2);
    % above, ExpT was the contribution of one peak to the B-field trace
    % we're adding the peaks up, one after the other
    % to the Zeeman spectrum given in "Exp"
    Exp = Exp + ExpT;
end

%% Plotting part
% subfunctions for data visualization

ImportData;
% imports experimental data (Zeeman splitting)


EnsembleSplitting;
% plots three panel plot:
% 1. experimental Zeeman splitting,
% 2. experimental Zeeman splitting + transition frequencies as solid
%    lines (plot T vs. B)
```

```
% 3. simulated Zeeman splitting
%    (variable "Exp" vs. a meshgrid made of (Ef, Bf), and the predicted


LevelSplitting;
% plots the level splitting (Ee and Eg vs. B)


PolarizationGraph(ILHWP(1,:), ILHWP(2:end,:), T(:,1));
% plots the polarization graphs for B = 0T (corresp. to T(:,1)
end
%% end of function SiVModel
%% ----------------------------------------------------------


%% ----------------------------------------------------------
%% Transitions:
function [T, Tlbl, I, Ax, Ay, Az, ILHWP] = Transitions(Eg,Ee,Vg,Ve)
kB = 1.38065E-23/6.6261E-34; % Boltzman constant for thermalization
etaX = 1; etaY = 0.642; etaZ = 0.823; % dipole collection efficiencies

% Dipole operator matrices
px = [1 0; 0 -1];
py = [0 -1; -1 0];
pz = 2.*[1 0; 0 1];

% expand to spin space
I2 = [1 0; 0 1];
Px = kron(px,I2);
Py = kron(py,I2);
Pz = kron(pz,I2);

labl = {'A','B','C','D'};

% calculate transition dipole strength
for g=1:length(Eg)
    for e=1:length(Ee)
        t = length(Ee)*(g-1) + e;
        T(t,1) = Ee(e) - Eg(g);
        Tlbl(t,:) = sprintf('%s%u',labl{e},g);
        vg = Vg(:,g)/norm(Vg(:,g));
        ve = Ve(:,e)/norm(Ve(:,e));
        Ax(t,1) = vg'*Px*ve;
        Ay(t,1) = vg'*Py*ve;
        Az(t,1) = vg'*Pz*ve;
        Ix(t,1) = abs(Ax(t,1))^2;
        Iy(t,1) = abs(Ay(t,1))^2;
        Iz(t,1) = abs(Az(t,1))^2;
        % The factor (exp(...)) is due to the Boltzmann population
        % of the exc. states
        I(t,1) = (etaX*Ix(t,1) + etaY*Iy(t,1) + etaZ*Iz(t,1)) ...
                    .* exp(-(Ee(e) - Ee(1))./(kB.*12));

        ILHWPa = Polarization(sqrt(etaX).*Ax(t,1), ...
                              sqrt(etaY).*Ay(t,1), ...
```

```
                              sqrt(etaZ).*Az(t,1));
        ILHWP(:,1) = ILHWPa(:,1);
        ILHWP(:,t+1) = ILHWPa(:,2);
    end
end
end
%% end of function Transitions
%% --------------------------------------------------------------


%% --------------------------------------------------------------
function H = Hamiltonian(D,B,a,b,f,eps)
% Calculate the total Hamiltonian

% electron and spin g-factors in Hz
ge = 28e9;
gL = 1*ge/2;

Lx = [0 1; 1 0];
Ly = [0 1i; -1i 0];
Lz = diag([1 -1]);

Sx = [0 1; 1 0]/2;
Sy = 1i*[0 -1; 1 0]/2;
Sz = [1 0; 0 -1]/2;

I2 = diag([1 1]);

Bx = B(1);
By = B(2);
Bz = B(3);

H = - D*kron(Ly,Sz) ... spin-orbit coupling
    + f*gL*kron(Bz.*Ly,I2) ... orbital Zeeman effect
    + ge*kron(I2,Bz*Sz) ... spin Zeeman effect, x-component
    + ge*kron(I2,Bx*Sx) ... spin Zeeman effect, y-component
    + ge*kron(I2,By*Sy) ... spin Zeeman effect, z-component
    + a*kron(Lz,I2) ... Jahn-Teller in x-direction
    + b*kron(Lx,I2); ...Jahn-Teller in y-direction


% if we add the uniaxial stress, uncomment the following line
Hstress = StressUniaxial(eps);
H = H + Hstress;

end
%% end of function Hamiltonian
%% --------------------------------------------------------------


%% --------------------------------------------------------------
%% Stress Hamiltonian for stress along the [100] crystal direction
function [HStressU] = StressUniaxial(eps)
    I2 = diag([1 1]);
    % for stress along the [100] direction
```

```
    Hstress2dim = eps.*[-1 sqrt(3); sqrt(3) 1];
    % uncomment for stress along arbitrary directions
    % alpha = real(eps);
    % beta = imag(eps);
    % Hstress2dim = [alpha beta; beta -alpha];
    HStressU = kron(Hstress2dim,I2);
end
%% end of function StressUniaxial
%% ------------------------------------------------------------


%% ------------------------------------------------------------
function ILHWP = Polarization(Ax,Ay,Az)
    %polarization for SiV
    % lab frame: orientation of diamond sample
    % along 100 growth direction
    % defect frame: (z defect axis) one of
    % the four possible 111 orientations

    % polar angle (td), azimutal angle (pd)
    % of the z defect axis in the lab frame
    td = acos(1/sqrt(3));
    % pd = 0 because sample edges are (110)
    pd = 0;
    % polar angle of integration between 0 and t0
    t = 0;
    % azimutal angle for integration between 0 and 2pi
    p = 0;
    %number of polarization angle data points
    Npp = 72;
    ILHWP=zeros(Npp,2);

    %projection of defect frame onto lab frame
    C1 = [cos(p) -sin(p); sin(p) cos(p)];
    C2 = [cos(t)*cos(p), cos(t)*sin(p), -sin(t); -sin(p), cos(p), 0];
    Rd = [cos(td)*cos(pd), -sin(pd), sin(td)*cos(pd);
          cos(td)*sin(pd), cos(pd), sin(td)*sin(pd);
          -sin(td), 0, cos(td)];

    % 2x1 vector containing e field components without optical elements
    E = C1 * C2 * (Rd) * [Ax; Ay; Az];


    % jones matrix: linear polarizer with horizontal transmission
    Pol=[1 0; 0 0];

    % the following loop calculates, for all angles n=ILHWP(j,1),
    % the intensities ILHWP(j,2) behind the HWP and polarizer
    j=1;
    for n=0:(2*pi)/(Npp-1):2*pi
        % jones matrix: hwp with angle n
        HWP=[cos(-2*n) sin(-2*n); sin(-2*n) -cos(-2*n)];
  % e field components after hwp and polarizer
        M = Pol * HWP * E;
        ILHWP(j,1)=n; % angle hwp
```

```
        ILHWP(j,2)=M'*M; % intensities after hwp/polarizer
        j=j+1;
    end
    clear j;
    clear n;

end
%  end of function Polarization
%%--------------------------------------------------------------


%% Potting the Polarization
%%--------------------------------------------------------------
function [pp,I] = PolarizationGraph(pp, IIb, T)
    % Plots the polarization graphs for the four SiV fine structure peaks
    % at B = 0T.
    % input paramters: pp - angles of the HWP
    %                  IIb - intensity behind the HWP and lin. pol.
    %                  T - dipole strengths for each possible transition
    % output parameters: pp - angles HWP
    %                    I - polarization curves of the polar diagrams

    % Constants
    GHz = 10e9;
    dw = 1e9;
    NE = 400;
    minE = -400*GHz;
    maxE= 400*GHz;

    % simulate again the spectrum using Lorentzian, similar to
    % the simulation of the Zeeman spectra, but this time, ExpT
    % scales with IIb (= intensity behind the polarizer)
    Ef = minE:(maxE-minE)/(NE-1):maxE;
    E = Ef'*ones(size(pp));
    dimension = ones(size(Ef))';
    Exp = dimension*ones(size(pp))*0;

    for t = 1:size(T,1)
        TT = T(t,1)*ones(size(pp));
        ExpT = dimension*IIb(t,:)./(1+(E - dimension*TT).^2/dw^2);
        Exp = Exp + ExpT;
    end

    % import data file and conversions
    file = 'EmUdS5Pol.txt';
    data=importdata(file,'\t',0);
    theta = data(:,1);
    data(:,1) = [];
    [dimY,dimX] = size(data);
    helpdata = data;
    for n = 1:4
        data(:,n) = helpdata(:,5-n);
    end

    % Normalization of the data
```

```
    for k=1:dimX
        MaxInt(k,:)=max(data(:,k));
    end
    for n=1:dimX
        NormInt(:,n)=data(:,n)/MaxInt(n,:);
    end

    % find the four maxima in the simulated spectrum, corresponding to
    % the four fine structure peaks and check that splittings
    % G1, G2 correspond to exp. values
    [~,Ind] = findpeaks(Exp(:,1),'NPEAKS',4);
    G1 =   Ef(1,Ind(4))./GHz - Ef(1,Ind(1))./GHz;
    G2 =   Ef(1,Ind(3))./GHz - Ef(1,Ind(2))./GHz;

    % take the peak values at the four maxima, and assign them to "I"
    for n = 1:4
        I(:,n) = Exp(Ind(n),:);
    end

    % plot the data in four subplots,
    % take only half of the HWP rotation angle
    figure(6);
    for n = 1:4
        subplot(2,4,4+n);
        actplot = polar(2.*pp(1:37)',I(1:37,n)./max(I(1:37,n)));
        set(actplot,'LineWidth',2,'Color','r');
        Polplot(n) = gca;
        hold on;
        actplot = polar(2.*pi.*theta(1:37)./180 , NormInt(1:37,n),'o');
        set(actplot,'MarkerSize',10,'LineWidth',2)
        title(sprintf('Peak at %3.0f GHz',Ef(1,Ind(n))./GHz));
        hold off;
    end

    % cosmetics...
    for n = 1:4
    set(Polplot(n),'Position',[0.02+(n-1).*0.25, 0.05, 0.23 , 0.4]);
    end

end
% end of function PolarizationGraph
%%---------------------------------------------------------------
```

Bibliography

[1] M. Fox, *Quantum optics: an introduction* (Oxford University Press, Oxford, 2006).

[2] P. Zoller, T. Beth, D. Binosi, R. Blatt, H. Briegel, D. Bruss, T. Calarco, J. I. Cirac, D. Deutsch, J. Eisert, A. Ekert, C. Fabre, N. Gisin, P. Grangiere, M. Grassl, S. Haroche, A. Imamoglu, A. Karlson, J. Kempe, L. Kouwenhoven, S. Kröll, G. Leuchs, M. Lewenstein, D. Loss, N. Lütkenhaus, S. Massar, J. E. Mooij, M. B. Plenio, E. Polzik, S. Popescu, G. Rempe, A. Sergienko, D. Suter, J. Twamley, G. Wendin, R. Werner, A. Winter, J. Wrachtrup, and A. Zeilinger, “Quantum information processing and communication.” Eur. Phys. J. D **36**, 203–228 (2005).

[3] T. Sleator and H. Weinfurter, “Realizable Universal Quantum Logic Gates.” Phys. Rev. Lett. **74**, 4087–4090 (1995).

[4] P. Shor, “Algorithms for quantum computation: discrete logarithms and factoring.” in “Proc. 35th Annu. Symp. Found. Comput. Sci.”, (IEEE Comput. Soc. Press, 1994), pp. 124–134.

[5] C. H. Bennett and G. Brassard, “Quantum cryptography: Public key distribution and coin tossing.” Proc. IEEE Int. Conf. Comput. Syst. Signal **175**, 8 (1984).

[6] R. P. Feynman, “Simulating physics with computers.” Int. J. Theor. Phys. **21**, 467–488 (1982).

[7] R. Schirhagl, K. Chang, M. Loretz, and C. L. Degen, “Nitrogen-vacancy centers in diamond: nanoscale sensors for physics and biology.” Annu. Rev. Phys. Chem. **65**, 83–105 (2014).

[8] D. L. Moehring, P. Maunz, S. Olmschenk, K. C. Younge, D. N. Matsukevich, L.-M. Duan, and C. Monroe, “Entanglement of single-atom quantum bits at a distance.” Nature **449**, 68–71 (2007).

[9] R. Blatt and D. Wineland, “Entangled states of trapped atomic ions.” Nature **453**, 1008–15 (2008).

[10] C. Negrevergne, T. Mahesh, C. Ryan, M. Ditty, F. Cyr-Racine, W. Power, N. Boulant, T. Havel, D. Cory, and R. Laflamme, “Benchmarking Quantum Control Methods on a 12-Qubit System.” Phys. Rev. Lett. **96**, 170501 (2006).

[11] L. M. Vandersypen, M. Steffen, G. Breyta, C. S. Yannoni, M. H. Sherwood, and I. L. Chuang, "Experimental realization of Shor's quantum factoring algorithm using nuclear magnetic resonance." Nature **414**, 883–7 (2001).

[12] L. DiCarlo, J. M. Chow, J. M. Gambetta, L. S. Bishop, B. R. Johnson, D. I. Schuster, J. Majer, A. Blais, L. Frunzio, S. M. Girvin, and R. J. Schoelkopf, "Demonstration of two-qubit algorithms with a superconducting quantum processor." Nature **460**, 240–4 (2009).

[13] M. Ansmann, H. Wang, R. C. Bialczak, M. Hofheinz, E. Lucero, M. Neeley, a. D. O'Connell, D. Sank, M. Weides, J. Wenner, a. N. Cleland, and J. M. Martinis, "Violation of Bell's inequality in Josephson phase qubits." Nature **461**, 504–6 (2009).

[14] C. Rigetti, J. M. Gambetta, S. Poletto, B. L. T. Plourde, J. M. Chow, a. D. Córcoles, J. A. Smolin, S. T. Merkel, J. R. Rozen, G. A. Keefe, M. B. Rothwell, M. B. Ketchen, and M. Steffen, "Superconducting qubit in a waveguide cavity with a coherence time approaching 0.1 ms." Phys. Rev. B **86**, 100506 (2012).

[15] J. M. Chow, A. D. Córcoles, J. M. Gambetta, C. Rigetti, B. R. Johnson, J. a. Smolin, J. R. Rozen, G. A. Keefe, M. B. Rothwell, M. B. Ketchen, and M. Steffen, "Simple all-microwave entangling gate for fixed-frequency superconducting qubits." Phys. Rev. Lett. **107**, 080502 (2011).

[16] R. Hanson, J. R. Petta, S. Tarucha, and L. M. K. Vandersypen, "Spins in few-electron quantum dots." Rev. Mod. Phys. **79**, 1217–1265 (2007).

[17] M. Atatüre, J. Dreiser, A. Badolato, A. Högele, K. Karrai, and A. Imamoglu, "Quantum-dot spin-state preparation with near-unity fidelity." Science **312**, 551–3 (2006).

[18] D. Press, T. D. Ladd, B. Zhang, and Y. Yamamoto, "Complete quantum control of a single quantum dot spin using ultrafast optical pulses." Nature **456**, 218–21 (2008).

[19] P. Neumann, R. Kolesov, B. Naydenov, J. Beck, F. Rempp, M. Steiner, V. Jacques, G. Balasubramanian, M. L. Markham, D. J. Twitchen, S. Pezzagna, J. Meijer, J. Twamley, F. Jelezko, and J. Wrachtrup, "Quantum register based on coupled electron spins in a room-temperature solid." Nat. Phys. **6**, 249–253 (2010).

[20] P. Neumann, N. Mizuochi, F. Rempp, P. Hemmer, H. Watanabe, S. Yamasaki, V. Jacques, T. Gaebel, F. Jelezko, and J. Wrachtrup, "Multipartite entanglement among single spins in diamond." Science **320**, 1326–9 (2008).

[21] M. V. G. Dutt, L. Childress, L. Jiang, E. Togan, J. R. Maze, F. Jelezko, A. S. Zibrov, P. R. Hemmer, and M. D. Lukin, "Quantum register based on individual electronic and nuclear spin qubits in diamond." Science **316**, 1312–6 (2007).

[22] E. Knill, R. Laflamme, and G. J. Milburn, "A scheme for efficient quantum computation with linear optics." Nature **409**, 46–52 (2001).

[23] J. L. O'Brien, G. J. Pryde, A. G. White, T. C. Ralph, and D. Branning, "Demonstration of an all-optical quantum controlled-NOT gate." Nature **426**, 264–7 (2003).

[24] J. L. O'Brien, "Optical quantum computing." Science **318**, 1567–70 (2007).

[25] A. Politi, J. C. F. Matthews, and J. L. O'Brien, "Shor's quantum factoring algorithm on a photonic chip." Science **325**, 1221 (2009).

[26] D. P. DiVincenzo, "The Physical Implementation of Quantum Computation." Fortschritte der Phys. **48**, 771–783 (2000).

[27] T. D. Ladd, F. Jelezko, R. Laflamme, Y. Nakamura, C. Monroe, and J. L. O'Brien, "Quantum computers." Nature **464**, 45–53 (2010).

[28] H. J. Kimble, "The quantum internet." Nature **453**, 1023–30 (2008).

[29] J. Franson, "Bell inequality for position and time." Phys. Rev. Lett. **62**, 2205–2208 (1989).

[30] M. Halder, A. Beveratos, N. Gisin, V. Scarani, C. Simon, and H. Zbinden, "Entangling independent photons by time measurement." Nat. Phys. **3**, 692–695 (2007).

[31] B. B. Blinov, D. L. Moehring, L.-M. Duan, and C. Monroe, "Observation of entanglement between a single trapped atom and a single photon." Nature **428**, 153–7 (2004).

[32] J. Hofmann, M. Krug, N. Ortegel, L. Gérard, M. Weber, W. Rosenfeld, and H. Weinfurter, "Heralded entanglement between widely separated atoms." Science **337**, 72–5 (2012).

[33] M. Schug, J. Huwer, C. Kurz, P. Müller, and J. Eschner, "Heralded Photonic Interaction between Distant Single Ions." Phys. Rev. Lett. **110**, 213603 (2013).

[34] E. Togan, Y. Chu, A. S. Trifonov, L. Jiang, J. R. Maze, L. Childress, M. V. G. Dutt, A. S. Sø rensen, P. R. Hemmer, A. S. Zibrov, and M. D. Lukin, "Quantum entanglement between an optical photon and a solid-state spin qubit." Nature **466**, 730–4 (2010).

[35] H. Bernien, B. Hensen, W. Pfaff, G. Koolstra, M. S. Blok, L. Robledo, T. H. Taminiau, M. Markham, D. J. Twitchen, L. Childress, and R. Hanson, "Heralded entanglement between solid-state qubits separated by three metres." Nature **497**, 86–90 (2013).

[36] A. M. Zaitsev, *Optical Properties of Diamond: A Data Handbook* (Springer-Verlag, Berlin, 2001).

[37] C. D. Clark and C. A. Norris, "Photoluminescence associated with the 1.673, 1.944 and 2.498 eV centres in diamond." J. Phys. C Solid State Phys. **4**, 2223–2229 (1971).

[38] G. Davies and M. F. Hamer, "Optical Studies of the 1.945 eV Vibronic Band in Diamond." Proc. R. Soc. A Math. Phys. Eng. Sci. **348**, 285–298 (1976).

[39] A. Gruber, A. Dräbenstedt, C. Tietz, L. Fleury, J. Wrachtrup, and C. Borczyskowski, “Scanning confocal optical microscopy and magnetic resonance on single defect centers.” Science **276**, 2012–2014 (1997).

[40] R. C. Albrecht, “Coupling of a Single Nitrogen-Vacancy Center in Diamond to a Fiber-Based Microcavity.” Dissertation, Universität des Saarlandes (2014).

[41] J. R. Maze, A. Gali, E. Togan, Y. Chu, A. Trifonov, E. Kaxiras, and M. D. Lukin, “Properties of nitrogen-vacancy centers in diamond: the group theoretic approach.” New J. Phys. **13**, 025025 (2011).

[42] M. Doherty and N. Manson, “The negatively charged nitrogen-vacancy centre in diamond: the electronic solution.” New J. Phys. **13**, 025019 (2011).

[43] G. Balasubramanian, P. Neumann, D. Twitchen, M. Markham, R. Kolesov, N. Mizuochi, J. Isoya, J. Achard, J. Beck, J. Tissler, V. Jacques, P. R. Hemmer, F. Jelezko, and J. Wrachtrup, “Ultralong spin coherence time in isotopically engineered diamond.” Nat. Mater. **8**, 383–7 (2009).

[44] H. S. Knowles, D. M. Kara, and M. Atatüre, “Observing bulk diamond spin coherence in high-purity nanodiamonds.” Nat. Mater. **13**, 21–5 (2014).

[45] J. Volz, M. Weber, D. Schlenk, W. Rosenfeld, J. Vrana, K. Saucke, C. Kurtsiefer, and H. Weinfurter, “Observation of Entanglement of a Single Photon with a Trapped Atom.” Phys. Rev. Lett. **96**, 030404 (2006).

[46] A. Batalov, V. Jacques, F. Kaiser, P. Siyushev, P. Neumann, L. Rogers, R. McMurtrie, N. Manson, F. Jelezko, and J. Wrachtrup, “Low Temperature Studies of the Excited-State Structure of Negatively Charged Nitrogen-Vacancy Color Centers in Diamond.” Phys. Rev. Lett. **102**, 195506 (2009).

[47] P. Neumann, R. Kolesov, V. Jacques, J. Beck, J. Tisler, A. Batalov, L. Rogers, N. B. Manson, G. Balasubramanian, F. Jelezko, and J. Wrachtrup, “Excited-state spectroscopy of single NV defects in diamond using optically detected magnetic resonance.” New J. Phys. **11**, 013017 (2009).

[48] G. D. Fuchs, V. V. Dobrovitski, R. Hanson, A. Batra, C. D. Weis, T. Schenkel, and D. D. Awschalom, “Excited-State Spectroscopy Using Single Spin Manipulation in Diamond.” Phys. Rev. Lett. **101**, 117601 (2008).

[49] P. Tamarat, T. Gaebel, J. Rabeau, M. Khan, A. Greentree, H. Wilson, L. Hollenberg, S. Prawer, P. Hemmer, F. Jelezko, and J. Wrachtrup, “Stark Shift Control of Single Optical Centers in Diamond.” Phys. Rev. Lett. **97**, 083002 (2006).

[50] K.-M. C. Fu, C. Santori, P. E. Barclay, L. J. Rogers, N. B. Manson, and R. G. Beausoleil, “Observation of the Dynamic Jahn-Teller Effect in the Excited States of Nitrogen-Vacancy Centers in Diamond.” Phys. Rev. Lett. **103**, 256404 (2009).

[51] C. Simon and W. Irvine, “Robust Long-Distance Entanglement and a Loophole-Free Bell Test with Ions and Photons.” Phys. Rev. Lett. **91**, 110405 (2003).

[52] L. M. Duan, M. D. Lukin, J. I. Cirac, and P. Zoller, "Long-distance quantum communication with atomic ensembles and linear optics." Nature **414**, 413–8 (2001).

[53] H. Bernien, L. Childress, L. Robledo, M. Markham, D. Twitchen, and R. Hanson, "Two-Photon Quantum Interference from Separate Nitrogen Vacancy Centers in Diamond." Phys. Rev. Lett. **108**, 043604 (2012).

[54] I. Aharonovich, A. D. Greentree, and S. Prawer, "Diamond photonics." Nat. Photonics **5**, 397–405 (2011).

[55] A. Schell, J. Wolters, T. Schröder, and O. Benson, "Using defect centres in diamonds to build photonic and quantum optical devices." in "Quantum Inf. Process. with Diam.", , S. Prawer and I. Aharonovich, eds. (Woodhead Publishing Ltd., Cambridge, UK, 2014), chap. 7, pp. 160–194.

[56] E. Neu, D. Steinmetz, J. Riedrich-Möller, S. Gsell, M. Fischer, M. Schreck, and C. Becher, "Single photon emission from silicon-vacancy colour centres in chemical vapour deposition nano-diamonds on iridium." New J. Phys. **13**, 025012 (2011).

[57] C. Wang, C. Kurtsiefer, H. Weinfurter, and B. Burchard, "Single photon emission from SiV centres in diamond produced by ion implantation." J. Phys. B At. Mol. Opt. Phys. **39**, 37–41 (2006).

[58] E. Neu, M. Fischer, S. Gsell, M. Schreck, and C. Becher, "Fluorescence and polarization spectroscopy of single silicon vacancy centers in heteroepitaxial nanodiamonds on iridium." Phys. Rev. B **84**, 205211 (2011).

[59] I. Aharonovich, S. Castelletto, B. C. Johnson, J. C. McCallum, D. a. Simpson, A. D. Greentree, and S. Prawer, "Chromium single photon emitters in diamond fabricated by ion implantation." Phys. Rev. B **81**, 121201 (2010).

[60] D. Gatto Monticone, P. Traina, E. Moreva, J. Forneris, P. Olivero, I. P. Degiovanni, F. Taccetti, L. Giuntini, G. Brida, G. Amato, and M. Genovese, "Native NIR-emitting single colour centres in CVD diamond." New J. Phys. **16**, 053005 (2014).

[61] A. Sipahigil, K. D. Jahnke, L. J. Rogers, T. Teraji, J. Isoya, A. S. Zibrov, F. Jelezko, and M. D. Lukin, "Indistinguishable photons from separated silicon-vacancy centers in diamond." (2014), arXiv:1406.4268.

[62] C. D. Clark, H. Kanda, I. Kiflawi, and G. Sittas, "Silicon defects in diamond." Phys. Rev. B **51**, 16681–16688 (1995).

[63] U. F. S. D'Haenens-Johansson, A. M. Edmonds, B. L. Green, M. E. Newton, G. Davies, P. M. Martineau, R. U. A. Khan, and D. J. Twitchen, "Optical properties of the neutral silicon split-vacancy center in diamond." Phys. Rev. B **84**, 245208 (2011).

[64] T. Müller, "Novel colour centres in diamond: Silicon-vacancy and chromium centres as candidates for quantum information applications." Ph.d. thesis, University of Cambridge (2012).

[65] T. Müller, C. Hepp, B. Pingault, E. Neu, S. Gsell, M. Schreck, H. Sternschulte, D. Steinmüller-Nethl, C. Becher, and M. Atatüre, "Optical signatures of silicon-vacancy spins in diamond." Nat. Commun. **5**, 3328 (2014).

[66] A. Krüger, *Neue Kohlenstoffmaterialien* (B.G. Teubner Verlag, Wiesbaden, 2007).

[67] R. Robertson, J. J. Fox, and a. E. Martin, "Two Types of Diamond." Philos. Trans. R. Soc. A Math. Phys. Eng. Sci. **232**, 463–535 (1934).

[68] J. Walker, "Optical absorption and luminescence in diamond." Reports Prog. Phys. **42**, 1605–1659 (1979).

[69] D. W. Olson, "2011 Minerals Yearbook: Diamond, Industrial." Tech. Rep. March, U.S. Geological Survey (2011).

[70] H. P. Bovenkerk, F. P. Bundy, H. T. Hall, H. M. Strong, and R. H. Wentorf, "Preparation of Diamond." Nature **184**, 1094–1098 (1959).

[71] H. M. Strong and R. M. Chrenko, "Diamond growth rates and physical properties of laboratory-made diamond." J. Phys. Chem. **75**, 1838–1843 (1971).

[72] H. Sumiya and S. Satoh, "High-pressure synthesis of high-purity diamond crystal." Diam. Relat. Mater. **5**, 1359–1365 (1996).

[73] E. Neu, "Silicon vacancy color centers in chemical vapor deposition diamond: New insights into promising solid state single photon sources." Dissertation, Universität des Saarlandes (2012).

[74] T. Teraji, "Chemical Vapor Deposition of Homoepitaxial Diamond Films." in "Phys. Appl. CVD Diam.", , S. Koizumi, C. E. Nebel, and M. Nesládek, eds. (Wiley-VCH Verlag, Weinheim, 2008).

[75] S. Matsumoto, Y. Sato, M. Tsutsumi, and N. Setaka, "Growth of diamond particles from methane-hydrogen gas." J. Mater. Sci. **17**, 3106–3112 (1982).

[76] M. Kamo, Y. Sato, S. Matsumoto, and N. Setaka, "Diamond synthesis from gas phase in microwave plasma." J. Cryst. Growth **62**, 642–644 (1983).

[77] Y. Hirose, S. Amanuma, and K. Komaki, "The synthesis of high-quality diamond in combustion flames." J. Appl. Phys. **68**, 6401 (1990).

[78] S. Gsell, T. Bauer, J. Goldfuß, M. Schreck, and B. Stritzker, "A route to diamond wafers by epitaxial deposition on silicon via iridium/yttria-stabilized zirconia buffer layers." Appl. Phys. Lett. **84**, 4541 (2004).

[79] C. Y. Fong, "Methods Used for Calculating Band Structures of Layered Materials." in "Electrons Phonons Layer. Cryst. Struct.", , T. Wieting and M. Schlüter, eds. (Springer Netherlands, 1979), pp. 59–144.

[80] W. Saslow, T. Bergstresser, and M. Cohen, "Band Structure and Optical Properties of Diamond." Phys. Rev. Lett. **16**, 354–356 (1966).

[81] J. R. Rabeau, Y. L. Chin, S. Prawer, F. Jelezko, T. Gaebel, and J. Wrachtrup, "Fabrication of single nickel-nitrogen defects in diamond by chemical vapor deposition." Appl. Phys. Lett. **86**, 131926 (2005).

[82] A. Magyar, W. Hu, T. Shanley, M. E. Flatté, E. Hu, and I. Aharonovich, "Synthesis of luminescent europium defects in diamond." Nat. Commun. **5**, 3523 (2014).

[83] M. Dresselhaus and R. Kalish, *Ion Implantation in Diamond, Graphite and Related Materials* (Springer-Verlag, Berlin, 1992).

[84] B. Dischler, *Handbook of Spectral Lines in Diamond* (Springer-Verlag, Berlin, 2012).

[85] E. D. Palik, *Handbook of Optical Constants of Solids*, vol. 2 (Academic Press, San Diego, 1985).

[86] J. Riedrich-Möller, L. Kipfstuhl, C. Hepp, E. Neu, C. Pauly, F. Mücklich, A. Baur, M. Wandt, S. Wolff, M. Fischer, S. Gsell, M. Schreck, and C. Becher, "One- and two-dimensional photonic crystal microcavities in single crystal diamond." Nat. Nanotechnol. **7**, 69–74 (2012).

[87] A. Faraon, C. Santori, Z. Huang, V. M. Acosta, and R. G. Beausoleil, "Coupling of Nitrogen-Vacancy Centers to Photonic Crystal Cavities in Monocrystalline Diamond." Phys. Rev. Lett. **109**, 033604 (2012).

[88] C. F. Wang, R. Hanson, D. D. Awschalom, E. L. Hu, T. Feygelson, J. Yang, and J. E. Butler, "Fabrication and characterization of two-dimensional photonic crystal microcavities in nanocrystalline diamond." Appl. Phys. Lett. **91**, 201112 (2007).

[89] B. J. M. Hausmann, B. J. Shields, Q. Quan, Y. Chu, N. P. de Leon, R. Evans, M. J. Burek, A. S. Zibrov, M. Markham, D. J. Twitchen, H. Park, M. D. Lukin, and M. Lonc R, "Coupling of NV centers to photonic crystal nanobeams in diamond." Nano Lett. **13**, 5791–6 (2013).

[90] A. Faraon, C. Santori, Z. Huang, K.-M. C. Fu, V. M. Acosta, D. Fattal, and R. G. Beausoleil, "Quantum photonic devices in single-crystal diamond." New J. Phys. **15**, 025010 (2013).

[91] B. J. M. Hausmann, B. Shields, Q. Quan, P. Maletinsky, M. McCutcheon, J. T. Choy, T. M. Babinec, A. Kubanek, A. Yacoby, M. D. Lukin, and M. Loncar, "Integrated diamond networks for quantum nanophotonics." Nano Lett. **12**, 1578–82 (2012).

[92] B. A. Fairchild, P. Olivero, S. Rubanov, A. D. Greentree, F. Waldermann, R. A. Taylor, I. Walmsley, J. M. Smith, S. Huntington, B. C. Gibson, D. N. Jamieson, and S. Prawer, "Fabrication of Ultrathin Single-Crystal Diamond Membranes." Adv. Mater. **20**, 4793–4798 (2008).

[93] T. M. Babinec, B. J. M. Hausmann, M. Khan, Y. Zhang, J. R. Maze, P. R. Hemmer, and M. Loncar, "A diamond nanowire single-photon source." Nat. Nanotechnol. **5**, 195–9 (2010).

[94] J. P. Hadden, J. P. Harrison, A. C. Stanley-Clarke, L. Marseglia, Y.-L. D. Ho, B. R. Patton, J. L. O'Brien, and J. G. Rarity, "Strongly enhanced photon collection from diamond defect centers under microfabricated integrated solid immersion lenses." Appl. Phys. Lett. **97**, 241901 (2010).

[95] P. Siyushev, F. Kaiser, V. Jacques, I. Gerhardt, S. Bischof, H. Fedder, J. Dodson, M. Markham, D. Twitchen, F. Jelezko, and J. Wrachtrup, "Monolithic diamond optics for single photon detection." Appl. Phys. Lett. **97**, 241902 (2010).

[96] A. Beveratos, R. Brouri, T. Gacoin, J.-P. Poizat, and P. Grangier, "Nonclassical radiation from diamond nanocrystals." Phys. Rev. A **64**, 061802 (2001).

[97] I. Aharonovich and S. Prawer, "Fabrication strategies for diamond based ultra bright single photon sources." Diam. Relat. Mater. **19**, 729–733 (2010).

[98] P. W. May, "Diamond thin films: a 21st-century material." Philos. Trans. R. Soc. A Math. Phys. Eng. Sci. **358**, 473–495 (2000).

[99] V. Vavilov, A. Gippius, A. Zaitsev, B. Deryagin, B. Spitsyn, and A. Aleksenko, "Investigation of the cathodoluminescence of epitaxial diamond films." Sov. Phys. Semicond. **14**, 1078–1079 (1980).

[100] A. Zaitsev, V. Vavilov, and A. Gippius, "Cathodoluminescence of diamond associated with silicon impurity." Sov. Phys. Lebedev Inst. Rep **10**, 20–23 (1981).

[101] L. Robins, L. Cook, E. Farabaugh, and A. Feldman, "Cathodoluminescence of defects in diamond films and particles grown by hot-filament chemical-vapor deposition." Phys. Rev. B **39**, 13367–13377 (1989).

[102] A. A. Gorokhovsky, A. V. Turukhin, R. R. Alfano, and W. Phillips, "Photoluminescence vibrational structure of Si center in chemical-vapor deposited diamond." Appl. Phys. Lett. **66**, 43 (1995).

[103] M. Stammler, H. Eisenbeiß, J. Ristein, J. Neubauer, M. Göbbels, and L. Ley, "Growth of high-quality homoepitaxial diamond films by HF-CVD." Diam. Relat. Mater. **11**, 504–508 (2002).

[104] K. Iakoubovskii and G. Adriaenssens, "Photoluminescence in CVD diamond films." Phys. status solidi(a) **172**, 123–130 (1999).

[105] I. I. Vlasov, A. S. Barnard, V. G. Ralchenko, O. I. Lebedev, M. V. Kanzyuba, A. V. Saveliev, V. I. Konov, and E. Goovaerts, "Nanodiamond Photoemitters Based on Strong Narrow-Band Luminescence from Silicon-Vacancy Defects." Adv. Mater. **21**, 808–812 (2009).

[106] B. G. Yacobi, A. R. Badzian, and T. Badzian, "Cathodoluminescence study of diamond films grown by microwave plasma assisted chemical vapor deposition." J. Appl. Phys. **69**, 1643 (1991).

[107] D. Musale, S. Sainkar, and S. Kshirsagar, “Raman, photoluminescence and morphological studies of Si- and N-doped diamond films grown on Si(100) substrate by hot-filament chemical vapor deposition technique.” Diam. Relat. Mater. **11**, 75–86 (2002).

[108] C. Clark and C. Dickerson, “The 1.681 eV centre in polycrystalline diamond.” Surf. Coatings Technol. **47**, 336–343 (1991).

[109] J. Ruan, W. J. Choyke, and W. D. Partlow, “Si impurity in chemical vapor deposited diamond films.” Appl. Phys. Lett. **58**, 295 (1991).

[110] J. Ruan, K. Kobashi, and W. J. Choyke, “Effect of oxygen on boron doping in chemical vapor deposition of diamond as deduced from cathodoluminescence studies.” Appl. Phys. Lett. **60**, 1884 (1992).

[111] J. Ruan, W. J. Choyke, and K. Kobashi, “Oxygen-related centers in chemical vapor deposition of diamond.” Appl. Phys. Lett. **62**, 1379 (1993).

[112] L. Bergman, B. Stoner, K. Turner, J. Glass, and R. Nemanich, “Microphotoluminescence and Raman scattering study of defect formation in diamond films.” J. Appl. Phys. **73**, 3951–3957 (1993).

[113] J. Barjon, E. Rzepka, F. Jomard, J.-M. Laroche, D. Ballutaud, T. Kociniewski, and J. Chevallier, “Silicon incorporation in CVD diamond layers.” Phys. Status Solidi **202**, 2177–2181 (2005).

[114] E. Neu, R. Albrecht, M. Fischer, S. Gsell, M. Schreck, and C. Becher, “Electronic transitions of single silicon vacancy centers in the near-infrared spectral region.” Phys. Rev. B **85**, 1–9 (2012).

[115] E. Neu, C. Hepp, M. Hauschild, S. Gsell, M. Fischer, H. Sternschulte, D. Steinmüller-Nethl, M. Schreck, and C. Becher, “Low-temperature investigations of single silicon vacancy colour centres in diamond.” New J. Phys. **15**, 043005 (2013).

[116] E. Neu, C. Arend, F. Guldner, E. Gross, C. Hepp, D. Steinmetz, E. Zscherpel, S. Ghodbane, H. Sternschulte, D. Steinmueller-Nethl, Y. Liang, A. Krueger, and C. Becher, “Narrowband fluorescent nanodiamonds produced from chemical vapor deposition films.” Appl. Phys. Lett. **98**, 4 (2011).

[117] E. Neu, M. Agio, and C. Becher, “Photophysics of single silicon vacancy centers in diamond: implications for single photon emission.” Opt. Express **20**, 19956–19971 (2012).

[118] Y. Bar-Yam and T. D. Moustakas, “Defect-induced stabilization of diamond films.” Nature **342**, 786–787 (1989).

[119] L. Allers and A. Mainwood, “Surface vacancies in CVD diamond.” Diam. Relat. Mater. **7**, 261–265 (1998).

[120] A. M. Edmonds, U. F. S. D'Haenens-Johansson, R. J. Cruddace, M. E. Newton, K.-M. C. Fu, C. Santori, R. G. Beausoleil, D. J. Twitchen, and M. L. Markham, "Production of oriented nitrogen-vacancy color centers in synthetic diamond." Phys. Rev. B **86**, 035201 (2012).

[121] M. Lesik, J.-P. Tetienne, A. Tallaire, J. Achard, V. Mille, A. Gicquel, J.-F. Roch, and V. Jacques, "Perfect preferential orientation of nitrogen-vacancy defects in a synthetic diamond sample." Appl. Phys. Lett. **104**, 113107 (2014).

[122] J. P. Goss, R. Jones, S. Breuer, P. Briddon, and S. Öberg, "The Twelve-Line 1.682 eV Luminescence Center in Diamond and the Vacancy-Silicon Complex." Phys. Rev. Lett. **77**, 3041–3044 (1996).

[123] S. S. Moliver, "Electronic structure of neutral silicon-vacancy complex in diamond." Tech. Phys. **48**, 1449–1453 (2003).

[124] K. Iakoubovskii, G. J. Adriaenssens, M. Nesladek, and L. M. Stals, "Photoluminescence excitation and quenching spectra in CVD diamond films." Diam. Relat. Mater. **8**, 717–720 (1999).

[125] J. Perdew, "Density functional theory and the band gap problem." Int. J. Quantum Chem. **19**, 491–523 (1986).

[126] J. P. Goss, P. R. Briddon, and M. J. Shaw, "Density functional simulations of silicon-containing point defects in diamond." Phys. Rev. B **76**, 75204 (2007).

[127] A. Gali and J. R. Maze, "Ab initio study of the split silicon-vacancy defect in diamond: Electronic structure and related properties." Phys. Rev. B **88**, 235205 (2013).

[128] A. Szabo and N. S. Ostlund, *Modern Quantum Chemistry* (Dover Publications, Mineola, N.Y., 1996), revised ed.

[129] W. Demtröder, *Experimentalphysik 3–Atome, Moleküle und Festkörper* (Springer-Verlag, Berlin, 2005), 3rd ed.

[130] U. Bangert, M. H. Gass, a. L. Bleloch, R. R. Nair, and J. Eccles, "Nanotopography of graphene." Phys. Status Solidi **206**, 2115–2119 (2009).

[131] A. A. Kaplyanskii, "Noncubic Centers in Cubic Crystals and their Spectra in External Fields." J. Phys. Colloq. **C 4**, C 39–48 (1967).

[132] M. Tinkham, *Group theory and quantum mechanics* (Dover Publications, Mineola, N.Y., 1964).

[133] H. Sternschulte, K. Thonke, J. Gerster, W. Limmer, R. Sauer, J. Spitzer, and P. C. Münzinger, "Uniaxial stress and Zeeman splitting of the 1.681 eV optical center in a homoepitaxial CVD diamond film." Diam. Relat. Mater. **4**, 1189–1192 (1995).

[134] S. Brown and S. Rand, "Site symmetry analysis of the 738 nm defect in diamond." J. Appl. Phys. **78**, 4069–4075 (1995).

[135] A. A. Kaplyanskii, "Computation of Deformation Splitting of Spectral Transitions in Cubic Crystals." Opt. Spectrosc. **16**, 557 (1964).

[136] A. A. Kaplyanskii and V. N. Medvedev, "Noncubic centers in cubic crystals and their piezospectroscopic investigations." Opt. Spectrosc. **16**, 329 (1964).

[137] H. Sternschulte, K. Thonke, R. Sauer, P. C. Münzinger, and P. Michler, "1.681-eV luminescence center in chemical-vapor-deposited homoepitaxial diamond films." Phys. Rev. B **50**, 14554–14560 (1994).

[138] T. Feng and B. D. Schwartz, "Characteristics and origin of the 1.681 eV luminescence center in chemical-vapor-deposited diamond films." J. Appl. Phys. **73**, 1415 (1993).

[139] G. Davies, "The Jahn-Teller effect and vibronic coupling at deep levels in diamond." Reports Prog. Phys. **44**, 787–830 (1981).

[140] A. T. Collins, L. Allers, C. J. Wort, and G. A. Scarsbrook, "The annealing of radiation damage in De Beers colourless CVD diamond." Diam. Relat. Mater. **3**, 932–935 (1994).

[141] K. Iakoubovskii and G. Adriaenssens, "Optical detection of defect centers in CVD diamond." Diam. Relat. Mater. **9**, 1349–1356 (2000).

[142] A. T. Collins, M. Kamo, and Y. Sato, "A spectroscopic study of optical centers in diamond grown by microwave-assisted chemical vapor deposition." J. Mater. Res. **5**, 2507–2514 (1990).

[143] H. Kimble, M. Dagenais, and L. Mandel, "Photon Antibunching in Resonance Fluorescence." Phys. Rev. Lett. **39**, 691–695 (1977).

[144] F. Diedrich and H. Walther, "Nonclassical radiation of a single stored ion." Phys. Rev. Lett. **58**, 203–206 (1987).

[145] H. F. Hess, E. Betzig, T. D. Harris, L. N. Pfeiffer, and K. W. West, "Near-field spectroscopy of the quantum constituents of a luminescent system." Science **264**, 1740–5 (1994).

[146] E. Betzig and R. J. Chichester, "Single molecules observed by near-field scanning optical microscopy." Science **262**, 1422–5 (1993).

[147] B. Lounis and M. Orrit, "Single-photon sources." Reports Prog. Phys. **68**, 1129–1179 (2005).

[148] T. Gaebel, I. Popa, A. Gruber, M. Domhan, F. Jelezko, and J. Wrachtrup, "Stable single-photon source in the near infrared." New J. Phys. **6**, 98–98 (2004).

[149] R. Loudon, *The Quantum Theory of Light* (Oxford University Press, Oxford, 2000), 3rd ed.

[150] A. T. Collins, M. F. Thomaz, and M. I. B. Jorge, "Luminescence decay time of the 1.945 eV centre in type Ib diamond." J. Phys. C Solid State Phys. **16**, 2177–2181 (1983).

[151] C. Bradac, T. Gaebel, N. Naidoo, M. J. Sellars, J. Twamley, L. J. Brown, A. S. Barnard, T. Plakhotnik, a. V. Zvyagin, and J. R. Rabeau, "Observation and control of blinking nitrogen-vacancy centres in discrete nanodiamonds." Nat. Nanotechnol. **5**, 345–9 (2010).

[152] J. Wolters, N. Sadzak, A. Schell, T. Schröder, and O. Benson, "Measurement of the Ultrafast Spectral Diffusion of the Optical Transition of Nitrogen Vacancy Centers in Nano-Size Diamond Using Correlation Interferometry." Phys. Rev. Lett. **110**, 027401 (2013).

[153] K.-M. C. Fu, C. Santori, P. E. Barclay, and R. G. Beausoleil, "Conversion of neutral nitrogen-vacancy centers to negatively charged nitrogen-vacancy centers through selective oxidation." Appl. Phys. Lett. **96**, 121907 (2010).

[154] K. C. Molloy, *Group Theory for Chemists* (Woodhead Publishing Ltd., Cambridge, 2011), 2nd ed.

[155] M. Dresselhaus, G. Dresselhaus, and A. Jorio, *Group Theory: Application to the Physics of Condensed Matter* (Springer-Verlag, Berlin, 2008).

[156] M. Cardona and P. Yu, *Fundamentals of Semiconductors* (Springer-Verlag, Berlin, 2005), 2nd ed.

[157] J. R. Maze, "Quantum manipulation of nitrogen-vacancy centers in diamond: from basic properties to applications." Thesis, Harvard University (2010).

[158] H. A. Jahn and E. Teller, "Stability of Polyatomic Molecules in Degenerate Electronic States. I. Orbital Degeneracy." Proc. R. Soc. A Math. Phys. Eng. Sci. **161**, 220–235 (1937).

[159] E. Jäger, "Jahn-Teller effect at lattice sites of symmetry D3d." Phys. Status Solidi **25**, K43–K46 (1968).

[160] M. C. M. O'Brien, "The Jahn-Teller effect: An introduction and current review." Am. J. Phys. **61**, 688 (1993).

[161] P. Jacobs, *Group Theory with Applications in Chemical Physics* (Cambridge University Press, Cambridge, 2005).

[162] T. A. Abtew, Y. Y. Sun, B.-C. Shih, P. Dev, S. B. Zhang, and P. Zhang, "Dynamic Jahn-Teller Effect in the NV- Center in Diamond." Phys. Rev. Lett. **107**, 146403 (2011).

[163] F. Ham, "Dynamical Jahn-Teller effect in paramagnetic resonance spectra: Orbital reduction factors and partial quenching of spin-orbit interaction." Phys. Rev. **138**, A1727–A1740 (1965).

[164] A. E. Hughes and W. A. Runciman, "Uniaxial stress splitting of doubly degenerate states of tetragonal and trigonal centres in cubic crystals." Proc. Phys. Soc. **90**, 827–838 (1967).

[165] J. Nye, *Physical Properties of Crystal* (Oxford University Press, Oxford, 1957).

[166] G. Davies and M. Nazaré, "Uniaxial stress splitting of E to E transitions at trigonal centres in cubic crystals: the 594 nm band in diamond." J. Phys. C Solid State Phys. **13**, 4127 (1980).

[167] M. Nazaré, A. Neves, and G. Davies, "Optical studies of the 1.40-eV Ni center in diamond." Phys. Rev. B **43**, 14196–14205 (1991).

[168] L. C. Bassett, F. J. Heremans, C. G. Yale, B. B. Buckley, and D. D. Awschalom, "Electrical Tuning of Single Nitrogen-Vacancy Center Optical Transitions Enhanced by Photoinduced Fields." Phys. Rev. Lett. **107**, 266403 (2011).

[169] J. N. Becker, "Spectroscopic investigation and theoretical modeling of the electronic structure of the silicon vacancy colour centre in diamond." Masterarbeit, Universität des Saarlandes (2013).

[170] T. Müller, I. Aharonovich, L. Lombez, Y. Alaverdyan, a. N. Vamivakas, S. Castelletto, F. Jelezko, J. Wrachtrup, S. Prawer, and M. Atatüre, "Wide-range electrical tunability of single-photon emission from chromium-based colour centres in diamond." New J. Phys. **13**, 075001 (2011).

[171] J. Minguzzi and J. R. Maze, "Effect of an electric field on negatively charged SiV centers in diamond." Priv. Commun. (2014).

[172] E. Tosatti, N. Manini, and O. Gunnarsson, "Surprises in the orbital magnetic moment and g factor of the dynamic Jahn-Teller ion C60-." Phys. Rev. B **54**, 17184–17190 (1996).

[173] I. V. Hertel and C.-P. Schulz, *Atome, Moleküle und optische Physik 1*, Springer-Lehrbuch (Springer-Verlag, Berlin, Heidelberg, 2008).

[174] F. Ham, "Effect of Linear Jahn-Teller Coupling on Paramagnetic Resonance in a E2 State." Phys. Rev. **166**, 307–321 (1968).

[175] M. S. Child and H. C. Longuet-Higgins, "Studies of the Jahn-Teller Effect III. The Rotational and Vibrational Spectra of Symmetric-top Molecules in Electronically Degenerate States." Philos. Trans. R. Soc. A Math. Phys. Eng. Sci. **254**, 259–294 (1961).

[176] L. J. Rogers, K. D. Jahnke, M. W. Doherty, A. Dietrich, L. P. McGuinness, C. Müller, T. Teraji, H. Sumiya, J. Isoya, N. B. Manson, and F. Jelezko, "Electronic structure of the negatively charged silicon-vacancy center in diamond." Phys. Rev. B **89**, 235101 (2014).

[177] E. Hecht, *Optik* (Oldenbourg Verlag, München, 2005), 4th ed.

[178] M. L. Goldman, A. Sipahigil, N. Y. Yao, S. D. Bennett, M. Markham, D. J. Twitchen, A. Kubanek, and M. D. Lukin, "Phonon-Induced Population Dynamics and Intersystem Crossing in Nitrogen-Vacancy Centers." (2014), arXiv:1406.4065.

[179] R. H. Webb, "Confocal optical microscopy." Rep. Prog. Phys. **59**, 41 (1996).

[180] L. Novotny and B. Hecht, *Principles of Nano-Optics* (Cambridge University Press, Cambridge, 2006).

[181] E. D. Black, "An introduction to Pound-Drever-Hall laser frequency stabilization." Am. J. Phys. **69**, 79 (2001).

[182] M. Leifgen, T. Schröder, F. Gädeke, R. Riemann, V. Métillon, E. Neu, C. Hepp, C. Arend, C. Becher, K. Lauritsen, and O. Benson, "Evaluation of nitrogen- and silicon-vacancy defect centres as single photon sources in quantum key distribution." New J. Phys. **16**, 023021 (2014).

[183] P. McMillan, B. Piriou, and R. Couty, "A Raman study of pressure-densified vitreous silica." J. Chem. Phys. **81**, 4234–4236 (1984).

[184] A. S. Diehl, "Einzelphotonenpolarimeter: Aufbau eines Polarimeters für die Untersuchung einzelner Farbzentren in Diamant." Bachelorarbeit, Universität des Saarlandes (2012).

[185] B. E. A. Saleh and M. C. Teich, *Fundamentals of Photonics* (John Wiley & Sons, Inc., New York, 2007), 2nd ed.

[186] D. W. Pohl, "Dynamic piezoelectric translation devices." Rev. Sci. Instrum. **58**, 54 (1987).

[187] D. Kirillov and G. J. Reynolds, "Linewidths of phonon lines of natural and synthetic diamonds." Appl. Phys. Lett. **65**, 1641 (1994).

[188] H. Okushi, "High quality homoepitaxial CVD diamond for electronic devices." Diam. Relat. Mater. **10**, 281–288 (2001).

[189] C. Hepp, "Spektroskopische Untersuchungen an optisch aktiven Defektzentren in CVD-Diamantfilmen." Diplomarbeit, Universität des Saarlandes (2008).

[190] D. Steinmetz, "Ni/Si-basierte Farbzentren in Diamant als Einzelphotonenquellen." Dissertation, Universität des Saarlandes (2011).

[191] I. I. Vlasov, A. A. Shiryaev, T. Rendler, S. Steinert, S.-Y. Lee, D. Antonov, M. Vörös, F. Jelezko, A. V. Fisenko, L. F. Semjonova, J. Biskupek, U. Kaiser, O. I. Lebedev, I. Sildos, P. R. Hemmer, V. I. Konov, A. Gali, and J. Wrachtrup, "Molecular-sized fluorescent nanodiamonds." Nat. Nanotechnol. **9**, 54–8 (2014).

[192] S. Gsell, T. Bauer, J. G. Schreck, M, and B. Stritzker, "A route to diamond wafers by epitaxial deposition on silicon via iridium/yttria-stabilized zirconia buffer layers." Appl. Phys. Lett. **84**, 4541–4543 (2004).

[193] J. Lindhard, M. Scharff, and H. Schiø tt, "Range concepts and heavy ion ranges." Mat. Fys. Medd. Dan. Vid. Selsk. **33** (1963).

[194] J. F. Ziegler, M. Ziegler, and J. Biersack, "SRIM - The stopping and range of ions in matter (2010)." Nucl. Instruments Methods Phys. Res. Sect. B Beam Interact. with Mater. Atoms **268**, 1818–1823 (2010).

[195] P. R. Hanley, M. R. Cleland, C. F. Mason, K. H. Morganstern, and C. C. Thompson, "The Tandem Dynamitron." IEEE Trans. Nucl. Sci. **16**, 90–95 (1969).

[196] G. D. Alton, "High-intensity, heavy negative ion sources based on the sputter principle." Rev. Sci. Instrum. **65**, 1141 (1994).

[197] R. Van De Graaff, "Tandem Electrostatic Accelerators." Nucl. Instruments Methods **8**, 195–202 (1960).

[198] C. Wang, "A Solid-State Single Photon Source Based on Color Centers in Diamond." Dissertation, Ludwig-Maximilians-Universität München (2007).

[199] C. Uzan-Saguy, C. Cytermann, R. Brener, V. Richter, M. Shaanan, and R. Kalish, "Damage threshold for ion-beam induced graphitization of diamond." Appl. Phys. Lett. **67**, 1194 (1995).

[200] E. Gross, "Spektroskopische Untersuchung von Farbzentren in Diamant im sichtbaren und infraroten Spektralbereich." Diplomarbeit, Universität des Saarlandes (2011).

[201] E. Neu and C. Becher, "Diamond-based single-photon sources and their application in quantum key distribution." in "Quantum Inf. Process. with Diam.", , S. Prawer and I. Aharonovich, eds. (Woodhead Publishing Ltd., Cambridge, UK, 2014), chap. 6, pp. 127–159.

[202] A. Bommer, "Erhöhung der Sammeleffizienz einzelner Photonen mit Hilfe von Festkörper-Immersionslinsen." Bachelorarbeit, Universität des Saarlandes (2011).

[203] W. Barnes, G. Björk, J. Gérard, P. Jonsson, J. Wasey, P. Worthing, and V. Zwiller, "Solid-state single photon sources: light collection strategies." Eur. Phys. J. D - At. Mol. Opt. Phys. **18**, 197–210 (2002).

[204] B. D. Terris, H. J. Mamin, D. Rugar, W. R. Studenmund, and G. S. Kino, "Near-field optical data storage using a solid immersion lens." Appl. Phys. Lett. **65**, 388 (1994).

[205] L. Marseglia, J. P. Hadden, A. C. Stanley-Clarke, J. P. Harrison, B. Patton, Y.-L. D. Ho, B. Naydenov, F. Jelezko, J. Meijer, P. R. Dolan, J. M. Smith, J. G. Rarity, and J. L. O'Brien, "Nanofabricated solid immersion lenses registered to single emitters in diamond." Appl. Phys. Lett. **98**, 133107 (2011).

[206] L. Giannuzzi and F. Stevie, "A review of focused ion beam milling techniques for TEM specimen preparation." Micron **30**, 197–204 (1999).

[207] C. A. Volkert and A. M. Minor, "Focused Ion Beam Microscopy and Micromachining." MRS Bull. **32**, 389–399 (2011).

[208] M. Hauschild, "Hochauflösende Spektroskopie an SiV-Zentren in Diamant." Diplomarbeit, Universität des Saarlandes (2009).

[209] A. Bergman, A. Zaitsev, and A. Gorokhovsky, "Polarization of luminescence and site symmetry of the Xe center in diamond." J. Lumin. **125**, 92–96 (2007).

[210] D. Steinmetz, E. Neu, J. Meijer, W. Bolse, and C. Becher, "Single photon emitters based on Ni/Si related defects in single crystalline diamond." Appl. Phys. B **102**, 451–458 (2011).

[211] J. R. Rabeau, A. Stacey, A. Rabeau, S. Prawer, F. Jelezko, I. Mirza, and J. Wrachtrup, "Single Nitrogen Vacancy Centers in Chemical Vapor Deposited Diamond Nanocrystals." Nano Lett. **7**, 3433–3437 (2007).

[212] R. Brouri, A. Beveratos, J.-P. P. Poizat, and P. Grangier, "Photon antibunching in the fluorescence of individual color centers in diamond." Opt. Lett. **25**, 1294–1296 (2000).

[213] C. Hepp, T. Müller, V. Waselowski, J. N. Becker, B. Pingault, H. Sternschulte, D. Steinmüller-Nethl, A. Gali, J. R. Maze, M. Atatüre, and C. Becher, "Electronic Structure of the Silicon Vacancy Color Center in Diamond." Phys. Rev. Lett. **112**, 036405 (2014).

[214] J. Riedrich-Möller and C. Becher, "Deterministic coupling of a single silicon-vacancy color center to a photonic crystal cavity in diamond." submitted (2014).

[215] K. Gottfried and T.-M. Yan, *Quantum mechanics: Fundamentals* (Springer-Verlag, Berlin, 2003), 2nd ed.

[216] A. M. Stoneham, *Theory of Defects in Solids* (Oxford University Press, Oxford, 1975).

[217] N. Vamivakas, Y. Zhao, C.-Y. Lu, and M. Atatüre, "Spin-resolved quantum-dot resonance fluorescence." Nat. Phys. **5**, 198–202 (2009).

[218] A. Ahlrichs, C. Berkemeier, B. Sprenger, and O. Benson, "A monolithic polarization-independent frequency-filter system for filtering of photon pairs." Appl. Phys. Lett. **103**, 241110 (2013).

[219] L. J. Rogers, R. L. McMurtrie, M. J. Sellars, and N. B. Manson, "Time-averaging within the excited state of the nitrogen-vacancy centre in diamond." New J. Phys. **11**, 063007 (2009).

[220] J. Birman, "Theory of Infrared and Raman Processes in Crystals: Selection Rules in Diamond and Zincblende." Phys. Rev. **131**, 1489 (1963).

[221] S. Solin and A. Ramdas, "Raman Spectrum of Diamond." Phys. Rev. B **1** (1970).

[222] M. Grimsditch and A. Ramdas, "Brillouin scattering in diamond." Phys. Rev. B **11**, 3139 (1975).

[223] T. D. Merson, S. Castelletto, I. Aharonovich, A. Turbic, T. J. Kilpatrick, and A. M. Turnley, "Nanodiamonds with silicon vacancy defects for nontoxic photostable fluorescent labeling of neural precursor cells." Opt. Lett. **38**, 4170–3 (2013).

[224] J. Michl, T. Teraji, S. Zaiser, I. Jakobi, G. Waldherr, F. Dolde, P. Neumann, M. W. Doherty, N. B. Manson, J. Isoya, and J. Wrachtrup, "Perfect alignment and preferential orientation of nitrogen-vacancy centers during chemical vapor deposition diamond growth on (111) surfaces." Appl. Phys. Lett. **104**, 102407 (2014).

[225] B. Pingault, "Personal Communication." (2014).

[226] F. Jelezko, T. Gaebel, I. Popa, A. Gruber, and J. Wrachtrup, "Observation of Coherent Oscillations in a Single Electron Spin." Phys. Rev. Lett. **92**, 076401 (2004).

[227] R. Feynman, *Surely You're Joking, Mr. Feynman!: Adventures of a Curious Character.* (W W Norton & Company Inc, New York, 1985).

Publications

- D. Steinmetz, E. Neu, C. Hepp, R. Albrecht, W. Bolse, J. Meijer, D. Rogalla, and C. Becher, “Single-photon emission from Ni-related color centers in CVD diamond.” Proc. SPIE **7727**, Quantum Optics, 77270P (2010)
- E. Neu, C. Arend, F. Guldner, E. Gross, C. Hepp, D. Steinmetz, E. Zscherpel, S. Ghodbane, H. Sternschulte, D. Steinmüller-Nethl, Y. Liang, A. Krüger, and C. Becher, “Narrowband fluorescent nanodiamonds produced from chemical vapor deposition films.” Appl. Phys. Lett. **98**, 4 (2011)
- J. Riedrich-Möller, L. Kipfstuhl, C. Hepp, E. Neu, C. Pauly, F. Mücklich, A. Baur, M. Wandt, S. Wolff, M. Fischer, S. Gsell, M. Schreck, and C. Becher, “One- and two-dimensional photonic crystal microcavities in single crystal diamond.” Nat. Nanotechnol. **7**, 69–74 (2012).
- E. Neu, C. Hepp, M. Hauschild, S. Gsell, M. Fischer, H. Sternschulte, D. Steinmüller-Nethl, M. Schreck, and C. Becher, “Low-temperature investigations of single silicon vacancy colour centres in diamond.” New J. Phys. **15**, 043005 (2013).
- M. Leifgen, T. Schröder, F. Gädeke, R. Riemann, V. Métillon, E. Neu, C. Hepp, C. Arend, C. Becher, K. Lauritsen, and O. Benson, “Evaluation of nitrogen- and silicon-vacancy defect centres as single photon sources in quantum key distribution.” New J. Phys. **16**, 023021 (2014).
- C. Hepp, T. Müller, V. Waselowski, J. N. Becker, B. Pingault, H. Sternschulte, D. Steinmüller-Nethl, A. Gali, J. R. Maze, M. Atatüre, and C. Becher, “Electronic Structure of the Silicon Vacancy Color Center in Diamond”. Phys. Rev. Lett. **112**, 036405 (2014).
- T. Müller, C. Hepp, B. Pingault, E. Neu, S. Gsell, M. Schreck, H. Sternschulte, D. Steinmüller-Nethl, C. Becher, and M. Atatüre, “Optical signatures of silicon-vacancy spins in diamond.” Nat. Commun. **5**, 3328 (2014).
- S. Zaske, A. Lenhard, C. A. Keßler, J. Kettler, C. Hepp, C. Arend, R. Albrecht, W.-M. Schulz, M. Jetter, P. Michler, and C. Becher, “Visible-to-Telecom Quantum Frequency Conversion of Light from a Single Quantum Emitter.” Phys. Rev. Lett. **109**, 147404 (2012).

Danksagung

Am Ende dieser Arbeit gilt es Danke zu sagen. Diese Arbeit wäre nicht möglich gewesen ohne die Mithilfe vieler Menschen. An erster Stelle steht mein Betreuer Christoph Becher, der in den vergangenen Jahren stets sein Vertrauen in mich gesetzt hat, der mich motiviert und angespornt hat, und der mir gezeigt hat, was es bedeutet, nie aufzugeben. Gleichzeitig hat er mich gelehrt, wie man mit Begeisterung Physik vermitteln kann, und auch dafür bin ich sehr dankbar. Ich bedanke mich darüber hinaus ganz herzlich bei Gregor Jung für die Zweitkorrektur dieser Arbeit. I am indebted to Mete Atatüre for the opportunity to work in his research group. The welcoming atmosphere and the vivid discussions were inspiring, and I am thankful for having experienced this wonderful time. In the same breath, my gratitude goes to Tina Müller and Benjamin Pingault, who were wonderful colleagues in Cambridge and became true friends.

There have been countless discussions about the theory developed in this work with Jeronimo Maze, Adam Gali, Victor Waselowski and Joaquín Minguzzi. Thank you for introducing me to the concept of group theory and always being there for my numerous questions.

Darüber hinaus hat diese Arbeit enorm von der Kooperation und dem Austausch mit weiteren Arbeitsgruppen profitiert. Die Ionenimplantation wurde durchgeführt in Zusammenarbeit mit Jan Meijer und dem Team vom RUBION in Bochum, allen voran Detlef Rogalla und Hans-Werner Becker. An dieser Stelle ein riesiges Dankeschön für den herzlichen Empfang und die tolle Unterstützung. Die Diamantproben in dieser Arbeit wurden hergestellt von Matthias Schreck und seiner Gruppe an der Universität Augsburg (insbesondere Martin Fischer und Stefan Gsell) sowie von Hadwig Sternschulte aus München. Danke für die tollen Proben, die lehrreichen Gespräche und dafür, dass wir immer wieder mit verrückten Ideen zu Euch kommen durften. Die Festkörper-Immersionslinsen wurden von Christoph Pauly aus der Arbeitsgruppe Mücklich, dem besten FIB-Operator an der Saar, in den Diamant geschnippelt. Für Rat und Tat in und um den Reinraum bedanke ich mich beim Team des Nano-Structuring-Centers der TU Kaiserslautern, Sandra Wolff, Bert Lägel und Christian Dautermann. Weiterhin bin ich dankbar für die stets inspirierenden Diskussionen mit Stefan Kück von der PTB in Braunschweig, Anke Krüger in Würzburg, Dong Hun Lee und Alexander Zaitsev.

Auch die Hilfe von Seiten der Universität des Saarlandes sei nicht verschwiegen: Allen voran bedanke ich mich bei Elke Huschens, unserer Sekretärin für ihren tadellosen administrativen Beistand, der mir oft den Weg durch das Chaos des Uni-Dschungels gewiesen hat. Die mechanischen Aufbauten dieser Arbeit wären nicht möglich gewesen ohne die Präzision und den Eifer von Michael Schmidt und seinen exzellenten Mitarbeitern in den

Metallwerkstätten. Mein Dank gilt weiterhin den Elektronikern Rolf Kiefer und Stefan Löw für ihre Hilfe in allen elektronischen Lebensfragen sowie der chemisch-technischen Assistentin Karin Kretsch, die sichergestellt hat, dass ich mich im Chemielabor nicht in die Luft jage. Heinz Schmitt hat der Arbeitsgruppe Becher die Herstellung von Diamanten nähergebracht und mir in vielen physikalischen Fragen sehr geholfen.

Ich bedanke mich bei Christian Wagner, Malte Henkel und Roland Sanctuary, den Programmbeauftragten des Saar-Lor-Lux Studiengangs in Physik für die Möglichkeit, den Studiengang in der Welt bekannt zu machen, und junge Menschen für die Physik jenseits von Landesgrenzen begeistern zu dürfen. Bei meiner Arbeit für den Studiengang hat mich Thomas John unterstützt, der meine Arbeit weiterführen wird, und dem ich dazu Alles Gute wünsche.

Ein Gruß ergeht an alle derzeitigen und ehemaligen Mitglieder der Arbeitsgruppe Becher. Ich bedanke mich für Euren immerwährenden moralischen und physikalischen Beistand, die vielen lehrreichen Diskussion in und zwischen den Gruppensitzungen und dafür, dass Ihr die besten, lustigsten und verrücktesten Kollegen seid, die man sich nur wünschen kann. David und Elke, Ihr habt mich gelehrt, wie man Spektroskopie betreibt und ein konfokales Mikroskop justiert – dafür bin ich Euch immer dankbar. Besonders toll waren die außeruniversitären Aktivitäten, wobei besonders die Weinfeste (Danke Andreas), die vielfältigen Grillveranstaltungen (Danke Carsten und Alexander) und das Skifahren (Danke Roland) genannt werden sollen. Ich wünsche allen Mitgliedern der Arbeitsgruppe, dass sie die bestehende gute Atmosphäre beibehalten und als Team zusammen erfolgreich sind. Alles Gute für Eure Zukunft. Einen besonderen Gruß sende ich an die Diplomanden und Bachelor-Studenten, die ich in den vergangenen Jahren betreut habe: Michel, Elke, Andreas, Annika und Jonas – ich danke Euch sehr für den Beitrag, den Ihr zu den Experimenten dieser Arbeit geleistet habt. Ich hoffe, ich war ein geduldiger und guter Lehrer, und wünsche auch Euch Alles Gute für Eure Zukunft.

Ich bedanke mich bei meinen Freunden, einschließlich meiner Band dafür, dass sie mich aus dem zuweilen frustrierenden Physikerleben zurück in die Realität geholt haben. Ich bin sehr froh für den Rückhalt, den ich in meiner Familie während meiner Promotion genossen habe. Meinen Eltern danke ich besonders, dass sie mein Studium in jeder Beziehung bedingungslos unterstützt haben. Ich durfte Euch alle immer mit meinen Physik-Problemen bequatschen und meistens haben sie sich – wie ihr immer sagtet – irgendwie gelöst.

Am Schluss danke ich meiner geliebten Frau Anne-Katrin für ihre Liebe und für ihre Unterstützung bei diesem abenteuerlichen Unterfangen namens Doktorarbeit. Dank Dir wache ich jeden Morgen als glücklichster Mensch der Welt auf.